

Report

P-18-05

February 2020



EBS TF – THM modelling

Homogenisation task

Lennart Börgesson

Mattias Åkesson

Jan Hernelind

SVENSK KÄRNBRÄNSLEHANTERING AB

SWEDISH NUCLEAR FUEL
AND WASTE MANAGEMENT CO

Box 3091, SE-169 03 Solna
Phone +46 8 459 84 00
skb.se

SVENSK KÄRNBRÄNSLEHANTERING

ISSN 1651-4416

SKB P-18-05

ID 1695688

February 2020

EBS TF – THM modelling

Homogenisation task

Lennart Börgesson, Mattias Åkesson
Clay Technology AB

Jan Hernelind, 5T Engineering AB

This report concerns a study which was conducted for Svensk Kärnbränslehantering AB (SKB). The conclusions and viewpoints presented in the report are those of the authors. SKB may draw modified conclusions, based on additional literature sources and/or expert opinions.

Data in SKB's database can be changed for different reasons. Minor changes in SKB's database will not necessarily result in a revised report. Data revisions may also be presented as supplements, available at www.skb.se.

A pdf version of this document can be downloaded from www.skb.se.

© 2020 Svensk Kärnbränslehantering AB

Preface

A modelling task, denoted the Homogenisation task (Task 5), has been performed within the SKB Task Force on Engineered Barrier Systems (EBS). This report presents the task descriptions and the contributions from two modelling groups financed by SKB.

Jan Hernelind sadly passed away in the beginning of 2020 after a short time of disease. His contributions to modelling different scenarios with the finite element code Abaqus, reported here and in other reports, were necessary and irreplaceable. His modelling skill was outstanding and he never gave up but always came to a solution however difficult the problem seemed to be.

Abstract

As part of the Äspö EBS TF the homogenization processes of bentonite after completed water saturation have been investigated by modelling a number of well-defined small scale laboratory tests with simple geometries and one large scale laboratory tests with complicated geometry. Two groups financed by SKB have been working with these tasks using different approaches and codes.

A number of different well defined basic laboratory tests have been used to calibrate and evaluate material models for swelling of MX-80 bentonite as Subtask 1. Two test scales have been used in the laboratory tests. The original tests included in the task descriptions and intended to be used for the calibration were made in cells with the diameter 5 cm. The small test size made measurements and sampling with high enough accuracy difficult. Therefore tests in a larger scale in cells with the diameter 10 cm was also made.

In addition a large scale so called Self-Healing test SH1 has been modelled as Subtask 2. The test concerned swelling and self-healing of two cavities with the dimensions $35 \times 50 \times 70$ mm cut in a bentonite block with the diameter 300 mm and the height 100 mm. The test included measurement of swelling pressure in 9 positions and suction in 2 positions. The test was terminated after equilibrium and vastly sampled. The density and water ratio of the samples were determined. The test ran for 2 years and 8 months.

The modelling group named SKB2 has used the finite element code Abaqus for modelling the small scale tests and the large scale SH1 test with the following techniques and results:

In Subtask 1 four different test types have been modelled, namely axial swelling, radial outwards swelling, radial inwards swelling and isotropic swelling.

The models used are elastic-plastic models. The elastic part of the model is a so called porous elastic model that has a logarithmic relation between void ratio and average stress. Two different models have been used for the plastic part of the model, Drucker-Prager plasticity model and Claytech plastic cap model.

The axial swelling test was used for checking and calibrating the material models and the other tests were used to evaluate the derived model. For the axial swelling test the Drucker-Prager model could not yield acceptable results regarding the swelling pressure evolution and the final gradient in density that occurred after equilibrated swelling. Instead the Claytech model described already by Börgesson et al. (1995) was used with parameter values derived at that time. However, in order to get the best agreement between measured and modelled results the parameters of the elastic model, the plastic model and the hydraulic conductivity had to be somewhat changed.

Then the calibrated model was checked by modelling the radial outwards swelling test and good agreement was achieved, which confirmed the model.

The models were 2D axial symmetric element meshes and included contact surfaces between the bentonite material and the restraining outer cell surfaces. These contacts were applied with simulated friction with a friction angle of 7° , which was taken as an average of the friction angle of the bentonite at the actual density divided by two (according to friction tests described in Appendix 3).

In order to investigate the influence of friction against the steel surfaces identical calculations were made with the friction angle 0° . The results showed that the density distribution was very little affected by friction. Only if detailed information about the stress distribution is requested the friction must be included. Another conclusion was that the lack of external friction was compensated by the internal friction and that smooth surfaces does not reduce the density gradients significantly.

The radial inwards swelling test was also modelled without friction against the walls. The model did not manage to get complete filling of the central hole. The reason is not clear but it is judged to be caused by numerical imperfections and has been observed in other similar calculations. Otherwise the test and the simulation agreed fairly well.

Finally, a test with the intention to have isotropical swelling was performed and modelled. However, isotropic swelling without Mises stresses cannot occur since water available in the bentonite boundary yields successive swelling from the surface since water is not distributed simultaneously in the entire bentonite specimen.

The overall conclusion of the calibration and evaluation models is that the model simulates bentonite swelling well within a limited density interval but that modelling problems occur at swelling into a cavity.

As Subtask 2 the large scale so called Self-Healing test SH1 was modelled.

A blind prediction was done and delivered before start of the test. The new Plastic Cap material model that had been calibrated and verified in Subtask 1 of the homogenisation task was used for the prediction.

Before termination of the test a number of additional calculations were made in order to improve the results, but without changing the material model or the parameters. Large problems with convergence of the calculations were met with.

The test was also modelled using the old Drucker-Prager plastic material model that had been used for SR-Site.

Finally, the results from the prediction and the other calculations were compared to the measured results. The comparisons yielded the following observations and conclusions:

The calculated time to reach equilibrium of the homogenisation phase was generally 2–3 times shorter than the measured for all calculations. The main reason is judged to be caused by the difference in modelled and actual initial conditions. The actual initial degree of saturation was $S_r = 95\% - 97\%$ compared to the modelled $S_r = 100\%$, which means that some additional water must be taken up by the bentonite. In the model virtually all water needed was already in the bentonite from start. In addition the actual size of the bentonite block was slightly smaller than the inner boundaries of the steel cylinders, which means that some swelling was required.

All models yielded a remaining gap of a few mm in parts of the final contact between the different walls of the cavity. One reason is the element size in the model. Smaller elements would probably reduce the gap but would also mean increased number of elements and cause even larger convergence problems. The Drucker-Prager model yielded slightly smaller remaining gap than the blind prediction.

The spreading of the stresses in the measuring points was larger in the models than measured. Both the blind prediction and the Drucker-Prager model yielded the highest stress 9.5 MPa in the measuring point located furthest away from the cavity and the lowest stress 2.0 MPa in the centre of the cavity while the measurements in corresponding places were 6.0 MPa and 3.3 MPa respectively.

The blind prediction yielded higher void ratio $e = 1.2$ in the centre of the cavity than the measured void ratio $e = 1.0$. The Drucker-Prager model yielded $e = 1.05$, which is in better agreement with measured results. This was also generally the case for the void ratio distribution.

The trials to improve the results by elaborating with the element mesh (but not the material model) were not successful. No better results were achieved.

A general conclusion is thus that the Plastic Cap model underestimated the self-healing ability (or the homogenisation) of the bentonite in the test by yielding too high void ratio and too low stresses in the former cavity. The Drucker-Prager plastic model captured the homogenisation better with a void ratio distribution that agreed rather well with the measured and smaller remaining gaps in the former cavity. However, also this model yielded the same too low stresses in the cavity.

Thus, modelling Subtask 2 with a large scale complicated geometry yielded better results when the Drucker-Prager model was used while Subtask 1 (Börgesson et al. 2015) with small scale simple swelling models yielded much better results when the Plastic Cap model was used. The reason for the better homogenisation and better results of the Drucker-Prager model for Subtask 2 is judged to be that the material model is simpler and convergence much easier to obtain.

The SKB1 modelling group analysed Subtask 1, and the performed work was pursued with two different approaches: i) through attempts to analyse the homogenization tests within the frameworks of the established constitutive models (BBM and BExM) by using Code_Bright; and ii) through development of a new material model based on a body of empirical data from different lab scale experiments, and a thermodynamic relation for the chemical potential of clay water.

With the former approach, emphasis was put on incorporating fundamental properties (i.e. swelling pressure and shear strength) into the established model framework. The actual modelling work was limited to simple geometries with one or two homogeneous elements which were manipulated by stepwise changing one state-variable at the time. However, it was found that the BBM model displays several limitations, e.g. regarding the behaviour during unloading at constant water content and yield surface contraction, and it was therefore not considered meaningful to analyse the BBM any further. The BExM has a consistent representation of unloading and can capture yield surface contraction, and effort was given to the adoption of parameters to the BExM model, so that relevant void ratio dependences for both the swelling pressure and the pre-consolidation stress could be captured. However, the mechanism behind yield surface contraction is attributed to the macro voids in BExM, even at water saturated conditions. The prospects for extending the approach to capture yield surface contraction for water unsaturated conditions didn't therefore look promising,

With the latter approach a model was defined for water saturated conditions and was based on a description for which a clay potential Ψ (defined as stress + suction) for a specific void ratio is assigned in an allowed interval bounded by two lines, for swelling ($\Psi_M - \Delta\Psi/2$) and consolidation ($\Psi_M + \Delta\Psi/2$), respectively. The actual state between these lines is controlled by a path variable (f), with values between -0.5 and $+0.5$, which in turn is governed by the strain (ϵ) history. A stress-strain relation is defined for each principal direction. With this description, the void ratio and the suction are scalars, whereas the stress, the strain and the clay potential are tensors. Numerical solutions for simple 1D geometries (axial, radial and spherical) were developed in an advanced spreadsheet software (MathCad). These solutions also included Darcy's law (and water mass balance) together with a void ratio dependence of the hydraulic conductivity. These calculations demonstrated that the main features (evolution of stresses and final dry density distribution) of the homogenisation tests could be reproduced.

Sammanfattning

Som en del i Äspö EBS TF har homogeniseringsprocesser i bentonit vid full vattenmättnad undersökts genom att dels ett antal väldefinierade små-skaliga laboratorieförsök med enkla geometrier och dels ett storskaligt laboratorieförsök med komplicerad geometri modellerats (Homogenization task). Två grupper som finansierats av SKB har arbetat med denna uppgift och därvid använt olika metoder och koder.

Som Subtask 1 har ett antal väldefinierade laboratorieförsök använts för att kalibrera och utvärdera materialmodeller av svällande MX-80 bentonit. I dessa försök har två olika skalor använts. De ursprungliga försöken införda i uppgiftsbeskrivningen gjordes i celler med diametern 5 cm. Den lilla skalan gjorde mätningar och provtagning svåra att utföra med tillräcklig noggrannhet. Därför gjordes också försök i större skala i celler med diametern 10 cm.

Som Subtask 2 ansattes ett storskaligt laboratorieförsök kallat Self-Healing test SH1. Försöket omfattade svällning och homogenisering av två kaviteter med dimensionerna $35 \times 50 \times 70$ mm som skurits ut i ett bentonitblock med diametern 300 mm och höjden 100 mm. Försöket inkluderade mätning av svälltryck i 9 positioner och porundertryck i 2 positioner. Försöket avslutades efter det att jämnvikt uppnåtts och därefter gjordes en omfattande provtagning och bestämning av vattenkvot och densitet. Försöket pågick i 2 år och 8 månader.

Modelleringsgruppen kallad SKB2 har använt finita elementprogrammet Abaqus för att modellera både de småskaliga försöken och det storskaliga försöket SH1 med följande metoder och resultat:

I Subtask 1 har fyra olika försöksuppställningar modellerats, nämligen axiell svällning, radiell utåtriktad svällning, radiell inåtriktad svällning mot ett hålrum och isotrop svällning.

De mekaniska materialmodellerna är elastisk-plastiska. Den elastiska delen av modellen är en s k "porous elastic model" vilket innebär att den har ett logaritmiskt samband mellan portal och medelspanning. Två olika modeller har använts för den plastiska delen, "Drucker-Prager plasticity model" och "Claytech plastic cap model".

Försöket med axiell svällning användes först för att kontrollera och kalibrera materialmodellerna och de andra användes för att utvärdera modellerna. För den axiella svällningen ledde Drucker-Prager modellen inte till acceptabla resultat varken beträffande svälltrycksutvecklingen eller den slutliga densitetsfördelningen, som uppstod efter avslutad svällning. Istället testades den Claytech-model som utvecklades i Börgesson et al. (1995) med parametrar som togs fram då. Emellertid fick parametrarna i den plastiska modellen och hydrauliska konduktiviteten justeras något för att nå bäst överensstämmelse med mätningarna.

Därefter kontrollerades den kalibrerade modellen genom att modellera försöket med utåtriktad radiell svällning och mycket god överensstämmelse uppnåddes, vilket bekräftade modellens giltighet.

Elementnäten bestod av 2D axialsymmetriska element och inkluderade kontaktytor mellan bentoniten och de yttre begränsningsytorna. Dessa kontakter inkluderade friktion med friktionsvinkeln 7 grader vilket motsvarar ett medelvärde av halva friktionsvinkeln hos bentonit i det aktuella densitetsintervallet (enligt friktionstesterna beskrivna i Appendix 3).

Effekten av friktion mellan stålet i testcellerna och bentonit undersöktes genom att sätta friktionsvinkeln till noll grader. Resultaten visade att densitetsfördelningen påverkades obetydligt. Friktionen behöver bara inkluderas om detaljerad information om spänningsfördelningen önskas. En annan slutsats var att avsaknad av yttre friktion kompenseras av den inre friktionen i bentoniten så att glatta kontaktytor inte påverkar densitetsgradienten signifikant.

Radiell inåtriktad svällning mot ett hålrum modellerades också. Det centrala hålrummet fylldes inte helt i denna modell. Orsaken är inte helt klarlagd men bedöms orsakas av numeriska problem och har även observerats i liknande beräkningar. Förutom detta problem överensstämde beräkningsresultaten väl med försöksresultaten.

Slutligen modellerades ett försök som syftade till att motsvara isotrop svällning. Men isotrop svällning utan Mises-spänningar kan inte inträffa eftersom vattentillgång i randen medför succesiv svällning från ytan eftersom vatten inte fördelas samtidigt i hela bentoniten.

Den övergripande slutsatsen av de beskrivna modelleringarna är att materialmodellen simulerar bentonitens svällning väl inom ett visst densitetsintervall men att problem uppstår vid svällning in i hålrum.

Som Subtask 2 modellerades det storskaliga så kallade "Self-Healing test SH1".

En beräkning en sk blind prediktion gjordes och levererades innan start av försöket. Den nya materialmodellen "Plastic Cap model", som hade kalibrerats och verifierats i Subtask 1, användes för prediktionen.

Innan försöket avslutades gjordes ett antal nya beräkningar för att försöka förbättra resultaten, men utan att ändra materialmodellen eller parametrarna. Dessa beräkningar medförde stora problem med att få beräkningarna att konvergera och gå till slut.

Försöket modellerades också genom att använda den gamla materialmodellen Drucker Prager Plasticity, som hade använts för SR-Site-beräkningarna.

Slutligen utvärderades resultaten av prediktionen och de andra beräkningarna genom att jämföra med mätningar. Dessa jämförelser ledde till följande observationer och slutsatser:

Den beräknade tiden för att uppnå jämnvikt under homogeniseringsfasen var i allmänhet 2–3 gånger kortare än den mätta. Orsaken bedöms orsakas av skillnader i starttillstånd ("initial conditions"). Den verkliga vattenmättnadsgraden var $S_r = 95\% - 97\%$ emedan $S_r = 100\%$ antogs i modellen, vilket betyder att ytterligare vatten behövde tas upp i bentoniten till skillnad från i modellen där allt vatten från början fanns i bentoniten. Dessutom var det verkliga bentonitblocket något mindre än de inre gränserna av stålcyldrarna, vilket betyder att en viss svällning krävdes i verkligheten.

Alla modeller hade ett litet återstående mellanrum på några mm i delar av det slutliga kontaktområdet mellan de olika väggarna i kaviteten. Detta beror delvis på elementstorleken i modellen. Mindre element skulle troligen medföra mindre mellanrum men skulle också kräva ökning av antalet element och orsaka ännu större konvergensproblem. Drucker-Prager-modellen ledde till en viss minskning i mellanrumsstorlek i jämförelse med den blinda prediktionen.

Spridningen i svälltryck i mätpunkterna var större i modellerna än i mätningarna. Både prediktionen och Drucker-Prager-modellen gav största spänningen 9.5 MPa i mätpunkten längst från kaviteten och 2.0 MPa i centrum av kaviteten, medan mätningarna i motsvarande positioner gav 6.0 MPa och 3.3 MPa vid jämnvikt.

Prediktionen gav högre portal $e = 1.2$ i centrum av kaviteten än det uppmätta portalet $e = 1.0$. Drucker-Prager-modellen gav $e = 1.5$, som stämmer bättre med mätresultatet. Detta var också i allmänhet fallet för portalsfördelningen.

Försöken att förbättra resultaten genom att förändra elementmodellen var inte lyckosamma. Bättre resultat åstadkoms inte.

En allmän slutsats är att Plastic Cap modellen underskattade självläkningsförmågan (eller homogeniseringen) hos bentoniten i försöket genom att ge för höga portal och för små svälltryck i den tidigare kaviteten. Modellen med Drucker-Prager-plasticitet fångade homogeniseringen bättre med en portalsfördelning som stämde ganska bra med mätningarna och med en mindre återstående öppning. Men även denna modell gav för låga svälltryck i kaviteten.

Så, Subtask 2 med stor komplicerad geometri, gav bäst resultat med Drucker-Prager-modellen, medan Subtask 1 (Börgesson et al. 2015) med små enkla geometrier, gav mycket bättre resultat med Plastic Cap modellen. Anledningen till att Drucker-Prager-modellen gav bättre lösning för Subtask 2 bedöms vara att materialmodellen är enklare och att lösningen konvergerade mycket lättare.

Modelleringsgruppen SKB1 analyserade Subtask 1 med två olika angreppssätt:

i) genom att försöka analysera homogeniseringsförsöken inom ramverken för de etablerade konstitutiva modellerna (BBM and BExM) genom att använda Code_Bright; och ii) genom utveckling av en ny materialmodell vilken baseras på en stor mängd data från olika laboratorieexperiment, samt en termodynamisk relation för den kemiska potentialen för vattnet i bentoniten.

I det första fallet lades stor vikt vid att inkorporera de fundamentala materialegenskaperna (svälltryck och skjuvhållfasthet) till ramverken för de etablerade modellerna. Det faktiska modelleringsarbetet begränsades till enkla geometrier med ett eller två homogena element vilka manipulerades genom att stegvis ändra en tillståndsvariabel åt gången. Det noterades dock att BBM modellen uppvisade flera begränsningar, t ex beträffande beteendet vid avlastning med konstant vattenkvot och gällande flytytans kontraktion, och därför bedömdes det inte som meningsfullt att undersöka BBM ytterligare. BExM modellen har en sammanhängande representation av avlastning med konstant vattenkvot och kan också beskriva flytytans kontraktion. Stor vikt lades därför på bestämningen av BExM modellens parametervärden så att relevanta portalsberoende hos svälltryck och förkonsolideringstryck skulle kunna erhållas. I BExM modellen tillskrivs mekanismen bakom flytytans kontraktion dock makro-porerna, även vid vattenmättade förhållanden. Förutsättningarna för att kunna utöka metodiken för att även hantera flytytans kontraktion vid omättade förhållanden framstod därför inte som lovande.

I det andra fallet definierades en modell för vattenmättade förhållanden. Denna baserades på antagandet att lerpotentialen Ψ (definierat som spänning + suction) för ett visst portal antar värden inom ett intervall vilket avgränsas av två linjer, för svällning ($\Psi_M - \Delta\Psi/2$) respektive konsolidering ($\Psi_M + \Delta\Psi/2$). Det faktiska tillståndet mellan dessa linjer bestäms av en väg-variabel (f), med värden mellan -0.5 och $+0.5$, vilken i sin tur styrs av den tidigare utvecklingen hos töjningen (ϵ). Ett spännings-töjnings-samband kan därmed definieras för varje huvudspänningsriktning. Enligt denna beskrivning är portal och suction skalärer, medan spänningar, töjningar och lerpotentialer är tensorer. Numeriska lösningar för homogeniseringsproblem i enkla 1D geometrier (axiell, radiell och sfärisk) utvecklades med en avancerad kalkyleringsmjukvara (MathCad). Dessa lösningar inkluderade även Darcy's lag (och en vatten massbalans) tillsammans med ett portalsberoende för den hydrauliska konduktiviteten. Dessa beräkningar visade att huvuddragen i resultaten från homogeniseringstesterna kunde reproduceras.

Contents

1	Introduction	13
2	Task descriptions	15
3	Modelling Task 1 with Abaqus (group SKB2)	17
3.1	General	17
3.2	Modelled laboratory tests	18
3.2.1	Axial swelling	18
3.2.2	Radial outwards swelling	18
3.2.3	Radial inwards swelling	19
3.2.4	Isotropic swelling	22
3.3	Finite element model	23
3.3.1	Hydraulic model	23
3.3.2	Mechanical models	23
3.3.3	Contact properties	25
3.4	Axial swelling	26
3.4.1	Finite element model	26
3.4.2	Modelling with Drucker-Prager	27
3.4.3	Modelling with Claytech plastic cap model	29
3.5	Radial outwards swelling	34
3.5.1	Finite element model	34
3.5.2	Modelling results	34
3.6	Influence of friction against the walls	38
3.7	Radial inwards swelling	40
3.7.1	Finite element model	40
3.7.2	Modelling results	41
3.8	Isotropic swelling	43
3.8.1	Finite element model	43
3.8.2	Modelling results	44
3.9	Summary and conclusions	48
4	Modelling Task 2 with Abaqus (group SKB2)	51
4.1	Task description	51
4.2	Finite element model	53
4.2.1	Hydraulic model	53
4.2.2	Mechanical models	53
4.2.3	Contact properties	55
4.2.4	Element mesh	56
4.2.5	Modelling	56
4.3	Blind prediction	57
4.3.1	General	57
4.3.2	Model	57
4.3.3	Results	57
4.3.4	Conclusions drawn at the blind prediction	60
4.4	Measured results	61
4.4.1	Data readings	61
4.4.2	Sampling results	63
4.5	Comparison with measurements	64
4.5.1	General	64
4.5.2	Transducer measurements	64
4.5.3	Density distribution	66
4.5.4	Conclusions	68

4.6	Updated calculations	68
4.6.1	General	68
4.6.2	Example 1	68
4.6.3	Example 2	70
4.6.4	Conclusions	72
4.7	Calculation with the old Drucker-Prager model	72
4.7.1	General	72
4.7.2	Results	72
4.7.3	Conclusions	75
4.8	Comments and conclusions	75
5	Evaluation of swelling tests with BBM and BExM (SKB1)	77
5.1	Introduction	77
5.2	Barcelona Basic Model	81
5.2.1	Elements of the BBM and the hydraulic model	81
5.2.2	Parameter value adoption	82
5.2.3	“One-element” analysis	84
5.2.4	“Two-element” analysis	88
5.2.5	Unloading step	91
5.3	Barcelona Expansive Model (BExM)	92
5.3.1	Elements of BExM	92
5.3.2	Swelling/consolidation cycle with BExM	94
5.3.3	Basic parameter value adoption for BExM	96
5.3.4	Isotropic swelling with Code_Bright	99
5.3.5	“One-element” analysis – uniaxial swelling with Code_Bright	100
5.4	Concluding remarks	103
6	Development and application of a new material model (SKB1)	105
6.1	Introduction	105
6.2	Definition of stress-strain relations	107
6.3	Method for solving 1D homogenization problems	110
6.4	Parameter value adoption	114
6.5	Model results for 1D homogenization problems	116
6.6	Concluding remarks	123
	References	125
Appendix 1	Task 1 Basic tests for model development – task description and results	127
Appendix 2	Task 1 HR tests – additional tests with high resolution, descriptions and results	139
Appendix 3	Task 1 Description of test techniques and test results from an isotropic swelling test	153
Appendix 4	Task 2 Self Healing Test – task description	157
Appendix 5	Task 2 Self Healing Test – dismantling	163
Appendix 6	Photos of the bentonite ring and equipment used for the test SH1	175
Appendix 7	Timetable for SH1 during start and end of test	177
Appendix 8	Tabulated values of water content after dismantling of SH1	179
Appendix 9	Claytech plastic cap model	185

1 Introduction

The Task Force on Engineered Barrier System (EBS) is an international project arranged by SKB with the purpose to verify and evaluate the capability to model THM-processes in unsaturated and saturated buffer materials and to further develop the codes.

Phase 2 of the EBS Task Force on modelling THM processes in buffer and backfill materials for nuclear waste disposal has been running from 2011. This phase includes a number of THM (thermo-hydro-mechanical) tasks for modelling both well-defined laboratory tests and large scale field tests.

The Task Force is initiated and managed by SKB under supervision by Anders Sjöland, SKB. Antonio Gens, UPC is chairman and Lennart Börgesson, Clay Technology AB is secretary. In addition there is a C-group for modelling geochemical processes that is running in parallel with joint meetings. Twice a year there is a Task Force meeting for a couple of days where the tasks, the modelling results and comparison between results and measurements were presented and discussed.

All defined tasks are given in Table 1-1. Participating organisations besides SKB are for this phase BMWi (Germany), CRIEPI (Japan), Nagra (Switzerland), Posiva (Finland), NWMO (Canada), DOE/UFD (USA), NDA (Great Britain) and RAWRA (Czech Republic).

Table 1-1. Tasks in the EBS Task Force on modelling THM processes; phase 2.

-
1. Sensitivity analysis.
 2. Homogenisation.
 3. Task 8, hydraulic interaction rock/bentonite (common with TF Groundwater Flow).
 4. Prototype Repository.
-

SKB is participating in the THM modelling with two modelling groups with mainly the following persons:

SKB 1: Mattias Åkesson, Ola Kristensson and Daniel Malmberg, Clay Technology AB.

SKB 2: Lennart Börgesson, Clay Technology AB and Jan Hernelind, 5T Engineering AB.

The motivation for having two teams is that different codes with different capabilities and advantages have been used by the two teams. SKB 1 has mainly uses Code Bright while SKB 2 uses the code Abaqus. Both these codes have been used in the modelling for SR-Site.

The homogenisation task is related to erosion and loss of buffer and backfill and subsequent homogenisation afterwards but can also refer to homogenisation in general. The general understanding of bentonite is that it has excellent swelling properties but the homogenisation is not complete due to friction, hysteresis effects and anisotropic stress distributions.

The task involves two parts. In the first part a number of well-defined laboratory swelling tests that have been made are modelled and used for calibration and evaluation of the mechanical model. In the second part a large laboratory scale test that simulates bentonite lost in a deposition hole will be modelled.

In this report the results from the modelling of the homogenisation tasks by the two SKB groups will be presented.

The work performed by the SKB1 modelling team addressed Subtask 1 and was pursued along two paths: i) through attempts to analyse the homogenization tests within the frameworks of the established constitutive models (BBM and BExM), with the emphasis on incorporating fundamental properties (i.e. swelling pressure and shear strength) into model framework; and ii) through development of new material model based on a body of empirical data from different lab scale experiments and a thermodynamic relation for clay water chemical potential. This work also entailed the development of numerical solutions for analysis of the homogenisation tests at hand. These two approaches are described in Chapter 5 and 6, respectively.

2 Task descriptions

All task descriptions are shown as Appendices. Additional information about the tasks, the results of the tests and additional tests done and used for modelling are also presented as Appendices. The following appendices are included:

Appendix 1. Task 1. Basic tests for model development. Task description and results.

Appendix 2. Task 1. HR tests. Additional tests with high resolution. Descriptions and results.

Appendix 3. Task 1. Description of test techniques and test results from an isotropic swelling test.

Appendix 4. Task 2. Self Healing Test. Task description.

Appendix 5. Task 2. Self Healing Test. Dismantling.

3 Modelling Task 1 with Abaqus (group SKB2)

3.1 General

SKB2 (Lennart Börjesson and Jan Hernelind) has used Abaqus finite element program to model and solve the tasks. Abaqus is a general purpose code especially designed for non-linear problems. Abaqus contains a capability of modelling a large range of processes in many different materials as well as complicated three-dimensional geometry.

The code includes special material models for rock and soil and ability to model geological formations with infinite boundaries and in situ stresses by e.g. the own weight of the medium. It also includes capability to make substructures with completely different finite element meshes and mesh density without connecting all nodes. Detailed information of the available models, application of the code and the theoretical background is given in the Abaqus Manuals as well as by Börjesson et al. (2016b).

The homogenisation task includes two parts. In the first part three small well-defined basic laboratory tests are used to calibrate and validate the material models and calculation techniques. This subtask is described in the task description added as Appendix 1. In these tests oedometers with the diameter 50 mm were used.

However, these tests described in the task description have not been used for the model calibration described here since the resolution of test results was not very good due to the small size of the specimen. Instead other tests made in the same way but in a larger scale in oedometers with the diameter 100 mm have been used. These new tests were described in an additional PM appended as Appendix 2, which also includes tests to determine the friction between steel and bentonite.

Figure 3-1 illustrates the basic tests used for subtask 1.

In addition results from another test in the same scale with 100 mm diameter but with isotropic swelling have been reported and can be used for the model check. This test is described in Appendix 3. Figure 3-2 illustrates that test.

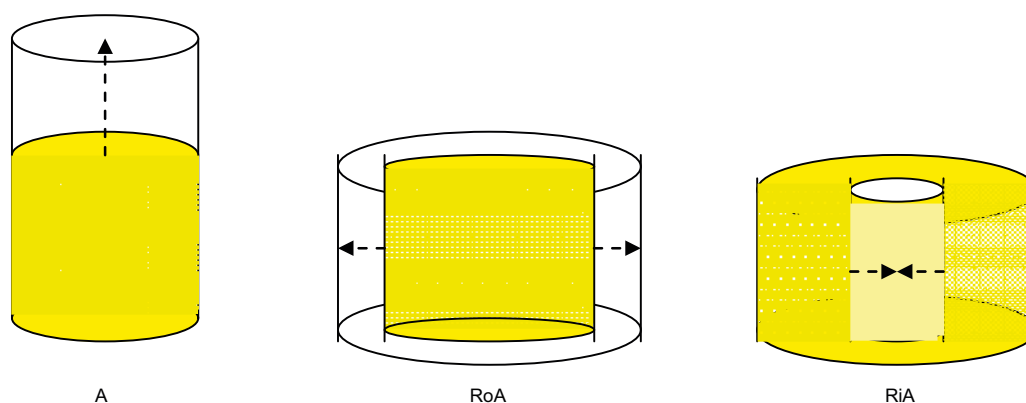


Figure 3-1. Illustration of the geometry of the test types carried out.

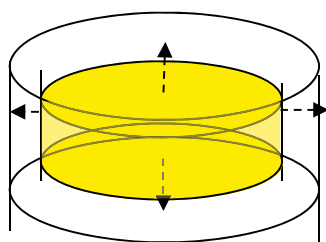


Figure 3-2. Illustration of the isotropic swelling test.

3.2 Modelled laboratory tests

Four tests have been modelled in order to calibrate and evaluate the material model and to investigate if there are some problems or traps in the modelling that can be avoided or reduced. Only the HR-tests have been modelled. All specimens were fully water saturated from start.

3.2.1 Axial swelling

The axial swelling test is described in Appendix 2. The axial stress is measured in the swelling direction and the radial stress is measured in 3 points at the periphery. Figure 3-3 shows the set up.

Radial swelling pressure was measured 15 mm, 30 mm and 45 mm from the bottom of the oedometer.

The initial dry density was 1666 kg/m^3 corresponding to a void ratio of $e = 0.67$. The swelling was $\Delta V/V = 26\text{--}32\%$ depending on how it was measured. The reason for this discrepancy is not clear. The higher value was used in the modelling. The test ran for about 70 days. The results are shown in Appendix 3 and in Chapter 5.

3.2.2 Radial outwards swelling

The radial outwards swelling test is described in Appendix 2. Figure 3-4 shows the set-up.

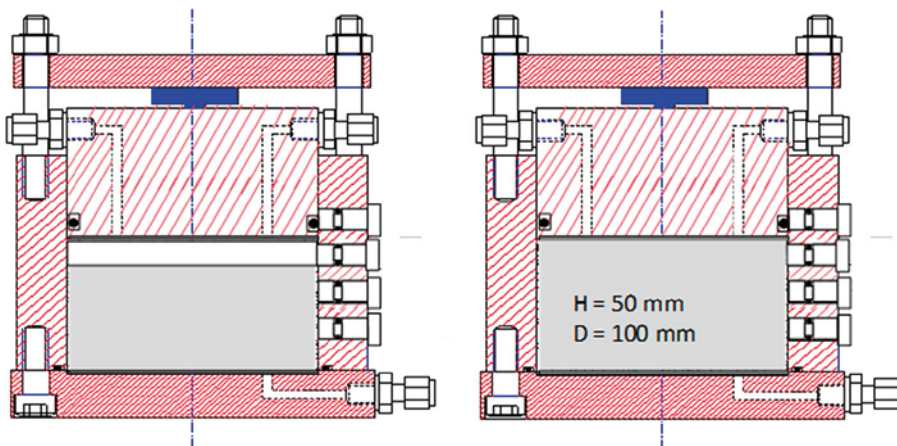


Figure 3-3. Set-up used for the axial swelling tests (HR-A). Water is only supplied from a filter placed above the specimen.

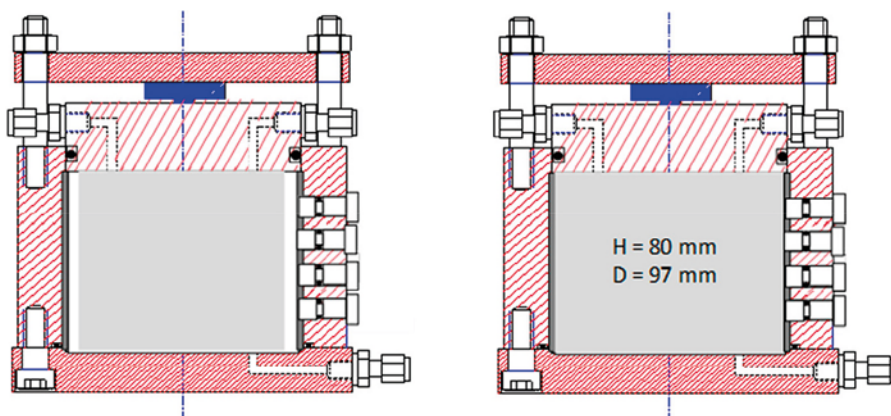


Figure 3-4. Set-up used for the radial outward swelling tests (HR-Ro). Water is supplied from a radial filter between the surrounding steel ring and the specimen.

Axial swelling pressure was measured on the top lid and radial swelling pressure was measured 15 mm, 30 mm, 45 mm and 60 mm from the bottom of the oedometer.

The initial dry density was 1666 kg/m^3 corresponding to a void ratio of $e = 0.67$. The swelling was $\Delta V/V = 42\text{--}43\%$ and the test ran for about 55 days. The results are shown in Appendix 2.

3.2.3 Radial inwards swelling

The equipment used for the radial inwards swelling test is identical to the one used for the outwards swelling and described in Appendix 2. Figure 3-5 shows the set-up.

Axial swelling pressure was measured on the top lid and radial swelling pressure was measured 40 mm from the bottom of the oedometer. Only one of the radial transducers was used.

The initial dry density was 1666 kg/m^3 corresponding to a void ratio of $e = 0.67$. The swelling was about 40 % and the test ran for about 130 days.

Figure 3-6 shows the evolution of the measured stress.

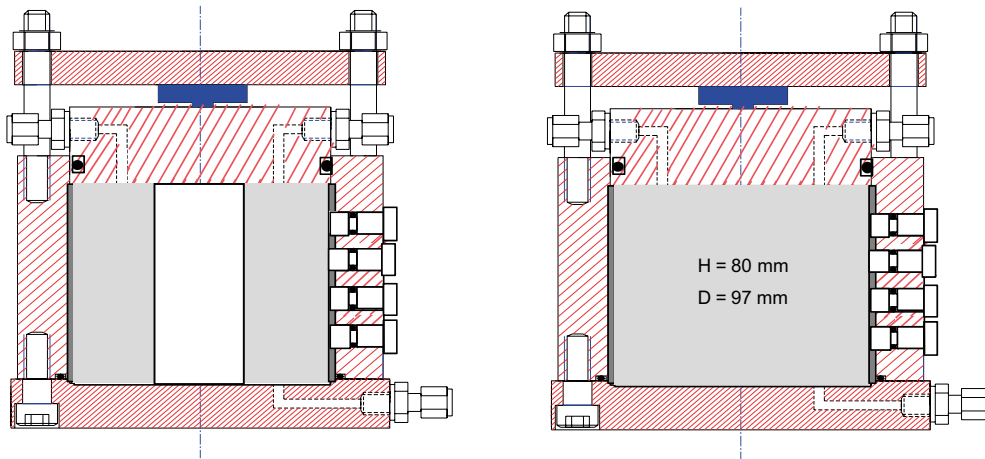


Figure 3-5. Set-up used for the inward radial swelling tests (HR-Ri). Water is initially filled into the cavity and then only supplied from a radial filter between the surrounding steel ring and the specimen.

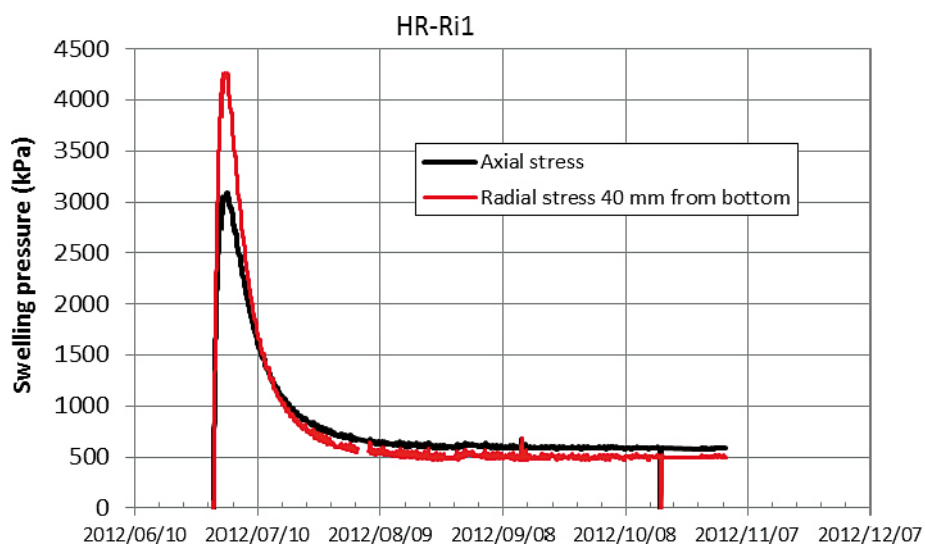


Figure 3-6. Evolution of the swelling pressure from test HR-Ri1.

The water ratio and density distribution after completed swelling after the test was measured by dividing the central part of the specimen in 5 mm pieces as shown in Figure 3-7. It is desired to have the sampling done so that the density distribution could be plotted as a function of the radius but since this would give too small samples close to the centre, the sampling had to be done as shown in the figure. The density distribution is shown in Figure 3-8. The degree of saturation was in average 100 %.

The results in Figure 3-8 are not a correct representation of the density as function of the radius since the average distance of the samples to the centre is larger than shown. The average distance of each sample is better represented by the blue line in Figure 3-7 since the x-axis is also a symmetry plane. This is analysed in Figure 3-9.

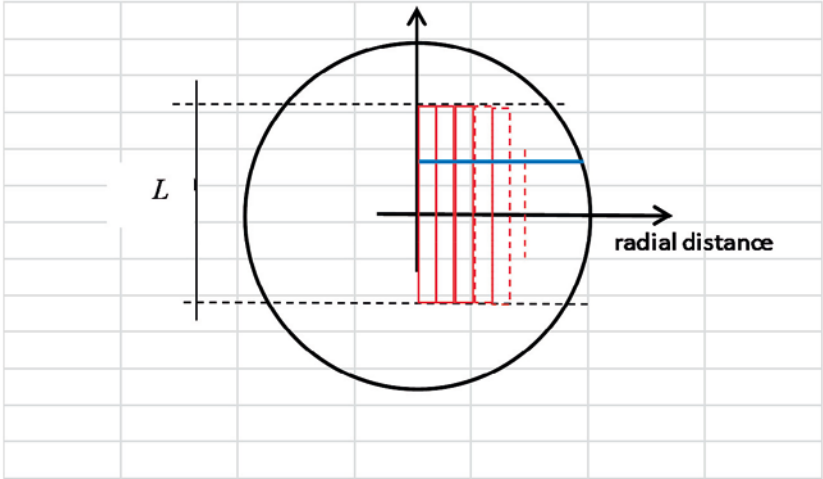


Figure 3-7. Sampling scheme for the HR-Ri1 test.

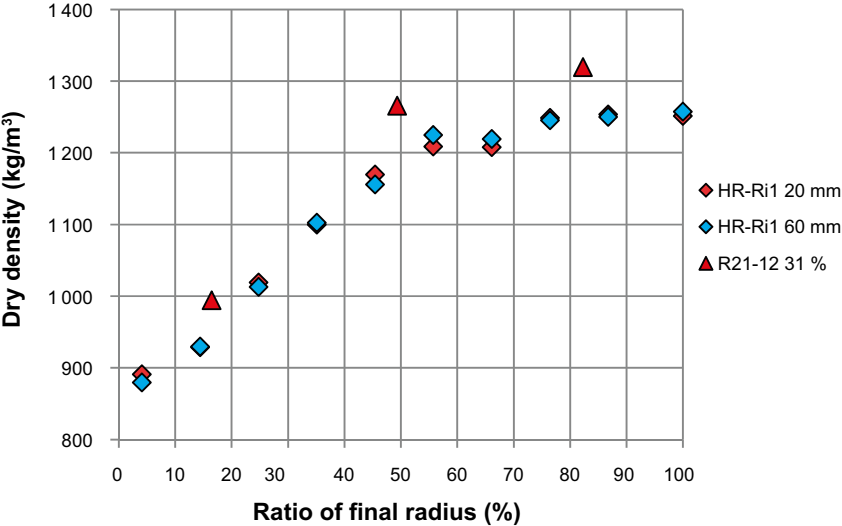


Figure 3-8. Dry density distribution measured in two levels. Results from a test in smaller scale (50 mm diameter) are also shown R21-12 (31 % swelling).

The centre of gravity of the samples is where the inclined arrow is pointed at since the horizontal line is a symmetry plane. The correct radius r_c will thus be expressed as a function of the apparent radius r_a according to Equation 3-1.

$$r_c = (r_a^2 + a^2)^{0.5} \quad (3-1)$$

For the HR-Ri1 test $L = 35$ mm, which yields $a = 8.75$ mm.

The corrected results are shown in Figure 3-10.

Similar problems are present for the outwards swelling tests, but the error is very small at the periphery so this correction has not been done for those tests.

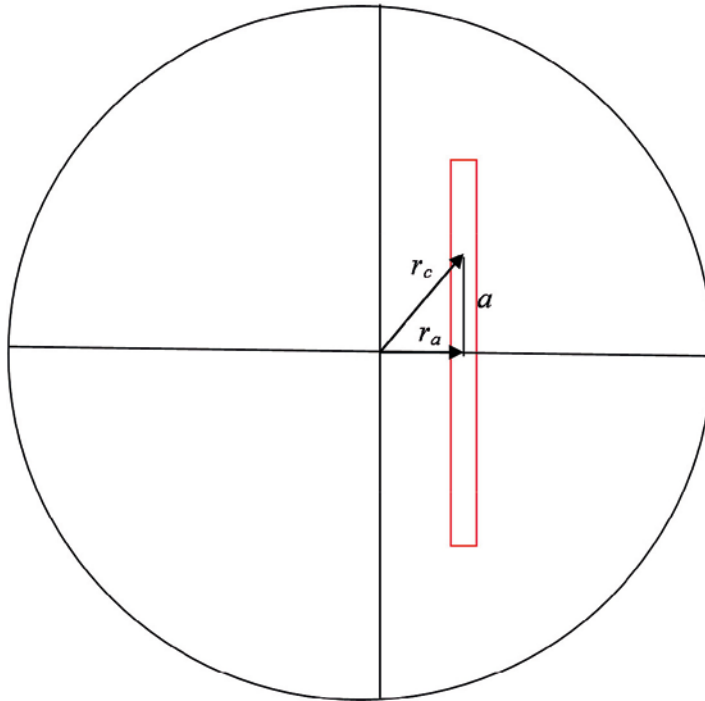


Figure 3-9. Calculation of the correct radius of the sampling.

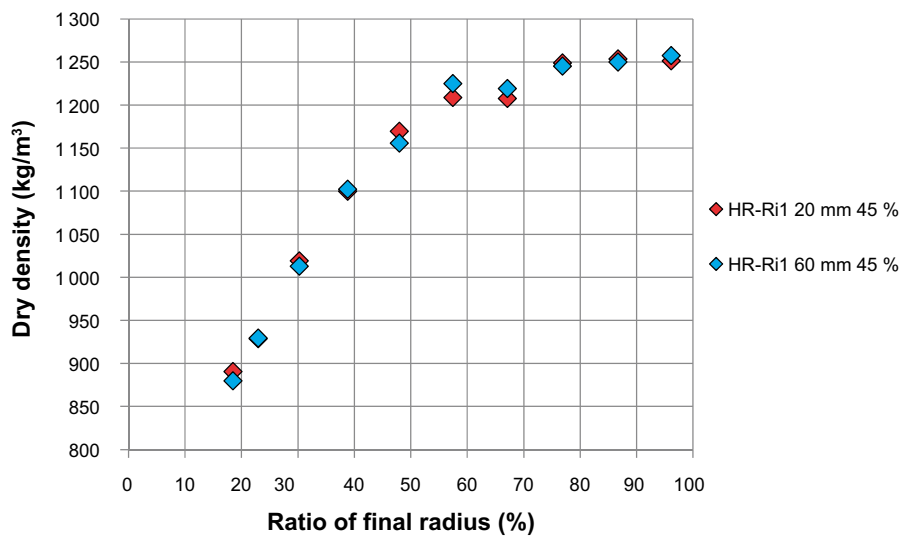


Figure 3-10. Dry density distribution expressed as function of the corrected radius.

3.2.4 Isotropic swelling

The isotropic swelling test is described in Appendix 4. The axial stress is measured in the lid and the radial stress is measured in 4 points at the periphery. Figure 3-11 shows the set up.

The initial dry density was 1684 kg/m^3 corresponding to a void ratio of $e = 0.65$. The swelling was $\Delta V/V = 34 \%$ and the test ran for about 130 days. The results described in Appendix 4 have been corrected in the same way as the inwards swelling test. The specimen was sliced horizontally in seven slices and the central ones have been used for determining the density distribution. Figure 3-12 shows the measured density distribution.

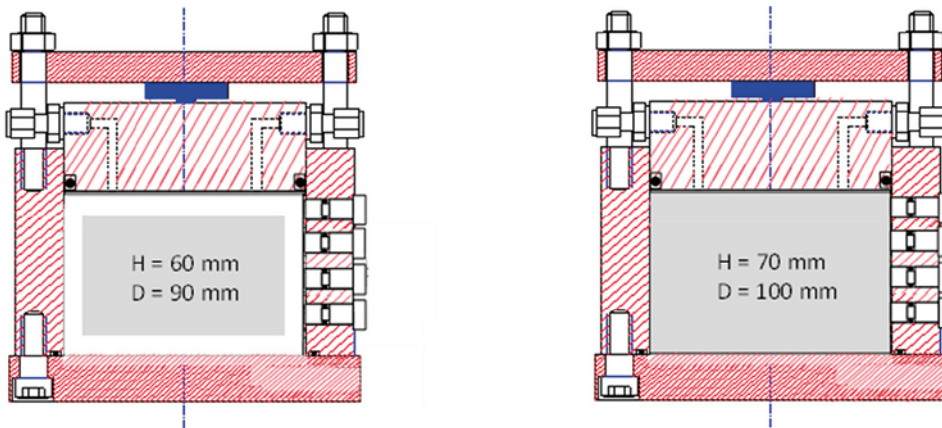


Figure 3-11. Set-up used for the test HR-Iso.

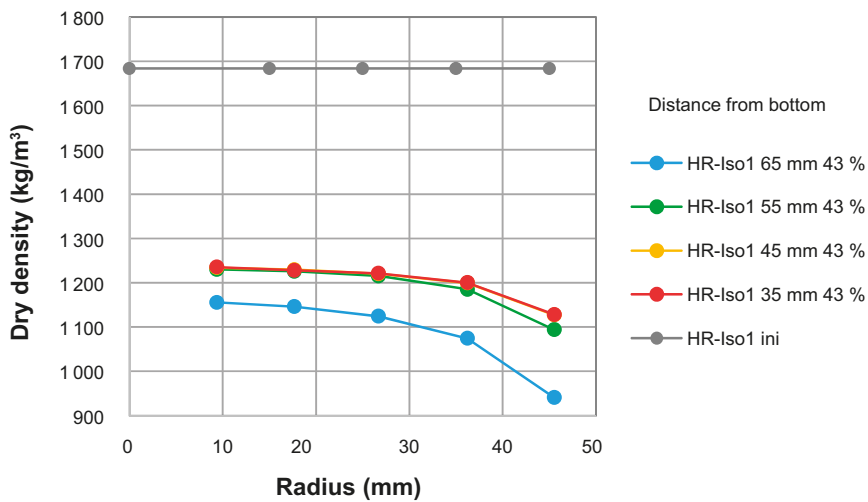


Figure 3-12. Measured density distribution in the central slices of the isotropic test. The values are corrected according to Equation (3-1).

3.3 Finite element model

The tests are modelled with the finite element code Abaqus. The code and the material model used for SR-Site are described by Åkesson et al. (2010a, b). The material models used for the present tests are described in detail by Börgesson et al. (1995). The code is also described by Börgesson et al. (2016a, b).

The material models are coupled hydro-mechanical with the effective stress theory as base. Full water saturation is assumed for these models. The hydraulic model use Darcy's law with hydraulic conductivity modelled as a function of the void ratio.

Two mechanical material models have been used. Both models are elastic-plastic models and use porous elasticity for the elastic model. One of the plastic models uses Drucker-Prager plasticity while the other one is a plastic cap model "Claytech model" derived by Börgesson et al. (1995). The models are described in Börgesson et al. (1995). The plastic cap model is also described in Appendix 9.

3.3.1 Hydraulic model

The original hydraulic conductivity relation taken from Börgesson et al. (1995) is shown in Figure 3-13.

3.3.2 Mechanical models

The original parameter values in the mechanical models are described below.

Porous elastic

Porous Elastic implies a logarithmic relation between the void ratio e and the average effective stress p according to Equation 3-2.

$$\Delta e = -\kappa \cdot \Delta \ln p \quad (3-2)$$

where κ = porous bulk modulus

Poisson's ratio ν is also required.

$$\kappa = 0.21$$

$$\nu = 0.4$$

Figure 3-14 illustrates Equation 3-2.

This relation is not valid for low densities (see Börgesson et al. 1995) but only in the interval $0.7 < e < 1.5$, which correspond to $1110 \text{ kg/m}^3 < \rho_d < 1635 \text{ kg/m}^3$. At lower densities the porous bulk modulus is much larger ($\kappa \approx 1.37$) but this change in modulus is not included in the model. If swelling causes a lower density the swelling will not be correctly modelled for that part.

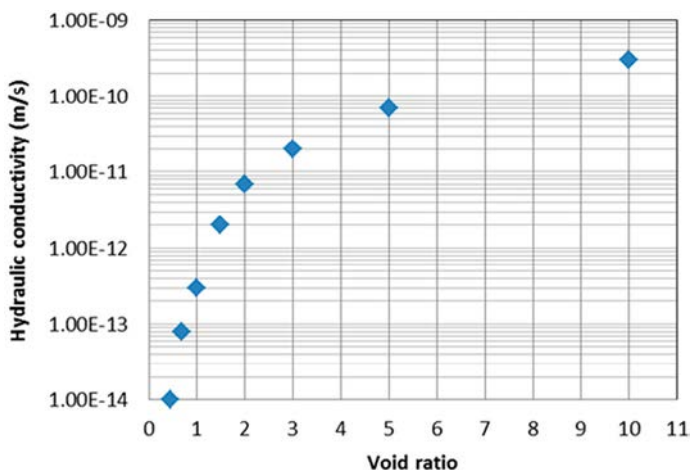


Figure 3-13. Original relation between hydraulic conductivity and void ratio.

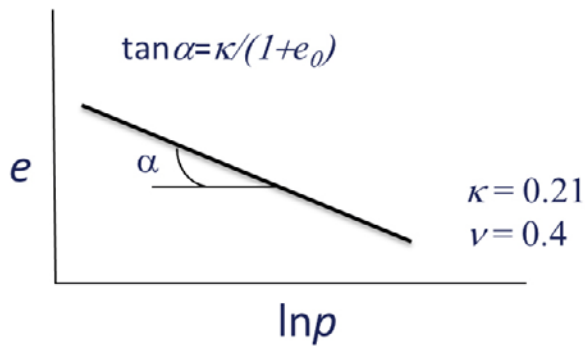


Figure 3-14. Illustration of Porous Elastic.

Drucker-Prager Plasticity model

Drucker-Prager Plasticity contains the following parameters:

β = friction angle in the p - q plane

δ = cohesion in the p - q plane

Ψ = dilation angle

$q = f(\epsilon_{pl}^d) =$ yield function

The parameter values in this model are as follows:

$\beta = 17^\circ$

$\delta = 100$ kPa

$\Psi = 2^\circ$

$q = f(\epsilon_{pl})$

Table 3-1. Yield function.

q (kPa)	ϵ_{pl}
112	0
138	0.005
163	0.02
188	0.04
213	0.1

Figure 3-15 illustrates the Drucker-Prager model.

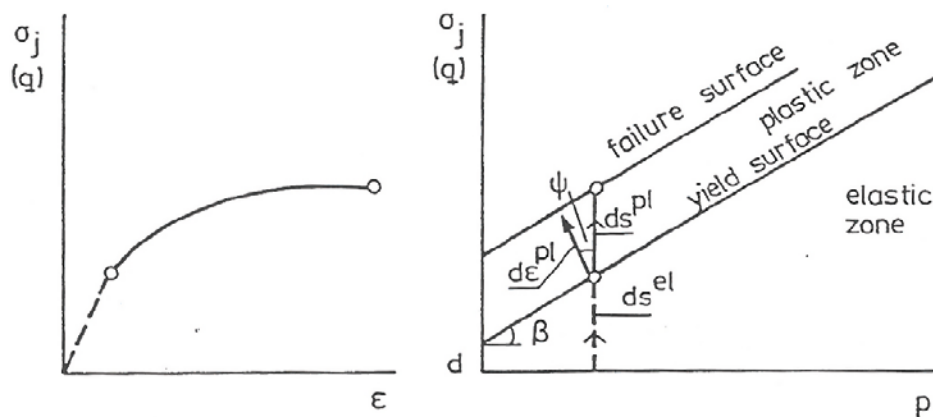


Figure 3-15. Illustration of the Drucker-Prager model.

Claytech plastic cap model

This model and its background are described in detail in Börjesson et al. (1995). An overview of the model and its parameters are given in Appendix 9.

The parameters of the model and their initial values taken from Börjesson et al. (1995) are

$$a = 2.45$$

$$c = 2.20$$

$$b = 0.77$$

$$K = 1.0$$

$$\gamma = 0.1$$

$$R = 0.1$$

$$p_b = 17\,000 \text{ kPa}$$

$$p_f = -25\,000 \text{ kPa}$$

Cap hardening = see Table 3-2

Table 3-2. Cap hardening function.

p (kPa)	$e^{\log(1+e^V_{pl})}$
100	0
200	0.103
400	0.192
750	0.264
1200	0.299
2000	0.323
3500	0.379
5500	0.396
8500	0.415
17000	0.444
30000	0.490

3.3.3 Contact properties

The shear resistance between the test specimen and the surrounding steel cylinder has been investigated with a large number of friction tests. The equipment is described in Appendix 2. Figure 3-16 shows some results (Dueck et al. 2014).

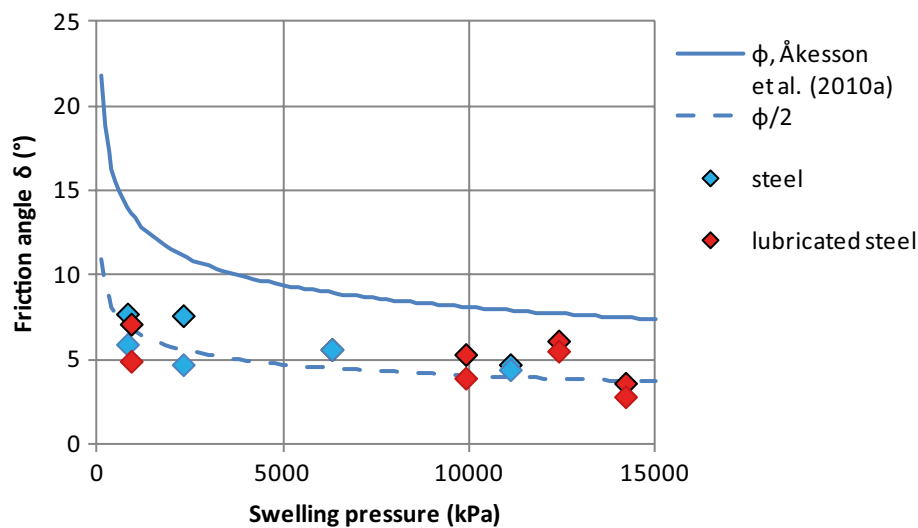


Figure 3-16. The friction angle between steel and bentonite δ evaluated from friction tests described in Appendix 2 and compared to the internal friction angle in bentonite ϕ .

The relation between the deviator stress at failure q_f and the average stress p is modelled according to Equation 3-3, which is in agreement with the failure envelop used in the Claytech cap model (Appendix 9).

$$q_f = q_{f0} \cdot \left(\frac{p}{p_0} \right)^b \quad (3-3)$$

where $q_{f0} = 500$ kPa $p_0 = 1\,000$ kPa and $b = 0.77$

The relation between the friction angle ϕ in the bentonite and p and q is calculated according to Equation 3-4.

$$\phi = \arcsin \left(\frac{3q}{q+6p} \right) \quad (3-4)$$

Figure 3-16 shows that the friction angle between bentonite and steel is about half the inner friction angle of bentonite. This has been used for the modelling.

The contact between the bentonite specimen and the surrounding steel tube or steel plate ϕ_c has been modelled according to Equation 3-5.

$$\phi_c = \phi/2 \quad (3-5)$$

3.4 Axial swelling

3.4.1 Finite element model

The axial swelling test in the larger cell (HR-A test) was modelled in order to check the results and calibrate the material model parameters. The test is described in 3.2.1 and Appendix 2. At first the Drucker-Prager model was used and then the Claytech Cap model with different parameter settings.

The finite element mesh and the initial conditions are the same for all simulations. The following geometry is used:

- Radius: 50 mm
- Start height: 37.4 mm
- End height: 50 mm

Start properties: $u_0 = -10$ MPa, $e_0 = 0.70$; $\rho_{d0} = 1\,635$ kg/m³

End average properties: $u = 0$ MPa, $e = 1.22$; $\rho_d = 1\,250$ kg/m³

Swelling $\Delta V/V = 33.6$ %

Swelling with water available at the top surface

Radial contact surface with friction $\phi = 7^\circ$

The mesh is shown in Figure 3-17.

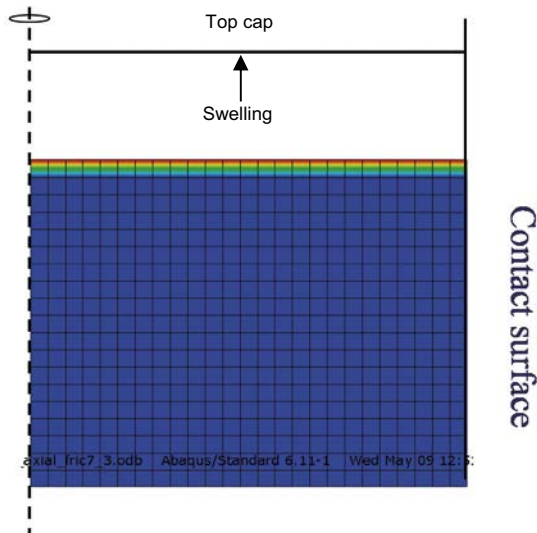


Figure 3-17. Element mesh for the axial swelling test. Axial symmetry at the left side and contact surfaces at the other sides.

3.4.2 Modelling with Drucker-Prager

The test was modelled with the Drucker-Prager plasticity model described in Section 3.3.2. The hydraulic model and the Porous Elastic models described in Sections 3.3.1 and 3.3.2 were used. Figure 3-18 shows the results at equilibrium after completed homogenisation regarding the void ratio distribution.

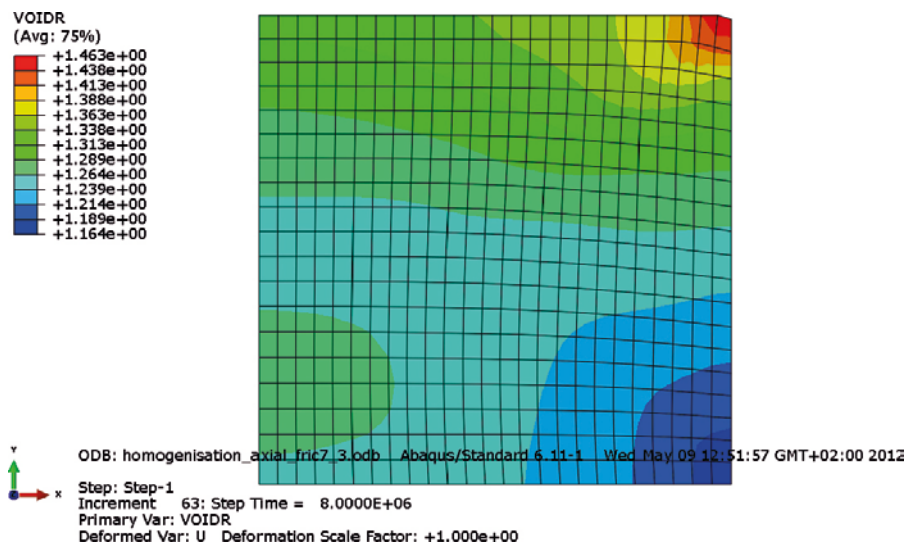


Figure 3-18. Void ratio distribution at equilibrium after 93 days. Axial symmetry at the left side and contact surface at the right side.

The influence of the friction is obvious with a much larger inhomogeneity along the outer surface. Figure 3-19 shows the dry density distribution in axial direction at different times.

Figure 3-20 shows comparison between modelled and measured results. The modelled dry density distribution along the outer periphery and along the symmetry axis is compared with the measured average density distribution. The comparison shows that the measured density, with a density gradient of 300 kg/m^3 over 5 cm (from 1350 kg/m^3 to 1050 kg/m^3), is more inhomogeneous than the modelled, which has a density difference of (taking the average) only 90 kg/m^3 (1260 kg/m^3 to 1170 kg/m^3). The model thus strongly underestimates the inhomogeneity.

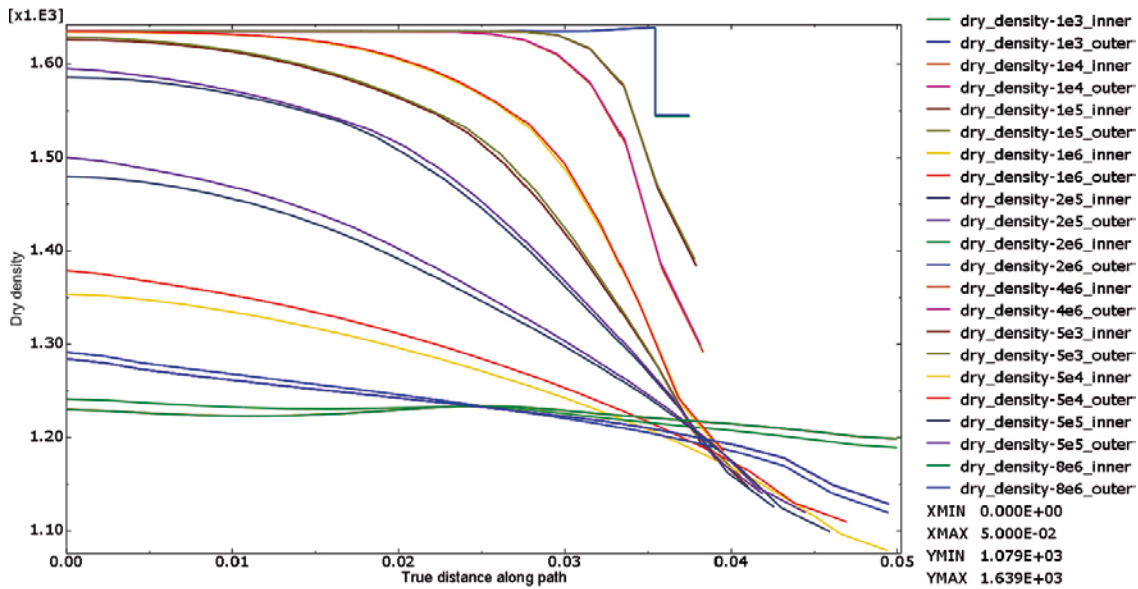


Figure 3-19. Dry density (kg/m^3) plotted as a function of the axial distance (m) from the bottom of the oedometer at different times (s). Two sections are plotted; outer = periphery of the cell; inner = symmetry axis.

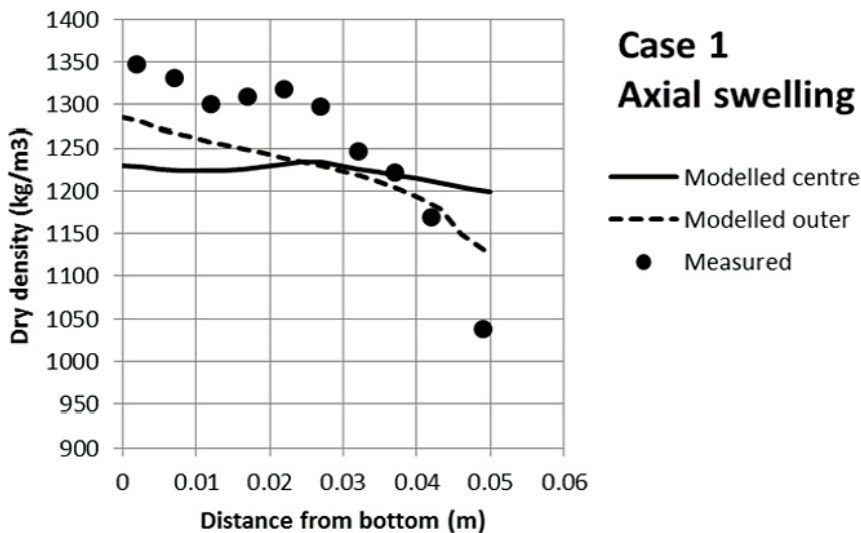


Figure 3-20. Drucker-Prager model. Modelled and measured density distribution.

Figure 3-21 shows the modelled normal stresses as a function of time and compares them to the measured ones. The figure shows that the modelled stresses are generally 25–50 % too low and that the modelled time evolution is too fast. The modelled equilibrium is reached about twice as fast as measured.

The conclusions from these analyses are thus

- A new model is needed in order to be able to better predict the remaining inhomogeneity after equilibrium.
- The hydraulic conductivity needs to be reduced with a factor of 2.

3.4.3 Modelling with Claytech plastic cap model

Original model parameters

The test was then modelled with the Claytech plastic cap model with the parameters shown in Section 3.3.2 and the following elastic model parameters:

$$\kappa = 0.21$$

$$\nu = 0.4$$

The hydraulic conductivity was reduced with a factor 2:

$$K' = K/2$$

Where K is the hydraulic conductivity described in Figure 3-13.

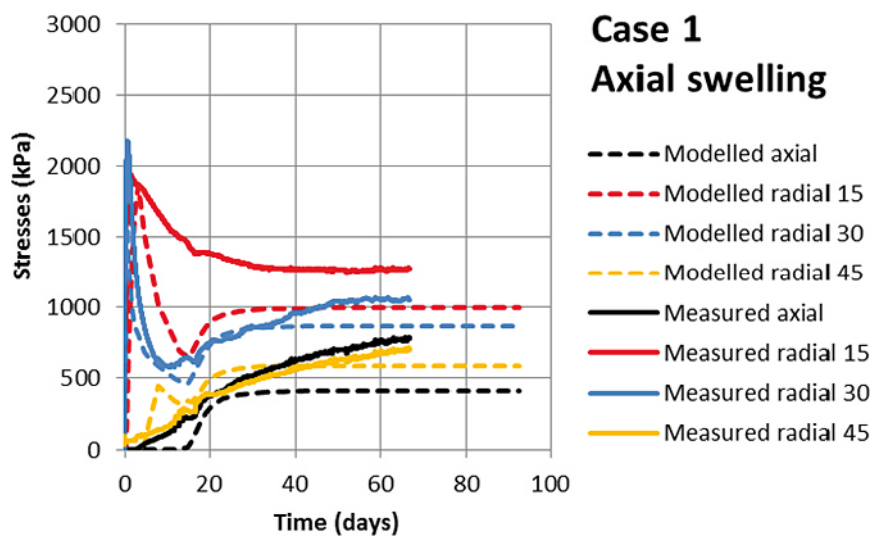


Figure 3-21. Drucker-Prager model. Modelled and measured evolution of normal stress.

Otherwise, identical geometry, material models and modelling technique were used. Figures 3-22 and 3-23 show the results and comparisons with measurements.

Figure 3-22 shows that the density distribution after equilibrium is quite well modelled. The modelled density gradient is (averaged) 310 kg/m^3 over 5 cm (1335 kg/m^3 to 1025 kg/m^3), which is very close to the measured gradient 300 kg/m^3 .

The normal stresses are however not well modelled as shown in Figure 3-23, which means that some parameters need to be changed.

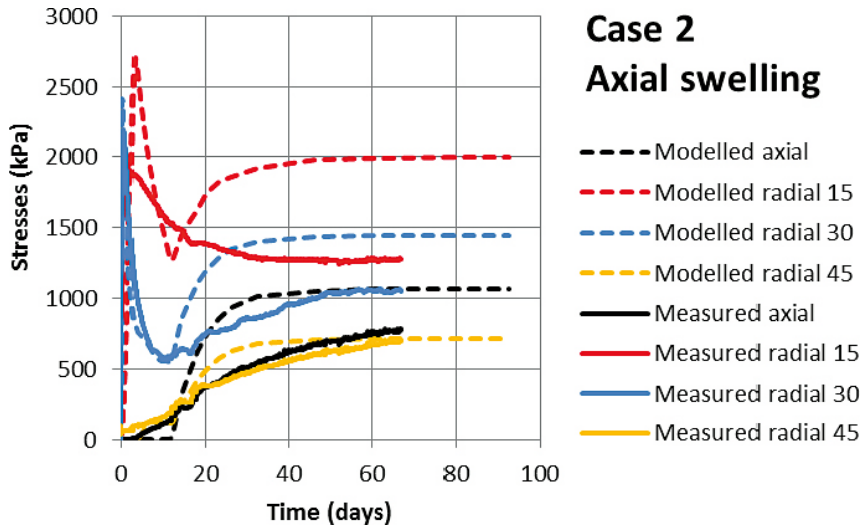


Figure 3-22. Claytech plastic cap model. Modelled and measured density distribution.

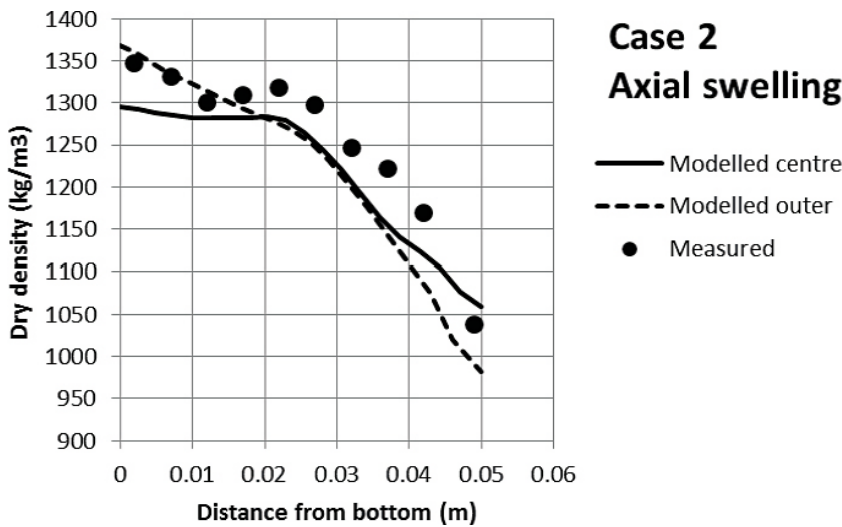


Figure 3-23. Claytech plastic cap model. Modelled and measured evolution of normal stress.

Calibrated model parameters

In order to reach a better agreement between measured and modelled stresses a number of calibration calculations were done. The following main parameter changes gave satisfactory results.

- The cap position was moved to $p_b = 30\,000$ kPa.
- Cap hardening was changed (Table 3-3).
- Porous elastic was changed to $\kappa = 0.175$.

These changes gave the following material parameters:

Porous elastic

$$\kappa = 0.175$$

$$\nu = 0.3$$

Claytech plastic cap model

$$a = 2.45$$

$$c = 2.20$$

$$b = 0.77$$

$$K = 1.0$$

$$\gamma = 0.2$$

$$R = 0.1$$

$$p_b = 30\,000 \text{ kPa}$$

$$p_f = -25\,000 \text{ kPa}$$

Cap hardening = see Table 3-3

Table 3-3. Cap hardening function.

p (kPa)	$e^{\log(1+e^{\nu} p)}$
100	0
331	0.1133
934	0.2112
2160	0.2904
3247	0.3289
4294	0.3553
8240	0.4169
10044	0.4356
12530	0.4565
13299	0.4621
17562	0.4884
30000	0.5390

Hydraulic conductivity = see Table 3-4

Table 3-4. Hydraulic conductivity as a function of void ratio.

e	k (m/s)
0.45	0.5×10^{-14}
0.70	4.0×10^{-14}
1.00	2.0×10^{-13}
1.5	1.0×10^{-12}
2.00	0.5×10^{-11}
3.00	1.0×10^{-11}
5.00	3.5×10^{-11}
10.00	1.5×10^{-10}
20.00	0.75×10^{-9}

Otherwise, identical geometry, material models and modelling technique were used as described in Section 3.4.1. Figures 3-24 and 3-25 show the results and comparisons with measurements.

The modelling results agree satisfactorily with the measuring results, which mean that these parameter values will be used for further modelling.

Figure 3-24 shows that the density distribution after equilibrium is quite well modelled. The modelled density gradient is (averaged) 350 kg/m^3 over 5 cm (1300 kg/m^3 to 1050 kg/m^3), which is close to the measured gradient 300 kg/m^3 .

Figure 3-25 shows that also the modelled evolution of the normal stress is fairly OK although not perfect. The two highest radial stresses agree well while the modelled lowest radial and axial stresses are lower than measured.

As shown in Figure 3-24 the modelled final average dry density is a little lower than the measured, which obviously must be caused by too low initial dry density in the model. So the modelled stresses are logically lower than the measured.

Some observations:

The initial phase of the stress evolution (10–20 days) agrees very well for the radial stress at 30 mm with a peak stress very early and then a decrease in stress followed by a new increase in stress. This phenomenon is also modelled for the stress at 15 mm but the strong reduction is not measured. The reason for this difference is not clear.

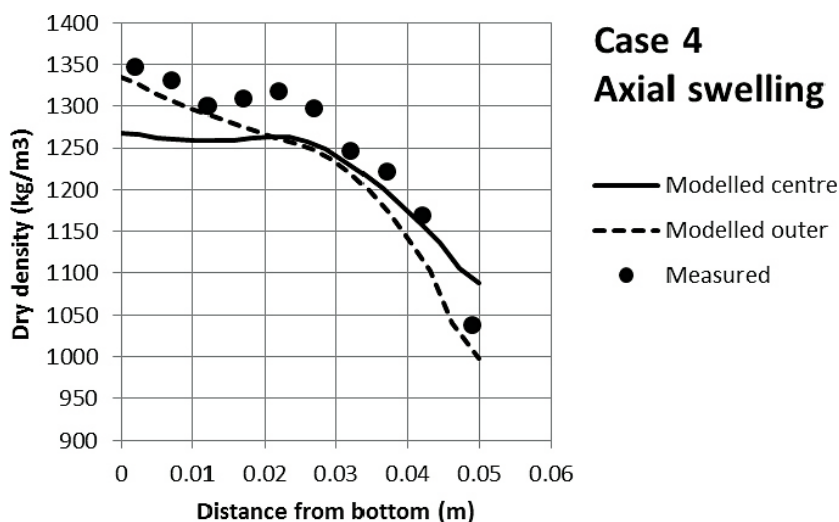


Figure 3-24. Calibrated Claytech plastic cap model. Modelled and measured density distribution.

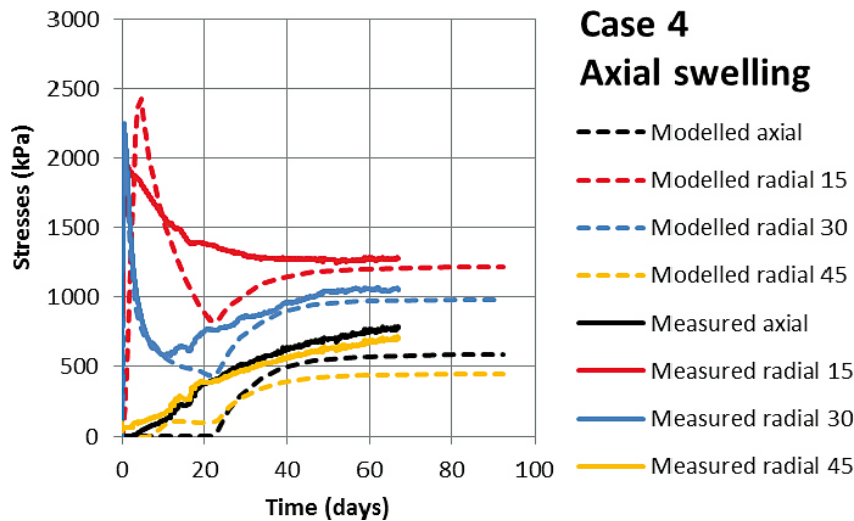


Figure 3-25. Calibrated Claytech plastic cap model. Modelled and measured evolution of normal stress.

The radial stress evolution at 45 mm and the axial stress distribution on top of the oedometer differ significantly from the measured during the first 20 days. According to the measurements the stress starts increasing very early while the modelled stress is very low and the axial stress zero during the first 20 days. The reason for this difference is probably mainly caused by the erroneous porous elastic modulus κ at high void ratios as pointed out earlier. The early swelling is strongly underestimated.

The evolution of the dry density distribution with paths at different times is shown in Figure 3-26.

Conclusions

The conclusion of the model calibration of the Claytech plastic cap model is that it can satisfactorily model the axial swelling in the HR test equipment. Now it remains to see if the model also works for other geometries and swelling scenarios.

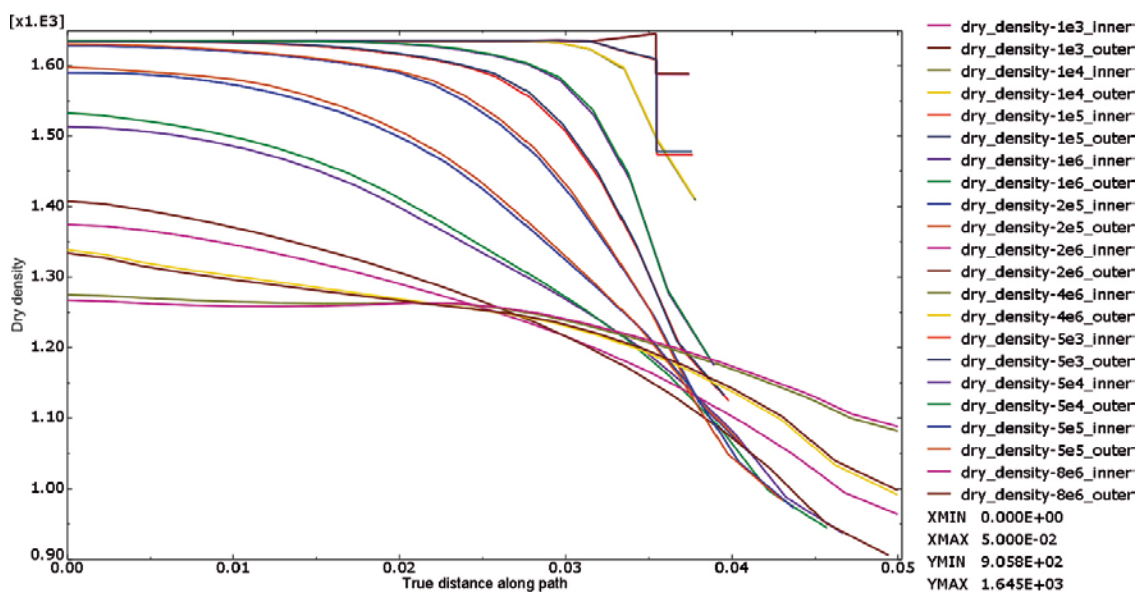


Figure 3-26. Calibrated Claytech plastic cap model. Dry density (kg/m^3) plotted as a function of the axial distance (m) from the bottom of the oedometer at different times shown in the legend (s). Two sections are plotted; outer = periphery of the cell; inner = symmetry axis.

3.5 Radial outwards swelling

3.5.1 Finite element model

The radial outwards swelling test in the larger cell (HR-Ro test) was modelled in order to validate that the material model parameters that were calibrated for the axial swelling also works for radial swelling. The test is described in Chapter 3.2.2 and Appendix 2.

The following geometry is used for modelling the test HR-Ro1:

- Height: 80 mm
- Start radius: 40.5 mm
- End radius: 48.5 mm

Start properties: $u_0 = -10$ MPa, $e_0 = 0.70$; $\rho_{d0} = 1\,635$ kg/m³

End average properties: $u = 0$ MPa, $e = 1.44$; $\rho_d = 1\,140$ kg/m³

Swelling $\Delta V/V = 43.4$ %

Swelling with water available at the outer radius confinement

Axial contact surfaces with friction $\phi = 7^\circ$

The mesh is shown in Figure 3-27.

3.5.2 Modelling results

The test was modelled with identical material model and modelling technique as the axial swelling test after parameter calibration (Section 3.4.3). Figure 3-28 shows the void ratio distribution at equilibrium after completed homogenisation.

The remaining heterogeneities in axial direction are consequences of the friction at the end phases (top and bottom).

Figures 3-29 and 3-30 show the modelling results and comparison with measured results.

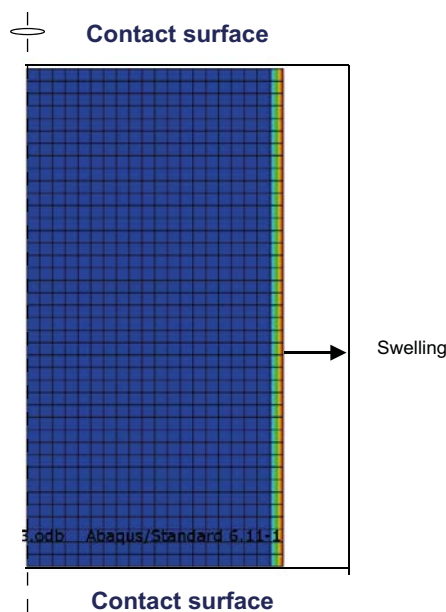


Figure 3-27. Element mesh for the radial swelling test. Axial symmetry at the left side and contact surfaces at the other sides.

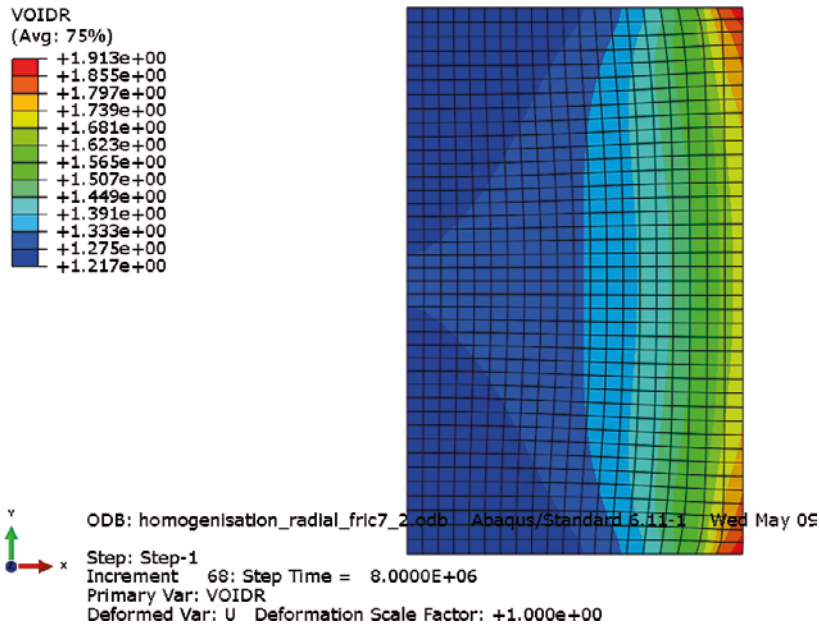


Figure 3-28. Void ratio distribution at equilibrium. Axial symmetry at the left side.

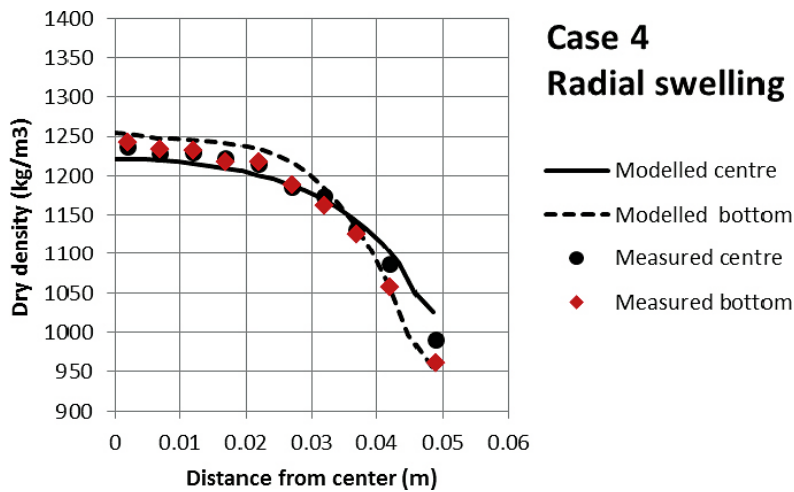


Figure 3-29. Modelled and measured dry density distribution.

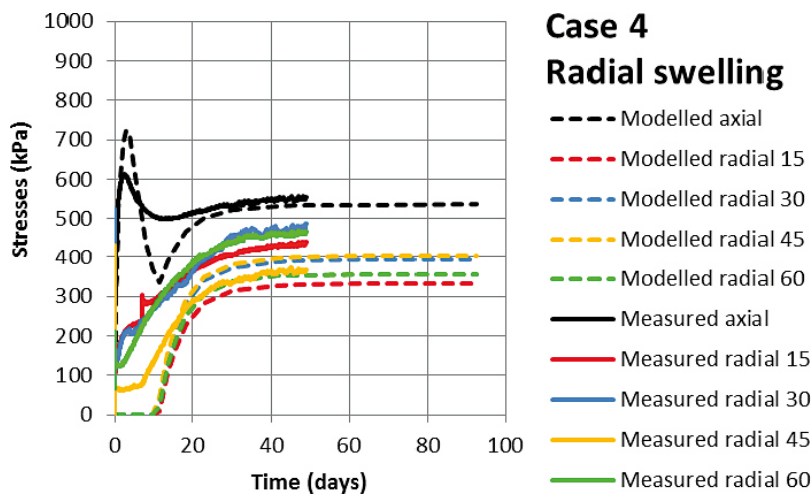


Figure 3-30. Modelled and measured evolution of normal stress.

The comparison shows that although the calibration was done for the axial swelling test the agreement for the radial swelling is very good, even better than for the axial test. The measured dry density distribution is located between the two modelled parts. The influence of the boundaries (bottom and top lids) are also seen with a larger density drop in the bottom than in the middle although the modelled results are more pronounced since the measurements include a larger part of the specimen.

The modelled and measured axial stress agrees very well although the extremes are less pronounced in the measurements. The measured radial stresses are in average a little higher than the simulated.

In general this simulation confirms the model.

Figure 3-31 shows the evolution of the swelling plotted as the density distribution at different times.

The swelling behaviour and its effect on the yield surface are shown in Figure 3-32. The stress path and the change in location of the yield surface are shown. At swelling the average stress decreases while the Mises stress increases until it hits the failure surface. Then the stress path follows the failure line during simultaneous dilatancy and resulting shrinkage of the yield surface.

The stress evolution of a point located close to the periphery is illustrated in Figure 3-33. The stress path starts at the initial condition p_0 and moves up to the failure line and follows the failure line until it reaches its lowest position at p_1 . At the same time the position of the yield surface moves from p_b to p_b' . Then the bentonite starts to consolidate from the swelling inner part of the specimen and the stress goes back to the final stress location at p_2 . The consolidation does not affect the yield surface since it is located further away.

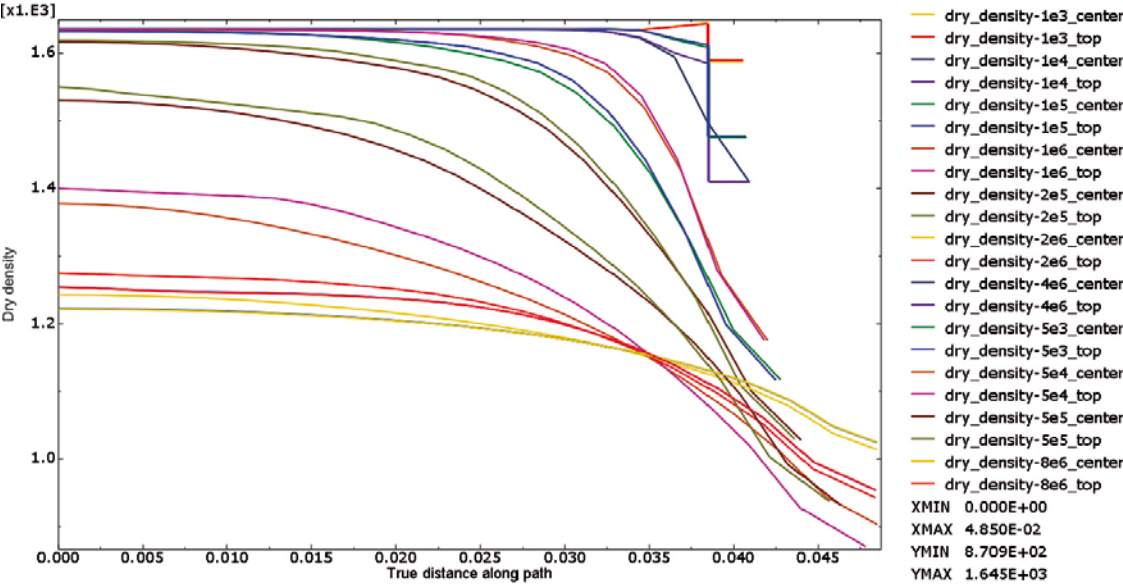


Figure 3-31. Dry density (kg/m^3) plotted as a function of the axial distance (m) from the bottom of the oedometer at different times (s). Two sections are plotted; top = upper element row; center = middle element row.

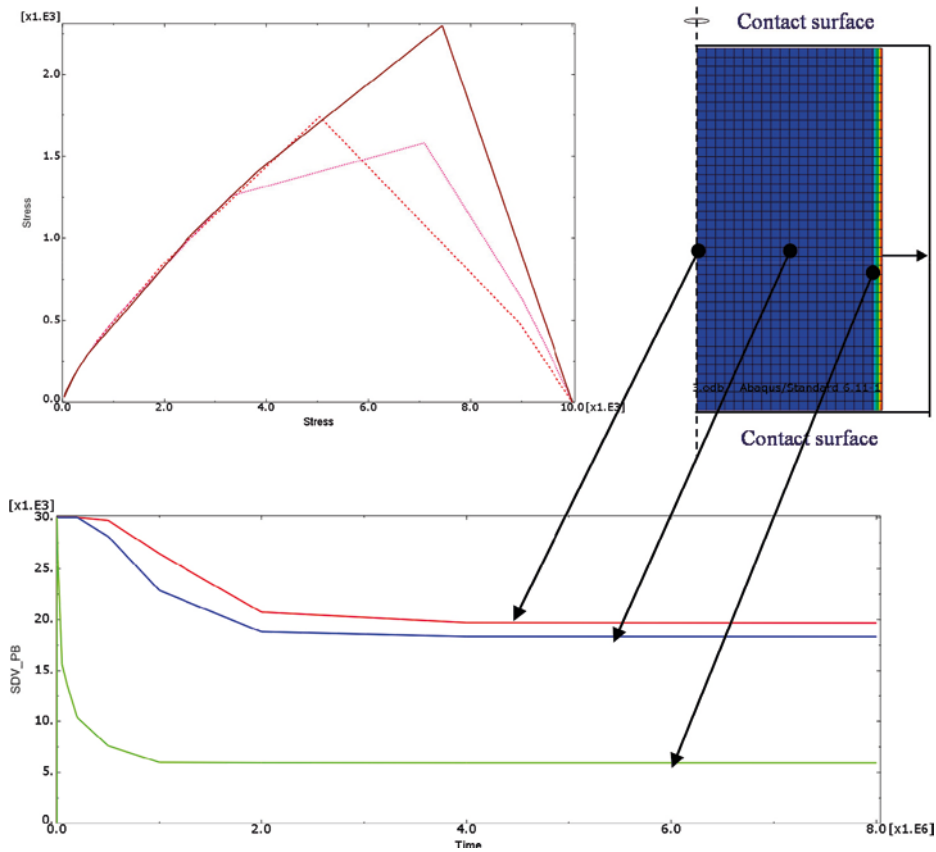


Figure 3-32. Stress path (upper left) plotted as Mises stress (kPa) as a function of the average stress (kPa) for three elements as marked. The lower figure shows the change in the location p_b (kPa) as function of time (s).

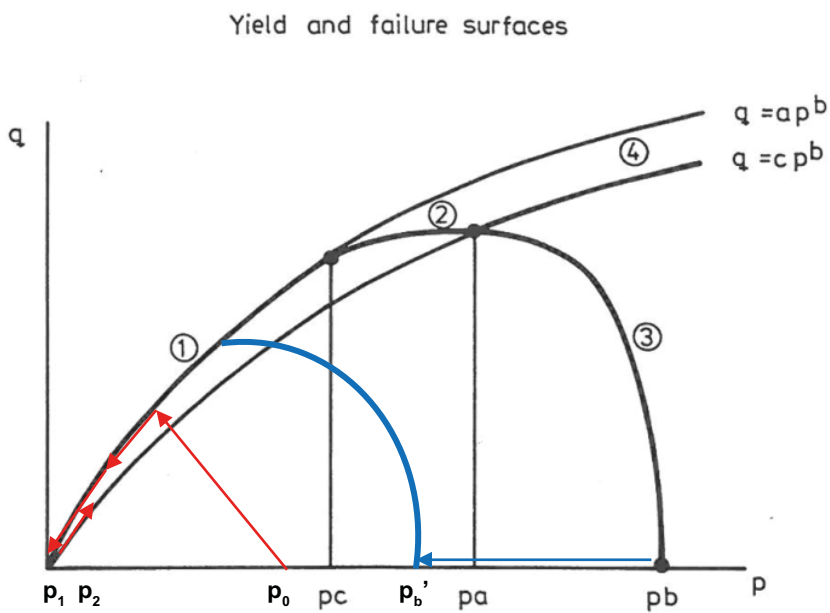


Figure 3-33. Illustration of the stress path (red arrows) of a point close to the swelling surface and its effect on the yield surface (3) that moves to the new position p'_b (blue arrow and curve).

3.6 Influence of friction against the walls

The test simulations included a friction angle of 7 degrees between the bentonite and the walls of the oedometers. In order to study the influence of this friction on the results identical simulations of the two tests with the friction angle 0 degrees have been done. The results are compared in Figure 3-34 and 3-35.

The comparison shows that the influence of the friction is very small. The only significant difference in stresses occurs for the axial stress in the axial swelling test where the stress increases from about 600 kPa to about 700 kPa if no friction is included. Figure 3-36 shows the axial shear stresses distribution along the steel tube.

The shear stress varies from about 180 kPa at the bottom to close to zero at the top with an average of about 120 kPa. The shear stress distribution fits well with the friction angle and the radial stresses and shows that full friction is mobilized. However, the resulting force from the shear stress must be taken by a difference in axial stress on the bottom and the top of about 500 kPa, which yields a vertical stress in the bottom of about 1 100 kPa. This is close to the radial stress 15 mm from the bottom (1 200 kPa) yielding a low deviatoric stress of only about 100 kPa in the friction case. In the friction free case the axial stress in the bottom is the same as in the top (700 kPa). Since the radial stress 15 mm from the bottom is about 1 200 kPa the resulting deviator stress will be about 500 kPa. So the lack of friction against the walls instead leads to a much higher deviator stress that limits the swelling and explains the small difference in density distribution. *A conclusion is thus that even if there is no friction against the walls the internal friction in the bentonite will limit swelling and cause a density gradient. Another conclusion is that the strongest effect of having low or no friction against the walls at axial swelling is a reduction in axial stress at the fixed end of the bentonite geometry.*

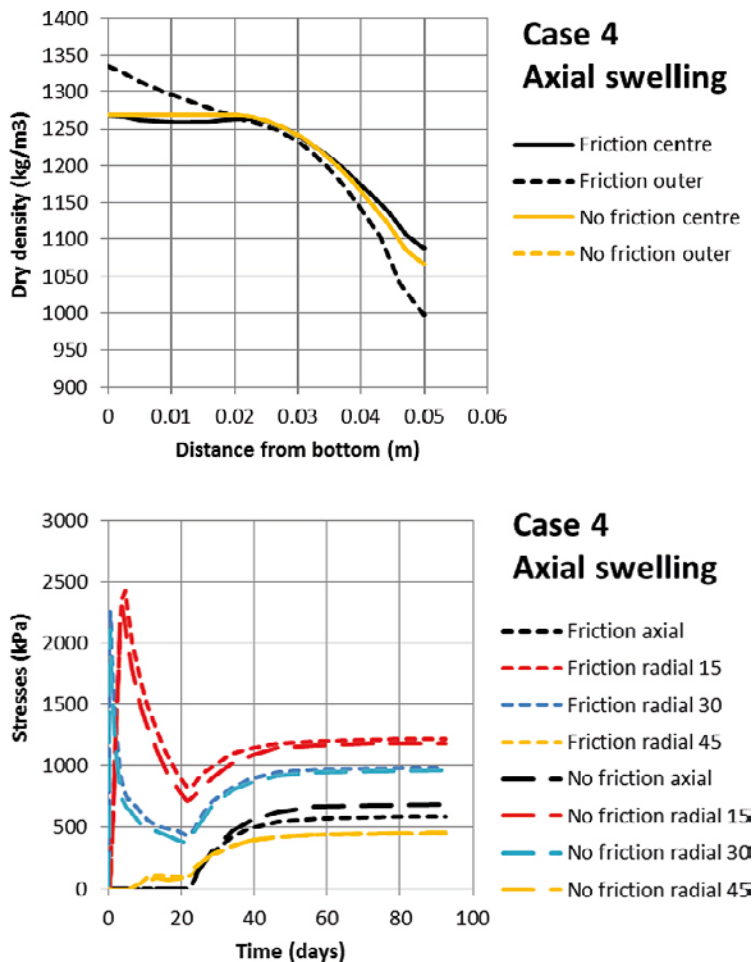


Figure 3-34. Comparison of modelling results of the axial swelling test described in Chapter 5.

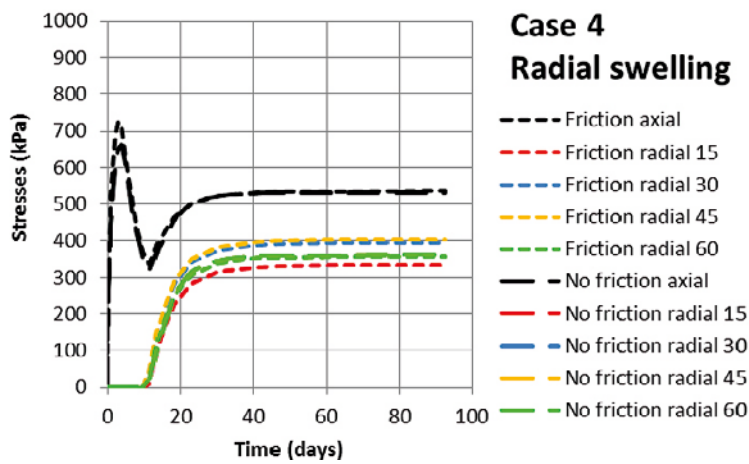
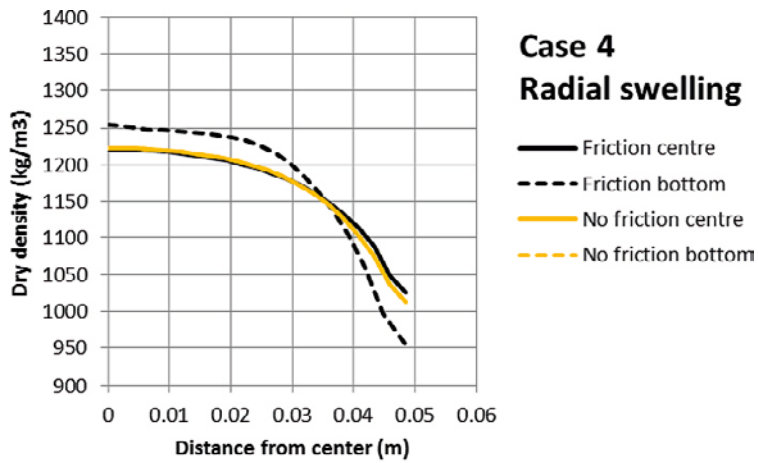


Figure 3-35. Comparison of modelling results of the radial outwards swelling test described in Chapter 6.

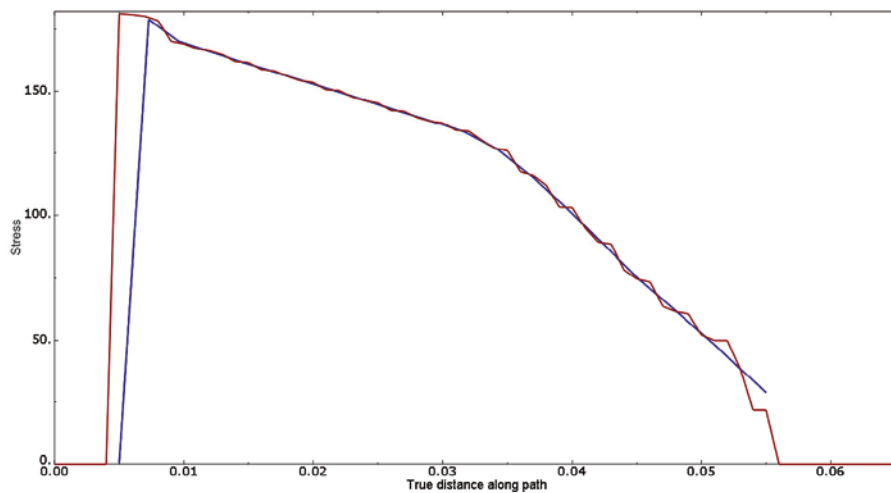


Figure 3-36. Modelled axial shear stress (kPa) distribution along the steel cylinder with the friction angle 7 degrees.

The dry density distribution is identical for the friction free case and the central section (radial swelling) and the symmetry axis (axial swelling) of the case with 7° friction. There is a significant difference between the friction free case and the element row located in contact with the contact surface (“bottom” or “outer”). However, this difference is concentrated to the outer 10–20 % of the sample height as shown in Figure 3-37, which is a contour plot of the void ratio at the end of the simulation.

Another conclusion is thus that if only an average density distribution is requested it is a fair approximation to use no friction in the model, which means that these types of tests do not need to be made in two dimensions but can be simplified by 1D geometries and meshes, but also that if detailed information about stress distribution is requested the friction must be included.

3.7 Radial inwards swelling

3.7.1 Finite element model

The radial inwards swelling test in the larger cell (HR-Ri test) was also modelled using the same model and parameters as the other two test types. The test is described in 3.2.3 and Appendix 2, where also the results are shown.

The following geometry is used for modelling the test HR-Ri1:

- Height: 80 mm
- Outer fixed radius: 49 mm
- Start inner radius: 26 mm

$$u_0 = -10 \text{ MPa}$$

Model

Start properties: $e_0 = 0.70$; $\rho_{d0} = 1635 \text{ kg/m}^3$

Swelling $\Delta V/V = 39 \%$

Average final properties: $e_0 = 1.36$; $\rho_{d0} = 1176 \text{ kg/m}^3$

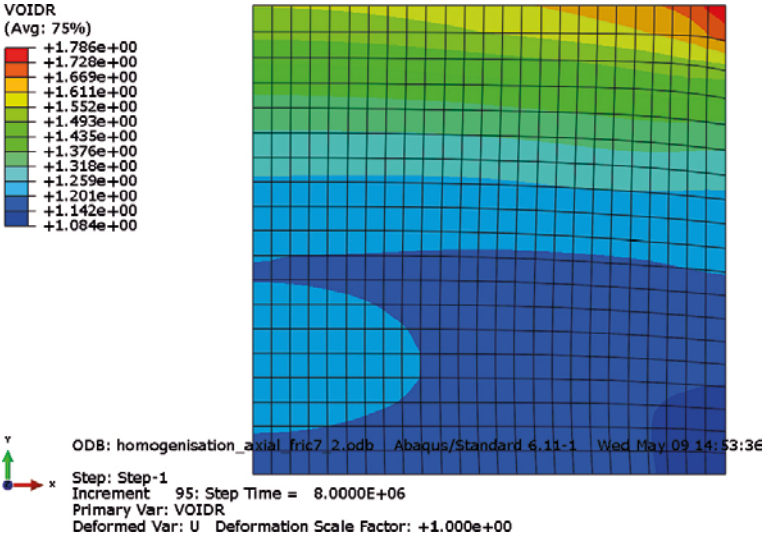


Figure 3-37. Contour plot of the void ratio distribution at the end of the test in the simulation with friction against the oedometer ring. Axial symmetry around the left boundary.

Test

Start properties: $e_0 = 0.67$; $\rho_{d0} = 1\,598 \text{ kg/m}^3$

Swelling $\Delta V/V = 37 \%$

Average final properties: $e_0 = 0.1.39$; $\rho_{d0} = 1\,166 \text{ kg/m}^3$

Swelling with water available at the outer radius confinement

Axial contact surfaces with no friction ($\phi = 0^\circ$)

Identical material model and modelling technique have been used as described earlier and used for the axial and outwards radial swelling simulations after calibration of the parameters.

There were problems with getting good results since a too large remaining cylindrical hole was the result of several simulations. In order to decrease the remaining unfilled cylinder hole an element model with 1 000 radial elements was used. No friction was used for simplification reason.

3.7.2 Modelling results

Figure 3-38 shows the evolution of the axial and radial stresses and comparison with measured values.

The following modelled and measured behaviour agree:

- The stress evolution with at first a peak and then a lower steady state stress.
- The difference between the radial and axial stress with about 100 kPa higher axial stress after equilibrium.
- The time until equilibrium.
- The value of the radial and axial stresses at equilibrium agree fairly well although not very well. The difference (about 200 kPa for both stresses) is probably caused by slightly higher density in the model than in the test.

The following modelled and measured behaviour disagree:

- The measured peak value is much higher than the modelled. This could be caused by the sparse values saved in the simulation meaning that the maximum peak is not plotted.
- The modelled drop below the value after equilibrium is not seen in the experiment.

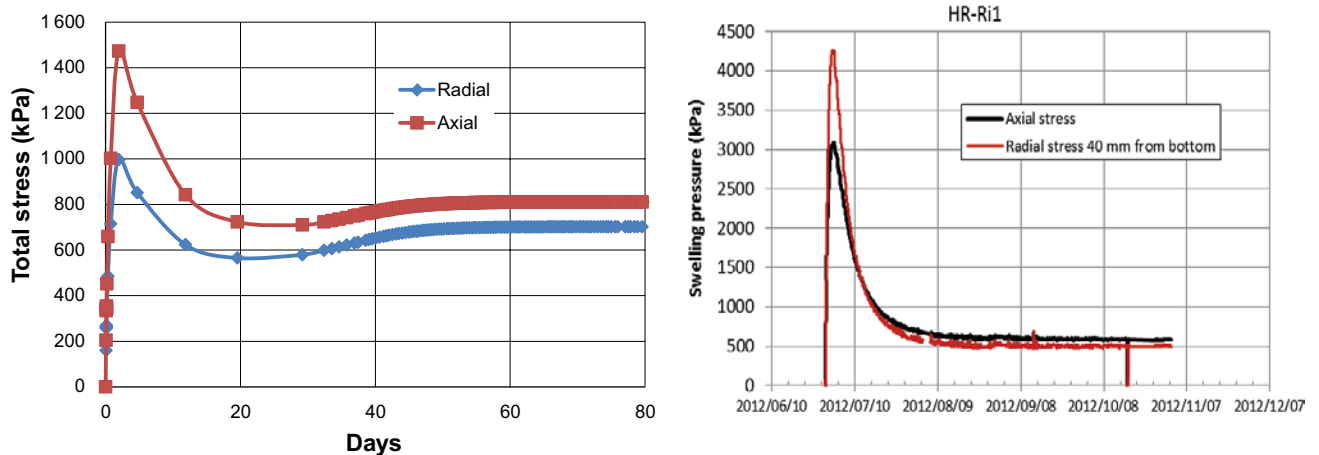


Figure 3-38. Modelled (left) and calculated evolution of axial and radial stresses.

Figure 3-39 shows a comparison between modelled and measured final dry density distribution.

Both diagrams in Figure 3-39 lack values close to radius zero but for different reasons. In the modelling the open tube did not completely close. There is a remaining open pipe with the radius 2.7 mm in the model and the reason is not lack of convergence because the simulation ran to complete equilibrium. The reason is not clear but it is judged to be caused by numerical imperfections and has been observed in other similar calculations not published. In addition the material model Porous Elastic is not valid for Na-bentonite at lower dry densities than about 1 000 kg/m³.

Regarding the measurements sampling problems yield that there is lack of data in the centre as described in Section 3.2.3.

The comparison shows that the drop in density from the periphery to the radius 1 cm (20 %) is similar.

Measured: 1 260 kg/m³ to 900 kg/m³ or a drop of 360 kg/m³

Modelled: 1 270 kg/m³ to 930 kg/m³ or a drop of 340 kg/m³

However, there is a difference in shape since the measured density is fairly constant at the outer 40 % of the radius and then there is a steep drop while the simulation shows a more even density drop.

The comparison shows that the agreement between modelled and measured results is good although not perfect.

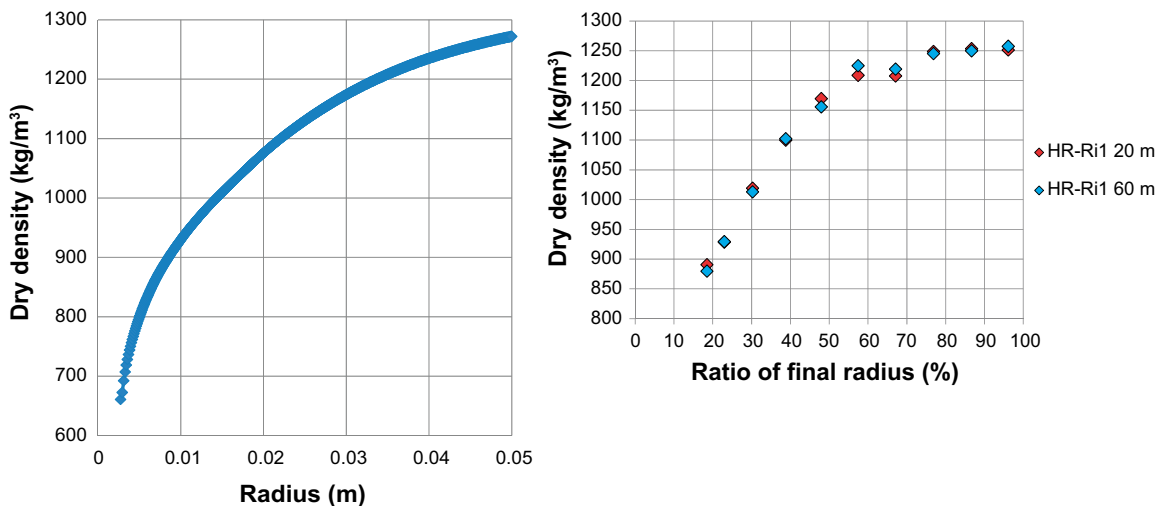


Figure 3-39. Modelled (left) and measured distribution of dry density (20 % correspond to 0.01 m).

3.8 Isotropic swelling

3.8.1 Finite element model

The isotropic swelling test is shown in Section 3.2.4 and in detail described together with test results in Appendix 3. The idea with the isotropic swelling was to make the compacted bentonite swell without hitting the failure surface and thus without any yielding and without moving the yield surface. This would be a check of the porous elastic relation. However, as will be shown in this chapter the major part of the bentonite did not swell isotropically.

Since the geometry of the test is cylindrical the swelling will be quite complicated to model. In order to simplify the model a spherical model has been made. The conditions of the model are the following:

Model

Initial radius $r_i = 44.4$ mm

Final radius $r_f = 50$ mm

Start properties: $u_0 = -10$ MPa, $e_0 = 0.70$; $\rho_{d0} = 1635$ kg/m³

End average properties: $u = 0$ MPa, $e = 1.43$; $\rho_d = 1143$ kg/m³

Swelling $\Delta V/V = 43$ %

The modelled swelling agrees with the swelling in the test but the densities are slightly lower.

Test

Start properties: $e_0 = 0.65$; $\rho_{d0} = 1684$ kg/m³

End average properties: $e = 1.36$; $\rho_d = 1180$ kg/m³

Swelling $\Delta V/V = 43$ %

Water is available at the spherical boundary. The element mesh is shown in Figure 3-40.

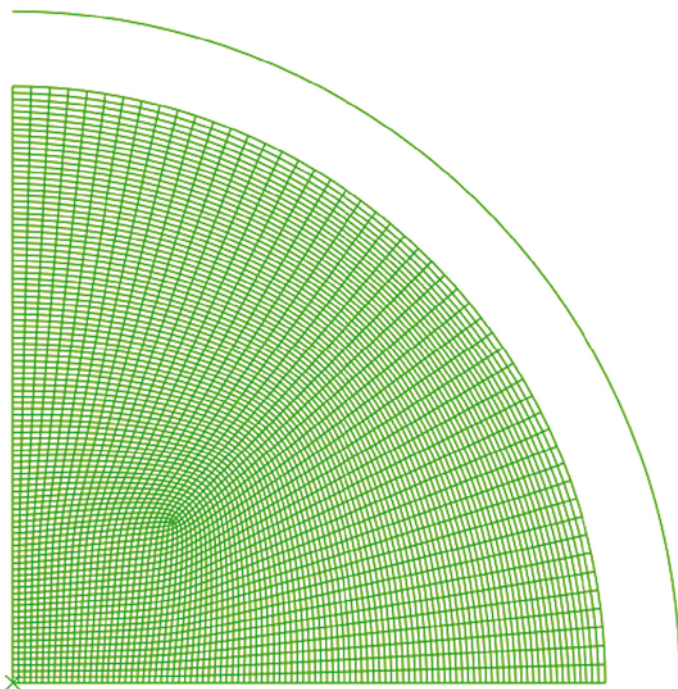


Figure 3-40. Element mesh for the swelling sphere. Axial symmetry around the left boundary and symmetry plane at the bottom boundary. Contact surfaces in the spherical slot.

3.8.2 Modelling results

Figure 3-41 shows the modelled total stress against the periphery and comparison with the measured stresses on the cylinder.

The stresses were measured in 5 different locations (one axial and four radial) and the results show that the stresses are very similar (except for one which fails during the test). This confirms that the swelling is equal in all parts. The measured stress is higher (around 400 kPa) than modelled (275 kPa), which partly can be explained by the higher density of the test specimen. The time until equilibrium is in both cases about 40 days but there is a delay until stress increase in the model on reasons discussed in Chapter 5.

After termination the water content and density were carefully measured. The measurements have been re-evaluated according to Section 3.2.3 since the delivery of the PM. Figure 3-42 shows the modelled and measured density distribution.

The modelling results show a surprising decrease in density close to the centre of the sphere. This is not seen in the measurements. However, there is no central sampling done since the slices taken cover a larger part of the specimen. But in spite of this lack of data there is no trend of such a decrease so it is not likely that the density in the centre is lower than further out.

There is thus a process in the simulation that makes the swelling stronger in the centre of the specimen that is unique for this type of test. Figure 3-43 shows the stress paths of some elements located along the bottom boundary.

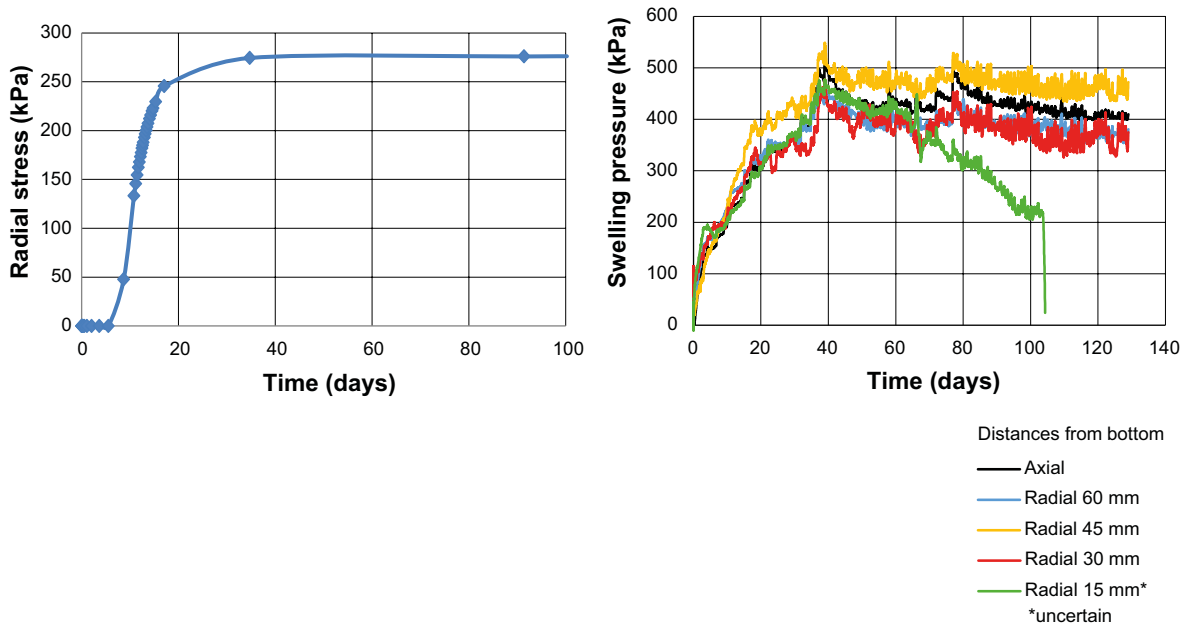


Figure 3-41. Modelled evolution of radial total stress (left) and measured stresses in axial and radial directions.

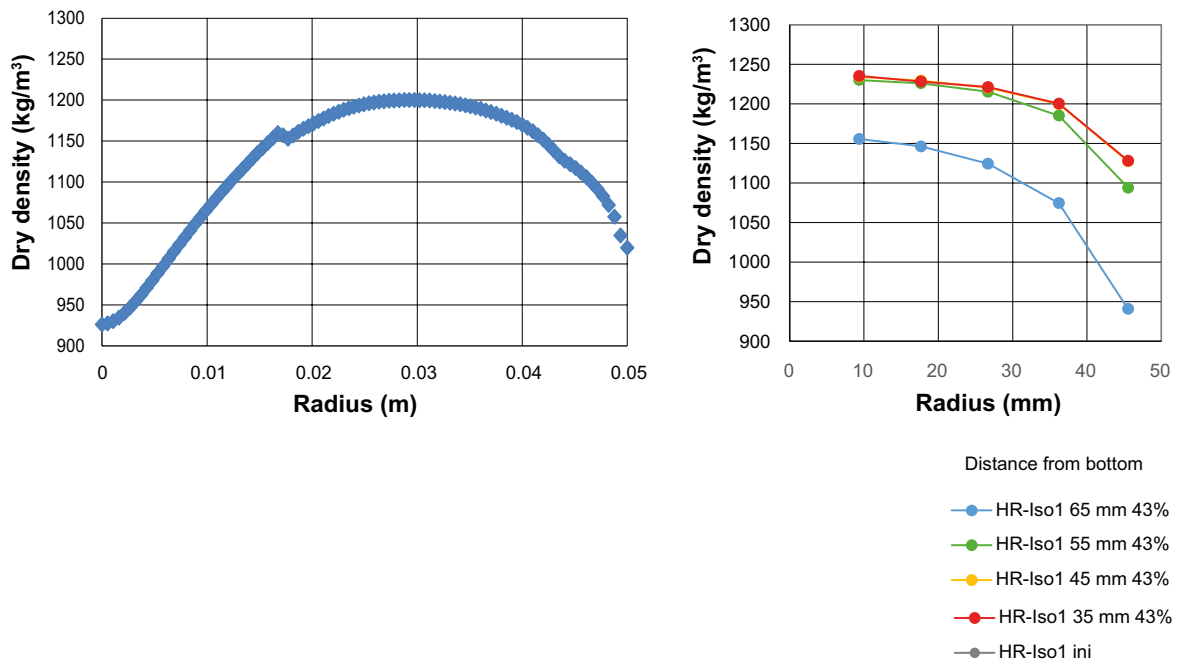


Figure 3-42. Modelled (left) and measured density distribution. The measured values are taken from the three most central slices.

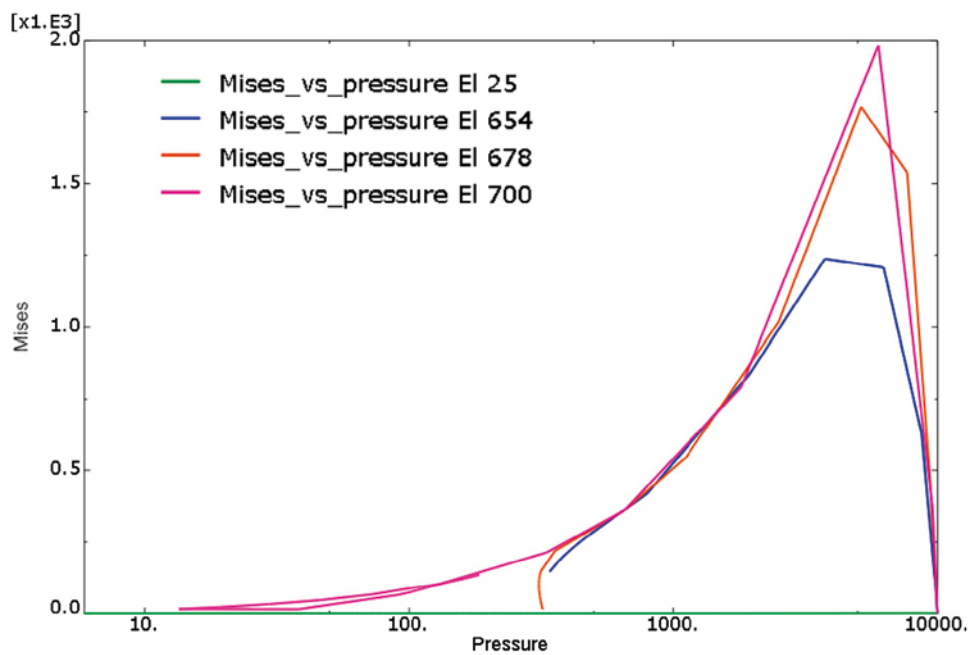


Figure 3-43. Mises stress (kPa) plotted as function of average stress (kPa). Observe the logarithmic scale. Element 25 is in the centre and element 700 at the periphery.

The figure shows that all stress paths hit the failure line with dilatant plastic strain except for the central element 25 where there is no Mises stress and thus no plastic strain. Element 25 thus behaves as desired for this isotropic test with pure elastic swelling while the other elements have non-isotropic swelling with plastic strains. This is also seen in Figure 3-44 where the total plastic strains and the location of the yield surface are shown after completed swelling.

Figure 3-44 shows that the inner part of the sphere has small or now plastic strain and little or no shrinkage of the yield surface. The inner thus swells without plastic strain. Figure 3-38 does not show the exact limit but a closer look at the data shows that it is located at the radius 0.015 m.

The density change with time is illustrated in Figure 3-45, where the density as a function of radius is plotted at different times.

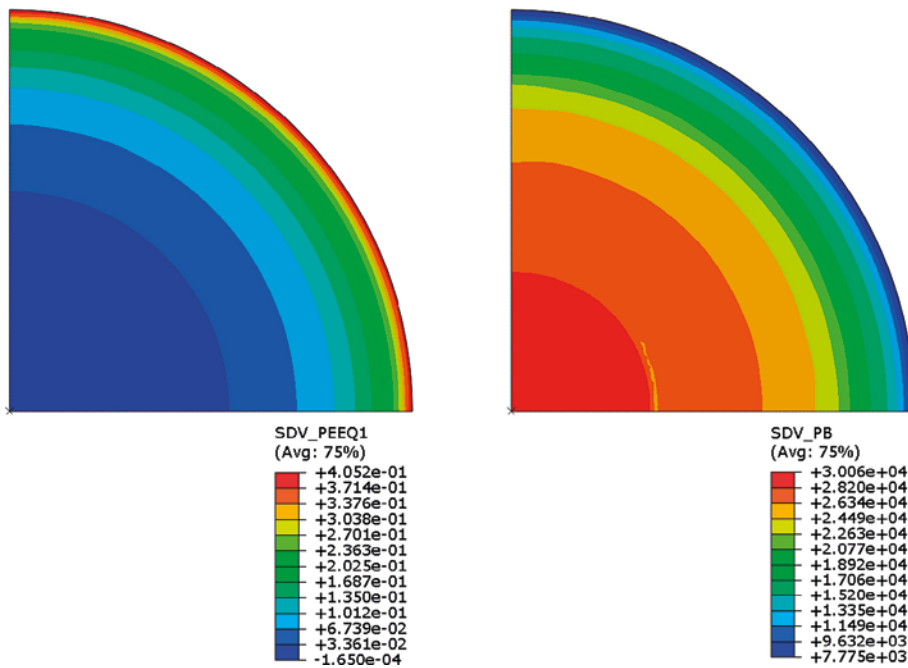


Figure 3-44. Plastic strain (left) and location of the yield surface at the end of the simulation.

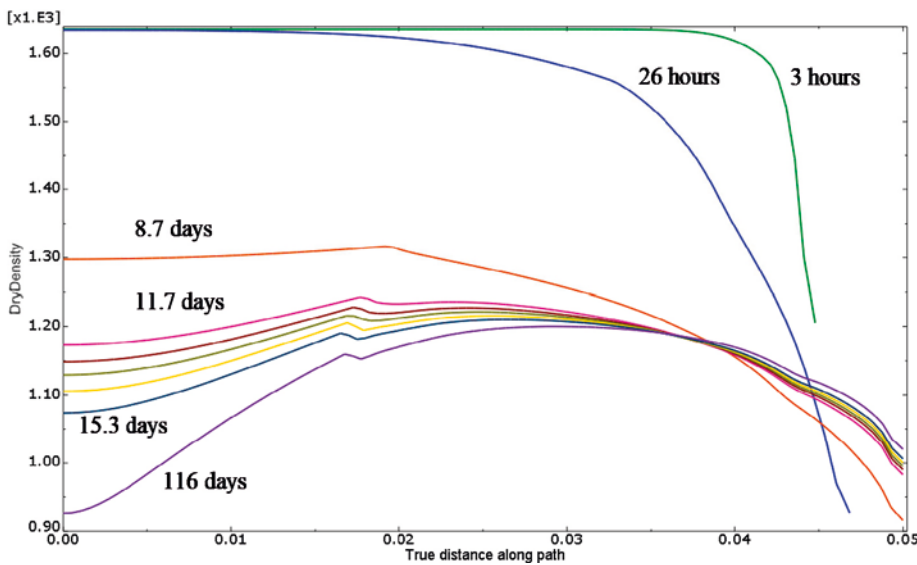


Figure 3-45. Dry density (kg/m^3) plotted as function of the radius (m) at different times.

The sphere swells and reaches the boundary after about 1 week. Then the swelling of the inner continues with a parallel compression of the material with radius larger than about 3.8 cm. However, the swelling of the inner not plasticised part continues with stronger swelling than the zone between 1.7 cm and 3.8 cm.

The reason for this behaviour is not clear. It could be (and is probably) caused by the difference in plasticity but this has not been possible to prove.

In order to simulate a completely isotropic swelling in every part of the material, water must be equally available in all parts or nodes of the specimen. This has been simulated and the result is (of course) an equal swelling without plastication yielding constant density distribution of $\rho_d = 1\,145\text{ kg/m}^3$ over the entire specimen. The radial total stress against the periphery was for this case 155 kPa.

Since the swelling is only elastic it will follow Equation 3-6:

$$\Delta e = -\kappa \Delta \ln p \quad (3-6)$$

where

$$\kappa = 0.175$$

$$e_0 = 0.70$$

$$p_0 = 10\,000\text{ kPa}$$

The final void ratio $e = 1.43$ yields that the final average stress p can be calculated

$$0.7 - 1.43 = -0.175(\ln 10\,000 - \ln p)$$

$$\ln 10\,000 - \ln p = 4.171$$

$$\ln p = 5.039$$

$$p = 154\text{ kPa}$$

This agrees with the simulation and confirms that the swelling is only elastic. But the modelled swelling pressure when swelling takes place with a large part plastic strains gives a higher pressure or 275 kPa, which agrees better with the relation derived by Börgesson et al. (1995):

$$e = e_0 \cdot \left(\frac{p}{p_0} \right)^\beta \quad (3-7)$$

or

$$p = p_0 \cdot \left(\frac{e}{e_0} \right)^{1/\beta} \quad (3-8)$$

where

$$\beta = -0.19$$

$$e_0 = 1.1$$

$$p_0 = 1\,000\text{ kPa}$$

which yields

$$p = 1\,000 \cdot 1.65 \cdot e^{-5.263}$$

$$e = 1.43\text{ yields}$$

$$p = 251\text{ kPa}$$

The measured stress 400 kPa relates to the somewhat higher density and lower void ratio in the test $e = 1.36$, which can be compared to the stress that can be derived from Equation 3-7:

$$p = 327\text{ kPa}$$

The measured and modelled stresses are thus a little higher than derived by Equation 3-8 but much higher than the pressure coming from purely elastic swelling. The reason is of course that porous elastic is too small to yield high enough pressure and plastic dilatancy is required.

Since isotropic swelling did not take place in this test it cannot be used to evaluate the elastic part of the model. A way to make a specimen swell isotropically may be to increase the relative humidity in the boundary so slowly that there will be very small gradients in RH in the sample, which means that it will be equivalent to if water is available in all points in the specimen.

The material model thus does not seem to work very well for isotropic swelling, but this is not an expected type of swelling since there are at least two processes that ensure plastic strains:

1. Irregular geometries.
2. The wetting always takes place from a boundary.

A possible improvement of the model would be to include plastic strain with dilatancy in the entire elastic zone of the p-q plane.

The conclusions from the isotropic swelling test and the simulation are:

- The test does not yield isotropic swelling more than perhaps in the inner part of the specimen, the main reason being that wetting takes place from the outer boundary which generates anisotropic deformations.
- Isotropic swelling can only take place if water is available in all nodes.
- A test that could simulate isotropic swelling might be to increase the RH so slowly that very small gradients will occur in the specimen.
- Isotropic swelling does not yield enough swelling by the material model since plastic dilatancy is required.
- An improvement of the model could be to include plastic strain with dilatancy in the entire elastic zone of the p-q plane.

3.9 Summary and conclusions

Four small scale basic laboratory tests with different test types have been modelled, namely axial swelling, radial outwards swelling, radial inwards swelling and isotropic swelling. The axial swelling test was used for checking and calibrating the material models and the other tests were used to evaluate the derived model.

The models used are elastic-plastic models. The elastic part of the model is a so called porous elastic model that has a logarithmic relation between void ratio and average stress. Two different models have been used for the plastic part of the model, Drucker-Prager plasticity model and Claytech plastic cap model.

The axial swelling test was at first used to check and calibrate the models. The Drucker-Prager model could not yield an acceptable result regarding the swelling pressure evolution and the final gradient in density that occurred after equilibrated swelling. Instead the Claytech model described already by Börgesson et al. (1995) was used with parameter values derived at that time. However, in order to get the best agreement between measured and modelled results the parameters of the elastic model, the plastic model and the hydraulic conductivity had to be somewhat changed.

Then the calibrated model was checked by modelling the radial outwards swelling test and good agreement was achieved, which confirmed the model.

The models were 2D axial symmetric element meshes and included contact surfaces between the bentonite material and the restraining outer cell surfaces. These contacts were applied with simulated friction with a friction angle of 7° , which was taken as an average of the friction angle of the bentonite at the actual density divided by two (according to friction tests described in Appendix 3).

In order to investigate the influence of friction against the steel surfaces identical calculations were made with the friction angle 0° . The results showed that the external stresses and the density distribution were very little affected by friction. Only if detailed information about the stress distribution is requested the friction must be included. Another conclusion was that the lack of external friction was compensated by the internal friction with high Mises stresses and that smooth surfaces does not reduce the density gradients significantly. However, the strongest effect of having low or no friction against the walls at axial swelling is a reduction in axial stress at the fixed end of the bentonite geometry.

The radial inwards swelling test was modelled without friction against the walls. The model did not manage to get complete filling of the central hole. The reason is not clear but it is judged to be caused by numerical imperfections and has been observed in other similar calculations. Otherwise the test and the simulation agreed fairly well.

Finally a new test with the intention to have isotropic swelling was performed and modelled, although the model was simplified as a swelling sphere instead of a filled cylinder. This simulation led to a number of observations and conclusions:

- The test does not yield isotropic swelling more than perhaps in the inner part of the specimen, the main reason being that wetting takes place from the outer boundary which generates anisotropic deformations.
- Isotropic swelling can only take place if water is available in all nodes.
- A test that could simulate isotropic swelling might be to increase the RH so slowly that very small gradients will occur in the specimen.
- Isotropic swelling does not yield enough swelling by the material model since plastic dilatancy is required.
- An improvement of the model could be to include plastic strain with dilatancy in the entire elastic zone of the p-q plane.

The overall conclusion of the calibration and evaluation is that the model simulates bentonite swelling well within a limited density interval but also that the model does not work well for the unlikely case of completely isotropic swelling.

Future work for refining the material model is proposed to include the following changes:

- Include plastic strain with dilatancy in the entire elastic zone of the p-q plane.
- Widen the validity of the Porous Elastic model to high and low voids ratios ($e > 1.5$ and $e < 0.7$) by including conditional subroutines.

4 Modelling Task 2 with Abaqus (group SKB2)

4.1 Task description

Subtask 2 is in detail described in Appendix 4 and the results after termination in Appendix 5. A summary will be given here.

The laboratory experiment named SH1 (Dueck et al. 2016) was made in a cell with very stiff and confined boundaries. A high density bentonite block was used to simulate loss of bentonite in a part of a deposition hole (Figure 4-1 and 4-2). The block had a diameter of 30 cm and a height of 10 cm. Two diametrically located irregular voids of $35 \times 50 \times 70 \text{ mm}^3$ were cut in the block before installation. Measurements of the total stress (in 9 positions) and RH (in 2 positions) were done during the entire test duration. Careful sampling and determination of density distribution for evaluating the homogenisation were done after termination of the test.

Water was supplied at the radial periphery through filters surrounding the block. The filter and the cavities were water filled at the start of the test.

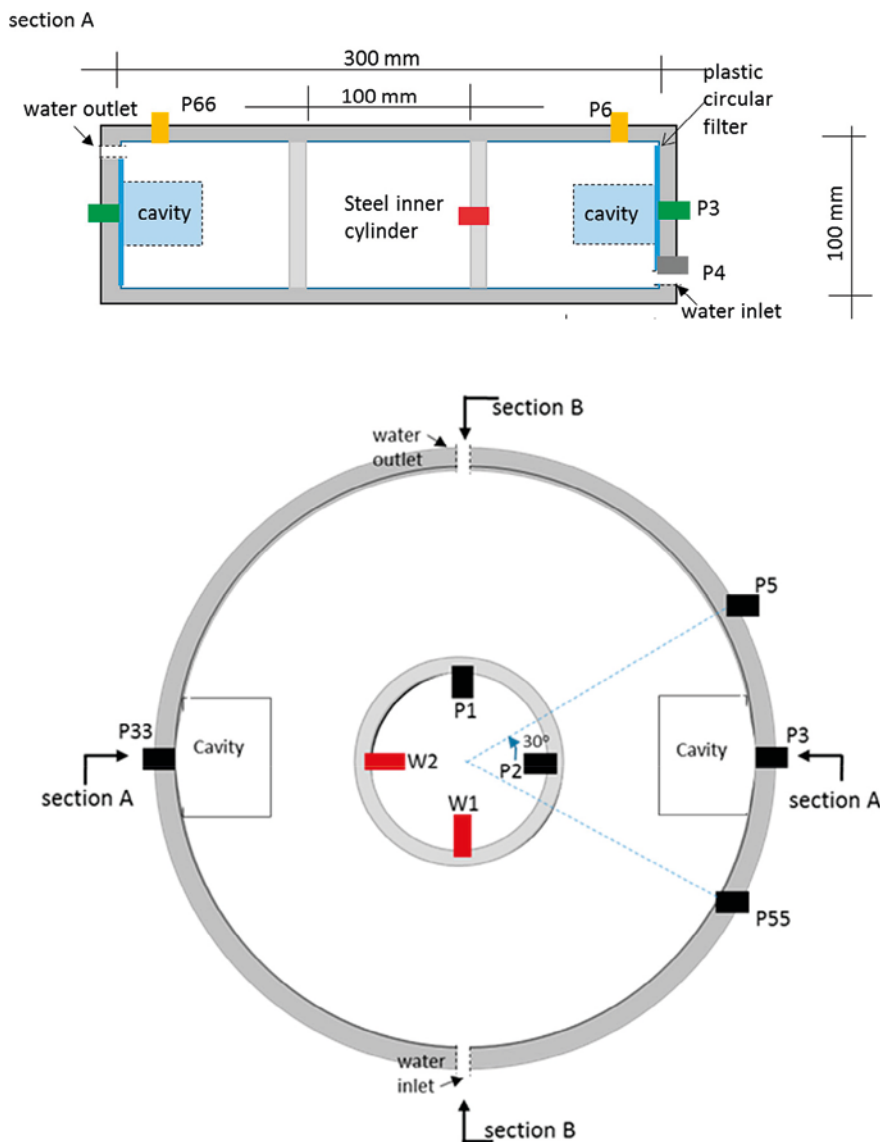


Figure 4-1. Test layout. Total stress is measured by sensors named P. RH is measured by sensors named W.

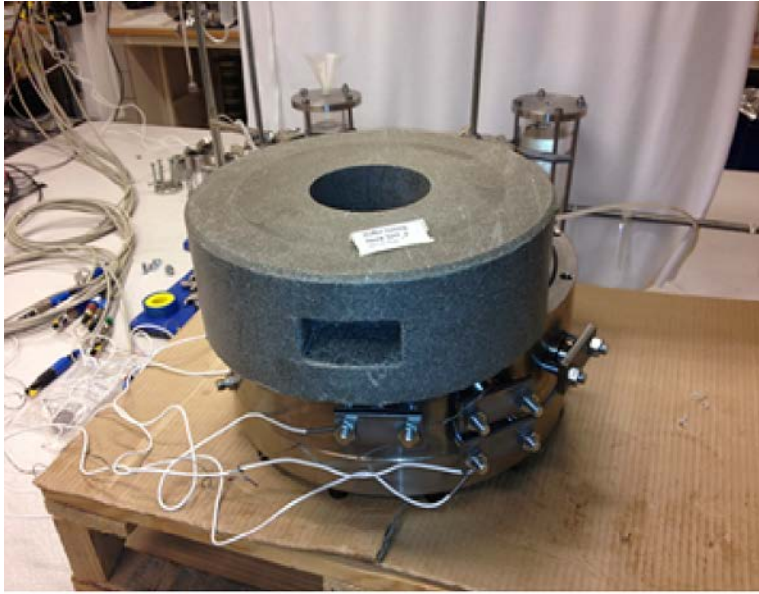


Figure 4-2. Photos taken just before start of the test SH1.

Another identical test SH2 was started at the same time. The only difference between the tests was that the cavities were slightly larger in SH2 since the height of the cavity was 50 mm instead of 35 mm. In addition SH2 was not instrumented.

Both tests were started in December 2012. The test SH2 was terminated and sampled in May 2013, 17 months after the start. The test SH1 was terminated and sampled in September 2015, 2 years and 9 months after the start.

The properties of the bentonite block are shown in Table 4-1.

Table 4-1. Properties of installed bentonite in test SH1.

Properties excluding the cavities	Density ρ (kg/m ³)	Particle density ρ_s (kg/m ³)	Water density ρ_w (kg/m ³)	Water content w (%)	Dry density ρ_d (kg/m ³)	Void ratio e	Degree of saturation S_r (%)
Initial conditions, final dimensions	2009	2780	1000	23.6	1626	0.71	95–97

4.2 Finite element model

The test is modelled with the finite element code Abaqus. The code and the material model used for SR-Site are described by Åkesson et al. (2010a, b). The material models used for the present tests are described in detail by (Börgesson et al. 1995). The code is also described by Börgesson et al. (2016a, b).

The material models are coupled hydro-mechanical with the effective stress theory as base. Full water saturation is assumed for these models. The hydraulic model use Darcy's law with hydraulic conductivity modelled as a function of the void ratio.

Two mechanical material models have been used. Both models are elastic-plastic models and use porous elasticity for the elastic model. One of the plastic models uses Drucker-Prager plasticity while the other one is a plastic cap model "Claytech model" derived by Börgesson et al. (1995). The models are described in Börgesson et al. (1995, 2015) as well as in Section 3.2.2.

The plastic cap model was calibrated and verified in Task 1 (Section 3.3). The parameter values will also be given in this chapter.

4.2.1 Hydraulic model

The original hydraulic conductivity relation is shown in Table 4-2.

Table 4-2. Hydraulic conductivity as a function of void ratio.

<i>e</i>	<i>k</i> (m/s)
0.45	0.5×10^{-14}
0.70	4.0×10^{-14}
1.00	2.0×10^{-13}
1.5	1.0×10^{-12}
2.00	0.5×10^{-11}
3.00	1.0×10^{-11}
5.00	3.5×10^{-11}
10.00	1.5×10^{-10}
20.00	0.75×10^{-9}

4.2.2 Mechanical models

Porous elastic

Porous Elastic implies a logarithmic relation between the void ratio *e* and the average effective stress *p* according to Equation 4-1.

$$\Delta e = -\kappa \cdot \Delta \ln p \quad (4-1)$$

where κ = porous bulk modulus

Poisson's ratio *v* is also required.

$$\kappa = 0.175$$

$$v = 0.3$$

This relation is not valid for low densities (see Börgesson et al. 1995) but only in the interval $0.7 < e < 1.5$, which correspond to $1110 \text{ kg/m}^3 < \rho_d < 1635 \text{ kg/m}^3$. At lower densities the porous bulk modulus is much larger ($\kappa \approx 1.37$) but this change in modulus is not included in the model. If swelling causes a lower density the swelling will not be correctly modelled for that part.

Drucker-Prager Plasticity model

Drucker-Prager Plasticity contains the following parameters:

β = friction angle in the p - q plane

δ = cohesion in the p - q plane

Ψ = dilation angle

$q = f(\epsilon_{pl}^d) = \text{yield function}$

The parameter values in this model are as follows:

$\beta = 17^\circ$

$\delta = 100 \text{ kPa}$

$\Psi = 2^\circ$

$q = f(\epsilon_{pl})$ according to Table 4-3.

Table 4-3. Yield function.

$q \text{ (kPa)}$	ϵ_{pl}
112	0
138	0.005
163	0.02
188	0.04
213	0.1

Figure 4-3 illustrates the Drucker-Prager model.

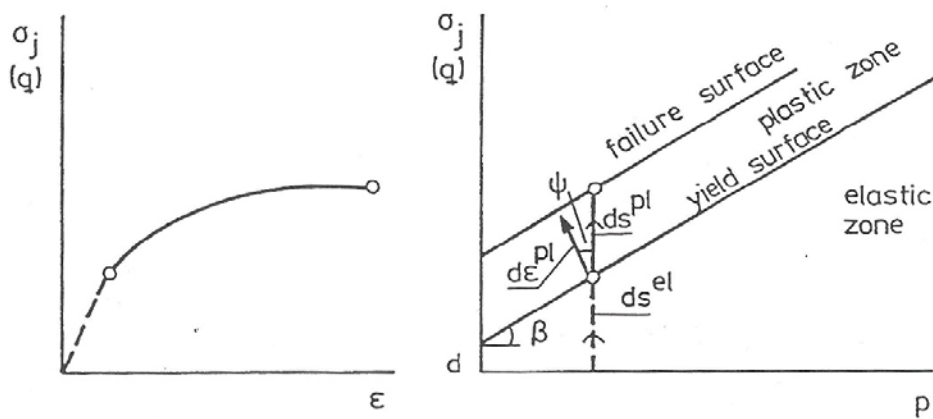


Figure 4-3. Illustration of the Drucker-Prager model.

Claytech Plastic Cap model

The calibrated parameters of the model (Section 3.4.3) are

Claytech plastic cap model

$$a = 2.45$$

$$c = 2.20$$

$$b = 0.77$$

$$K = 1.0$$

$$\gamma = 0.2$$

$$R = 0.1$$

$$p_b = 30\,000 \text{ kPa}$$

$$p_f = -25\,000 \text{ kPa}$$

Cap hardening = see Table 4-4

Table 4-4. Cap hardening function.

p (kPa)	$e^{\log(1+e^V_{pl})}$
100	0
331	0.1133
934	0.2112
2 160	0.2904
3 247	0.3289
4 294	0.3553
8 240	0.4169
10 044	0.4356
12 530	0.4565
13 299	0.4621
17 562	0.4884
30 000	0.5390

4.2.3 Contact properties

The shear resistance between the test specimen and the surrounding steel cylinder has been investigated with a large number of friction tests (see e.g. Börgesson et al. 2015 and Appendix 2).

The results show that the friction angle between bentonite and steel is about half the inner friction angle of bentonite ϕ . This has been used for the modelling.

The contact between the bentonite specimen and the surrounding steel tube or steel plate ϕ_c has thus been modelled according to Equation 3-2.

$$\phi_c = \phi/2 \tag{4-2}$$

Since ϕ is a function of the swelling pressure ϕ_c must be adapted to the swelling pressure in the tests, which varies with how close to the cavity the element is located. The final swelling pressure after completed homogenisation at the cavity is expected to vary between 2 MPa and 6 MPa. At the swelling pressure 4 MPa the friction angle is about 10 degrees according to Åkesson et al. (2010a, b) and the friction angle between the bentonite and the steel lids has accordingly been set to $\phi_c = 5^\circ$.

The friction angle between the bentonite and the filter is more difficult to settle. Tests show that the friction between plastic filter and bentonite is about 80 % of the inner friction of bentonite as peak value but after some displacement the residual friction is about 60 % (Dueck et al. 2016). Also for this part $\phi_c = 5^\circ$ has been applied.

4.2.4 Element mesh

The mesh can be simplified to cover only 1/8th of the test, due to symmetry planes. Figure 4-4 shows the location of the element mesh in the block. Figure 4-5 shows the element mesh.

4.2.5 Modelling

Initial conditions

The bentonite is assumed to be completely water saturated from start but without swelling pressure against the walls. The swelling pressure is instead taken by a negative pore water pressure, which means that the total stress initially is zero.

$$e_0 = 0.70$$

$$p_0 = 10\,000 \text{ kPa}$$

$$u_0 = -10\,000 \text{ kPa}$$

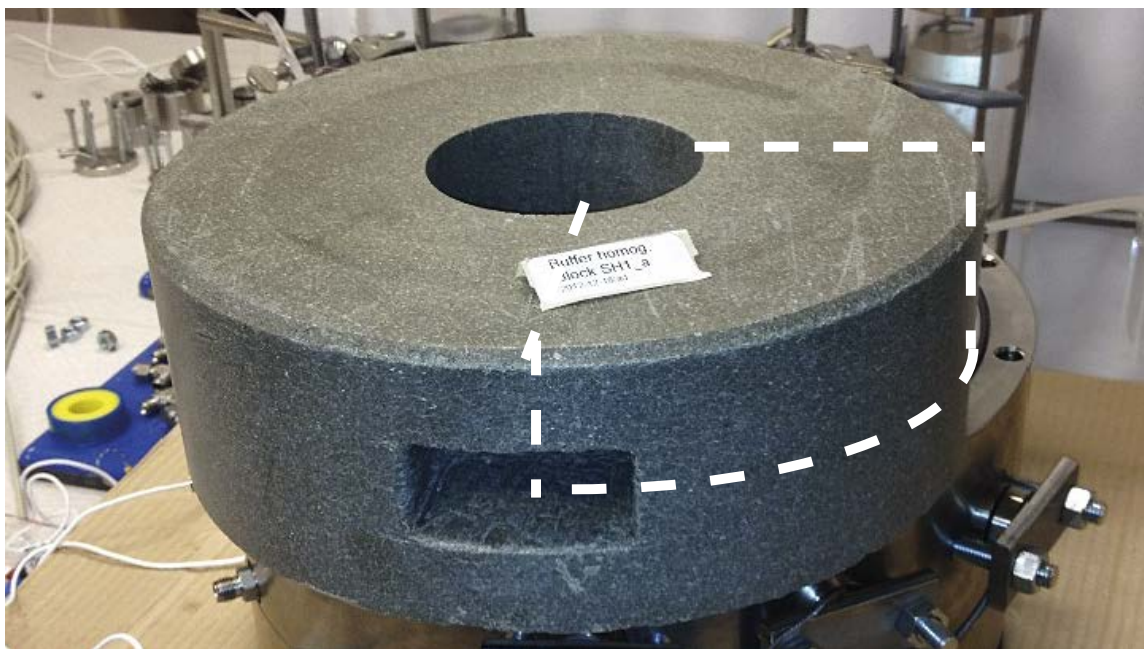


Figure 4-4. Illustration of how the 1/8th part of the bentonite block is used in the element mesh.

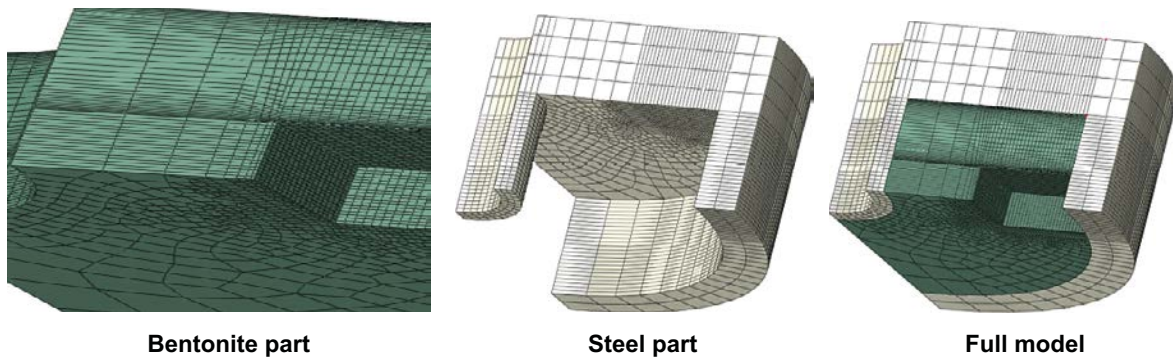


Figure 4-5. Element mesh used for the blind prediction (Section 4.3).

Steel confinement

The steel cylinders and the end lids are modelled as linear elastic with standard values of steel properties.

Calculation sequence

The initial value of the water pressure $-10\,000$ kPa is ramped down to 0 kPa in $10\,000$ seconds in the nodes of the cylinder wall surface where water is supplied through the filter and in the surface nodes of the cavities (simulating water filled cavity). The calculation was run for 3.17 years (10^8 seconds).

In order to improve the ability of the calculation to converge, a process that stabilizes the calculation by adding damping with counterforces is used.

4.3 Blind prediction

4.3.1 General

The SH1 test was started on December 18, 2012, in the afternoon by filling the filters and the cavities with water and applying a low water pressure (10 kPa). The modelling that is described in this chapter was done in November 2012, the figures plotted on December 12 and a PM describing the calculation was delivered before start of the test. So it was a true blind prediction.

4.3.2 Model

The element mesh, the material model, the parameters for the material model and the calculation technique are as described in Chapter 4.2. The Claytech Plastic Cap model was used.

4.3.3 Results

The results described in this section are mainly taken from the PM on the prediction, which has not been published.

The evolution of radial/axial stress in the measuring points and the final distribution of void ratio are reported and can be compared with measurements. These results and some other are also shown.

Of special interest (for estimating the required duration of the test) was the time until completed swelling, which is related to the time until pore pressure equilibrium. The modelled evolution of the negative pore pressure (suction) in the two most remote parts (W1 and W2) is shown in Figure 4-6.

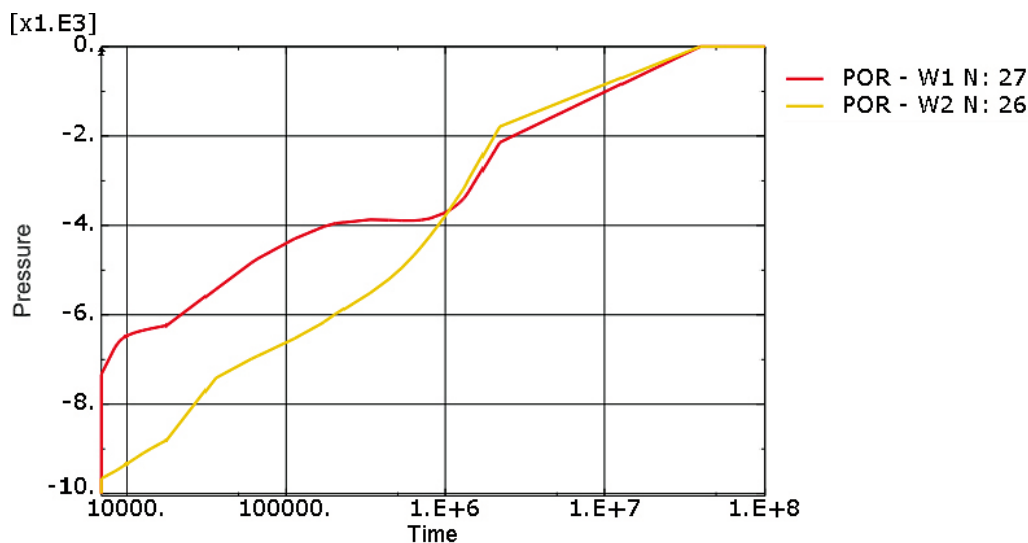


Figure 4-6. Modelled evolution of pore pressure (kPa) in the two points W1 and W2. (Time in seconds.)

The figure clearly shows that the pore pressure is equilibrated after 4×10^7 seconds. Unfortunately the plot only shows some very large calculation steps at the end of the calculation and the previous result point is 2×10^6 seconds.

Another way to investigate the time until the test is finished is to study the total energy in the model. When there is no energy produced and the increase in total energy has stopped equilibrium has been reached. Figure 4-7 shows the evolution of total energy and some other variables.

The figure shows that the total energy stops to increase at about 10^7 seconds, which correspond to 116 days or about 4 months. The results thus show a predicted time until the homogenisation is finished of 4 months. However, the actual degree of saturation of the bentonite block at start was 95–97 %, which means that some water needs to be transported into the bentonite that is not taken into account in the modelling. In addition there was an initial small gap of 0.65 mm between the block and the filter and an additional expected compression of the filter that are not taken into account.

Figure 4-7 also shows that the stabilization energy is levelling away after about 1.5×10^6 seconds, which means that the stabilization process does not affect the final part of the homogenisation and thus not the time to full homogenisation.

The modelled stresses in the measuring points are shown in Figure 4-8. Just as for the suction, there is data missing between 2×10^6 and 4×10^7 seconds. However, the final values are well stabilized and as shown in Figure 4-7 this stabilization has most likely already taken place after 10^7 seconds. The expected evolution is indicated with the hatched line for transducer P1.

Since the element mesh around the cavity is strongly deformed the stresses shown in Figure 4-8 are not taken from bentonite. Instead the stresses on the steel at the measuring points are plotted.

Figure 4-9 shows the closing of the gap and the void ratio distribution at some times.

As can be seen in Figure 4-9 the solution is not good at the contact surfaces between the swelling parts, since the gaps are not completely closed and there are peak values of high and low void ratio that are not relevant. These parts should not be considered, but instead some kind of average is probable. Another shortcoming of the calculation is the modelled slow swelling, which does not agree with the expected results. The expected fast soft gel swelling is not modelled since the material model is not valid for void ratios higher than 1.5.

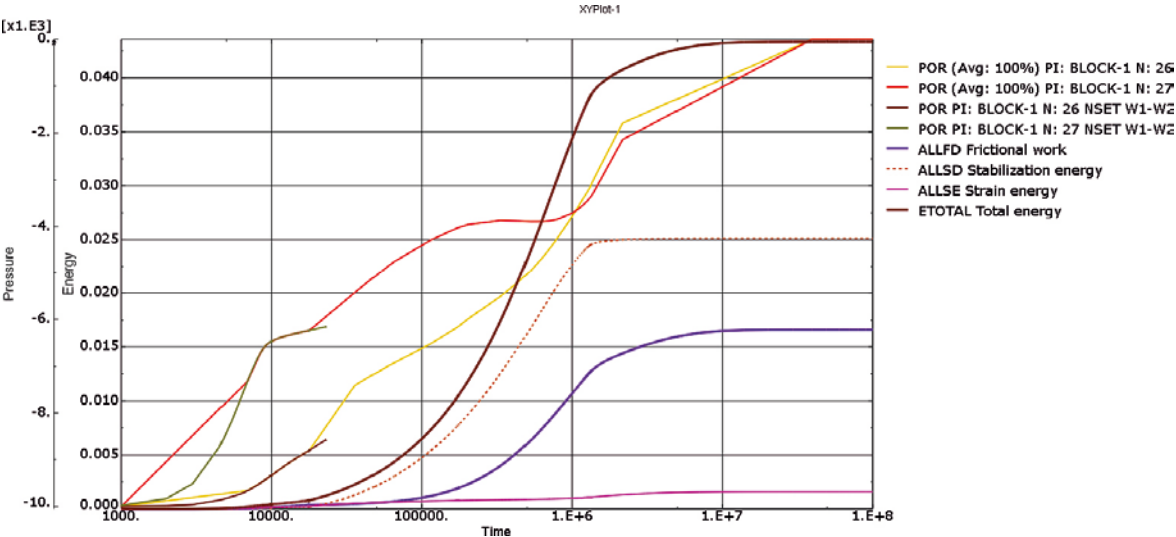


Figure 4-7. Evolution of pore pressure (POR), the total energy in the model (ETOTAL) and the stabilization energy (ALLSD).

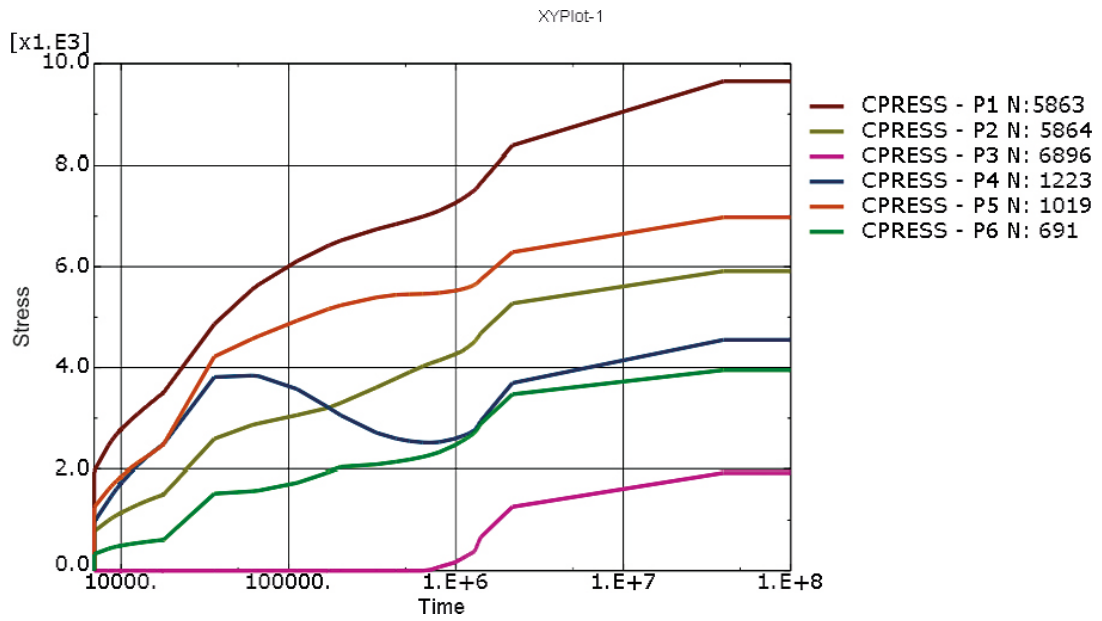


Figure 4-8. Modelled stresses in the measuring points P1–P6 (kPa). The hatched line is an evaluation of the stress based on Figure 4-7.

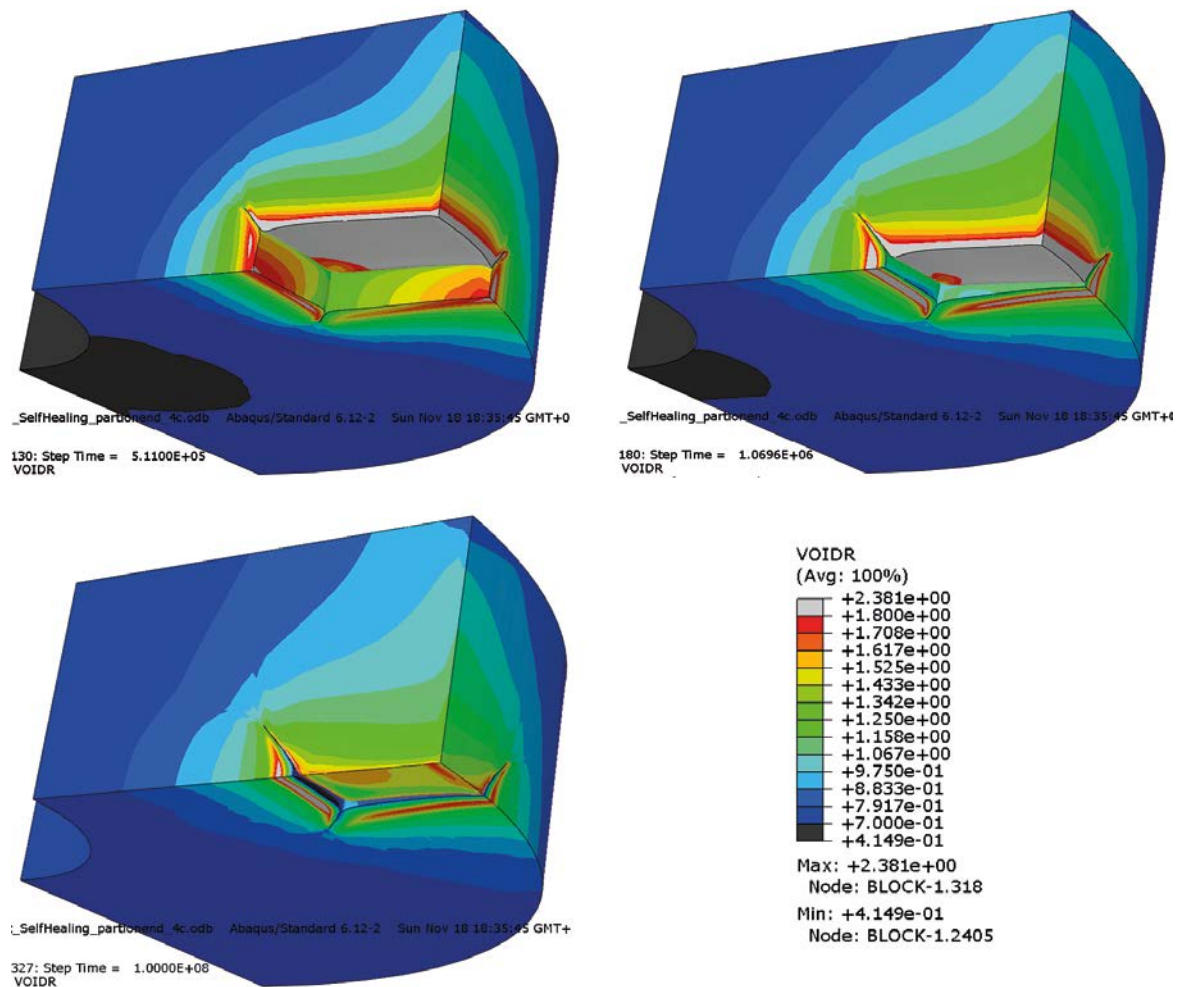


Figure 4-9. Modelled void ratio during swelling. Upper left: 6 days. Upper right: 12 days. Lower left: end state.

The void ratio distribution is also shown in Figure 4-10 in three vertical sections, cut with 2 cm equidistance.

The problems at the interfaces blur the results but if the results at areas close to the interfaces (a few mm) are neglected the highest predicted void ratio was about $e = 1.25$, which corresponds to a dry density of about $\rho_d = 1\,250\text{ kg/m}^3$.

The average stress at the end of the test is shown in Figure 4-11. If the results close to the interfaces between the contact-surfaces are neglected the lowest average stress seems to be about 1 MPa. This value fits better to the highest void ratio 1.25 than the predicted radial pressure in the measuring point P3 (2 MPa). The reason may be the anisotropic swelling situation. As seen in Figure 4-9 the gap is closed mainly by swelling parallel to the outer surface, which corresponds to axial swelling in the HR swelling tests with constant radius (see e.g. Börgesson et al. 2015). In these tests the stresses perpendicular to the swelling direction are higher than the stress parallel with the swelling.

4.3.4 Conclusions drawn at the blind prediction

The following conclusions were given in the PM (cited) before start of the test:

A true prediction of the homogenisation of an irregular cavity in a bentonite ring has been presented. The results show that complete homogenisation has occurred after about 4 months, the lowest swelling pressure at the centre of the cavity (P3) will be 1–2 MPa after completed homogenisation and the lowest void ratio will be about 1.25.

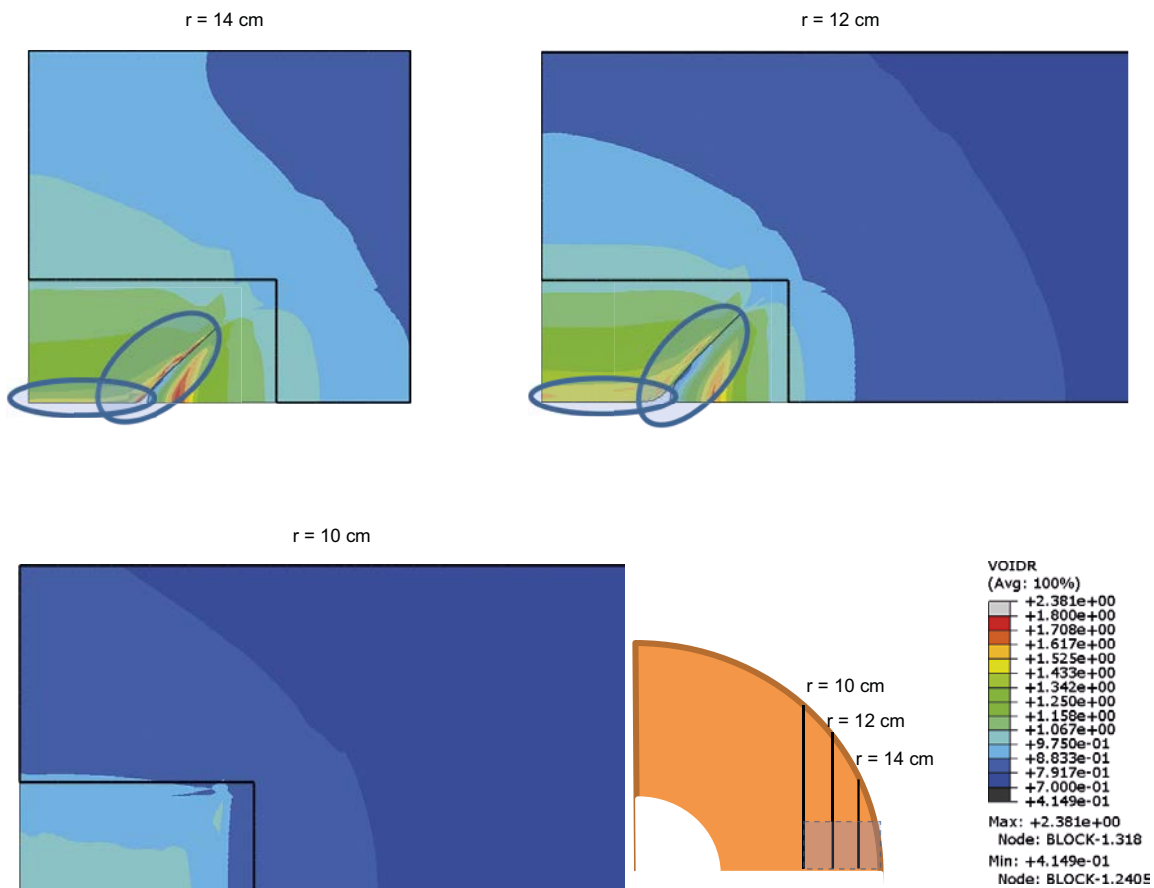


Figure 4-10. Void ratio distribution at three different sections after completed swelling. The initial cavity is indicated. The zones with irrelevant results are circled.

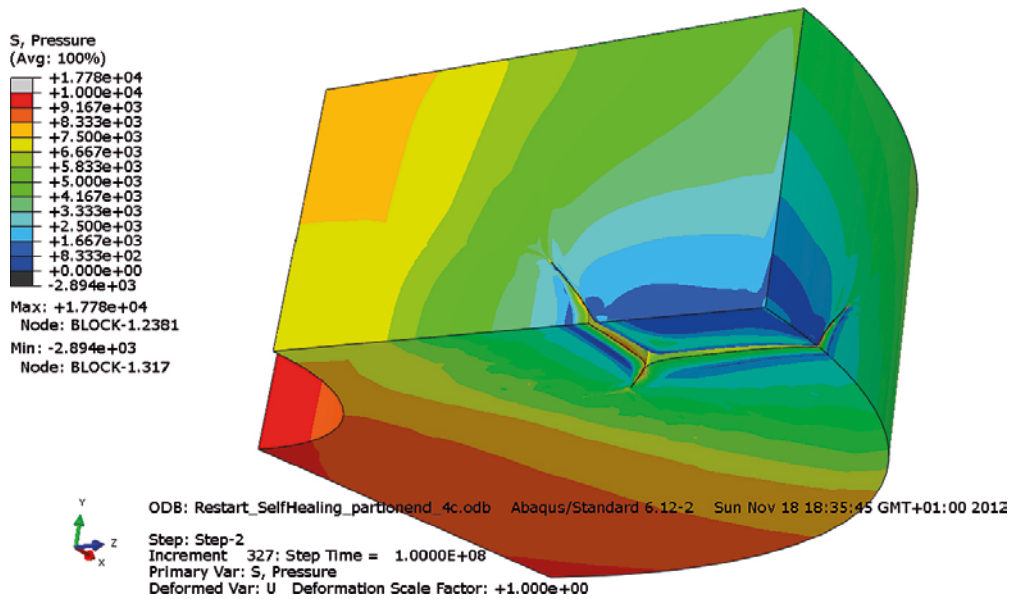


Figure 4-11. Final average stress distribution (kPa).

4.4 Measured results

The measured results including sensor data and the results from the sampling and determination of density and water content after termination have been presented in a short report, attached as Appendix 5. A short summary of the most relevant results used for comparison with modelled results will be shown in this chapter.

4.4.1 Data readings

Figure 4-12 shows the measured total stress (swelling pressure) as a function of date. The pressure curves show very small but clearly detectable momentary increased pressure in July–August, which are judged to be caused by increased temperature in the laboratory in summer. Ignoring these and especially the last one the results show that the pressure has equalized during the last year.

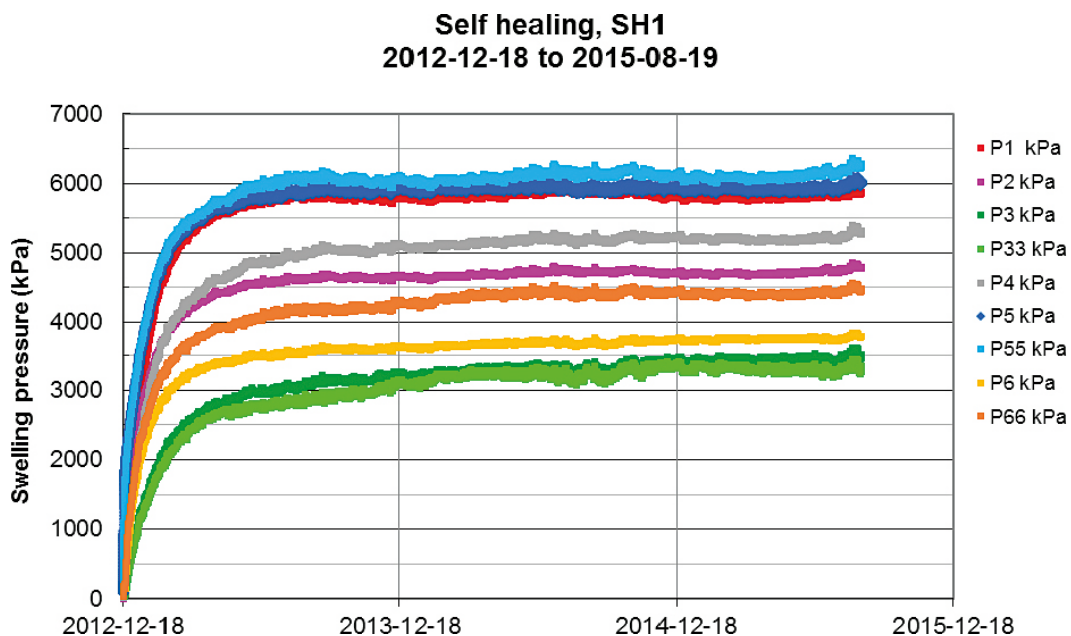


Figure 4-12. Evolution of swelling pressure measured by the transducers. The locations of the sensors are shown in Figure 4-1.

The results are nice and confirm the accuracy of the results since two of the three pairs of transducers located at symmetric positions show very similar results, namely the two transducers P3 and P33, which are located in the centre of the cavity at opposite sides and thus should have the lowest pressure. Also transducers P5 and P55 show very similar results. The only exception is transducers P6 and P66, which differ 0.7 MPa (4.5 MPa and 3.8 MPa).

Figure 4-13 shows the results of the measurement of suction.

The sensors are located on the inner periphery of the test and W1 is located furthest away from the wetting periphery and should yield the latest water saturation. The sensors start yielding results after about two months when the wetting has increased the RH or suction to about 5 MPa which is the limit where these sensors start working. Then the suction increases rather fast up to 2 MPa, with logically W1 at the head. Later on the readings of W1 ceases and those of W2 get messy.

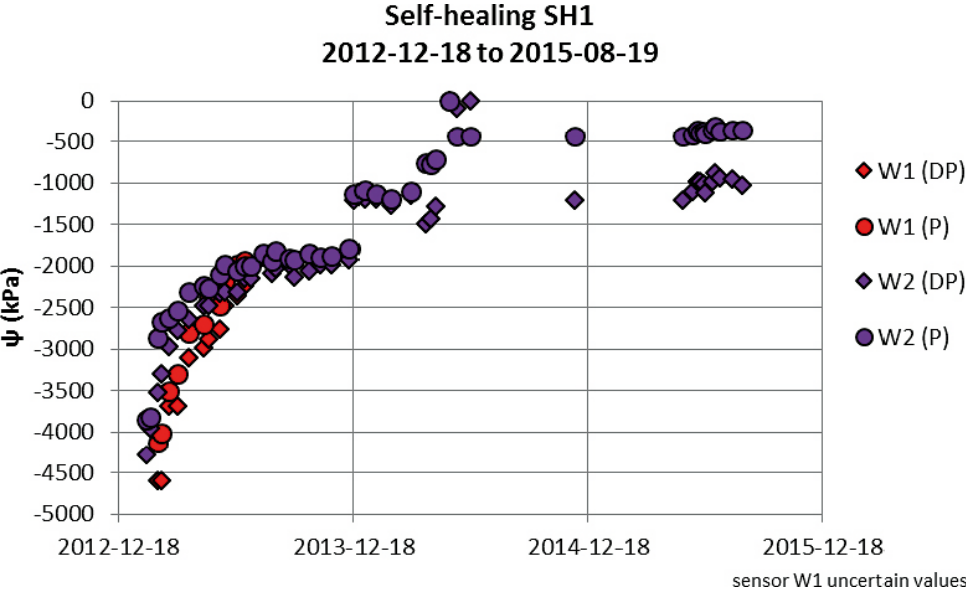


Figure 4-13. Evolution of water potential (suction) measured with thermocouple psychrometers. The evaluation was made by both the dew point method (DP) and the psychrometer method (P). The labels show the number of the sensor (W1, W2) and the evaluation method (DP, P). The locations of the sensors are shown in Figure 4-1.

4.4.2 Sampling results

The test was terminated and dismantled on 2015-08-19. An extensive sampling and determination of density and water content was then carried through. Figure 4-14 shows as example the dry density evaluated in the horizontal central section around the cavity. Other similar results are derived for other sections as shown in Appendix 5.

The average degree of saturation evaluated from the sampling was 101 %, which together with the measuring results showed that the test was completely water saturated. This was also confirmed by observations done in the holes for the psychrometers, where traces of free water were found at dismantling of the test.

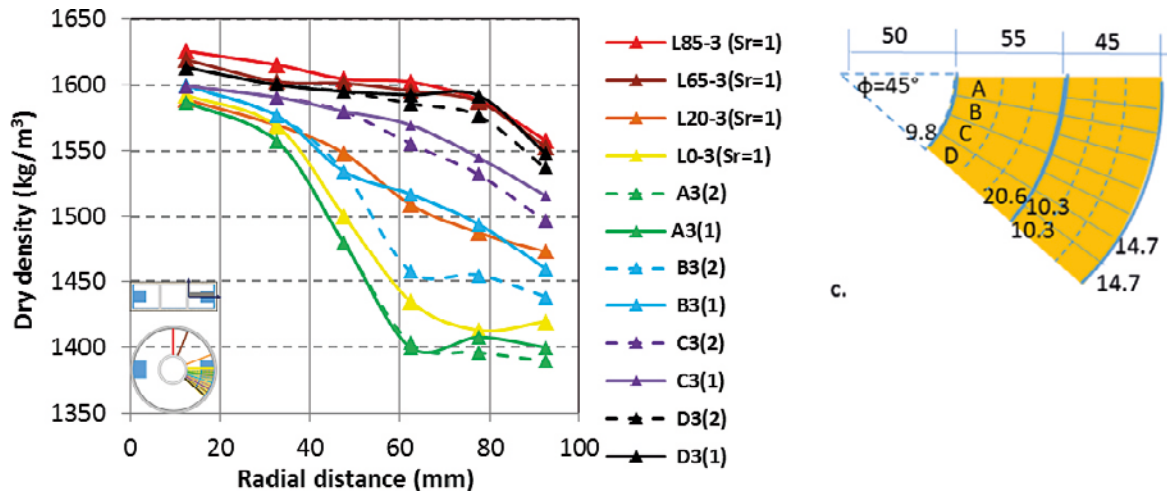


Figure 4-14. Distribution of dry density at the central horizontal symmetry plane at different angles from the vertical symmetry plane through the cavity. The colours (red, brown, orange, yellow, green, blue, purple, black) show the angles (85° , 65° , 20° , 0° , -6° , -17° , -28° , -39°) to the centre of the cavity. All values are evaluated from density and water content results except when the labels include ($Sr = 1$) when they are calculated from measured water contents and assumed 100 % water saturation.

4.5 Comparison with measurements

4.5.1 General

The measured time evolution of stresses and suction and the measured density distribution at the end of the test can be compared with the modelling results.

4.5.2 Transducer measurements

Figure 5-15 shows the measured and modelled total stresses in the true prediction. The comparison of the end values clearly shows that the modelled stress 2 MPa in the centre of the cavity (P3) is lower than the measured stress 3.3 MPa. On the other hand the stress at the inner steel cylinder P1 is overestimated by the modelling (9.7 MPa) compared to the measured stress 6 MPa. The modelled stress that agrees best with the measured is at the lid above the cavity (transducers P6 and P66) where the modelled stress is 4.0 MPa and the measured stresses are 3.8 MPa and 4.5 MPa.

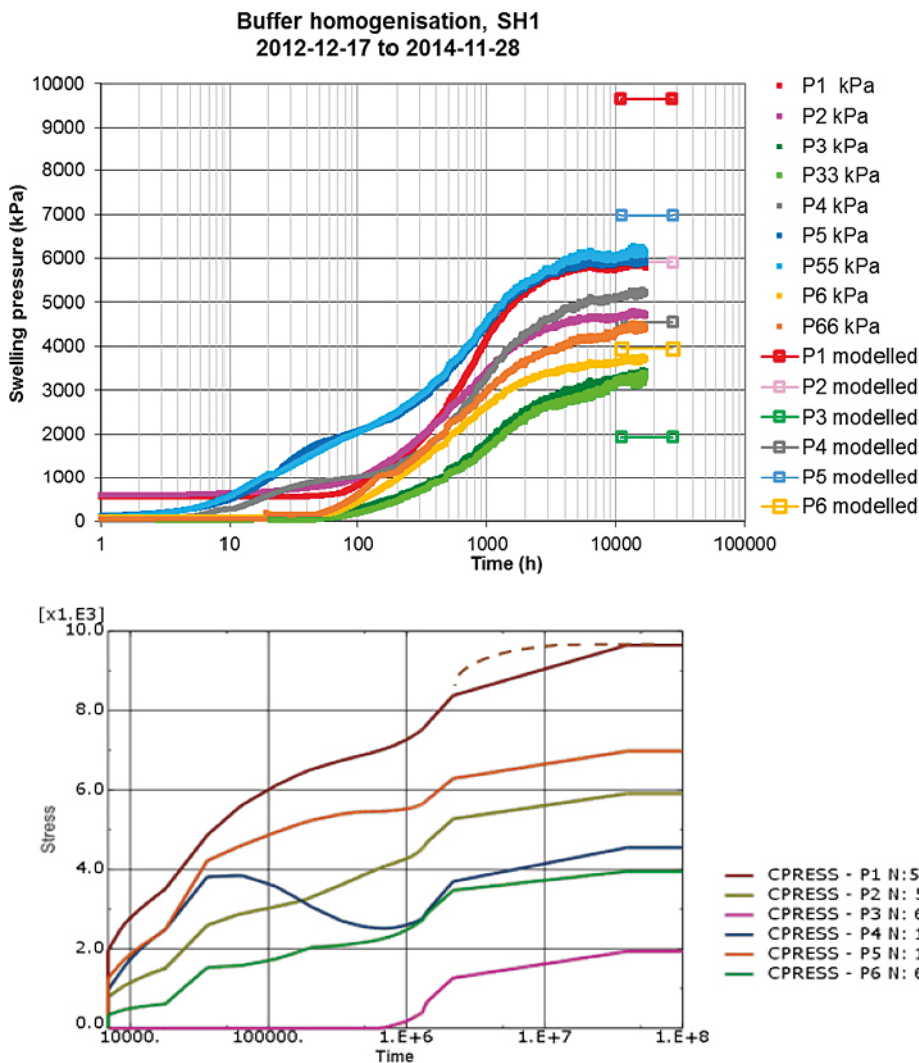


Figure 4-15. Measured and modelled stress evolution. The upper diagram shows the measured evolution and the final values of the modelled stresses. The lower diagram shows the modelled evolution (time in seconds and pressure in kPa). The time scale is the same in the two diagrams in the sense that 10^8 s corresponds to about 28 000 hours. See Figure 4-1 for location of transducers.

The measured time evolution seems to be slower than the modelled. Unfortunately the modelling data is missing when the stresses reach their final values, but an estimate yields that the modelled homogenisation goes 2–3 times faster than the measured. This is confirmed by the stress at P6 (which agreed well between measured and modelled final stress). The modelled stress at P6 is 3.5 MPa after about 700 hours, while the measured stress 3.5 MPa is reached after about 2 000 hours.

Figure 4-16 shows the measured and modelled suction.

The overestimation of the modelled equalisation rate is even larger (a factor of about 5) for the suction than for the total stresses.

The too fast homogenisation evolution can partly be explained by the fact that the model assumes complete water saturation from start and no slots between the bentonite block and the boundaries. However, the actual bentonite block was only saturated to about 96 % and the block did not completely fill up the space between the inner and outer cylinder. So there was a need for extra water to be transported into the bentonite both for saturation and for swelling, which delays the time to equilibrium.

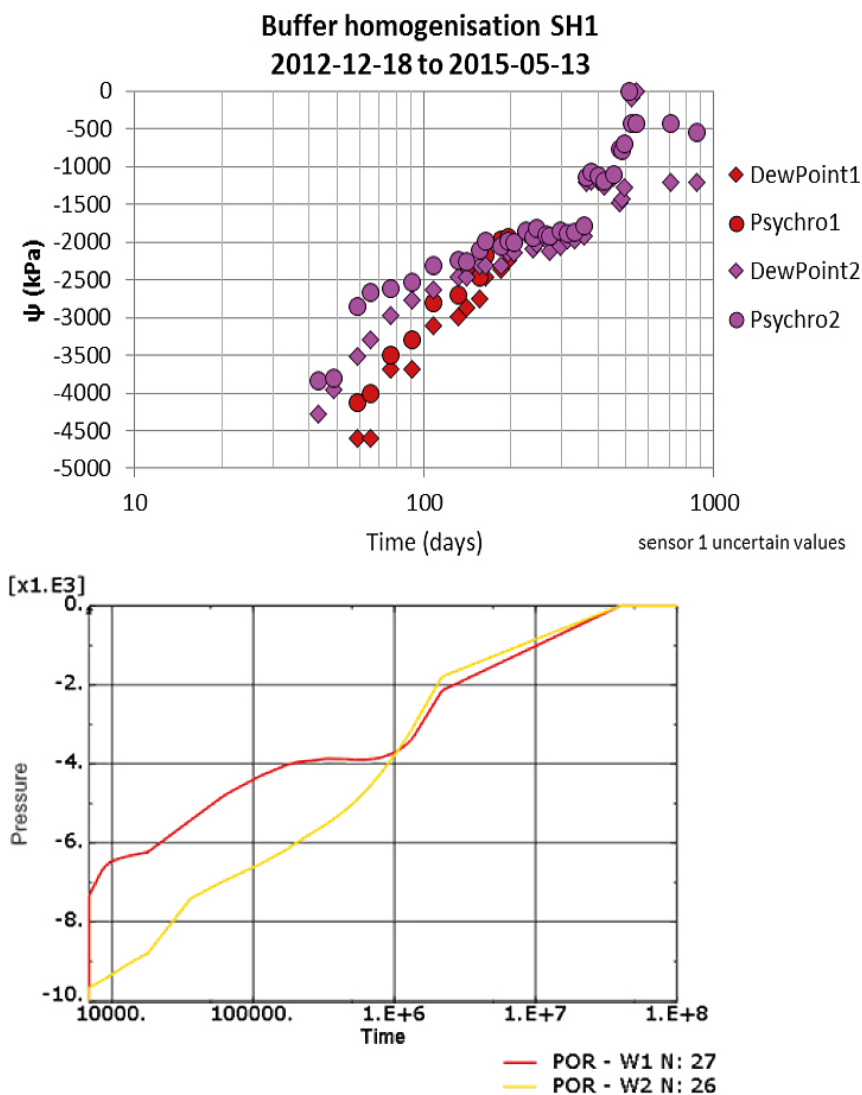


Figure 4-16. Measured and modelled pore water pressure. The upper diagram shows the measured evolution. The lower diagram shows the modelled evolution (time in seconds and pressure in kPa). See Figure 4-1 for location of transducers.

4.5.3 Density distribution

The comparison between modelled and measured density distribution is not so easy to make, since the samples taken from the test had volume of about $17 \times 17 \times 15 \text{ mm}^3$ and the modelling results have a resolution that is about 1 000 times larger. Figure 4-17 shows an attempt to evaluate the modelled void ratio in the cavity in a sample with the same dimension as the sample taken for determining void ratio in the centre of the cavity.

The measured void ratio distribution in the central section is shown in Figure 4-18 (recalculated to void ratio from Figure A5-13 in Appendix 5).

The extension of the sample shown in Figure 4-17 is so large that the modelled void ratio varies between about $1.8 < e < 1.0$. An evaluation of the average void ratio yields $e_a \approx 1.2$. This sample corresponds to the measured result encircled in Figure 4-17, which has $e = 1.0$. The modelling thus overestimates the void ratio, which agrees with the modelled too low radial stress at corresponding location where the total stress was measured with transducers P3 and P33 (2.0 MPa compared to the measured 3.3 MPa).

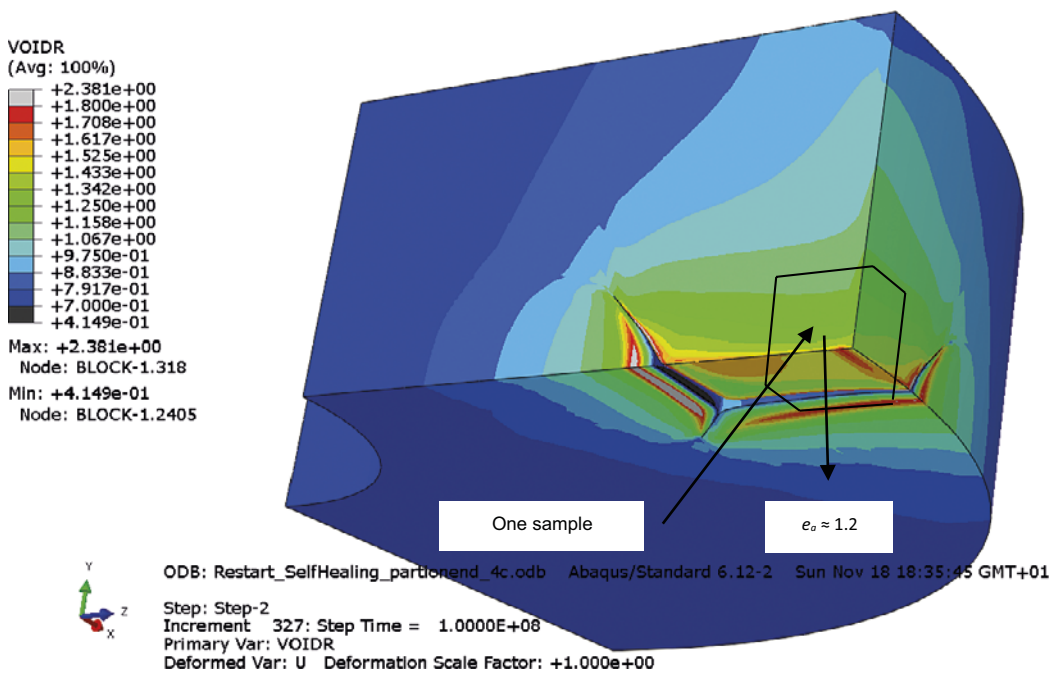


Figure 4-17. Modelling of the self-healing of the cavity. The picture shows the modelled void ratio distribution after completed homogenisation. The size of one sample taken after the test is illustrated. The evaluated average void ratio of that sample is $e_a \approx 1.2$.

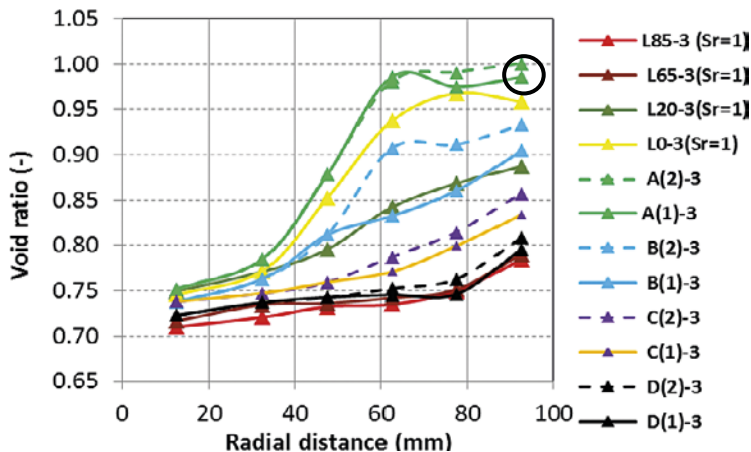


Figure 4-18. Measured void ratio distribution in the central section. The encircled value corresponds to the sample shown in Figure 4-17.

It is interesting to compare the void ratio with the modelled average stress in the corresponding sample volume and the measured and modelled total stress in the centre of the cavity (transducer P3). Figure 4-19 shows the modelled average stress.

Figure 4-19 shows that the modelled mean of the average stress p in the volume corresponding to the sample is about $p = 2$ MPa, which corresponds well to the modelled total stress in the centre of the cavity. However, the modelled average void ratio $e = 1.2$ should give the average stress $p = 0.5\text{--}0.8$ MPa according to measured relations (Börgesson et al. 1995) and according to the porous elastic model (Equation 3-1). This disagreement is caused by the dilatancy that takes place during the swelling when the stress paths hit the failure line. The dilatancy causes an extra volume expansion and a reduction of the cap extension, which can be seen as a decrease of the cap position p_b (see Figure 3-31 and Börgesson et al. 2015). Figure 4-20 shows the value of p_b at the end of the test.

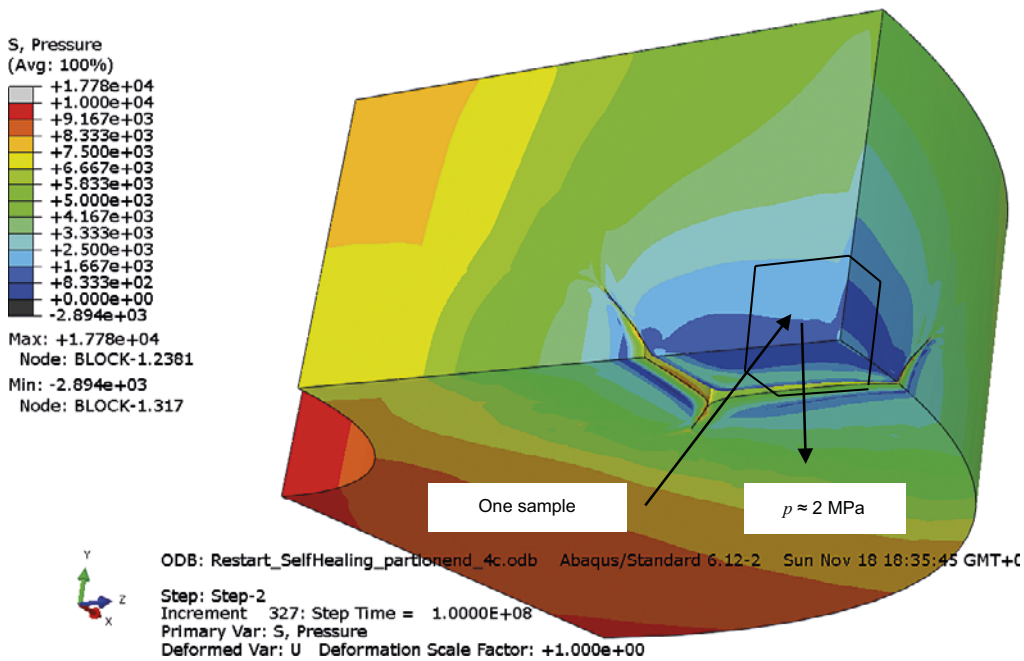


Figure 4-19. Modelled final average stress (kPa).

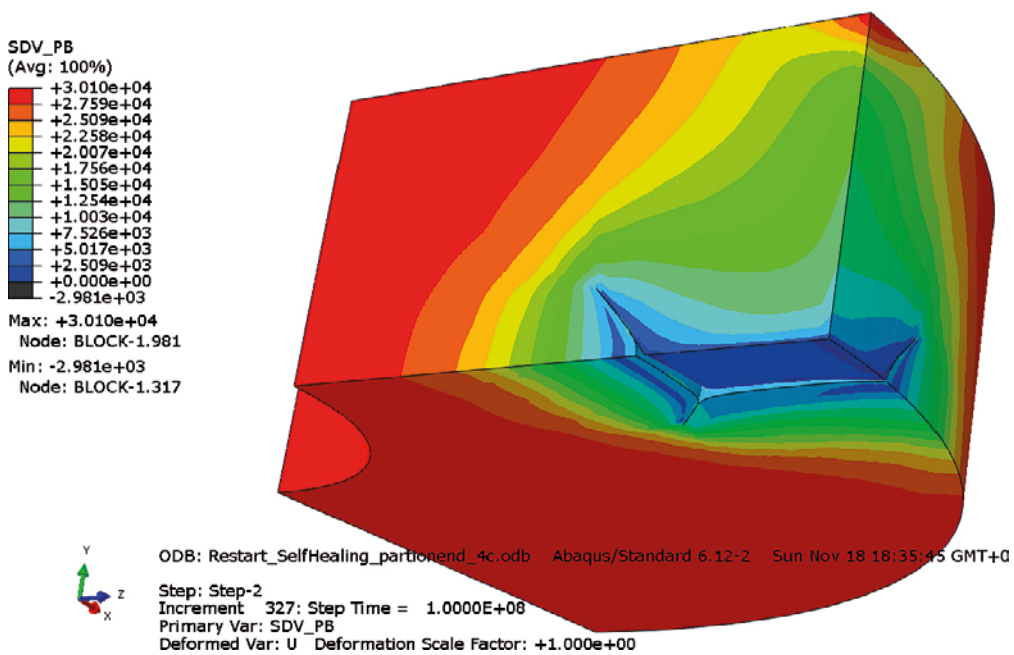


Figure 4-20. Location of the cap position p_b at the end of the test.

Figure 4-20 shows that the cap has decreased from the initial position $p_b = 30$ MPa to $p_b = 10$ MPa, which is the average value at the sample position shown in Figure 4-19.

If the same comparison between measured void ratio and measured total stress in the cavity is made, similar disagreement can be seen. The measured void ratio $e = 1.0$ should give the average stress $p = 1.8$ – 2.0 MPa according to measured relations (Börgesson et al. 1995) and according to the porous elastic model, which can be compared to the measured total stress 3.4 MPa.

Both the measured and modelled results thus yield higher stress than would be expected considering the void ratio (or density).

4.5.4 Conclusions

The calculated time to reach equilibrium of the homogenisation phase was 2–3 times shorter than the measured. The main reason is judged to be caused by the difference in modelled and actual initial conditions. The actual initial degree of saturation was $S_r = 95\% - 97\%$ compared to the modelled $S_r = 100\%$, which means that some additional water must be taken up by the bentonite. In the model virtually all water needed was already in the bentonite from start. In addition the actual size of the bentonite block was slightly smaller than the inner boundaries of the steel cylinders, which means that some swelling was required.

A remaining gap of a few mm in parts of the final contact between the different walls of the cavity was left in the calculation. One reason is the element size in the model. Smaller elements would probably reduce the gap but would also mean increased number of elements and cause even larger convergence problems.

The difference between the highest and lowest stress in the measuring points was larger in the models than measured. Both the blind prediction yielded the highest stress 9.5 MPa in the measuring point located furthest away from the cavity and the lowest stress 2.0 MPa in the centre of the cavity while the measurements in corresponding places were 6.0 MPa and 3.3 MPa respectively.

The blind prediction yielded higher void ratio $e = 1.2$ in the centre of the cavity than the measured void ratio $e = 1.0$.

A general conclusion is thus that the Plastic Cap model underestimated the self-healing ability (or the homogenisation) of the bentonite in the test by yielding too high void ratio and too low stresses in the former cavity.

4.6 Updated calculations

4.6.1 General

A number of new calculations have been done by refining the element mesh and playing with the stabilizing function and the tolerances. Unfortunately they have not been very successful and no very obvious improvement of the results has been achieved. There have also been large problems with convergence.

The struggle to reach better results will be illustrated with two examples.

4.6.2 Example 1

This calculation is named *Restart_SelfHealing_ver6132_6a*. There was a slight change in element mesh but the difficulty was to reach convergence. The stabilize process was required with a rather large stabilize factor. Rather large tolerances were also needed.

Figure 4-21 shows the results of the evolution of the stresses in the measuring points.

Figure 4-21 shows that the swelling is completed after 10^7 seconds or about 4 months, which agrees with the estimation done in the prediction. However, the difference from the predicted results is small. The only strong improvement is the measured final stress in point 3, which increased from 2.0 MPa at the prediction to 3.3 MPa at this calculation, which agrees very well with the measured value.

However, the deformed structure at the end of the calculation was not satisfactory. Larger remaining gap was left and the same too low void ratio in the cavity was derived as shown in Figure 4-22.

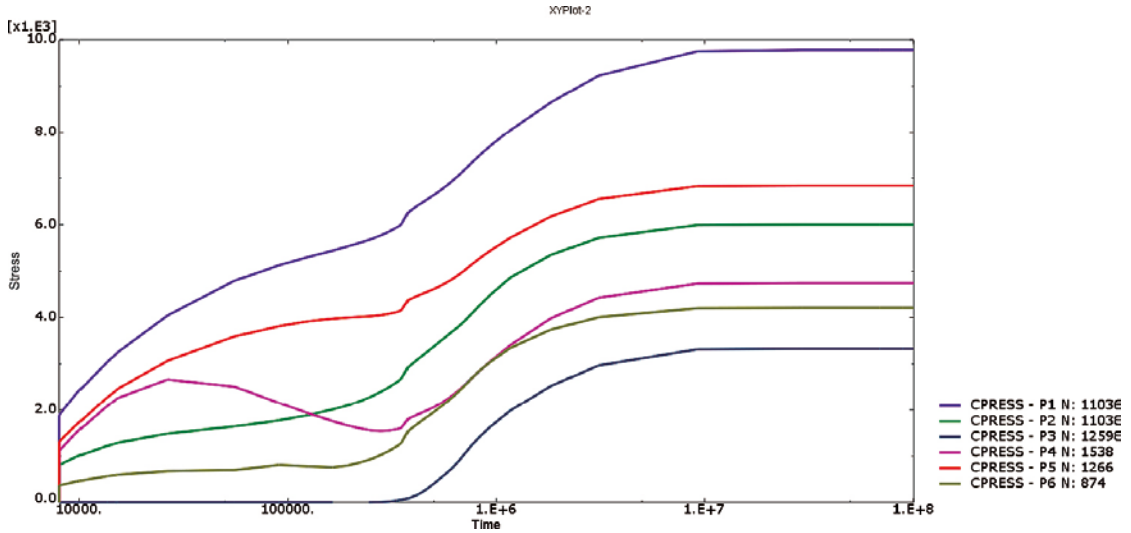


Figure 4-21. Modelled evolution of stresses in the measuring points (kPa).

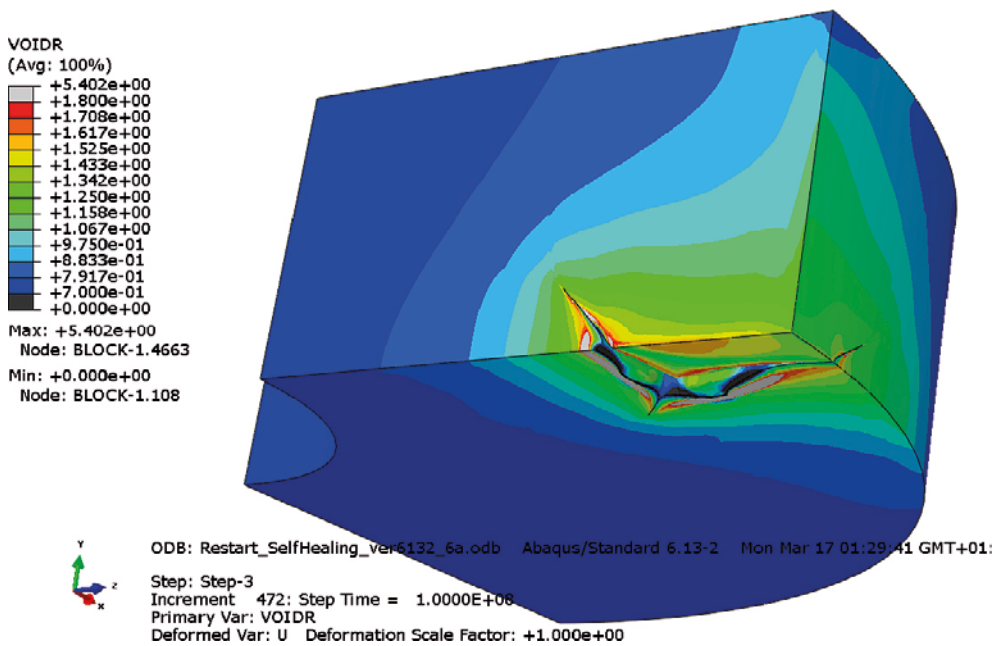


Figure 4-22. Void ratio distribution at the end of the calculation.

4.6.3 Example 2

This calculation was the final one and is named *Restart_SelfHealing_ver6132_7a*. Additional change in element mesh was done for this calculation but there were still large difficulties to reach convergence. The stabilize process was required with a rather high stabilize factor as well as rather large tolerances.

Figure 4-23 shows the element mesh in this calculation.

Table 4-5 shows how far the convergence reached at different (increasing) stabilize factors. The table shows that the stabilize factor needed to be 6×10^4 larger than the default value in order to fulfil the calculation.

Table 4-5. Stabilize factor and time when convergence failed.

Stabilize factor	Calculation stopped (sec.)	Remark
1.09×10^9	0	Default value
1×10^{10}	1.77×10^3	
1×10^{11}	7.83×10^3	
5×10^{11}	1.63×10^4	
1×10^{12}	3.55×10^4	
5×10^{12}	2.58×10^5	
8×10^{12}	3.96×10^5	
1×10^{13}	2.89×10^5	
2×10^{13}	1.22×10^6	
3×10^{13}	4.63×10^6	
6×10^{13}	-	Worked until end
1×10^{14}	-	Worked until end

Figure 4-24 shows the closing of the gap and the void ratio at half way swelling and after completed swelling.

Figure 4-24 shows that the mesh after completed swelling is quite nice and the remaining cavities very small. Evaluation of the average void ratio of the sample taken in the centre of the cavity in a way identical to that described in Figure 4-19 yields a similar average void ratio $e_a \approx 1.2$.

Figure 4-25 shows the results of the evolution of the stresses in the measuring points.

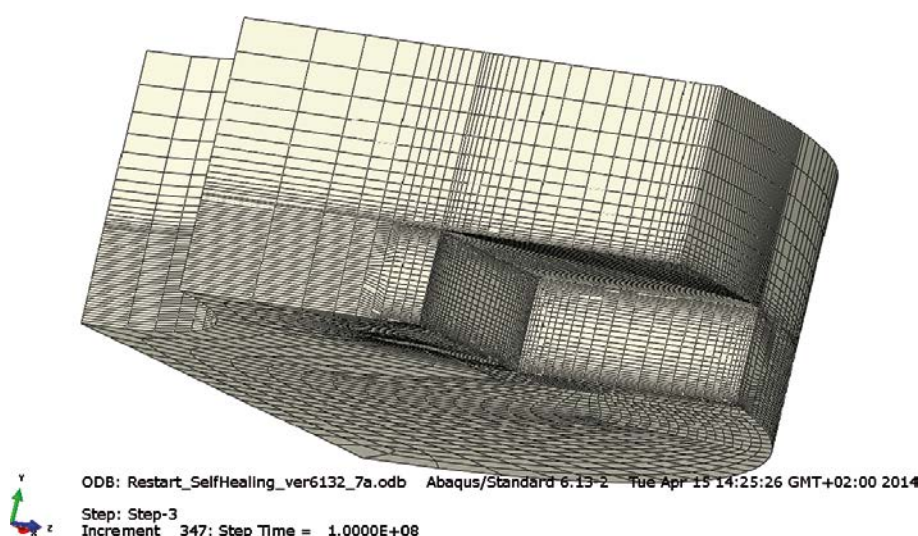


Figure 4-23. Element mesh of the bentonite block.

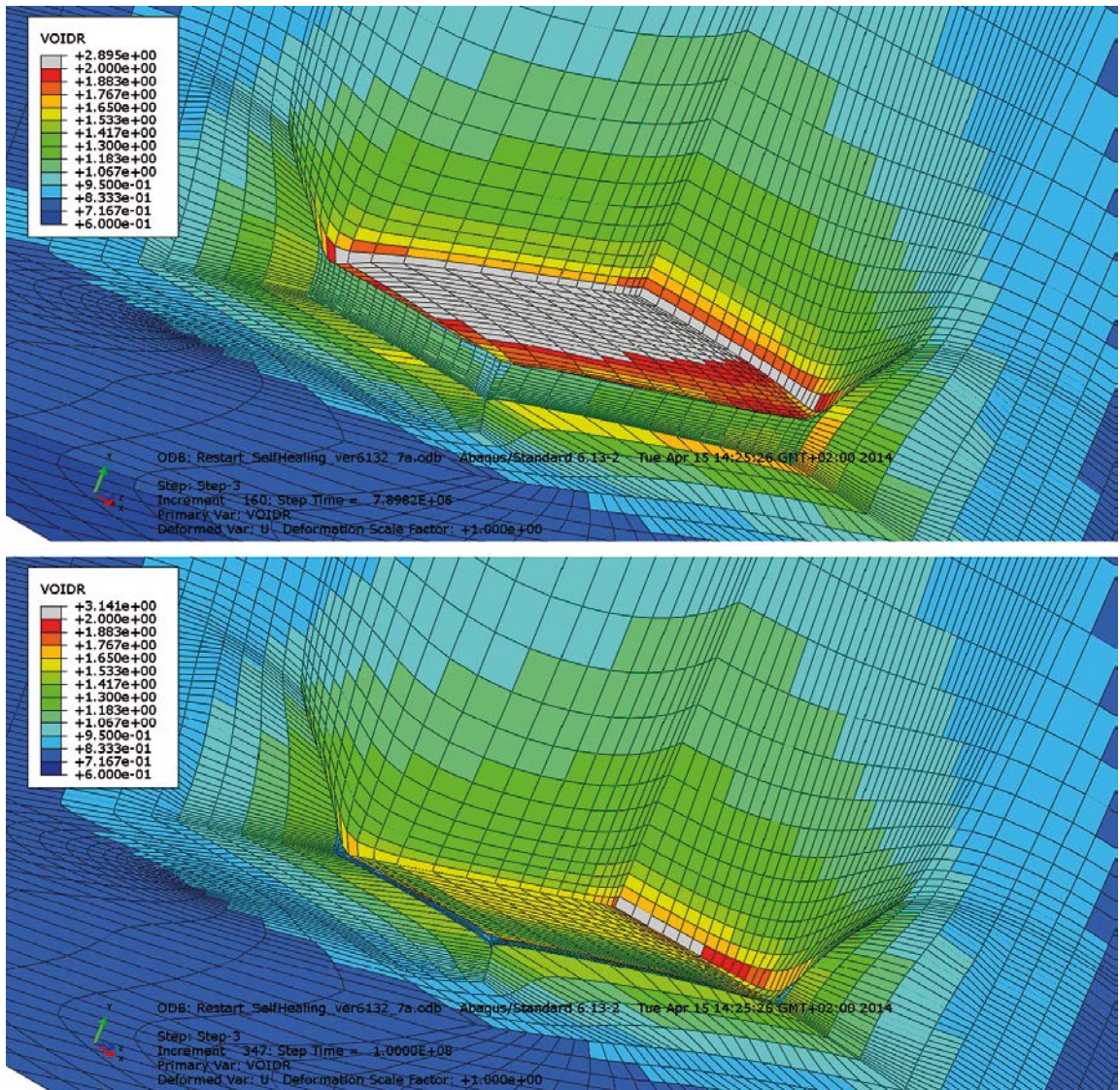


Figure 4-24. Void ratio after half way swelling and after completed swelling.

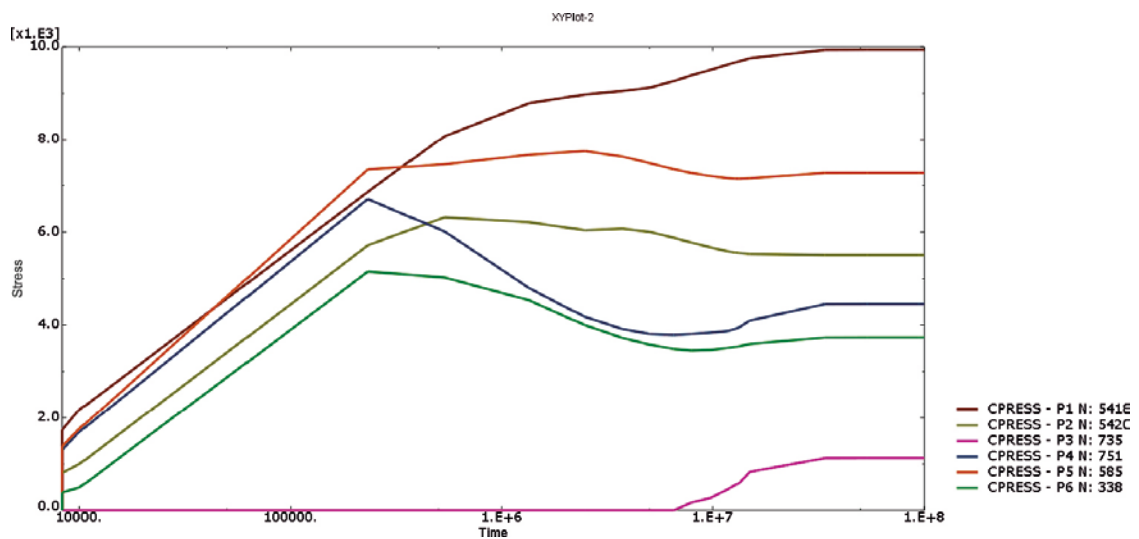


Figure 4-25. Modelled evolution of stresses in the measuring points (kPa).

The time scale is probably not relevant in this calculation since it differs substantially from the other calculations (much longer time until equilibrium). The reason is certainly the high stabilize factor. The stresses don't differ very much from the other calculations except for the stress at point 3, which is located in the centre of the cavity. The stress there is much lower or only 1.1 MPa, which can be compared to the measured stress 3.3 MPa.

It seems thus that the last calculation yields the best element mesh deformation but not the best results considering the low stress at the measuring point in the centre of the cavity. It also seems that the needed stabilize factor is too high to yield a reliable time evolution but it is difficult to know how much that has affected the end result.

4.6.4 Conclusions

The trials to improve the results by elaborating with the element mesh (but not the material model) were not successful. No better results were achieved.

4.7 Calculation with the old Drucker-Prager model

4.7.1 General

For comparison also the old Drucker-Prager model has been used for modelling SH1. This material model was used in SR-Site (Åkesson et al. 2010a) and in Task 1 of the small scale test task of TF EBS (Börgesson et al. 2015). The model is described in Section 3.3.

The relation between void ratio and hydraulic conductivity and the Porous Elastic ν differed somewhat:

$$K_{DP} = 2K_{PC}$$

where

K_{DP} = hydraulic conductivity in the Drucker-Prager model

K_{PC} = hydraulic conductivity in the Plastic Cap model

$\nu = 0.21$ in the Drucker-Prager model

The element mesh, the boundary conditions and the initial conditions were identical to the description made in Section 4.2.

4.7.2 Results

Many of the results are compared to the results of the prediction made with the Plastic Cap model presented in Section 4.3.

The modelled stress evolution is shown in Figure 4-26. Comparing these results with the Plastic Cap model (Figure 4-3) shows that the difference is very small. The lowest stress in the centre of the cavity is about 2.0 MPa, which is almost identical the result from the Plastic Cap model. The other stresses differ less than 0.5 MPa.

The void ratio distribution of the two models is compared in Figure 4-27.

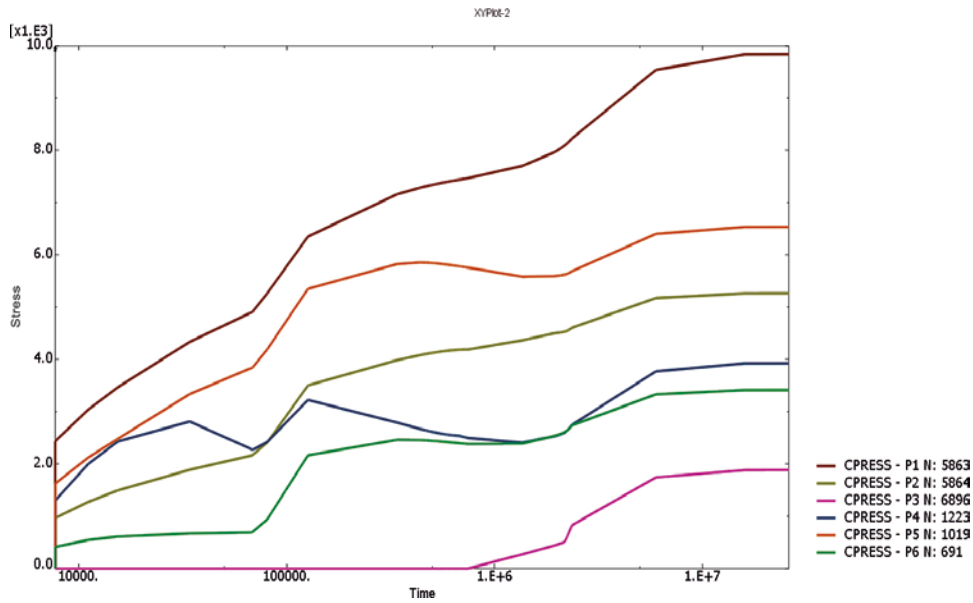


Figure 4-26. Modelled evolution of the stresses in the measuring points. Stresses (kPa) plotted versus time (s).

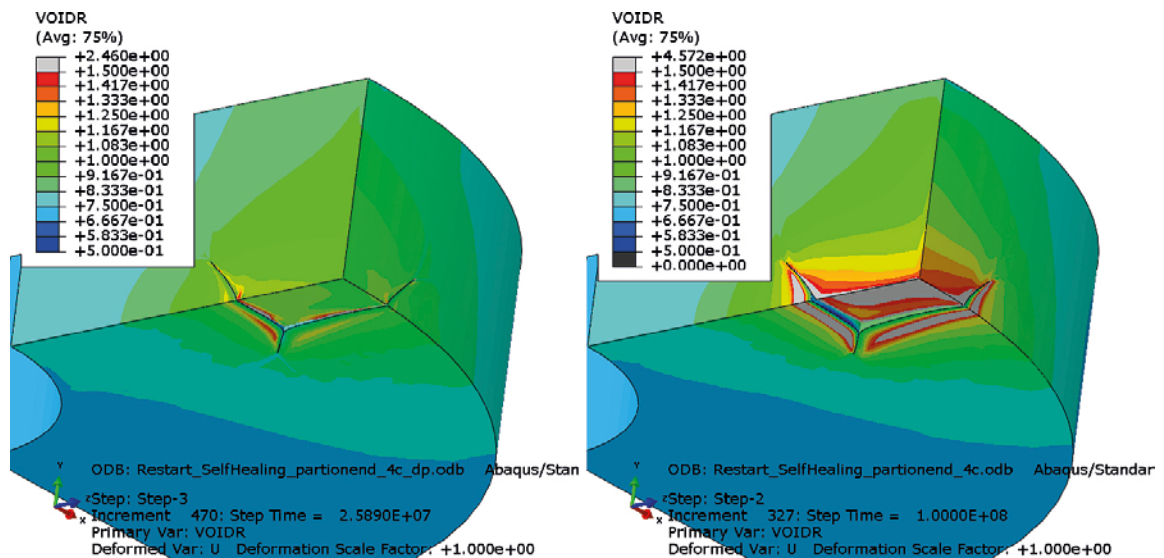


Figure 4-27. Void ratio distribution at the end of the test. The results of the Drucker-Prager model (left) are compared to the results of the prediction with the Plastic Cap model (right).

Figure 4-27 shows that the void ratios differ substantially between the two models. It is clearly lower for the D-P model. The figure also shows that the D-P model yields better closing of the cavity with smaller remaining gaps. An evaluation of the average void ratio in three sampling locations is shown in Figure 4-28.

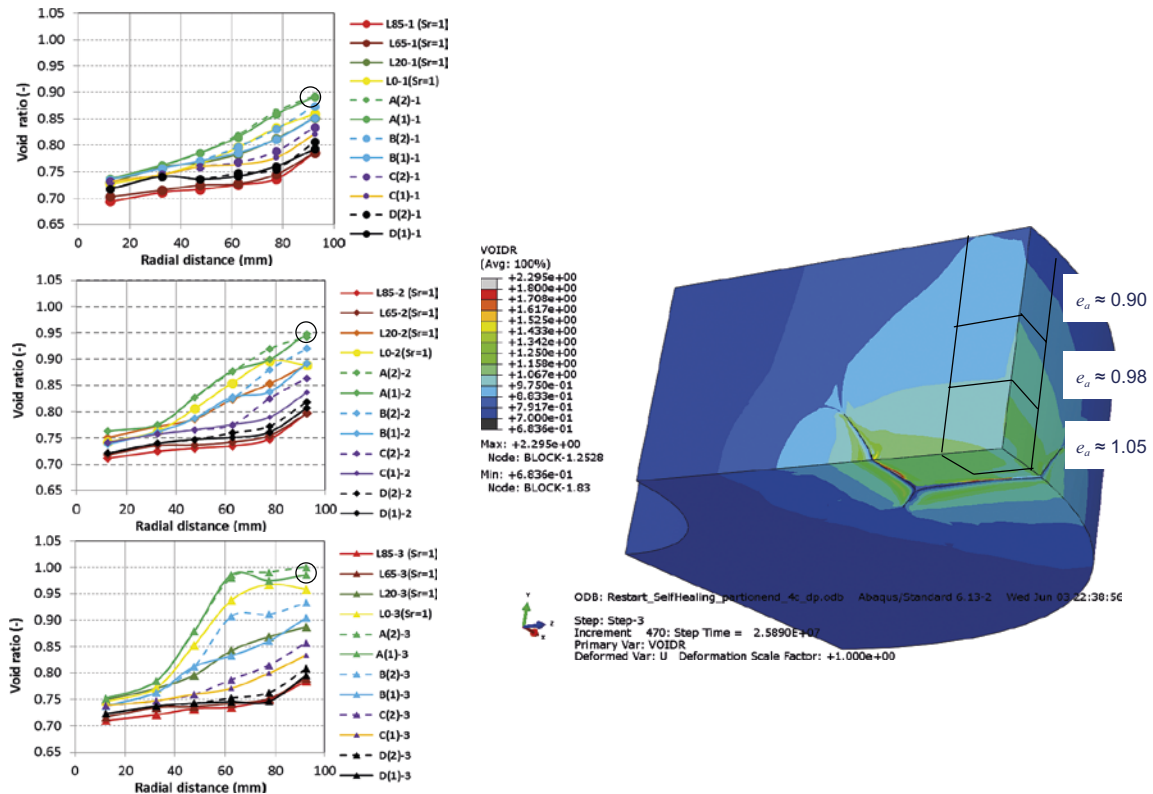


Figure 4-28. Evaluation of the void ratio in three sampling locations and comparison with measurements. The measured void ratio in the three sample positions are circled in the diagrams to the left.

Figure 4-28 shows that the modelled void ratios in the three sample positions agree fairly well with the measured values.

The modelled average stress for the two material models is compared in Figure 4-29.

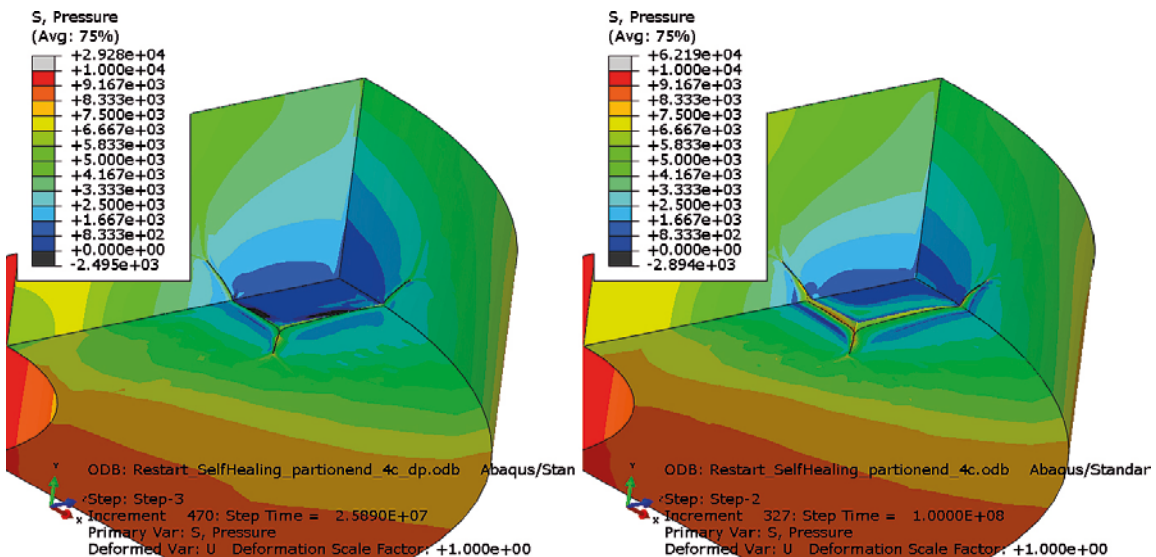


Figure 4-29. Distribution of average stress (kPa) at the end of the test. The results of the Drucker-Prager model (left) are compared to the results of the Plastic Cap model (right).

In contrary to the void ratio the average stress does not differ much between the two models. It is actually slightly higher for the P-C model than for the D-P model, which is unexpected considering that the void ratio was higher (lower density) for the P-C model. Both are in average a little lower than 2.0 MPa in the volume corresponding to the sample taken in the centre of the cavity.

There is thus a disagreement in void ratio between the two models but an agreement in stress. The modelled average void ratio $e_a = 1.05$ in the sampling point in the centre of the cavity should give the average stress $p = 1.3\text{--}1.5$ MPa according to measured relations (Börgesson et al. 1995) and according to the porous elastic model, which can be compared to the measured total stress $p = 3.3$ MPa. The difference between the two models is judged to be caused by the difference in dilatancy during plastic straining.

4.7.3 Conclusions

The difference between the highest and lowest stresses in the measuring points was also larger in the D-P model than measured. The Drucker-Prager model yielded the highest stress 9.5 MPa in the measuring point located furthest away from the cavity and the lowest stress 2.0 MPa in the centre of the cavity in agreement with the Plastic Cap model, while the measurements in corresponding places were 6.0 MPa and 3.3 MPa respectively.

The Drucker-Prager model yielded slightly smaller remaining gap than the blind prediction.

The Drucker-Prager plastic model captured the homogenisation well with a void ratio distribution that agreed rather well with the measured.

4.8 Comments and conclusions

The Self-Healing test SH1 has been modelled as Subtask 2 of the homogenisation task of phase 2 of the TF EBS with two different material models. The test concerned swelling and self-healing of two cavities with the dimensions $35 \times 50 \times 70$ mm cut in a bentonite block with the diameter 300 mm and the height 100 mm. The test included measurement of swelling pressure in 9 positions and suction in 2 positions. The test was terminated after equilibrium and vastly sampled. The density and water ratio of the samples were determined. The test ran for 2 years and 8 months.

A blind prediction was done and delivered before start of the test. The new Plastic Cap material model that had been calibrated and verified in Subtask 1 of the homogenisation task was used for the prediction.

Before termination of the test a number of additional calculations were made in order to improve the results, but without changing the material model or the parameters. Large difficulties with convergence of the calculations were met with.

The test was also modelled using the old Drucker-Prager plastic material model that had been used for SR-Site.

Finally, the results from the prediction and the other calculations were compared to the measured results. The comparisons yielded the following observations and conclusions:

The calculated time to reach equilibrium of the homogenisation phase was generally 2–3 times shorter than the measured for all calculations. The main reason is judged to be caused by the difference in modelled and actual initial conditions. The actual initial degree of saturation was $S_r = 95\% - 97\%$ compared to the modelled $S_r = 100\%$, which means that some additional water must be taken up by the bentonite. In the model virtually all water needed was already in the bentonite from start. In addition the actual size of the bentonite block was slightly smaller than the inner boundaries of the steel cylinders, which means that some swelling was required.

All models yielded a remaining gap of a few mm in parts of the final contact between the different walls of the cavity. One reason is the element size in the model. Smaller elements would probably reduce the gap but would also mean increased number of elements and cause even larger convergence problems. The Drucker-Prager model yielded slightly smaller remaining gap than the prediction.

The difference between the highest and lowest stresses in the measuring points was larger in the models than measured. Both the blind prediction and the Drucker-Prager model yielded the highest stress 9.5 MPa in the measuring point located furthest away from the cavity and the lowest stress 2.0 MPa in the centre of the cavity while the measurements in corresponding places were 6.0 MPa and 3.3 MPa respectively.

The blind prediction yielded higher void ratio $e = 1.2$ in the centre of the cavity than the measured void ratio $e = 1.0$. The Drucker-Prager model yielded $e = 1.05$, which is in better agreement with measured results. This was also generally the case for the void ratio distribution.

The trials to improve the results by elaborating with the element mesh (but not the material model) were not successful. No better results were achieved.

A general conclusion is thus that the Plastic Cap model underestimated the self-healing ability (or the homogenisation) of the bentonite in the test by yielding too high void ratio and too low stresses in the former cavity. The Drucker-Prager plastic model captured the homogenisation better with a void ratio distribution that agreed rather well with the measured and smaller remaining gaps in the former cavity. However, also this model yielded the same too low stresses in the cavity.

Thus, modelling Subtask 2 with a large scale complicated geometry yielded better results when the Drucker-Prager model was used while Subtask 1 (Börgesson et al. 2015) with small scale simple swelling models yielded much better results when the Plastic Cap model was used. The reason for the better homogenisation and better results of the Drucker-Prager model for Subtask 2 is judged to be that the material model is simpler and convergence much easier to obtain.

5 Evaluation of swelling tests with BBM and BExM (SKB1)

5.1 Introduction

Engineered Barrier Systems (EBS) are often composed of different components with different initial dry density, for instance bentonite blocks, bentonite pellets-filled slots, or open (air-filled) slots. The homogenization process is generally understood as a process through which the initial differences in dry density in such systems tend to decrease with time. Some level of remaining heterogeneities can be expected, rather than a complete convergence of dry density.

The processes can occur under either saturated or unsaturated conditions. In both cases, the homogenization is driven by the hydration, and consequently the swelling, of the bentonite. The geometry of the system, including the position of the water inlet, therefore has an influence on the process.

The main elements of an axial homogenization process are schematically illustrated in Figure 5-1. The first step is the initial establishment of a swelling pressure, and this is illustrated with two large arrows representing the axial and radial stresses. The second step is the axial release of the specimen, and this implies that the axial stresses are eliminated, while the radial stresses are substantially decreased. The third step is the hydration and swelling of a peripheral part of the specimen, which fills an adjacent void space, and builds up a very small swelling pressure. The fourth and final step is the hydration and swelling of the remaining high-density part of the specimen, which in turn leads the compression of the low-density part in the peripheral part. This final part will lead to the build-up of axial stresses.

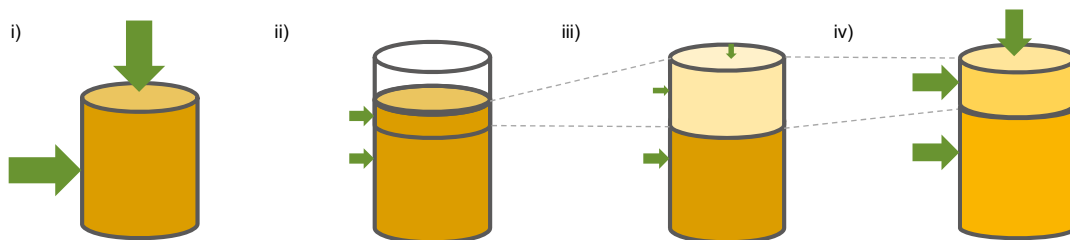


Figure 5-1. Schematic outline of axial homogenization.

Homogenisation calculations with TEP laws

The process can be further illustrated by a model of backfill homogenization, presented by Åkesson et al. (2010b). This was represented with an 1D axisymmetric geometry, consisting of initially unsaturated bentonite blocks in the central part of a tunnel, and a pellets-filled slot close to a tunnel wall (not included in the model), see Figure 5-2 (left). Water was supplied by keeping a large part of the pellets filling at an atmospheric liquid pressure throughout the calculation. The materials were represented by a slightly modified version of the TEP laws (thermoelasto-plastic model based on BBM) in Code_Bright. Nodes in the central parts of the bentonite blocks displayed some swelling and ended up precisely on the assumed swelling pressure curve (red and yellow lines in Figure 5-2, left). This was facilitated by the void ratio dependence introduced in the function for the employed swelling modulus (see Section 5.2.1). The stress paths for nodes in the pellets-filling (blue line), on the other hand, were to a large extent characterized by consolidation, which in turn was governed by the assigned value of the plastic stress-strain modulus (λ), and the extent of the yield surface. It can be noted that this stress path extends beyond the swelling pressure curve, and first exhibit a low slope caused by the elastic strains, and subsequently a steep slope caused by plastic strains. A similar behaviour can be noted for the peripheral parts of the blocks (green line) which had undergone significant swelling during the initial phase of the homogenization process.

The model thus illustrates the notion that material that swells ends up on, and subsequently follows, the swelling pressure curve, while material that consolidates “goes beyond” the swelling pressure curve and follows the outer part of yield surface (Figure 5-2, right). The contraction of the yield surface due to (isotropic) swelling is thus an important behaviour, which very well has to be represented in order to make a relevant model of the homogenization processes.

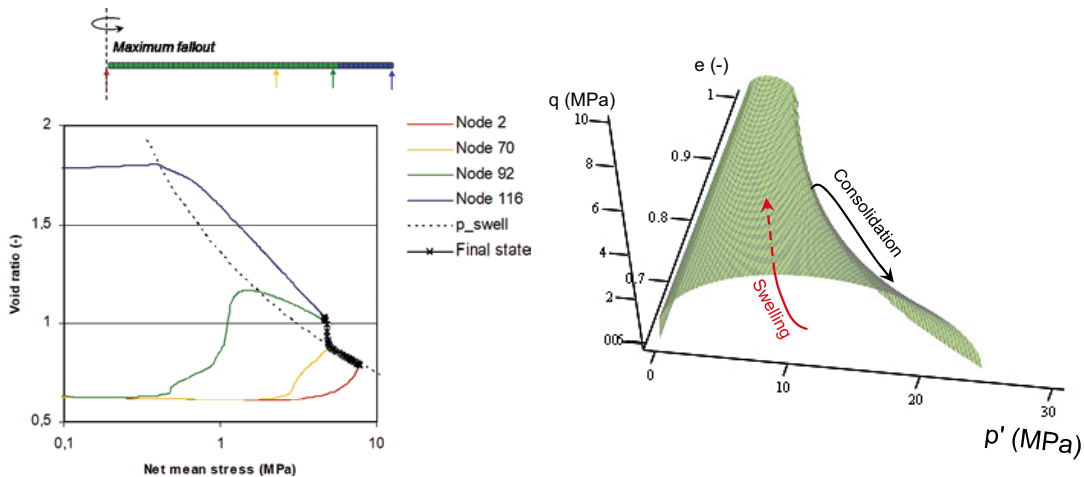


Figure 5-2. Backfill homogenization model: geometry and calculated stress paths for selected nodes (left).

Hydromechanical properties

Two hydromechanical properties of the bentonite are regarded to be of major relevance for the homogenization process: the swelling pressure and the shear strength.

For THM modelling purposes, the swelling pressure is regarded to be a net (or effective) mean stress. Results from a number of swelling pressure measurements of MX-80 (p_{swell}) were compiled and evaluated as functions of the bentonite dry density (ρ_d) by Åkesson et al. (2010a) (see Figure 5-3). Functions were adopted on the following form:

$$\log^{10}(p_{swell}) = c_2 \cdot \rho_d^2 + c_1 \cdot \rho_d + c_0 \quad (5-1)$$

The following parameter values were adopted from data on water retention measurements (see Figure 5-3): $c_0 = -1.74$, $c_1 = 4.12 \cdot 10^{-3}$, $c_2 = -3.94 \cdot 10^{-7}$ (p_{swell} in kPa; ρ_d in kg/m^3). In general, measured swelling pressure values exhibit a scatter, in which the highest values appear to be roughly twice as high as the lowest values. The adopted function approximately follows the lower end of this scatter, and this approach has been found to be of importance for hydro-mechanical modelling of the homogenization process.

The maximum deviatoric stress (or von Mises stress) at failure, is regarded as a measure of the shear strength of the bentonite, and this can be quantified through triaxial compression tests. Maximum deviatoric stresses from a number of triaxial tests with MX-80 (q) were compiled and evaluated as functions of the mean effective stress (p') by Børgesson et al. (1995), who adopted functions on the following form:

$$q = a \cdot p'^b \quad (5-2)$$

with the following parameter values: $a = 2.45$; $b = 0.77$ (p' and q in kPa) (see Figure 5-3).

It should be noted that during the course of work with this task, it was noticed that this description with relations for the swelling pressure and the shear strength can be developed into a potential function (corresponding to the sum of stress and suction) with two bounding lines (representing swelling and consolidation), see Section 6.1.

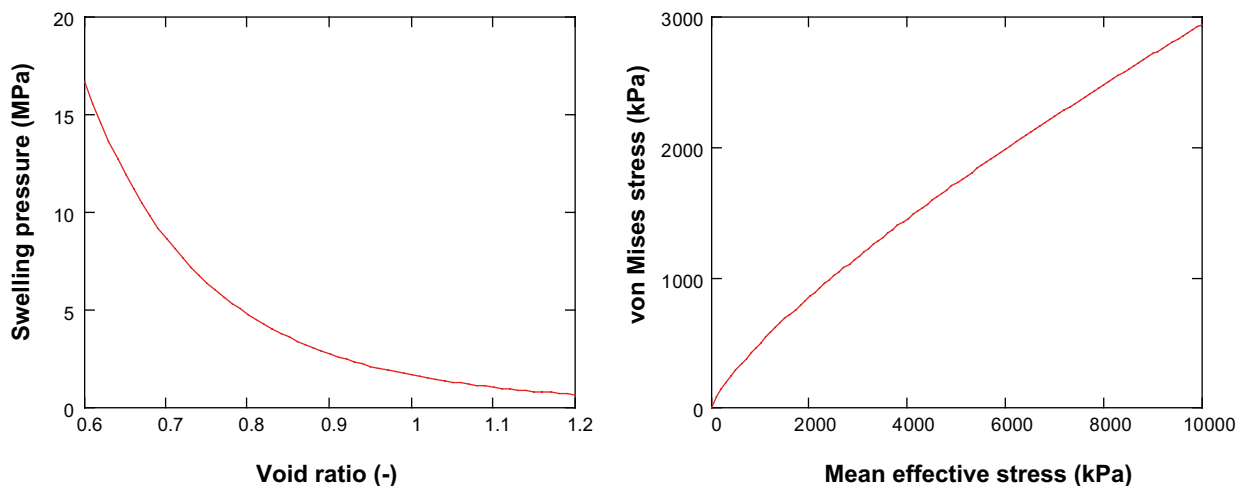


Figure 5-3. Swelling pressure and shear strength.

Homogenization tests

The extent of remaining heterogeneities can be illustrated through evaluation of the homogenization tests addressed in this task (see Appendix 1), see Figure 5-4. The net mean stress level of each test is here presented in relation to the range of measured void ratio values, while the mean void ratio (simple arithmetic value) is presented in relation to the range of measured stresses (generally one axial and one radial stress value). These “crosses” can be compared with the adopted swelling pressure curve (Equation (5-1)), and multiples of this curve.

It can be noted that the high density ends of the different tests coincide with the swelling pressure curve, whereas the low-density ends appear to correspond to approximately 2–3 times as high swelling pressure levels. The difference in void ratio appears to be most significant for tests with relatively low dry density.

Outline of work

The following evaluations were performed with Code_Bright and with simplified geometries, i.e. with volumes with homogenous conditions, rather than with continua with gradients, for example regarding suction or void ratio. These evaluations were performed on either one or two such volumes, denoted “one-element” or “two-element” analysis. The motive for this was to investigate specified stress paths and remaining density differences by controlling the evolution of suction, the axial stress or the axial displacement.

The main focus of the study was to obtain a description of the hydro-mechanical properties that was as accurate as possible. Suction was controlled in the entire model geometry which meant that the transport coefficient had no influence on the results. The time scales were also simplified since these could be chosen freely. Water unsaturated conditions were generally not of interest for this task, and this condition was largely overlooked in the analysis.

The first evaluation was an attempt to analyse the homogenisation tests in the framework of the Barcelona Basic Model (BBM) (Alonso et al. 1990). This material model was previously used to predict the homogenisation processes in initially water unsaturated KBS-3 buffer and backfill (Åkesson et al. 2010b), and the parameter value adoption followed the same strategy as was used in that work. The evaluation included analyses with one- and two-element geometries, which both were simplified representations of the test case with axial swelling (test A1, see Appendix 1). The evaluation also included a theoretical analysis of the unloading of a specimen with constant water content.

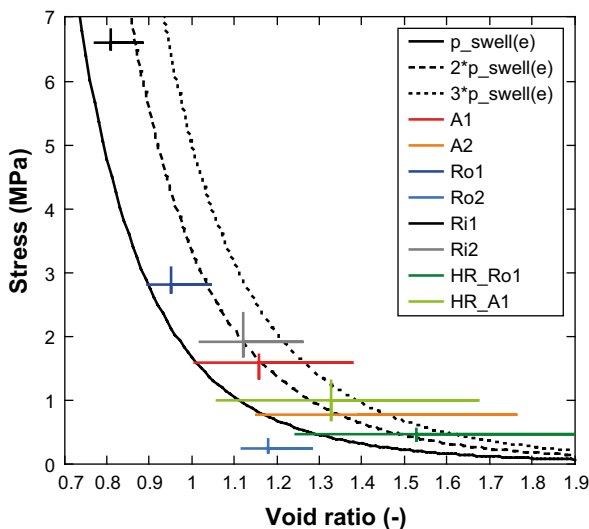


Figure 5-4. Final remaining heterogeneity in investigated homogenization tests and swelling pressure curve and multiples of this.

The second evaluation was a similar attempt to analyse the homogenisation process with the Barcelona Expansive Model (BExM) (Alonso et al. 1999). The presentation of this work begins with an overview of definitions and constitutive equations together with a description of the involved mechanisms for a swelling/consolidation cycle. This is followed by a presentation of an approach to adopt parameter values so that both the effective stress ($s+p'$) and the pre-consolidation stress (p_0^*) get the same slope in the $e-\ln(p)$ plane as an empirical swelling pressure curve. Finally, the results from two very simple one-element analyses are presented.

These analyses were not extensive and did not result in any complete model of the homogenisation tests, although they contribute to the understanding of the inner workings and limitations of the material models for this type of problem. Some additional comments on the limitations of these constitutive models is presented in Section 6.6.

5.2 Barcelona Basic Model

5.2.1 Elements of the BBM and the hydraulic model

The BBM model is an elasto-plastic model which can be viewed as a generalization of the Modified Cam Clay model for water-unsaturated conditions and uses the net mean stress (p') and suction (s) as independent state variables for representing isotropic stress states. The strain is composed two parts: a elastic (ε^e) and a plastic (ε^p). The elastic stress-strain relation is basically governed by the κ_i modulus while the hydraulic suction-strain relation is governed by the κ_s modulus (see Figure 5-5):

$$d\varepsilon_v^e = \frac{\kappa_i}{1+e} \frac{dp'}{p'} + \frac{\kappa_s}{1+e} \frac{ds}{s + p_{atm}} \quad (5-3)$$

Plastic deformations are activated once the yield surface is reached (Figure 5-5). This surface is composed of two functions in the $s-p'$ plane: the tensile strength (p_s) and the pre-consolidation stress (p_0), which both are expressed as functions of suction, and the latter is also a function of the pre-consolidation stress for saturated conditions (p_0^*). These lines are joined with an elliptic function in the $q-p'$ plane, described with p_s , p_0 and the critical state line parameter (M):

$$f = q^2 - M^2(p' + p_s)(p_0 - p') \quad (5-4)$$

The hardening law describes a relation between increments in the plastic volumetric strain and increments in p_0^* which is governed by the κ_i and λ_0 moduli:

$$d\varepsilon_v^p = \frac{\lambda_0 - \kappa_i}{1+e} \frac{dp_0^*}{p_0^*} \quad (5-5)$$

In the original formulation of BBM, the κ_i and κ_s parameters were regarded as constants. In the TEP constitutive laws of Code_Bright, however, they have been developed as functions. The κ_i is defined as a function of suction, while κ_s is defined as a function of p' , suction and the void ratio. The latter dependence is based on a defined swelling pressure relation, $p_{swell}(e)$, and this means that the swelling stops precisely when the mean stress reaches the swelling pressure for the current void ratio (Figure 5-5).

$$\kappa_s(p', e) = \kappa_{s,0} f(p', e) \quad f(p', e) = \begin{cases} 1 & \text{if } p' < p_{ref} \\ 10^{-20} & \text{if } p' > p_{swell}(e) \\ 1 - \frac{\ln p' - \ln p_{ref}}{\ln(p_{swell}(e)) - \ln p_{ref}} & \text{otherwise} \end{cases} \quad (5-6)$$

The hydraulic model essentially consists of two parts: Darcy's law and the water retention curve.

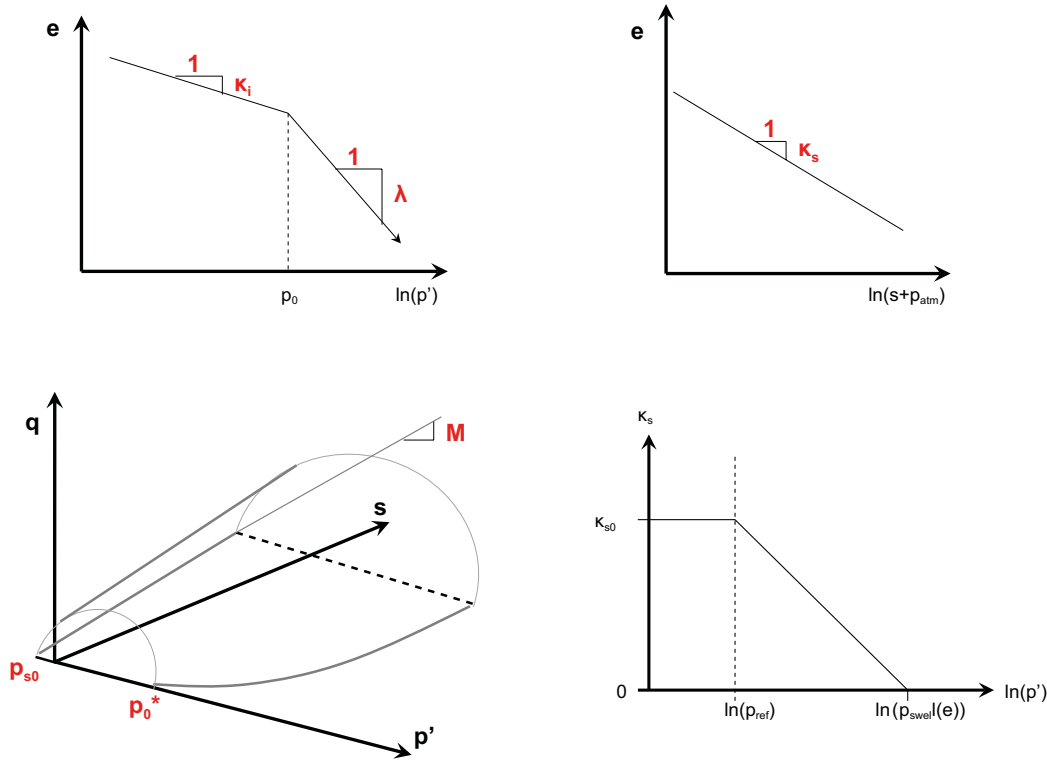


Figure 5-5. Elements of the BBM used in Code_Bright. Elastic and plastic stress-strain relations (upper left) and suction-strain relation (upper right). Yield surface (lower left) and void ratio dependence and pressure dependence of κ_s (lower right).

Darcy's describes a relation by which the liquid volumetric flux (q_l) is driven by gradients in liquid pressure (p_l) and by gravity (g):

$$\mathbf{q}_l = -\frac{\mathbf{k} \cdot k_{rl}}{\mu_l} [\nabla p_l - \rho_l \cdot \mathbf{g}] \quad (5-7)$$

where k is the intrinsic permeability, k_{rl} is the liquid relative permeability, ρ_l is the liquid density and μ_l is the liquid viscosity. The relative permeability is defined as a function of the degree of saturation (S_l), and in general increases towards the value 1 when S_l increases to 1; usually on the form $k_{rl} = (S_l)^3$.

The water retention curve describes a relation between the degree of saturation and the suction value, which in turn can be equated with the difference in gas and liquid pressure ($s = p_g - p_l$). The van Genuchten form of this curve is defined as:

$$S_l(P_l) = \left(1 + \left(\frac{P_g - P_l}{P_0} \right)^{\frac{1}{1-\lambda}} \right)^{-\lambda} \quad (P_l < P_g) \quad (5-8)$$

where λ and P_0 are parameters.

5.2.2 Parameter value adoption

The homogenization tests analysed in this study is presented in Appendix 1. According to this task assignment, the used specimens had an initial water content of 12 % and an initial void ratio of 0.68. This data corresponds to a saturation degree of 49 %. The water content was assessed to equilibrate to a RH of 51 % for free swelling MX-80 which corresponds to a suction value of 91 MPa. This initial point is plotted in Figure 5-6 together with water retention data for free swelling samples with initial water contents of 9.8 and 17.5 %, respectively, and adjusted for $e = 0.68$. A van Genuchten water retention curve (parameter $P_0 = 20.1$ MPa and $\lambda = 0.31$) was adopted from these data sets.

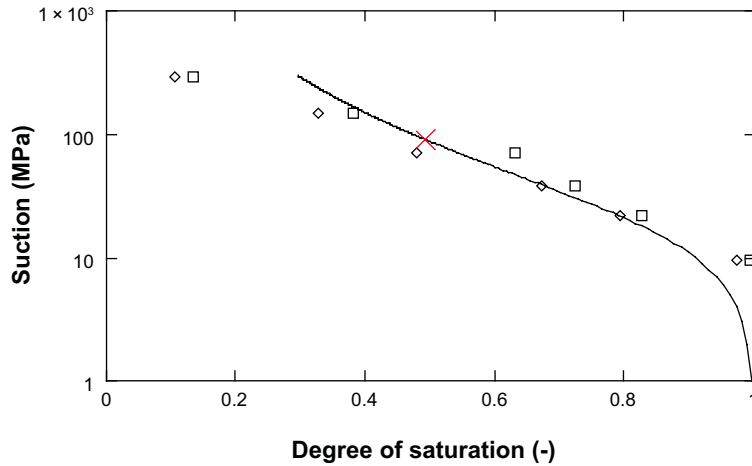


Figure 5-6. Adoption of water retention curve for the bentonite specimen (line). Initial point (x), and data for free swelling samples with initial water content of 9.8 % (◇) and 17.5 % (□) (data from Dueck (2004) and Dueck and Nilsson (2010)).

Parameter values for hydraulic and mechanical processes (see Table 5-1 and Table 5-2) were adopted in line with data report for THM modelling in SR-Site (Åkesson et al. 2010a). The work behind that report aimed (among other things) at developing a general and clear-cut method to quantify the mechanical parameters for all relevant dry densities (from buffer rings to pellets).

The elastic parameters (κ_i , κ_s , ν) were pragmatically based on results from compression and swelling tests with uniaxial strain. The plastic stress-strain modulus (λ) was based on the swelling pressure relation, and the suction dependence of this modulus was regarded to be insignificant. The plastic parameters describing the yield surface (p_s , p_0^* and M) were based on relations for swelling pressure, shear strength and tensile strength and could thus be evaluated as void ratio dependent functions. The BBM laws therefore imply that the yield surface can expand due to strain hardening (increased p_0^*) during consolidation. However, there is no corresponding mechanism for yield surface contraction during isotropic swelling. This limitation has motivated the parameter value adoption for components that will undergo swelling (i.e. high-density blocks) for a *homogenized target void ratio*, which corresponds to a complete homogenisation of the installed bentonite filling (e.g. for both blocks and pellets). For a pellet filling that will undergo compression, however, the parameters are adopted for the *initial void ratio*. For the analysis presented here, plastic parameter values were adopted for two void ratios: the initial value and the average final value (Table 5-2).

Table 5-1. Hydraulic and elastic parameter values.

k	k_r	κ_{i0}	α_i	ν	K_{min}	κ_{s0}	p_{ref}	e_{init}
3.1E-21 m ²	S_l^3	0.12	-0.01	0.2	20 MPa	0.3	1 MPa	0.68

Table 5-2. Plastic parameter values for two target void ratios.

e_{target}	λ	p_{s0}	p_0^*	M
0.68	0.157	2.7	22	0.232
1.1	0.224	0.7	2.8	0.296

No suction dependence of p_s , λ , p_0 .

5.2.3 “One-element” analysis

The geometry of the axial swelling tests was simplified in order to elucidate the inner workings of the BBM model and how this behaves during the homogenisation process. The principle of the one-element analysis is illustrated in Figure 5-7 and Table 5-3 and consists of 4 steps:

1. The axial displacement is kept at zero while the suction is decreased from the initial value to zero. From this follows a build-up of swelling pressure, which depends on the initial void ratio.
2. The axial stress is decreased from the swelling pressure to zero. This is an unloading at constant water content. From this follows an increase in axial displacement and suction.
3. The suction is decreased from this level, potentially to zero, while the axial stress is kept at zero. This condition is maintained until the axial displacement reaches a certain value (i.e. 25 % of the height).
4. The suction decrease to zero is completed while the axial displacement is kept constant. From this follows a build-up of swelling pressure.

Table 5-3. Main variables in one-element analysis. Controlled variables marked gray.

Step	Axial stress	Axial displacement	Suction
1	$0 \rightarrow p_s(\epsilon_{init})$	0	$s_{init} \rightarrow 0$
2	$p_s(\epsilon_{init}) \rightarrow 0$	$0 \rightarrow u_2$	$0 \rightarrow s_2$
3	0	$u_2 \rightarrow u_f$	$s_2 \rightarrow 0$
4	$0 \rightarrow \sigma_{a4}$	u_f	$s_2 \rightarrow 0$

A one-element analysis was performed with Code_Bright for a problem that resembled the axial swelling test A01-9. The 2D geometry, the grid and the boundary conditions of the model are shown in Figure 5-8. The geometry was a square, with side lengths of 20 mm, and divided in 9 elements. The mechanical boundaries were either roller boundaries, or a prescribed axial stress. The hydraulic boundary was a surface “boundary” which controlled the suction value completely in the model.



Figure 5-7. Schematic outline of four steps in the one-element analysis.

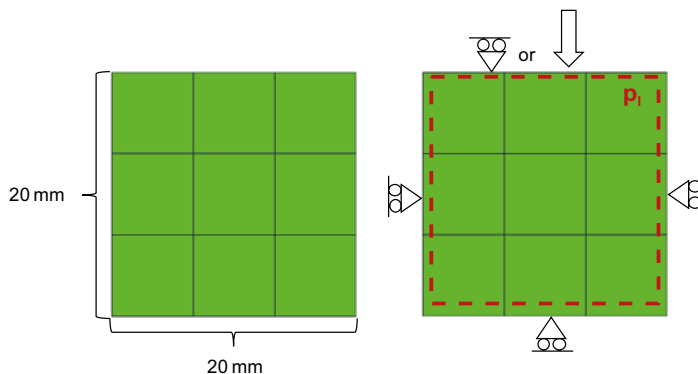


Figure 5-8. 2D geometry, grid and boundary conditions of one-element analysis.

The 1st case of the one-element analysis (model name: EH_T_07) was defined for a set of plastic parameters (Table 5-4) adopted for the initial void ratio, except for the λ value which was adopted for the homogenized void ratio.

The values of the boundary conditions in each step are shown in Table 5-5, which also shows the duration of each step. It can be noted that the unloading resulted in a displacement of 1.4 mm and a suction of 15 MPa. The maximum axial displacement was limited to 5 mm which corresponds to a swelling of 25 %. The modelled evolution of the two main stresses, the void ratio and the saturation degree are shown in Figure 5-9. The modelled stresses displayed some resemblance with the experimental data which also is shown in Figure 5-9.

Table 5-4. Plastic parameter values for 1st case.

λ	p_{s0}	p_0^*	M
0.224	2.7	22	0.232

Table 5-5. Values of main variables in one-element analysis. 1st case. Controlled variables marked gray.

Step	Day	σ_{ax} (MPa)	u (mm)	s (MPa)
1	0–14	0 → 9.8	0	91 → 0
2	14–15	9.8 → 0	0 → 1.4	0 → 14.7
3	15–21	0	1.4 → 5	14.7 → 7.2
4	21–28	0 → 0.17	5	7.2 → 0

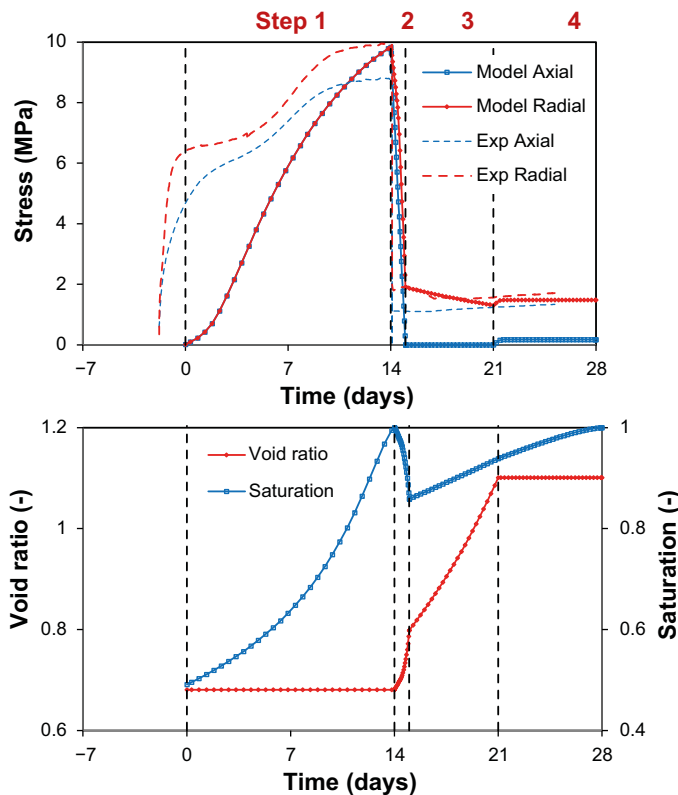


Figure 5-9. Results for 1st case. Evolution of axial and radial stresses in model and in experiment (A01-9) (upper), and evolution of the void ratio and saturation degree (lower).

The modelled results are shown as stress-paths in Figure 5-10, in which the four steps are marked. Three yield surfaces are shown in the lower graph and these lines represent the initial state (red), the condition after the unloading (green), and the final state (blue). The dashed line in the lower graph corresponds to stress states with zero axial stress. Two experimental points (after saturation and final state) are also shown in the lower graph.

The following comments can be made concerning the modelled paths:

- i. The stress state at the end of Step 1 could be regarded as satisfactory, although the deviatoric stress was zero while it was approx. 1 MPa in the experiment.
- ii. The change in p' was not equal to the negative value of the change in suction during the unloading at constant water content (Step 2). This is further commented on in Section 5.2.5.
- iii. The stress state at the end of Step 2 could be regarded as satisfactory since the radial stress was basically the same as in the experiment (2 MPa), see also Figure 5-9.
- iv. The deviatoric stress at the end of Step 4 was too high in comparison with the experimental results. This indicates that the yield surface was not contracted to a sufficient extent.

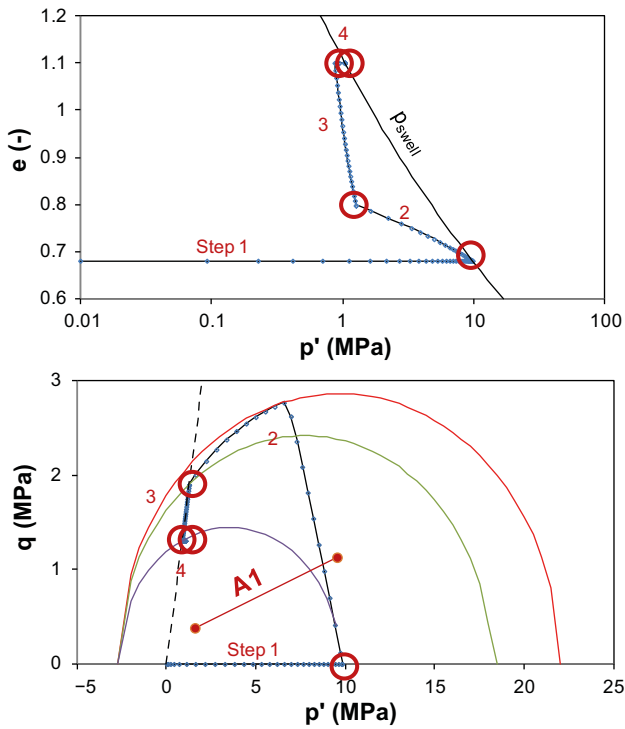


Figure 5-10. Stress-path in e - $\ln(p)$ plane (upper) and q - p plane (lower). 1st case. Experimental data (marked A1 in lower graph) shows two stress states: after saturation and final state.

The 2nd case of the one-element analysis (model name: EH_T_08) was defined for a modified λ value. This was decrease from 0.224 to 0.157 and therefore corresponds to the value adopted for the initial void ratio (Table 5-2). The values of the boundary conditions in each step are shown in Table 5-6, and the modelled results are shown as stress-paths in Figure 5-11.

The modelled final stress state was apparently in more agreement with experimental data with the lower λ value. The reason for this is probably that a lower λ -value corresponds to a stiffer behaviour, so that a given plastic strain leads to a larger reduction of the stresses.

The model results also shows that it is possible to obtain a "contraction of the yield surface" through "dilation at the dry side".

Table 5-6. Values of main variables in one-element analysis. 2nd case. Controlled variables marked gray.

Step	Day	σ_{ax} (MPa)	u (mm)	s (MPa)
1	0–14	0 → 9.8	0	91 → 0
2	14–15	9.8 → 0	0 → 1.5	0 → 15.4
3	15–21	0	1.5 → 5	15.4 → 7.3
4	21–28	0 → 0.45	5	7.3 → 0

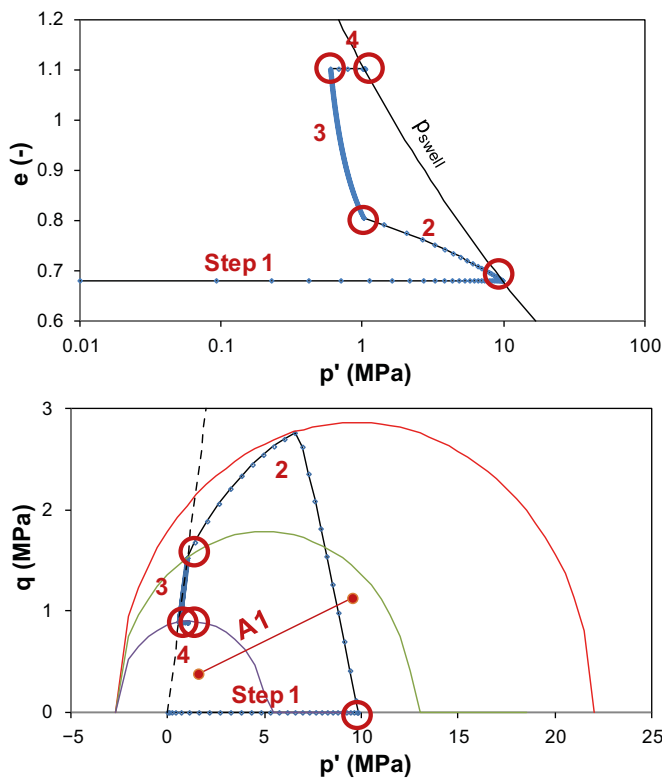


Figure 5-11. Stress-path in e - $\ln(p)$ plane (upper) and q - p plane (lower). 2nd case. Experimental data (marked A1 in lower graph) shows two stress states: after saturation and final state.

5.2.4 “Two-element” analysis

A slightly less simplified representation of the homogenisation process was provided by the two-element analysis. This is illustrated in Figure 5-12 and Table 5-7 and consists of 5 steps. The scheme is defined for two materials (upper and lower) with different suction protocols.

1. The axial displacement is kept at zero while the suction for both materials is decreased from the initial value to zero. From this follows a build-up of swelling pressure which depends on the initial void ratio.
2. The axial stress is decreased from the swelling pressure to zero. This is an unloading at constant water content. From this follows an increase in axial displacement and suction (for both materials).
3. The suction of the upper material is decreased from this level, potentially to zero, while the suction value for the lower material is kept constant, and the axial stress is kept at zero. This condition is maintained until the axial displacement reaches a specific value (i.e. 25 % of the height).
4. The suction decrease of the upper material to zero is completed, while the suction value for the lower material and the axial displacement is kept constant. From this follows a build-up of swelling pressure.
5. The suction of the lower element is decreased from its previous level to zero while the suction value for the upper material is kept at zero, and the axial displacement is kept constant. From this follows a further build-up of swelling pressure.



Figure 5-12. Schematic outline of five steps in the two-element analysis.

Table 5-7. Main variables in two-element analysis. Controlled variables marked gray.

Step	σ_{ax} (MPa)	u (mm)	s (MPa)	
			lower	upper
1	$0 \rightarrow p_s(e_{init})$	0	$s_{init} \rightarrow 0$	$s_{init} \rightarrow 0$
2	$p_s(e_{init}) \rightarrow 0$	$0 \rightarrow u_2$	$0 \rightarrow s_2$	$0 \rightarrow s_2$
3	0	$u_2 \rightarrow u_f$	s_2	$s_2 \rightarrow 0$
4	$0 \rightarrow \sigma_{a4}$	u_f	s_2	$s_2 \rightarrow 0$
5	$\sigma_{a4} \rightarrow \sigma_{af}$	u_f	$s_2 \rightarrow 0$	0

A two-element analysis was performed with Code_Bright for a problem that resembled the axial swelling test analysed previously (A01-9). The 2D geometry, the grid and the boundary conditions are shown in Figure 5-13. The geometry was a square, with side lengths of 20 mm, and divided in two equally large materials and 20 elements. The mechanical boundaries were either roller boundaries, or a prescribed axial stress. The maximum axial displacement was limited to 5 mm which corresponded to a swelling of 25 % (although this was slightly exaggerated with 5.1 mm). The hydraulic boundaries were two surface “boundaries” which controlled the suction value completely in the two materials. The middle row of elements was very thin and belonged to the lower material. The reason for this was that there had to be a row of elements on which both these two conditions could act.

The model (name: EH_2E_03) was for simplicity defined for a purely elastic case. The material parameters were the same as for the one-element analyses, but with two modifications:

- ν was set to 0.49 for both materials.
- p_{ref} was set to 0.1 MPa from the 3rd step onwards for the upper (swelling) material.

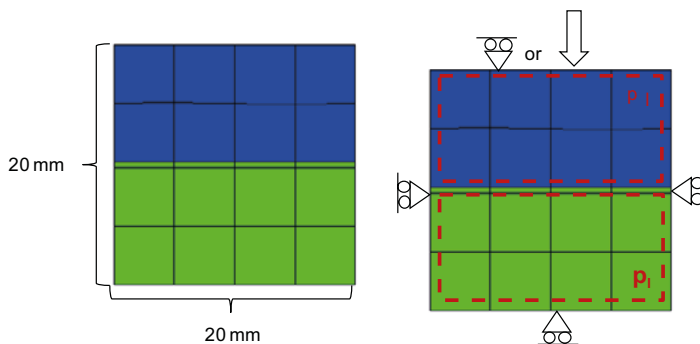


Figure 5-13. 2D geometry, grid and boundary conditions of two-element analysis.

The values of the boundary conditions for each step are shown in Table 5-8, and the modelled results are shown as stress-paths in Figure 5-14.

Table 5-8. Values of main variables in two-element analysis. Controlled variables marked gray.

Step	Day	σ_{ax} (MPa)	u (mm)	s (MPa)	
				lower	upper
1	0–14	0 → 9.8	0	91 → 0	91 → 0
2	14–15	9.8 → 0	0 → 1.7	0 → 17	0 → 17
3	15–18	0	1.7 → 5.1	17	17 → 0.3
4	18–21	0 → 0.04	5.1	17	0.3 → 0
5	21–28	0.04 → 1.7	5.1	17 → 0	0

The following comments can be made concerning the modelled paths:

- The stress paths for Step 1 were the same as for the one-element analyses.
- The stress paths for Step 2 were quite flat and ended at low p' and q values. This was a consequence of the used high Poisson' ratio value.
- The suction decrease in the upper material during Step 3 was quite extensive and reached almost the zero level. There were therefore no significant changes during Step 4.
- During Step 5 there was some swelling of the lower material and some compression of the upper material, but only elastic. The final stress state was quite similar to the measured stress state. The final void ratio of the two materials differed quite significantly (0.98 and 1.24, respectively) but these were fairly similar to the lowest and highest void ratios measured after the dismantling of the A01-9 test (1.01 and 1.38, respectively).

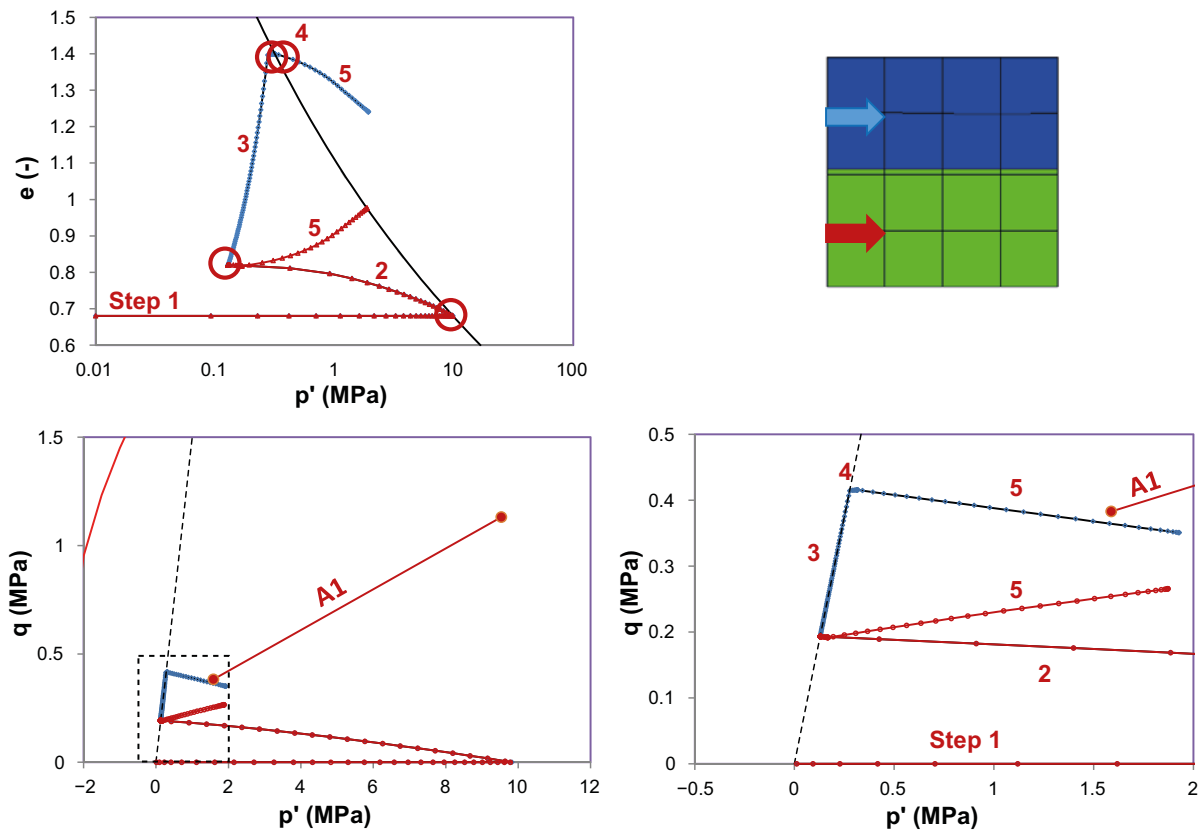


Figure 5-14. Stress-paths in e - $\ln(p)$ plane (upper left) and q - p plane (lower). Evaluated nodes marked on picture on upper right side, blue lines (upper material) and red lines (lower material). Experimental data (marked A1 in lower graphs) shows two stress states: after saturation and final state.

5.2.5 Unloading step

Unloading at constant water content is basically a fairly simple process, but in the framework of BBM it is influenced by quite a number of properties. If elastic and isotropic conditions are assumed, then there is a relation between the changes in void ratio ($d\varepsilon_v = -de/(1+e)$), net mean stress and suction:

$$-de = \frac{\kappa_i(s)}{p'} dp' + \frac{\kappa_s(p', e)}{s+0.1} ds \quad (5-9)$$

With the conditions of i) a constant water content, and ii) a defined retention curve, then a relation between changes in void ratio and suction can be derived:

$$de = \frac{de}{dS_l} \frac{dS_l}{ds} ds \quad (5-10)$$

The constant water condition implies that the derivative de/dS_l is equal to $-e/S_l$. The factor dS_l/ds is the derivative of the water retention curve. A relation between changes in net mean stress and suction can be derived from Equations 5-9 and 5-10:

$$ds = - \frac{\frac{\kappa_i(s)}{p'}}{\frac{de}{dS_l} \frac{dS_l}{ds} + \frac{\kappa_s(p', e)}{s+0.1}} \cdot dp' \quad (5-11)$$

The fraction on the right-hand side should be equal to unity, since ds should be equal to $-dp'$ due to thermodynamic considerations, at least close to water saturated conditions. This is however not the general case for given parameter setting. This was tested with a MathCad algorithm for a case corresponding to an isotropic version of the unloading step in the presented Code_Bright models (Figure 5-10). The net mean stress was reduced from 9.8 to 1 MPa, and the evolution of suction was integrated with Equation 5-11 from this condition. This was in turn used to calculate the evolution of the saturation degree and the void ratio. The suction was found to increase from zero to 13 MPa, whereas the void ratio increased from 0.68 to 0.77. The corresponding final values were 15 MPa and 0.8 in the one-element analysis (see Table 5-5 and Figure 5-9).

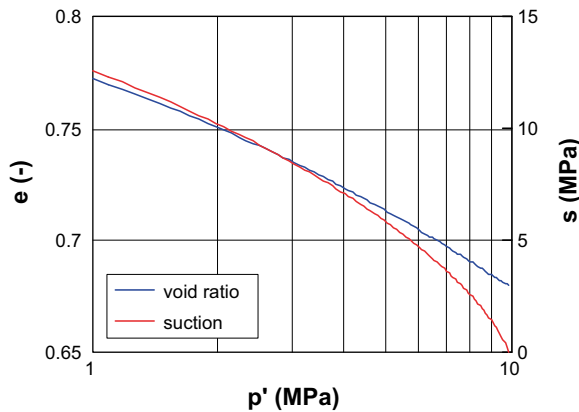


Figure 5-15. Increase of void ratio and suction due to unloading at constant water content.

5.3 Barcelona Expansive Model (BExM)

5.3.1 Elements of BExM

An overview of definitions of void ratios as used in the framework of the BBM and the BExM (Alonso et al., 1999) is illustrated in Figure 5-16. For the single porosity framework, the conventional definition of the void ratio (e) is used, i.e. the ratio between the pore volume and the solid volume. In the double porosity framework, implemented in Code_Bright, two types of pore volume and two void ratios are used: the micro (e_m) and the macro (e_M) void ratios. The definition of the micro void ratio is similar to the conventional one, the ratio between the micro pore volume and solid volume. The definition of the macro voids is however quite different, the ratio between the macro pore volume and the sum of the solid volume and the micro pore volume.

Volumetric strains of BBM

Two of the main stress-strain relations in the BBM are illustrated in Figure 5-17 (upper left). The elastic strain is given by changes in net mean stresses and in suction (not shown in figure):

$$d\varepsilon_v^e = \frac{\kappa_i}{1+e} \frac{dp'}{p'} + \frac{\kappa_s}{1+e} \frac{ds}{s + p_{atm}} \quad (5-12)$$

The plastic strain is given by changes in the pre-consolidation stress p_0^* .

$$d\varepsilon_v^p = \frac{\lambda_0 - \kappa_i}{1+e} \frac{dp_0^*}{p_0^*} \quad (5-13)$$

The yield curve (or the LC curve) and the elastic region in the s - p plane are illustrated in Figure 5-17 (upper right). For isotropic problems, the pre-consolidation stress can only be increased, i.e. through consolidation.

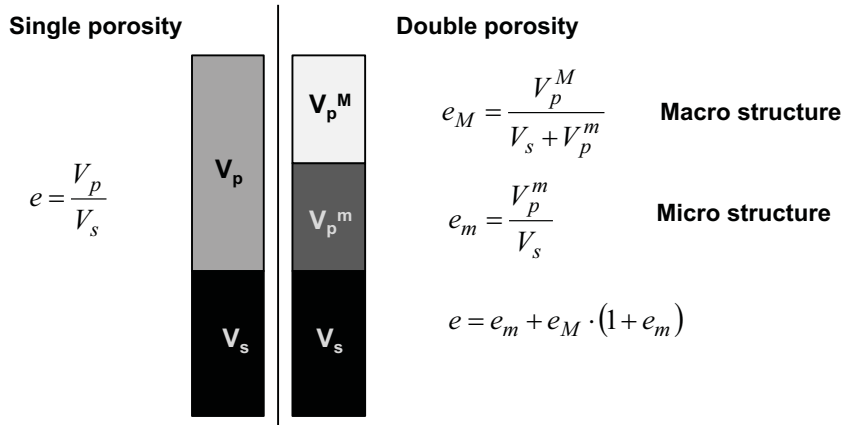


Figure 5-16. Void ratio definitions in BExM.

Volumetric strains of BExM

Due to the double porosity there are two types of strains in the BExM: at a macro level (ε_M) and a micro level (ε_m). The strains on the macro level are basically the same as for the BBM:

$$d\varepsilon_M^e = \frac{\kappa}{1+e_M} \frac{dp'}{p'} + \frac{\kappa_s}{1+e_M} \frac{ds}{s+p_{atm}} \quad (5-14)$$

$$d\varepsilon_M^{SD} + d\varepsilon_M^{SI} + d\varepsilon_M^{LC} = \frac{\lambda_0 - \kappa}{1+e_M} \frac{dp_0^*}{p_0^*} \quad (5-15)$$

The plastic strain increments on the left-hand side are taken into account if the SD, SI or LC yield curves are activated. The stress-strain relation for the micro level is described by the modulus κ_m . This is related to changes in effective stress (Figure 5-17, lower left):

$$d\varepsilon_m^e = \frac{\kappa_m}{1+e_m} \frac{d(p'+s)}{p'+s} \quad (5-16)$$

A coupling between the micro void strain and macro void strain is defined as:

$$d\varepsilon_M^{SD} + d\varepsilon_M^{SI} = \frac{\kappa_m}{1+e_m} \frac{d\gamma^{SD}}{p'+s} \cdot f^{SD} \quad (5-17)$$

where γ is the position of the yield curve (Figure 5-17, lower right) and f is an interaction function. This is activated when the stress state reaches the SD or SI (suction decrease or suction increase) line. Only elastic strains can occur between these lines. This means that a swelling at a constant low load will lead to a reduction in the pre-consolidation stress, i.e. a “contraction” of the (modified Cam Clay) yield surface.

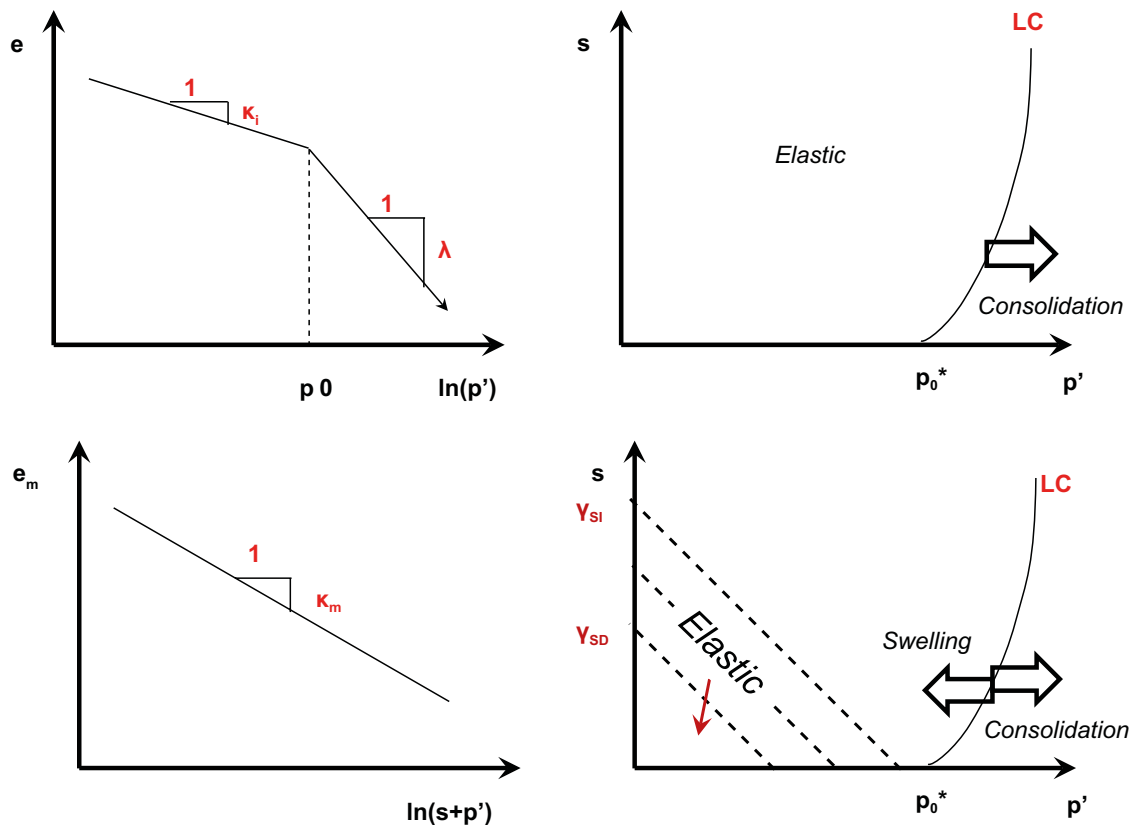


Figure 5-17. Stress-strain relations (left) and yield curves (right) according to BBM (upper) and BExM (lower).

Volumetric strains of BExM – simplified case

In order to simplify the problem so that the inner workings of the BExM could be understood, a number of terms and functions were omitted. The first simplification was that elastic strains of the macro voids, i.e. Equation 5-14 were set to zero.

Secondly, the plastic strains due to activation of the SI curve and the LC curve in Equation 5-15 and 5-17 were omitted:

$$d\varepsilon_M^{SD} = \frac{\lambda_0}{1 + e_M} \frac{dp_0^*}{p_0^*} \quad (5-18)$$

$$d\varepsilon_M^{SD} = \frac{\kappa_m}{1 + e_m} \frac{d\gamma^{SD}}{p^{1+s}} \cdot f^{SD} \quad (5-19)$$

Thirdly, the suction dependence of the λ function was omitted. This means that the $\lambda(s)$ function was treated as a constant. Finally, the load dependence of the coupling function was omitted. This meant that the $f^{SD}(p/p_0)$ function was treated as a constant.

Void ratio increments of BExM – simplified case

The strains were translated into void ratio increments in order to perform simple calculations within this framework. The strain on the micro level, Equation 5-16, was expressed in terms of micro void ratio increments ($d\varepsilon_m = -de_m/(1+e_m)$):

$$-\frac{de_m}{1+e_m} = \frac{\kappa_m}{1+e_m} \frac{d(p^{1+s})}{p^{1+s}} \quad (5-20)$$

In a similar way, the simplified strain on the macro level, Equations 5-18 and 5-19, was expressed in terms of macro void ratio increments ($d\varepsilon_M = -de_M/(1+e_M)$):

$$-\frac{de_M}{1+e_M} = \frac{\lambda_0}{1+e_M} \frac{dp_0^*}{p_0^*} \quad (5-21)$$

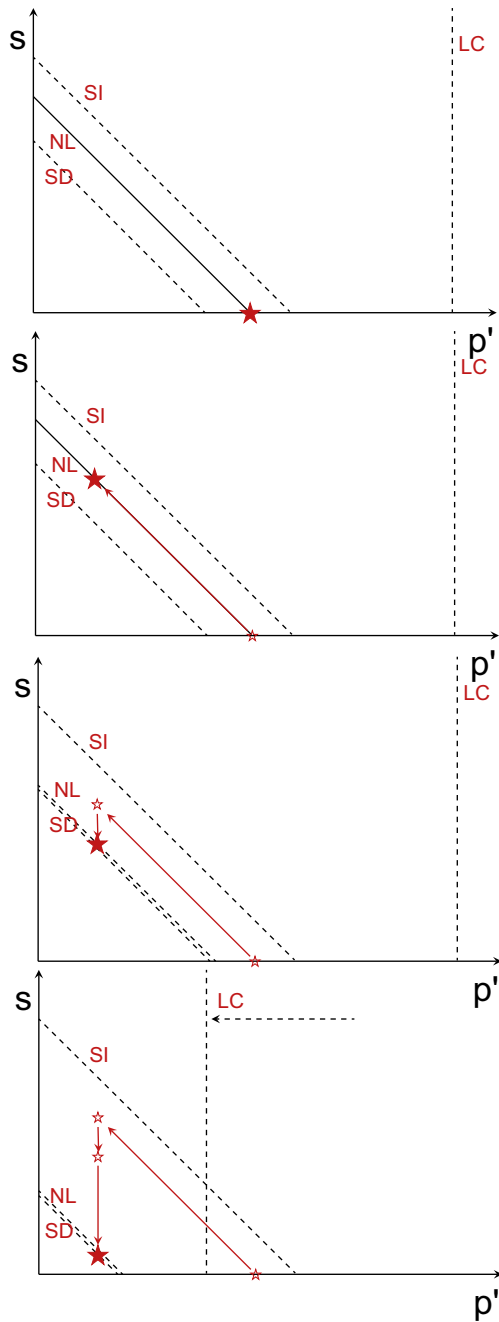
$$-\frac{de_M}{1+e_M} = \frac{\kappa_m}{1+e_m} \frac{d\gamma^{SD}}{p^{1+s}} \cdot f^{SD} \quad (5-22)$$

5.3.2 Swelling/consolidation cycle with BExM

A convenient way to begin an analysis of the homogenization process in the framework of BExM is to define a simple isotropic swelling/consolidation cycle. In the following description this has been made in six steps (see Figure 5-18 and Figure 5-19):

1. Unloading at constant water content, p is the governing variable.
2. Swelling at constant load – elastic, s is the governing variable.
3. Swelling at constant load – elastoplastic, s is the governing variable.
4. Swelling pressure buildup at constant volume, s is the governing variable.
5. Compression at constant zero suction – elastic, p is the governing variable.
6. Consolidation at constant zero suction – elastoplastic, p is the governing variable.

It should be noted that simplified procedures were adopted for both Step 1 and Step 4, which were based on the equality: $ds = -dp$.



1. Unloading: constant water content

Governing variable: $p' = p_i \rightarrow p_1$

Simplified calculation:

$$ds = -dp'$$

$$de_m = de_M = dp_0^* = 0$$

2. Swelling at constant load – elastic

Governing variable: $s = s_1 \rightarrow s_2$

$$dp' = 0 \quad de_m = -\frac{\kappa_m}{p' + s} \cdot ds \quad de_M = 0$$

3. Swelling at constant load – elastoplastic

Governing variable: $s = s_2 \rightarrow s_3$ (until $e = e_t$)

$$dp' = 0 \quad de_m = -\frac{\kappa_m}{p + s} \cdot ds$$

$$de_M = f^{SD} \cdot \frac{1 + e_M}{1 + e_m} de_m \quad dp_0^* = -\frac{P_0^*}{\lambda(0)} de_M$$

Figure 5-18. Stress paths in s - p' plane (Step 1–3).

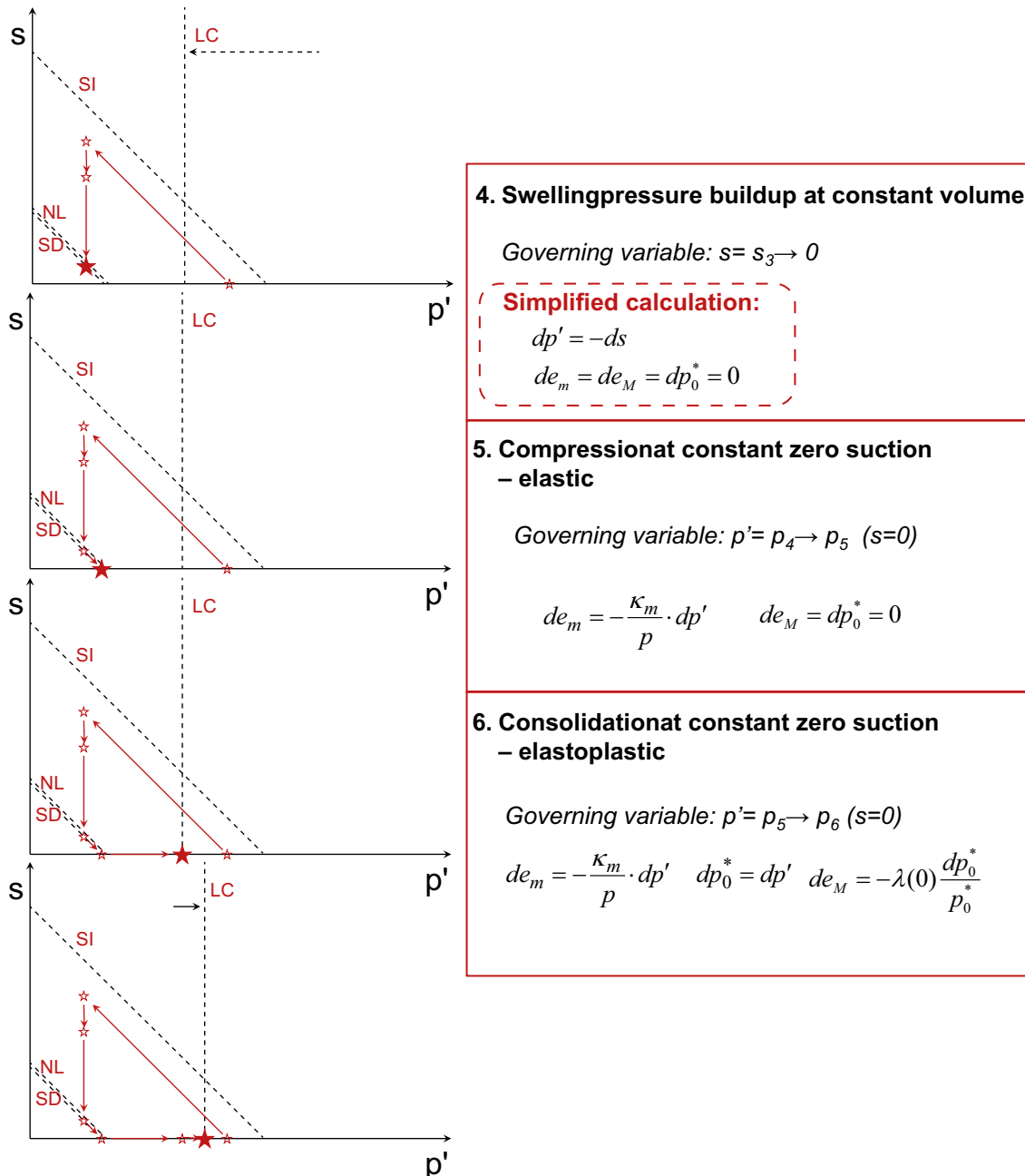


Figure 5-19. Stress paths in s - p' plane (Step 4–6).

5.3.3 Basic parameter value adoption for BExM

The most crucial step concerning the “contraction of the yield surface” is the third step with elastoplastic swelling at constant load. Four increments can be identified:

i) The constant load:

$$dp' = 0 \tag{5-23}$$

ii) The increment in micro void ratio, Equation 5-20:

$$de_m = -\frac{\kappa_m}{p' + s} \cdot ds \tag{5-24}$$

iii) The increment in macro void ratio. This can be derived from the micro level strain Equation 5-20 and the interaction function, Equation 5-22 under the condition that $d\gamma^{SD} = d(p'+s)$:

$$de_M = f^{SD} \cdot \frac{1+e_M}{1+e_m} de_m \leftrightarrow de_m = \frac{1}{f^{SD}} \cdot \frac{1+e_m}{1+e_M} de_M \quad (5-25)$$

iv) Finally, the increment in the pre-consolidation stress can be derived from the hardening law, Equation 5-21:

$$dp_0^* = -\frac{p_0^*}{\lambda(0)} de_M \quad (5-26)$$

The increment in total void ratio can be calculated from the increments in micro and macro void ratio:

$$de = (1+e_M) \cdot de_m + (1+e_m) \cdot de_M \quad (5-27)$$

The increment in total void ratio can be related to increments in suction or in pre-consolidation stress.

$$de = de_m \cdot (1+f^{SD})(1+e_M) = -\kappa_m (1+f^{SD})(1+e_M) \frac{ds}{p'+s} \quad (5-28)$$

$$de = de_M \cdot \left(1 + \frac{1}{f^{SD}}\right) (1+e_m) = -\lambda(0) \cdot \left(1 + \frac{1}{f^{SD}}\right) (1+e_m) \frac{dp_0^*}{p_0^*} \quad (5-29)$$

The modules of these two expressions are identified with the module of the swelling pressure curve, from here on denoted π (Figure 5-20).

$$de = -\pi \frac{ds}{p'+s} = -\pi \frac{dp_0^*}{p_0^*} \quad (5-30)$$

Finally, the value of the κ_m and λ can be expressed in terms of π , f and current micro and macro void ratios:

$$\kappa_m = \frac{\pi}{(1+f^{SD})(1+e_M)} \quad (5-31)$$

$$\lambda(0) = \frac{\pi}{\left(1 + \frac{1}{f^{SD}}\right) (1+e_m)} \quad (5-32)$$

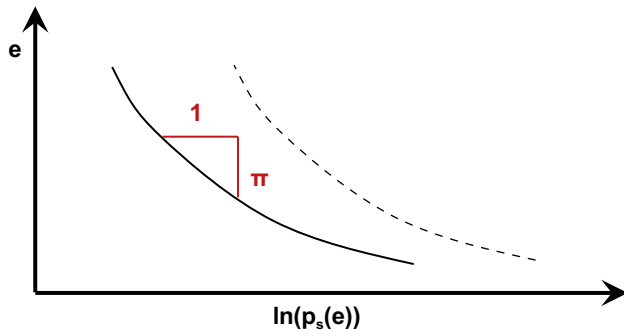


Figure 5-20. Definition of modulus π from swelling pressure relation. Dashed line represents the pre-consolidation stress (p_0^*).

Example

The value of the π modulus for the used swelling pressure curve, Equation 5-1, and a step between 0.68 and 1.1 in total void ratio is 0.187 (the void ratios were the initial and final value for the axial swelling test A1). After this adoption there are three more variables to be quantified: e_m , e_M and f_{SD} . The parameter adoption can thus be performed in several ways.

In the 1st case, all void space is assumed to belong to the micro voids ($e_m = 0.68$ and $e_M = 0$). In addition, the value of the coupling function is assumed to be $f_{SD} = 6$. With these assumptions the value of κ_m and λ can be calculated to 0.027 and 0.095, respectively.

In the second case the micro void ratio and the macro void ratio is assumed to be identical ($e_m = e_M = 0.296$) In addition, the value of the coupling function is assumed to be $f_{SD} = 1$. With these assumptions the value of κ_m and λ can both be calculated to 0.072.

The parameter values derived from these two assumptions were used in a simple MathCad algorithm in which the six steps in the outlined swelling/consolidation cycle were calculated. The initial total void ratio was 0.68 in both cases, while the initial pre-consolidation stress was 20 MPa and the initial γ_{SD} variable was set to 8 MPa. The mean stress was initially decreased from 10 to 0.5 MPa.

The results are illustrated in Figure 5-21. The upper graphs show the stress paths in the s - p' plane, as well as three values for the pre-consolidation stress: the initial, the minimum and the final value (dashed lines). The lower graphs show stress paths in the e - $\ln(p')$ plane; the net mean stress (p'), the effective stress ($p'+s$), and the pre-consolidation stress (p_0^*). In addition, the swelling pressure curve is marked, as well as a curve twice as high as the swelling pressure. The net mean stress (grey line) follows the unloading path, the constant value during swelling, the swelling pressure build-up, the elastic compression, and finally the consolidation. The effective stress (red line) follows the swelling pressure curve during the swelling step, after which it follows the build-up of the net mean stress. Finally, the pre-consolidation stress (yellow line) follows swelling pressure curve multiplied by two.

Due on the differences between the stress paths for the two cases, the 1st case was regarded to be most relevant for further analyses.

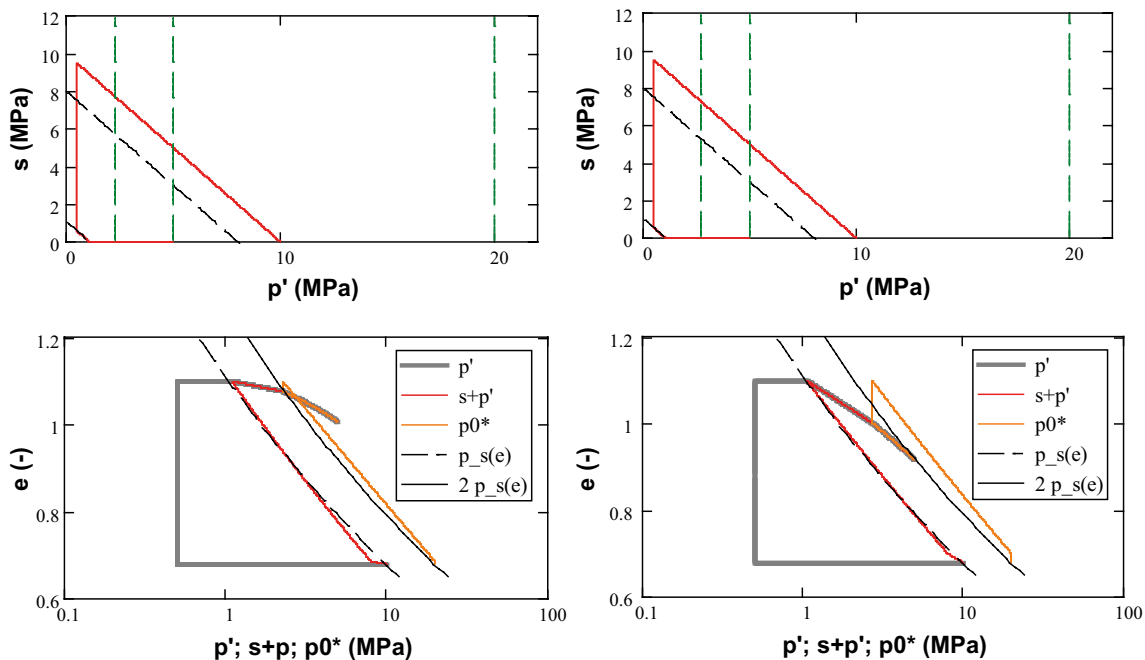


Figure 5-21. Stress-paths for two cases (left: 1st case; right: 2nd case) in s - p' plane (upper) and e - $\ln(p)$ plane (lower).

5.3.4 Isotropic swelling with Code_Bright

The implemented constitutive law in Code_Bright was investigated. The first analysis aimed at verifying the calculation of the isotropic swelling presented in the previous section. This was made with a cube with the side length of 20 mm which was divided in 27 elements (Figure 5-22).

The values of the main parameters were adopted according to the 1st case in the previous section: $\kappa_m = 0.027$; $\lambda(0) = 0.095$; $f_{SD0} = 6$ (Table 5-9). The elastic modules for the strains on the macro level were set low: $\kappa_s = 0$; $\kappa_i = 0.001$ (not zero due to numerical reasons). The λ parameter of the retention curve was set high (0.99) thereby keeping the saturation degree very close to unity.

Table 5-9. Parameter values following the Code_Bright framework for different constitutive laws (ICL) and types of constitutive laws (ITYCL). Values of significance for the problem marked red.

ICL	ITYCL	P1	P2	P3	P4	P5	P6	P7	P8
81 BExMo_ Elastic	1	k_mac 0.001	k_mic 0.027	-	-	K_s_mac 0	Nu_mac 0.49	Kmin_mac 0.01	Kmin_mic 0.01
82 BExMo_ coupling	1	xi0 0	C_b 0	f_SD0 6	f_SD1 0	Eta_SD 0	F_SI0 0	F_SI1 0	Eta_SI 0
83 BExMo_ Y.F._iso.	1	M 0.3	-	r_s 0	beta_s 0	pc 1	k_s 0	p_s 3	-
85 BExMo_ P.P._iso.	1	Omega 1	-	-	-	-	-	-	-
87 BExMo_ Hardening	1	lambda 0 0.095	eta_v 1	-	-	-	-	-	-
88 BExMo_ conver.	1	Tol 1E-8	-	-	-	1E-4	-	-	-
6 Retention_ curve	1	P0 20	Sigma 0 0	Lambda 0.99	Srl 0	Sls 1	-	-	-
7 Intrinsic_ Permeab.	1	K110 3.1E-21	K220 3.1E-21	K330 3.1E-21	Phi0 -	-	-	-	-
14 Liquid_ rel.permeab.	6	-	A 1	Lambda 3	Srl 0	Sls 1	-	-	-

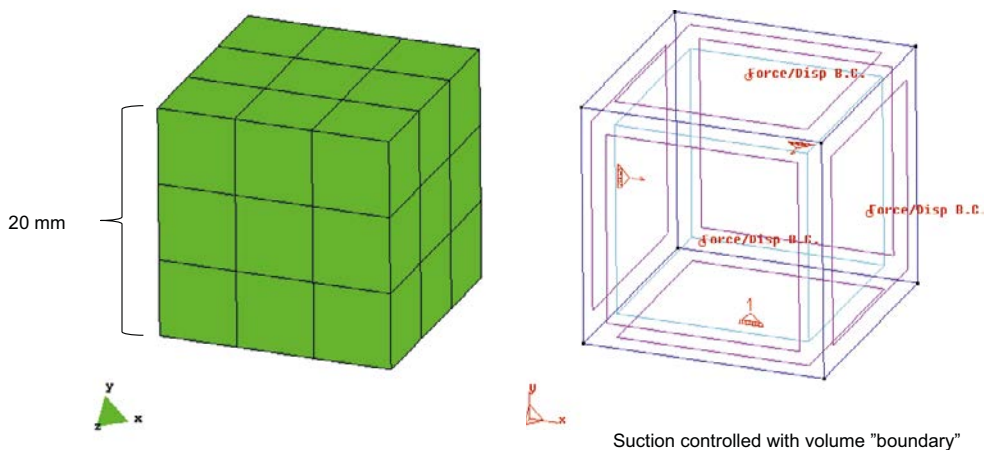


Figure 5-22. 3D geometry, grid and boundary conditions of Code_Bright models.

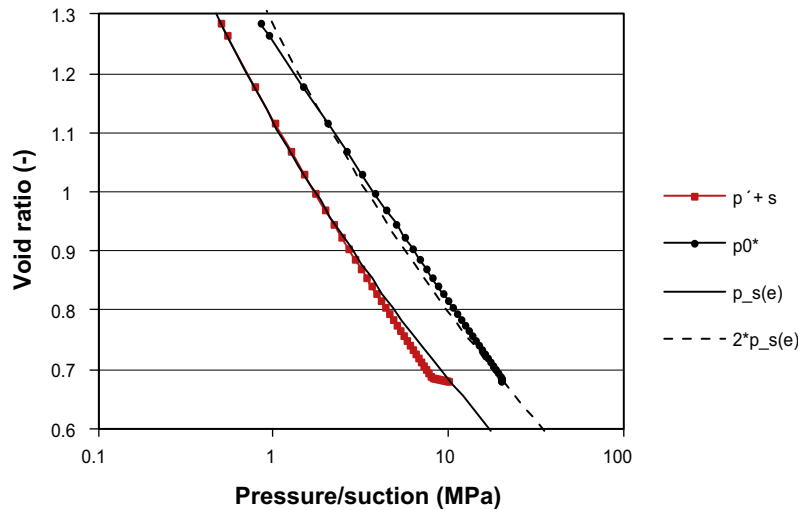


Figure 5-23. Stress-paths in $e-\ln(p')$ plane.

Constant boundary stresses were applied on three of the faces and roller boundaries were applied on the opposite three faces thereby keeping the net mean stress constant at 0.5 MPa, i.e. without any limiting confinement (Table 5-10). The liquid pressure was controlled with a volume “boundary” so that the suction value was decreased from 9.5 to zero MPa. In initial pre-consolidation stress was set to 20 MPa and the initial γ_{SD} variable was set to 8 MPa.

The results from the model (BEXM_n1) is illustrated as stress paths in the $e-\ln(p')$ plane: both the effective stress ($p'+s$) and the pre-consolidation stress (p_0^*). In addition, the swelling pressure curve is marked, as well as a curve twice as high as the swelling pressure. As in the previous section, the effective stress basically follows the swelling pressure curve, whereas the pre-consolidation stress follows the swelling pressure curve multiplied by two.

Table 5-10. Main variables in case with isotropic swelling.

Interval	n (-)	P_I (MPa)	σ (MPa)	P0* (MPa)	γ_{SD} (MPa)	γ_{SI} (MPa)
1	IC: 0.405	BC: -9.4 → 0.1	BC: -0.6	IC: 20	IC: 8	IC: 15

5.3.5 “One-element” analysis – uniaxial swelling with Code_Bright

The second analysis addressed the slightly more complicated test condition with axial swelling in a 2D geometry (plane strain) and with three confined boundaries (Figure 5-24).

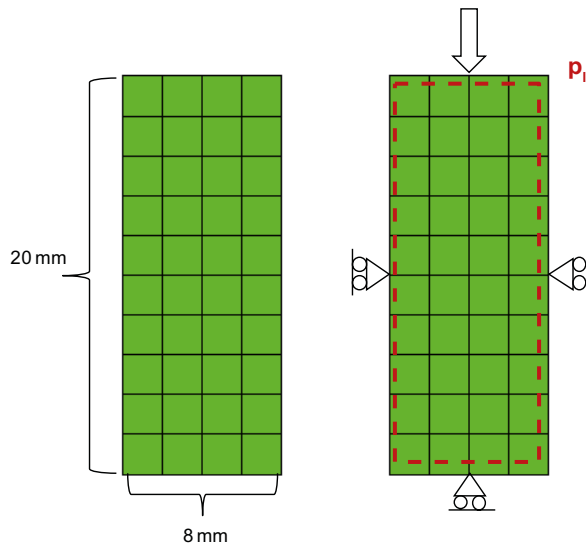


Figure 5-24. 2D geometry, grid and boundary conditions of one-element analysis.

The simulation was divided in two intervals (Table 5-11): i) with constant water content and therefore no hydraulic boundary, and with a reduced axial boundary stress; and ii) with constant axial boundary stress, and with controlled liquid pressure with a volume “boundary” so that the suction value was decreased from 9.8 to zero MPa.

The parameter setting was essentially the same as for the isotropic case (Table 5-9), but with some minor modifications: the critical state parameter M was set to 1 in order to avoid activation of LC curve. Apart from that, the effects of a number of parameter combinations were investigated (Table 5-12). The elastic macro level module κ_i was set to 0.001 during the first interval, while three different values: 0.001, 0.01 and 0.05; were tested for the second interval. In one case a lower γ_{SD} was applied, in order to maintain elastic conditions throughout the calculation. Finally, in the last case the $\lambda(0)$ value was increased with the value of κ_i .

Table 5-11. Main variables in case with uniaxial swelling.

Interval	Time	Hydraulic control	Mechanical boundary
1	0–1 d	Free (init 0.1 MPa)	-10.1 → -0.6 MPa
2	1–2 d	-9.672 → 0.1 MPa	-0.6 MPa

Table 5-12. Model versions and parameter variation.

Model version	κ_{mac} Interval 2	$\lambda(0)$	γ_{SD} (MPa)
BEXM_p25	0.001	0.095	8
BEXM_p22	0.01	0.095	8
BEXM_p27	0.05	0.095	8
BEXM_p26	0.05	0.095	0.1
BEXM_p28	0.05	0.145	8

Results for the four first cases are shown as stress paths in the s - p' plane in Figure 5-25 (left). The results for the first interval, the unloading at constant water content, were identical in the four cases. In the second interval, however, the different cases displayed major differences. In the purely elastic case ($\gamma_{SD} = 0.1$) there was no build-up of stresses. In contrast, in the case with a stiff micro level module ($\kappa_{mac} = 0.001$) there was a major build-up of stresses. In the case with a slightly softer material ($\kappa_{mac} = 0.01$) there was a minor build-up. Finally, in the case with the highest κ_{mac} value (0.05 and $\gamma_{SD} = 8$), there was almost no build-up of stresses at all. However, in this case the yield surface contracted to such an extent that the stress state in the q - p plane was reached (Figure 5-25, right).

The results for the four first cases are shown as stress paths in the e - $\ln(p'+s)$ plane and the e - $\ln(p_0^*)$ plane in Figure 5-26. In the purely elastic case there was no microstructure swelling and no change in p_0^* . In the case with a stiff macro level module ($\kappa_{mac} = 0.001$) the slopes of both the stress paths were as intended, although the extent of swelling was very limited. In the case with a slightly softer material ($\kappa_{mac} = 0.01$) the slopes of both the stress paths were also as intended, although the extent of swelling was limited to some extent. Finally, in the case with the highest κ_{mac} value (0.05 and $\gamma_{SD} = 8$), the slope of the stress path in the e - $\ln(p'+s)$ plane was as intended (at least until the yield surface reached the stress state), but the slope for the stress path in the e - $\ln(p_0^*)$ plane was significantly lower than intended.

In the last model version the $\lambda(0)$ value was increased with the value of κ_{mac} . This would therefore imply a modification of the parameter value adoption described earlier in Equation 5-32:

$$\lambda(0) = \frac{\pi}{\left(1 + \frac{1}{f_{SD}}\right)(1 + e_m)} + \kappa_{mac} \quad (5-33)$$

The results are shown as stress paths in the s - p' plane, the e - $\ln(p+s)$ plane and the e - $\ln(p_0^*)$ plane in Figure 5-27. The slopes of the stress paths were as intended, both for the e - $\ln(p+s)$ plane and the e - $\ln(p_0^*)$ plane. There was almost no build-up of stresses (due to the fairly high κ_i -value) which meant that there was almost no limitation of the swelling.

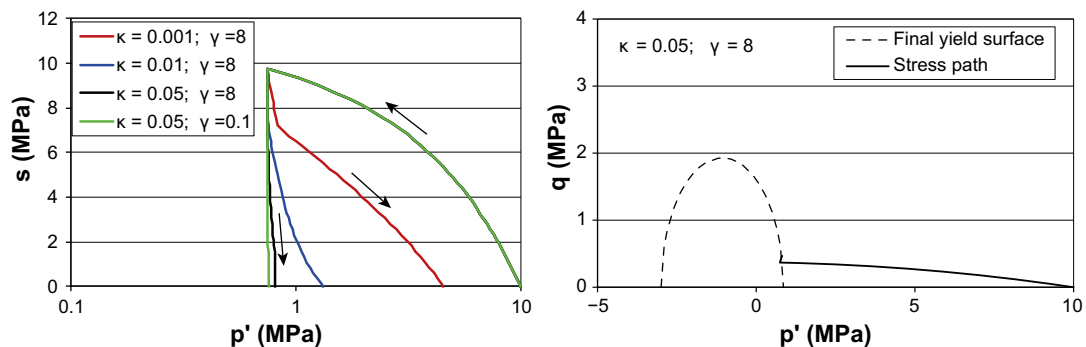


Figure 5-25. Stress-paths for different cases in s - p' plane (left) and q - p' plane (right).

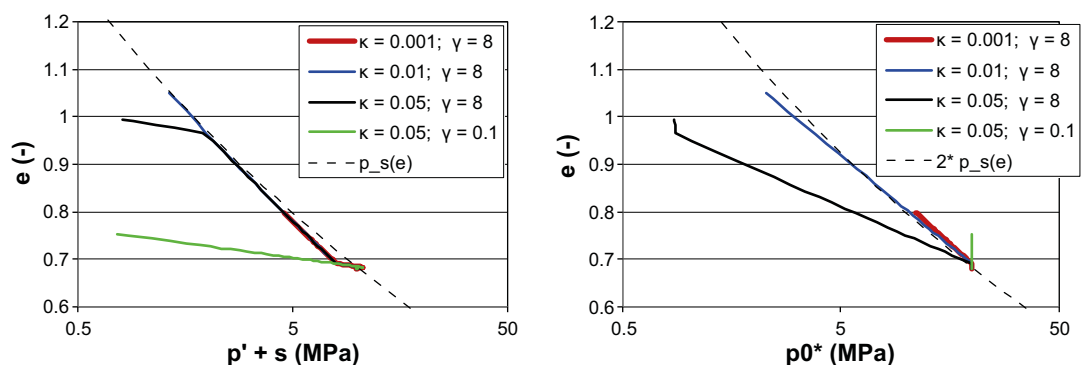


Figure 5-26. Stress-paths for different cases in e - $\ln(s+p')$ -plane (left) and e - $\ln(p_0^*)$ plane (right).

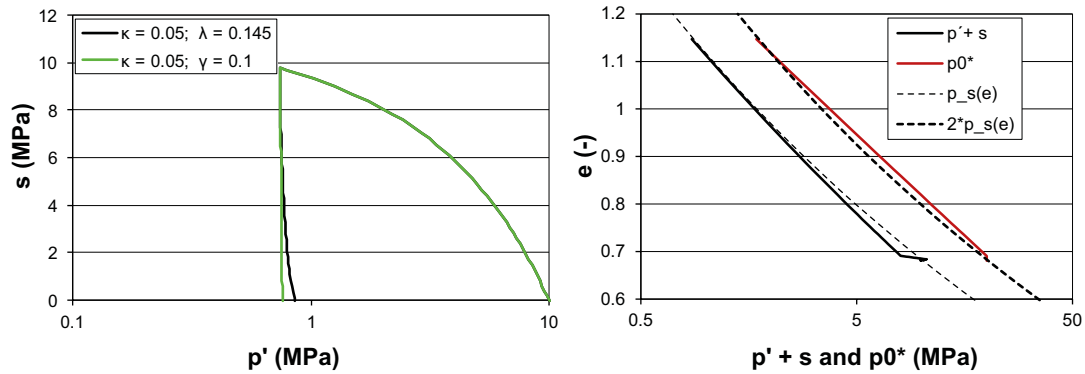


Figure 5-27. Stress-paths for different cases in s - p' plane (left) and e - $\ln(p')$ plane (right).

5.4 Concluding remarks

The following comments can be made from the presented evaluation of the homogenization process in the framework of BBM and the BExM:

A consistent representation of *loading and unloading for a water saturated specimen at constant water content* means that the suction increment is equal to the negative value of the stress increment ($ds = -dp'$). In the case of BBM such a behaviour requires a tuned set of retention, compression and swelling properties. For the BExM, however, this behaviour is directly given by the use of effective stress as a governing variable for the micro structure.

Reproduction of material undergoing extensive swelling/consolidation cycle requires a significant *contraction of the yield surface*. With BBM, this can only be accomplished through plastic dilatation at the dry side of the yield surface. This limitation has earlier been handled through adopting plastic parameter values for a “target void ratio” for material undergoing swelling (Åkesson et al. 2010a). In order to have robust material model which doesn't rely on such “beforehand knowledge” there are two options that potentially could be pursued for further investigations: i) by fine tuning of the plastic parameters to utilize the plastic dilation; or ii) to abandon the contraction of the yield surface by adopting a purely elastic approach. These options were however not considered to be meaningful to pursue and this was the motive for analysing BExM instead. With BExM, in contrast, it is possible to capture yield surface contraction during isotropic swelling and at constant load by using only three parameters: κ_m , λ_0 and f_{SD0} . Cases with uniaxial swelling are however complicated by the κ_{mac} parameter, which has to be set to a high value, which in turn will exaggerate the yield surface contraction. This can be compensated for by adjusting the λ_0 value.

However, the mechanism behind such a strain softening is attributed to the macro voids in BExM, even at water saturated conditions. This in turn means that the division of the void space in micro and macro voids has to be defined (and calibrated) in order to describe the irreversible loops (shown in Figure 5-21), while a more understandable definition would be based on the fluid in each void type, i.e. water in micro voids and gas in macro voids. The prospects for extending the approach to capture yield surface contraction and irreversible loops to water unsaturated conditions didn't therefore look promising, and this motivated the attempt to develop a completely new material model. Some additional remarks on the established material models are given in Section 6.6.

6 Development and application of a new material model (SKB1)

6.1 Introduction

Information on the hydro-mechanical behaviour of water saturated bentonite ultimately has to be based on the experimental results from different types of laboratory tests. The following five types are currently regarded to be the most important:

- *Water retention tests.* These are performed in closed containers in which specimens are left to equilibrate in different RH climates (corresponding to specific suction values) at free swelling conditions, after which the water content is measured (Dueck 2004, Dueck and Nilsson 2010). Compilations of results from such tests constitute specific water retention data sets, and different sets can be obtained for different initial water contents.
- *Oedometer tests.* These are performed on a water saturated specimen in a rigid steel cylinder, which ensures zero lateral strains, with free access of water through a filter, and by subjecting the specimen to stepwise increasing or decreasing axial loads. After each change in load, the specimen is left to equilibrate, i.e. through consolidation or swelling, and for these test conditions the axial and radial stresses as well as the void ratio are quantified (Börgesson et al. 1995, 2015).
- *Swelling pressure tests.* These are performed on a compacted, initially unsaturated, specimen in a rigid steel cell, with free access of water through a filter, and by measuring the axial force. The swelling pressure is evaluated as the axial stress after the water-uptake is completed (Karnland et al. 2000, 2006, 2009).
- *Homogenization tests.* Such a test is performed on a water-saturated bentonite specimen, which is confined in all directions except one, in which there is a slot and a hydraulic boundary with free access of water. The specimen will therefore swell and homogenize into this slot. The process is monitored by measuring stresses in different directions. After equilibrium has been reached, the specimen is dismantled, and the density distribution is quantified (Dueck et al. 2011a, 2014, 2016).
- *Shear strength tests.* These are usually performed on water-saturated bentonite specimen as either unconfined (Dueck et al. 2011b) or triaxial compression tests (Dueck et al. 2010). The latter type can be performed at either drained or undrained test conditions. The main test result is the von Mises stress at failure. This quantity can be related either to the mean effective stress or the dry density of the specimen.

A compilation of results from these types of tests is shown in Figure 6-1 together with two bounding functions ($\Psi_L(e)$ and $\Psi_H(e)$). The adoption of these functions is described in Section 6.4. The results from the water retention tests: RH and water content, were converted to suction (using Kelvin's law) and void ratio (assuming water saturated conditions). It can be noted that the experimental data from water retention tests, oedometer tests, swelling pressure tests and homogenisation tests generally fall within the interval described by these functions. In addition, the data from the unconfined compression tests (i.e. von Mises stress at failure) was generally half the value of the difference between the bounding functions.

Based on results from these types of tests, three basic characteristics can generally be identified:

- The swelling pressure is a *strictly decreasing function* of the void ratio, and correspondingly, the suction is a strictly decreasing function of the water content.
- Water retention data sets, and results from oedometer tests exhibit *path dependence*, so that bentonite undergoing a dehydration (or consolidation) path displays a higher suction value (or pressure) than a specimen which follows a hydration (or swelling) path.
- The bentonite has the ability to *sustain and to limit the difference between stresses in different directions*. The suction value in a water retention test does not display any direction dependence. In an oedometer test however the stresses are general non-isotropic, e.g. the axial stress exceeds the radial stress during consolidation, whereas the relation is the opposite during swelling. Yet, there are limits for how large the difference between the stresses in different directions can be.

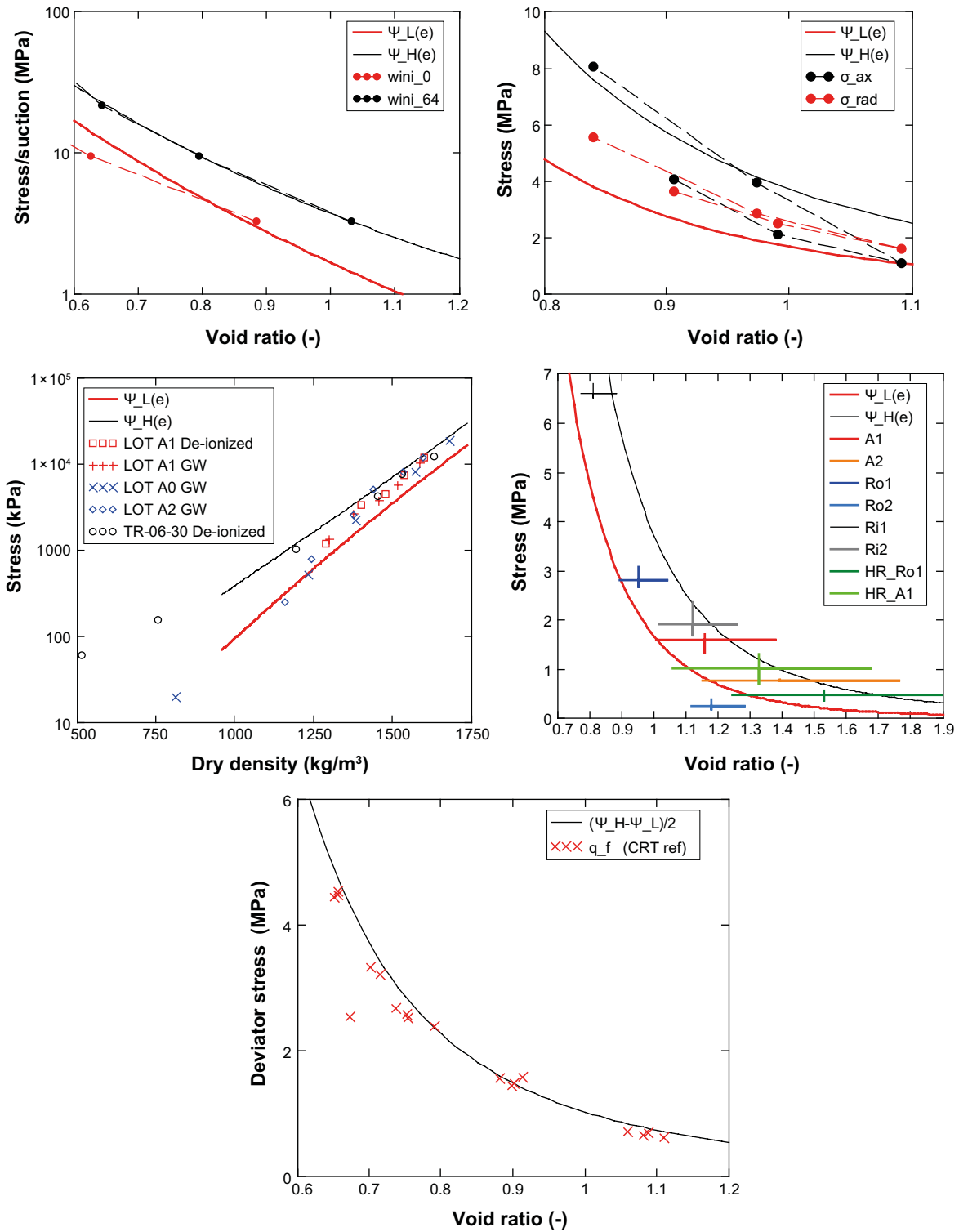


Figure 6-1. Compilation of experimental results from: water retention tests (Dueck and Nilsson 2010, upper left), oedometer tests (Börgesson et al. 2015, upper right), swelling pressure tests (Karlund et al. 2000, 2006, 2009, mid left), homogenization tests (Appendix 1 and 2, mid right), and unconfined compression tests (Dueck et al. 2011b, lower). Evaluated bounding functions ($\Psi_L(e)$ and $\Psi_H(e)$) shown for comparison.

Homogenization tests generally exhibit remaining heterogeneities. If wall friction effects can be ignored, then this illustrates that there is no unique relation between the void ratio and the stress in for instance the axial direction in an axial swelling test. Instead, this illustrates that a range of void ratio values can correspond to a single axial stress level. And consequently, that a range of swelling pressure (and suction) values can correspond to single void ratio (and water content) value. This was the main motive for pursuing an approach, in which the path dependences and the maximum allowed von Mises stress are regarded to be two aspects of the same basic material property. This approach is described in this report.

The development and definition of stress-strain relation are presented in Section 6.2. Simple tools for solving one-dimensional homogenization problems for three modes of swelling (axial, radial and spherical) are presented in Section 6.3. The adoption of parameter values is described in Section 6.4. Model results for the three modes of swelling are presented in Section 6.5. Finally, some concluding remarks are given in Section 6.6.

6.2 Definition of stress-strain relations

The chemical potential of the clay water (μ) was used as a starting point for the stress-strain relations of the model. This can be described as a function the water content (w) and the *pressure* (P) (e.g. Birgersson et al. 2010):

$$\mu = \mu_0 + RT \cdot \ln(RH(w)) + v_c \cdot P \quad (6-1)$$

where μ_0 is the chemical potential of a reference state, R is the universal gas constant, T is the absolute temperature, v_c is the molar volume of the clay water, and RH is the relative humidity of the clay at free swelling conditions. This can be rearranged as:

$$-\frac{\mu - \mu_0}{v_0} = -\frac{RT}{v_0} \cdot \ln(RH(w)) - \frac{v_c}{v_0} \cdot P \quad (6-2)$$

where v_0 is the molar volume of bulk water. The term on the left-hand side can be identified as *suction* (s), while the first term on the right-hand side from here on is denoted the *clay potential* (Ψ'). Assuming that v_0 and v_c are equal, this can simply be expressed as:

$$s = \Psi'(w) - P \quad (6-3)$$

It should be noted that the suction corresponds to the RH in an external gas phase. Correspondingly, it corresponds to the negative value of an external water pressure in equilibrium with the bentonite. This means that the clay potential is defined in a similar way as an *effective stress*.

It should also be noted that this description is based on the assumptions that the osmotic effect of any solution in the water can be disregarded and that the temperature is constant. It also assumes an *isotropic* stress state.

Moreover, the description doesn't include any path dependence. This is taken into account by first assuming water saturated conditions, which means that the clay potential can be defined as a function of the void ratio (e) instead of the water content (Ψ' is therefore replaced by Ψ), and secondly by introducing a *void ratio history*, which from here on simply is denoted with $e(t)$. With these notations, Equation 6-3 can be replaced with:

$$s = \Psi(e, e(t)) - P \quad (6-4)$$

The clay potential function is then developed on the following form:

$$\Psi(e, e(t)) = \Psi_M(e) + \Delta\Psi(e) \cdot f(e(t)) \quad (6-5)$$

where Ψ_M , $\Delta\Psi$ and f are denoted the *mid-line*, the *allowed span*, and the *path variable*, respectively. It can be noted that Ψ_M and $\Delta\Psi$ are defined functions of the void ratio, whereas f is a variable, with values between -0.5 and $+0.5$, which depends on the void ratio history. The clay potential is thus confined to a region with two bounding lines: $\Psi_M + \Delta\Psi/2$ (consolidation line) and $\Psi_M - \Delta\Psi/2$ (swelling line; see Figure 6-2, left).

For conditions with swelling (i.e. $de/dt > 0$) the f is defined with the following differential equation:

$$\frac{df}{de} = -\left(\frac{1}{2} + f\right) \cdot \frac{K'}{1 + e_{init}} \quad (6-6)$$

where K' is a parameter and e_{init} is the initial void ratio. Correspondingly, for conditions with consolidation ($de/dt < 0$) the f is defined as:

$$\frac{df}{de} = -\left(\frac{1}{2} - f\right) \cdot \frac{K'}{1 + e_{init}} \quad (6-7)$$

These two equations can be combined as:

$$\frac{df}{de} = -\left(\frac{1}{2} + \delta(e) \cdot f\right) \cdot \frac{K'}{1 + e_{init}} \quad (6-8)$$

where $\delta(e)$ is the sign of the time derivative of the void ratio:

$$\delta(e) = \text{sign}(de/dt) = \begin{cases} -1 & de/dt < 0 \\ 0 & de/dt = 0 \\ +1 & de/dt > 0 \end{cases} \quad (6-9)$$

The behaviour of these functions is illustrated in Figure 6-2.

The definition of the path variable is then generalized for strains instead of void ratio (Figure 6-3). For a volumetric strain: $\varepsilon = (e - e_{init})/(1 + e_{init})$, which means that $d\varepsilon/de = 1/(1 + e_{init})$, this means that the path variable simply can be defined as:

$$\frac{df}{d\varepsilon} = -\left(\frac{1}{2} + \delta(e) \cdot f\right) \cdot K' \quad (6-10)$$

To sum up: the relationship between suction, pressure, void ratio and strain history at water saturated, and isotropic, conditions is thus defined with the following set of equations:

$$s = \Psi(e, \varepsilon(t)) - P$$

$$\Psi(e, \varepsilon(t)) = \Psi_M(e) + \Delta\Psi(e) \cdot f(\varepsilon(t)) \quad (6-11)$$

$$\frac{df}{d\varepsilon} = -\left(\frac{1}{2} + \delta(e) \cdot f\right) \cdot K'$$

This set is finally generalized for non-isotropic conditions, which means that the set is enlarged threefold, and that stresses, strains, potentials and path variables are defined for three directions; here denoted x , y , and z :

$$\begin{aligned} s = \Psi^x - \sigma^x & \quad \Psi^x = \Psi_M + \Delta\Psi \cdot f^x & \quad \frac{df^x}{d\varepsilon^x} = -\left(\frac{1}{2} + f^x \cdot \delta(\varepsilon^x)\right) \cdot K \\ s = \Psi^y - \sigma^y & \quad \Psi^y = \Psi_M + \Delta\Psi \cdot f^y & \quad \frac{df^y}{d\varepsilon^y} = -\left(\frac{1}{2} + f^y \cdot \delta(\varepsilon^y)\right) \cdot K \\ s = \Psi^z - \sigma^z & \quad \Psi^z = \Psi_M + \Delta\Psi \cdot f^z & \quad \frac{df^z}{d\varepsilon^z} = -\left(\frac{1}{2} + f^z \cdot \delta(\varepsilon^z)\right) \cdot K \end{aligned} \quad (6-12)$$

It should be noted that the K parameter is three times higher than K' in Equation 6-11.

From this definition thus follows that suction and void ratio are scalars, whereas stress, clay potential and strain are tensors. The material properties are described by the two void ratio dependent functions for the clay potential (mid-line, Ψ_M , and the allowed span, $\Delta\Psi$) and the K parameter.

The equation set (6-12) may give the appearance that the stress-strain relations for each direction are independent of the other directions. However, they are indeed dependent through the void ratio dependence of the clay potential functions.

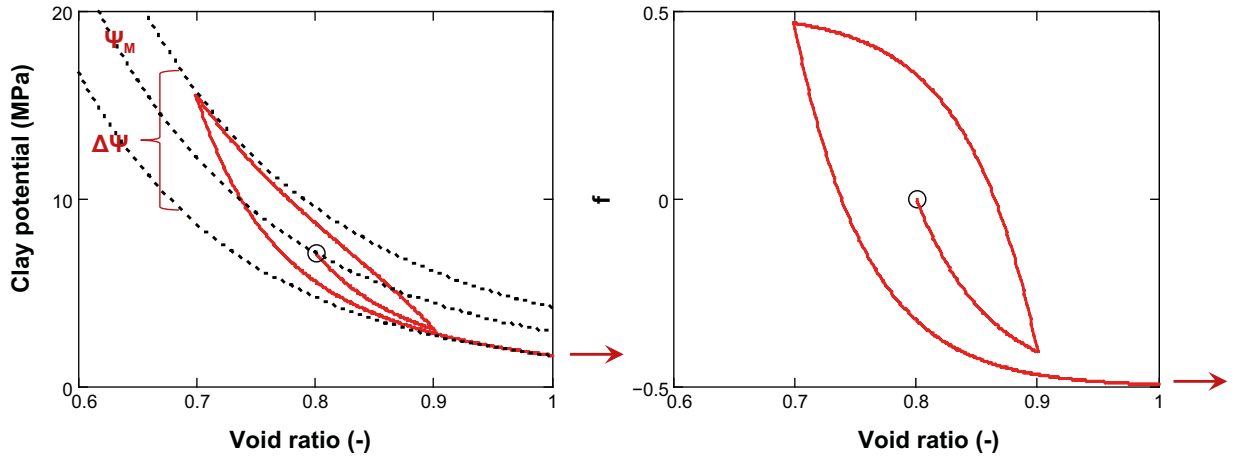


Figure 6-2. Clay potential and path variable (f) versus void ratio. Right graph shows an example of the path variable for a case with swelling, followed by consolidation and followed by swelling. Left graph shows the same path mapped on the region for the clay potential.

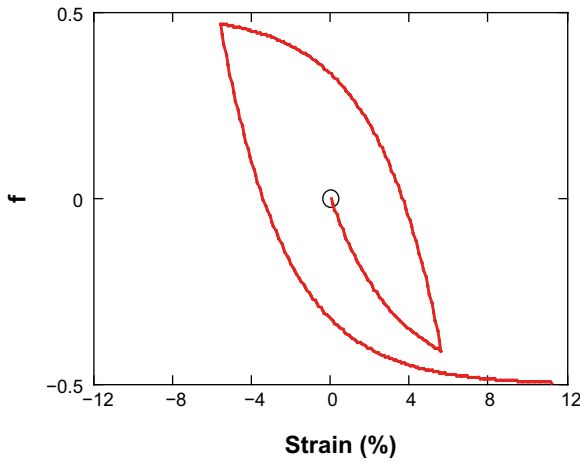


Figure 6-3. Path variable as a function of the strain history.

The equation set (6-12) can be formulated in matrix form. This is based on the (small strain) relation between the void ratio, the initial void ratio and the strains:

$$e = e_0 + (\varepsilon^x + \varepsilon^y + \varepsilon^z)(1 + e_0) \quad (6-13)$$

The relations for the clay potential (for direction k) and the void ratio (6-13) are then differentiated:

$$d\Psi^k = \frac{d\Psi_M}{de} de + \frac{d\Delta\Psi}{de} \cdot f^k de + \Delta\Psi \cdot \frac{df^k}{d\varepsilon^k} d\varepsilon^k \quad (6-14)$$

$$de = (d\varepsilon^x + d\varepsilon^y + d\varepsilon^z)(1 + e_0)$$

For simplification, two auxiliary quantities are defined as:

$$\alpha^k = \left(\frac{d\Psi_M}{de} + \frac{d\Delta\Psi}{de} \cdot \frac{\Psi^k - \Psi_M}{\Delta\Psi} \right) (1 + e_0) \quad (6-15)$$

$$\beta^k = \left(\frac{\Delta\Psi}{2} + (\Psi^k - \Psi_M) \cdot \delta(\varepsilon^k) \right) \cdot K$$

It should be noted that $(\Psi^k - \Psi_M)/\Delta\Psi$ was substituted for f^k . It should also be noted that the second quantity (β^k) include the sign of the time derivative of the strain $\delta(\varepsilon^k)$, which means that strain increments have to be known when β^k is calculated. With these two auxiliary quantities, the stress-strain relation can be formulated as:

$$\begin{pmatrix} ds + d\sigma^x \\ ds + d\sigma^y \\ ds + d\sigma^z \end{pmatrix} = \begin{pmatrix} \alpha^x - \beta^x & \alpha^x & \alpha^x \\ \alpha^y & \alpha^y - \beta^y & \alpha^y \\ \alpha^z & \alpha^z & \alpha^z - \beta^z \end{pmatrix} \begin{pmatrix} d\varepsilon^x \\ d\varepsilon^y \\ d\varepsilon^z \end{pmatrix} \quad (6-16)$$

The definition of the path variable for different directions was further refined so that the difference between f in different directions does not exceed 0.5. This was made by introducing variables for the maximum difference between the path variable in different directions, f_T :

$$f_T = \max[f_x; f_y; f_z] - \min[f_x; f_y; f_z] \quad (6-17)$$

and for the mean value of the highest and lowest path variable value, f_p :

$$f_p = \frac{\max[f_x; f_y; f_z] + \min[f_x; f_y; f_z]}{2} \quad (6-18)$$

A variable (f_D) which determines the limit for path variable for a specific direction (k) and strain direction $\delta(\varepsilon^k)$ is introduced:

$$f_D^k = f_T + \delta(\varepsilon^k) \cdot 2 \cdot f_p \quad (6-19)$$

With this framework, the generalized path variable definition given in Equation 6-12 can be refined as:

$$\frac{df^k}{d\varepsilon^k} = - \left(\frac{1}{2} - \Phi(f_D^k) \cdot \frac{f_D^k}{2} + \delta(\varepsilon^k) \cdot f^k \right) \cdot K \quad (6-20)$$

where Φ is the Heaviside step function.

Finally, during the course of this work it was found to be convenient (or maybe necessary) in many cases to define a relation between suction and the density of water thereby generalizing the compressibility of water (β) to “negative pore pressures”:

$$\rho_w(s) = \rho_0 \cdot \exp(-\beta \cdot s) \quad (6-21)$$

Since the density of water is related to both water content and void ratio ($\rho_w = \rho_s \cdot w/e$), this means that increments in suction is given by increments in water content and void ratio by the following simple relation:

$$ds = \frac{1}{\beta} \left[\frac{de}{e} - \frac{dw}{w} \right] \quad (6-22)$$

In the models developed in this work it could however be assumed that water is incompressible.

6.3 Method for solving 1D homogenization problems

This section describes simple tools (algorithms) for solving one-dimensional homogenization problems. Each of these consists of a water-saturated bentonite specimen, which is confined in all directions except one, in which there is a slot and a hydraulic boundary with free access of water. The specimen will therefore swell and homogenize into this slot.

Three different modes of swelling, i.e. geometries, have been analysed: axial, radial and spherical swelling. For each case, the geometry was discretized as an array of n elements (with index 0 to $n-1$) and with adjacent nodes (with index 0 to n), see Figure 6-4. The nodes and elements were numbered with zero at the fixed boundary (Figure 6-5, left). Several quantities were used in the analyses, and some of these were defined on nodes whereas others were defined on elements. The quantities defined on nodes were: distance from the fixed boundary, i.e. node position or radius (r), displacement (u) and flow rate (Q), and those defined on elements were: void ratio (e), volume (v), suction (s), clay potentials (Ψ^k), stresses (σ^k), strains (ε^k). The latter three quantities were defined for the three directions (k).

The algorithms were divided in two phases (Figure 6-5, right): one swelling phase, during which a small boundary stress was applied on the outermost element ($n-1$), and a redistribution phase, during which the outer boundary (node n) was fixed. These processes were driven by differences in suction: on one hand the suction given by the initial void ratio (or water content), and on the other the hydraulic boundary at which a zero suction level was maintained. The algorithms ended when the differences between the boundary suction, and the suction value of all elements were less than a defined limit.

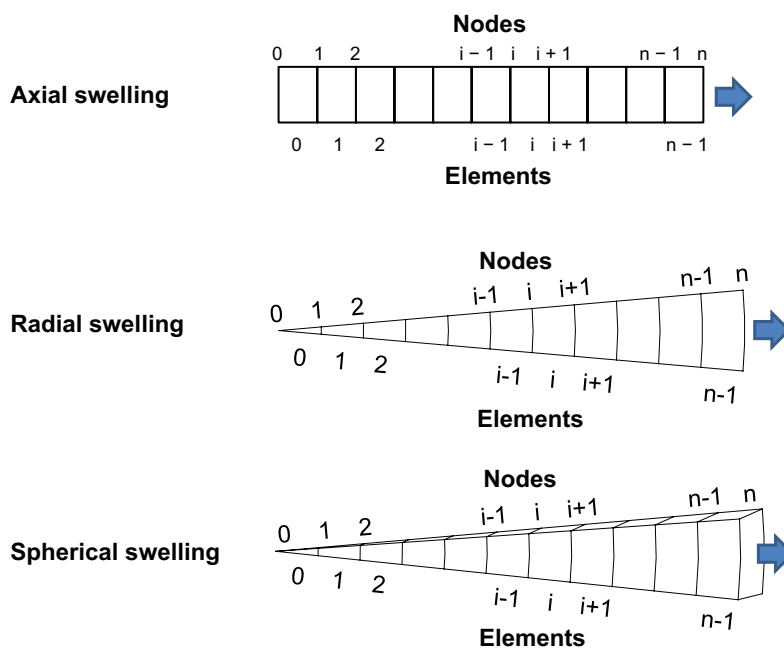


Figure 6-4. Three geometries for 1D homogenization problems. Discretization in elements and nodes. Swelling direction marked.

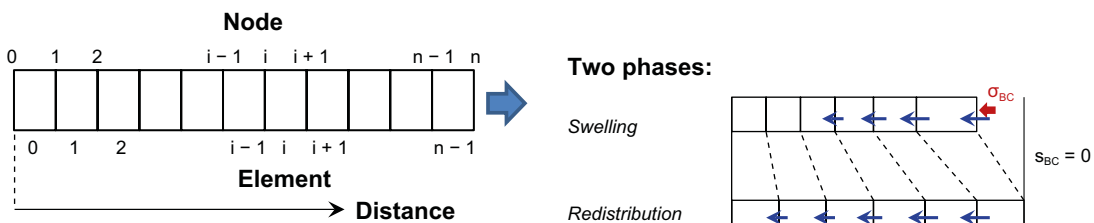


Figure 6-5. Geometry with defined distance from fixed boundary (left), and schematic illustration of two phases (right).

The boundary conditions (BC) for the fixed boundary were very simple, with no flow and no displacements throughout the analysis:

$$Q_0 = 0 \quad u_0 = 0 \quad (6-23)$$

The condition for the moving boundary during the swelling phase entailed a more complex hydraulic condition which was defined so that the outer element took up water as long as the suction value was higher than the boundary suction (i.e. zero) and by defining the numerical parameter q_{BC} . For the mechanics the stress in the swelling direction was set to a constant (low) boundary stress value (σ_{BC}):

$$Q_n = Q_{n-1} - q_{BC} \cdot s_{n-1} \cdot A_n \quad \sigma_{n-1}^x = \sigma_{BC} \quad (6-24)$$

During the redistributions phase the boundary conditions were very simple:

$$Q_n = 0 \quad \Delta u_n = 0 \quad (6-25)$$

With this framework of discretization and boundary conditions, and after assigning initial conditions to all quantities, the analysis was performed in a series of time steps quantified with a time-increment (Δt). The following eight operations were successively performed during each time step:

- i. Volumetric flow rates were calculated from the suction values.
- ii. Element volumes and void ratios were calculated from the flow rates and Δt .
- iii. Node positions and displacements were calculated from element volumes.
- iv. Strains were calculated from displacements, or void ratios.
- v. Path variable increments were calculated from the strain increments.
- vi. Clay potentials were calculated from void ratio and updated path variable.
- vii. Suction profile was integrated from stress equilibrium relations, clay potentials and BC.
- viii. Stresses were calculated from clay potentials and suction.

These operations are described in detail below. Elements and nodes numbers, and directions are indicated with i and k , respectively. For simplicity, no general index for time step is included in the mathematical description. However, in equations which includes quantities for different time steps, this is indicated with t and $t + \Delta t$, respectively.

i) Volumetric flow rates

These are given by the suction gradient, the hydraulic conductivity (K) defined as a function of the void ratio, the unit weight of water (γ_w) and the section area (A):

$$Q = K_H \frac{\partial s}{\partial r} \cdot A \quad K_H = K \cdot \gamma_w^{-1} \quad \gamma_w = 10^{-2} \text{ MPa} \cdot \text{m}^{-1} \quad (6-26)$$

This is implemented in the discretized framework as:

$$Q_i = [K_H(e_{i-1}) + K_H(e_i)] \frac{s_i - s_{i-1}}{r_{i+1} - r_{i-1}} \cdot A_i \quad (6-27)$$

The section area at node i is dependent of the geometry and defined as:

$$A_i = \begin{cases} 1 & \text{axial} \\ 2\pi \cdot r_i & \text{radial} \\ 4\pi \cdot r_i^2 & \text{spherical} \end{cases} \quad (6-28)$$

ii) Element volume and void ratio

The volume of each element is updated from the net influx and the time-increment:

$$v_i|_{t+\Delta t} = v_i|_t + (Q_i - Q_{i+1}) \cdot \Delta t \quad (6-29)$$

The void ratio of each element can be calculated directly from the current element volume and the initial volume and void ratio:

$$e_i = \frac{v_i}{v_i^{init}} (1 + e_i^{init}) - 1 \quad (6-30)$$

iii) *Node position and displacement*

The node positions are calculated iteratively so that r_i is calculated from r_{i-1} and v_{i-1} starting with $r_i = 0$ for node $i = 0$. The expression for this calculation is different for different geometries:

$$r_i = \begin{cases} v_{i-1} + r_{i-1} & \text{axial} \\ \sqrt{\frac{v_{i-1}}{\pi} + r_{i-1}^2} & \text{radial} \\ \sqrt[3]{\frac{v_{i-1}}{\pi} \frac{3}{4} + r_{i-1}^3} & \text{spherical} \end{cases} \quad (6-31)$$

Once the current radii are known, then the displacement for each node can be calculated as:

$$u_i = r_i - r_i^{init} \quad (6-32)$$

iv) *Strains*

The geometry with axial swelling is very simple, and the axial strain for each element can be calculated from the void ratio for the element in question, whereas the two radial (or lateral) strains are zero:

$$\varepsilon_i^a = \frac{e_i - e_i^{init}}{1 + e_i^{init}} \quad \varepsilon_i^r = 0 \quad (6-33)$$

The corresponding calculations for the other two geometries are slightly more complicated. These strains can generally be calculated from displacements and radii (node positions) for the adjacent nodes. For radial swelling the strains are given by:

$$\varepsilon_i^r = \frac{\partial u}{\partial r} = \frac{u_{i+1} - u_i}{r_{i+1} - r_i} \quad \varepsilon_i^\theta = \frac{u}{r} = \frac{u_{i+1} + u_i}{r_{i+1} + r_i} \quad \varepsilon_i^z = 0 \quad (6-34)$$

For spherical swelling the strains are given by:

$$\varepsilon_i^r = \frac{\partial u}{\partial r} = \frac{u_{i+1} - u_i}{r_{i+1} - r_i} \quad \varepsilon_i^\theta, \varepsilon_i^\phi = \frac{u}{r} = \frac{u_{i+1} + u_i}{r_{i+1} + r_i} \quad (6-35)$$

v) *Path variables*

Increments for the path variables (Δf_i^k) for each direction k , can be calculated from the strain increments ($\Delta \varepsilon_i^k = \varepsilon_i^k|_{t+\Delta t} - \varepsilon_i^k|_t$) for the corresponding directions:

$$\Delta f_i^k = -\Delta \varepsilon_i^k \left(\frac{1}{2} - \Phi(f_{Di}^k) \cdot \frac{f_{Di}^k}{2} + \delta(\varepsilon_i^k) \cdot f_i^k \right) \cdot K \quad (6-36)$$

where f_{Di}^k is calculated according to Equation 6-19.

vi) *Clay potential*

The clay potential for each direction can be calculated from the current void ratio and the clay potential function (the *mid-line* and the *allowed span*) and for the updated path variables for the corresponding directions:

$$\Psi_i^k|_{t+\Delta t} = \Psi_M(e_i|_{t+\Delta t}) + \Delta \Psi(e_i|_{t+\Delta t}) (f_i^k|_t + \Delta f_i^k) \quad (6-37)$$

vii) *Suction integration*

The integration of suction profiles is based on a stress equilibrium relation for the geometry in question, and the condition that the suction value equals the difference between the clay potential and the stress in each direction, see Equation 6-12. These two conditions therefore correspond to a relation between the suction gradient and the clay potentials. For axial swelling the equilibrium relation and the suction gradient are given as:

$$\frac{\partial \sigma^a}{\partial r} = 0 \quad \frac{\partial s}{\partial r} = \frac{\partial \Psi^a}{\partial r} \quad (6-38)$$

The corresponding relations for radial swelling are:

$$\frac{\partial \sigma^r}{\partial r} + \frac{\sigma^r - \sigma^\theta}{r} = 0 \quad \frac{\partial s}{\partial r} = \frac{\partial \Psi^r}{\partial r} + \frac{\Psi^r - \Psi^\theta}{r} \quad (6-39)$$

And for spherical swelling:

$$\frac{\partial \sigma^r}{\partial r} + \frac{2\sigma^r - 2\sigma^\theta}{r} = 0 \quad \frac{\partial s}{\partial r} = \frac{\partial \Psi^r}{\partial r} + 2 \frac{\Psi^r - \Psi^\theta}{r} \quad (6-40)$$

The suction integration is performed iteratively starting with the boundary condition at the outer element. This should ideally be equal to zero, but due to the definition of the boundary condition during the swelling phase, this is $s_{n-1} = \Psi_{n-1}^r - \sigma_{BC}$ instead. During the redistribution phase, however, the boundary suction value is equal to zero. The integration is based on the suction gradient relations above and is therefore geometry dependent. For axial swelling the adjacent suction value is simply given as:

$$s_i = s_{i+1} - (\Psi_{i+1}^a - \Psi_i^a) \quad (6-41)$$

The corresponding relation for radial swelling includes current values of clay potentials (radial and tangential) and radii:

$$s_i = s_{i+1} - \frac{r_{i+2} - r_i}{r_{i+2} + r_{i+1}} (\Psi_{i+1}^r - \Psi_{i+1}^\theta) - (\Psi_{i+1}^r - \Psi_i^r) \quad (6-42)$$

A similar relation is found for spherical swelling:

$$s_i = s_{i+1} - 2 \frac{r_{i+2} - r_i}{r_{i+2} + r_{i+1}} (\Psi_{i+1}^r - \Psi_{i+1}^\theta) - (\Psi_{i+1}^r - \Psi_i^r) \quad (6-43)$$

viii) *Stresses*

The last operation is simply the calculation of the stresses in each direction for the clay potential in the same direction, and the suction value:

$$\sigma_i^k = \Psi_i^k - s_i \quad (6-44)$$

6.4 Parameter value adoption

Introduction

The presented model is specified with three parameter sets: the clay potential (i.e. $\Psi_M(e)$ and $\Delta\Psi(e)$), the K parameter, and the hydraulic conductivity $K_H(e)$.

During the course of the development of the presented model a number of parameter sets were tested. The one presented here was developed once a maximum difference between the path variable in different directions, Equation 6-20 was defined. The parameter values were largely adopted from independent test, although the hydraulic conductivity function was calibrated in order to improve the agreement with the experiential data from the homogenization tests presented by Dueck et al. (2014, 2016).

Clay potential

Several avenues may be available for the quantification of the clay potential, e.g. from data on retention properties for free swelling samples and oedometer tests with free access of water. In order to adhere to previously adopted material models, at least as far as possible, the presented analysis was based on two empirical relations: one between the swelling pressure (p_{sw}) and the void ratio (actually the dry density, ρ_d), and one between the von Mises stress at failure in a unconfined compression test ($q_f = \sigma_1 - \sigma_3$) and the void ratio.

The swelling pressure function was adopted on the following form by Åkesson et al. (2010a), and with the following parameter values: $c_0 = -4.74$, $c_1 = 4.12 \times 10^{-3}$, $c_2 = -3.94 \times 10^{-7}$ (p_{swell} in MPa; ρ_d in kg/m^3):

$$\log^{10}[p_{sw}(\rho_d)] = c_2 \cdot \rho_d^2 + c_1 \cdot \rho_d + c_0 \quad (6-45)$$

The relation for the von Mises stress at failure was adopted on the following form from experimental data (see Figure 6-1):

$$q_f(e) = \frac{0.65}{(e - 0.14)^3} \quad (\text{MPa}) \quad (6-46)$$

The bounding lines was then simply quantified as (using $\rho_d = \rho_s/(1+e)$ where $\rho_s = 2780 \text{ kg/m}^3$).

$$\left\{ \begin{array}{l} \Psi_L(e) = p_{sw}(e) \\ \Psi_H(e) = p_{sw}(e) + 2 \cdot q_f(e) \end{array} \right. \quad (6-47)$$

A function with the same form as Equation 6-45 was adopted for the Ψ_H relation. The following parameter values were found: $c_0 = -2.675$, $c_1 = 2.101 \times 10^{-3}$, $c_2 = 1.669 \times 10^{-7}$ (MPa).

The evaluated bounding lines are shown in (see Figure 6-1). It should be noted that the used swelling pressure curve (6-45) to a large extent was based on free swelling retention data for an initial water content of 17 %. This curve is therefore less relevant for void ratios below a level of approximately 0.7.

These bounding functions were used to calculate the mid-line and allowed span used in the model: $\Psi_M = (\Psi_H + \Psi_L)/2$ and $\Delta\Psi = \Psi_H - \Psi_L$ (Figure 6-2, left).

K parameter

The adoption of the K parameter was made through numerical integration of Equations 6-12 and 6-20. This was made for three triaxial compression tests presented by Dueck et al. (2010), see Figure 6-6. The calculation was simplified by the conditions that: i) the radial stresses (σ_y and σ_z) were equal, ii) that the radial strains (ϵ_y and ϵ_z) were equal, and iii) that the void ratio was constant. The K value was then tuned to a value of 40 in order to get approximately correct q-value for an axial strain of 2 %.

Hydraulic conductivity

The hydraulic conductivity, in the form defined in Equation 6-26, and its void ratio dependence were taken from the adoption by Åkesson et al. (2010). Still, in order to mimic the results of the homogenization tests this parameterization was multiplied with 0.5.

$$K_H(e) = 0.5 \cdot 2.4 \cdot 10^{-13} \cdot e^{5.33} \cdot 10^2 \quad (\text{m/s} \cdot \text{m/MPa}) \quad (6-48)$$

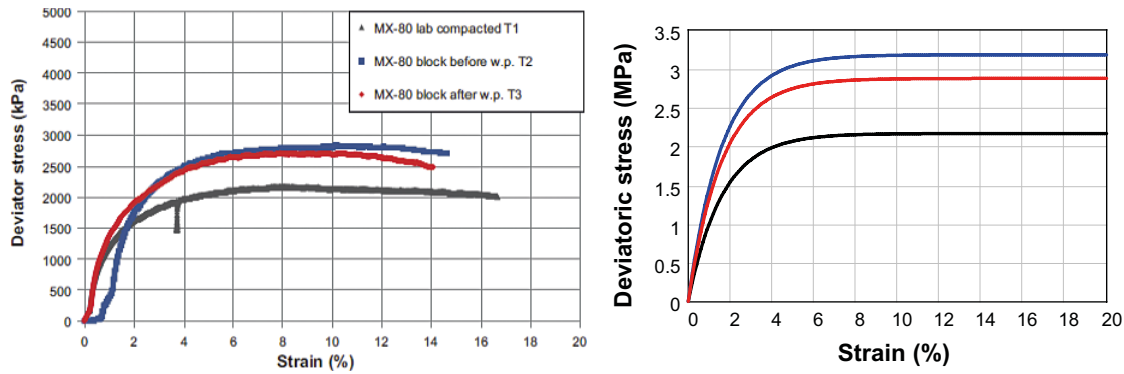


Figure 6-6. Stress paths in q - ε_{ax} plane for triaxial compression tests: experimental data, from Dueck et al. (2010) (left) and model results (right). Different colours denote different experiments.

6.5 Model results for 1D homogenization problems

The models were developed with the intention to mimic experimental results from homogenization tests presented by Dueck et al. (2014, 2016). Three experiments with the same mode of swelling as described in Chapter 6.3, so called high resolution swelling tests were used for this modelling task: axial swelling (HR-A1), radial outward swelling (HR-Ro1) and isotropic swelling (HR-Iso). The experimental conditions (initial void ratio and initial and final dimensions) were slightly adjusted in order to improve the consistency between different data sets, and to enable comparison with results from the SKB2 modelling team (see Chapter 3). These conditions are summarized in Table 6-1. Each model was discretized in 25 elements, all of which were assigned an initial state with the clay potential in all directions on the mid-line (Ψ_M) and with stresses in all directions equal to zero. The boundary stress during the swelling phase was set to 10 kPa. The numerical boundary parameter q_{BC} was set to $4 \times 10^{-7} \text{ m}/(\text{s} \cdot \text{MPa})$. The time increment was increased geometrically as $\Delta t_j \cdot (1 + \tau)^j$, where j was the time step, Δt_0 was set to 1 s, and τ was set to 5×10^{-5} . The parameter set described in Section 6.4 was used as a material description. The algorithms were implemented in a MathCad spreadsheets.

Modelled and measured evolutions of stresses are shown in Figure 6-7; axial swelling (upper), radial swelling (centre) and spherical swelling (lower). Dashed lines generally denote measured stresses, whereas solid lines denote model results (the measured axial stress in the case with isotropic swelling being the sole exception). All stress evolutions reflected the two phases with an initial swelling phase, with low constant stress, and the subsequent redistribution phase, with a significant buildup.

Four stresses were evaluated for the case with axial swelling: the axial stress (which was the same in all elements of the model) and the radial stress at three axial positions along the geometry (15, 35 and 45 mm from the confined boundary). It can be noted that the order of precedence of the experimental stress level at these four positions as well as the overall time evolution and axial stress level could be quite well mimicked with the model.

Two stresses were evaluated from the model with radial swelling: the axial stress (which was integrated along the geometry) and the radial stress (at the outer boundary), and these were compared with experimental data for the axial stress and the radial stress at four different positions. It can be noted that the overall time evolution and stress levels could be quite well mimicked with the model.

Only one stress was evaluated from the model with spherical swelling, i.e. the radial stress at the outer boundary. This was compared with experimental data for the axial stress and the radial stress at four different positions. Again, it can be noted that the overall time evolution and stress levels could be fairly well mimicked with the model.

A comparison of final dry density distributions for both experiments and models is shown Figure 6-8 (left). It can be noted that the overall profiles are in fairly good agreement, although the dry density level for the model with axial swelling was slightly under predicted. The dry density level for the model with spherical swelling was slightly over predicted. This difference should probably not be over interpreted due to the differences between the idealized geometry of model and the actual design of the

experiment. A systematic difference can be noted for the calculated models which displayed fairly flat profiles in the consolidated parts close to the outer boundary in a way that could not be observed in the experimental data sets.

The modelled final states in the q-p plane are shown together with the empirical relation, Equation 5-2 between the von Mises stress at failure and the mean effective stress in Figure 6-8 (right). It can generally be noted that all elements fell at or below the failure line. Very minor exceptions could be noted for the inner swelling parts in the models for axial and radial swelling, and for the outer consolidated parts in the models for spherical swelling.

Table 6-1. Initial void ratio and dimensions for different model cases.

	Case (geometry)		
	HR-A1 (axial)	HR-Ro1 (radial)	HR-Iso (spherical)
Init void ratio	0.7	0.7	0.7
Init length (mm)	37.4	40.5	44.5
Final length (mm)	50	48.5	50
Total swelling (%)	33.6	43.4	43

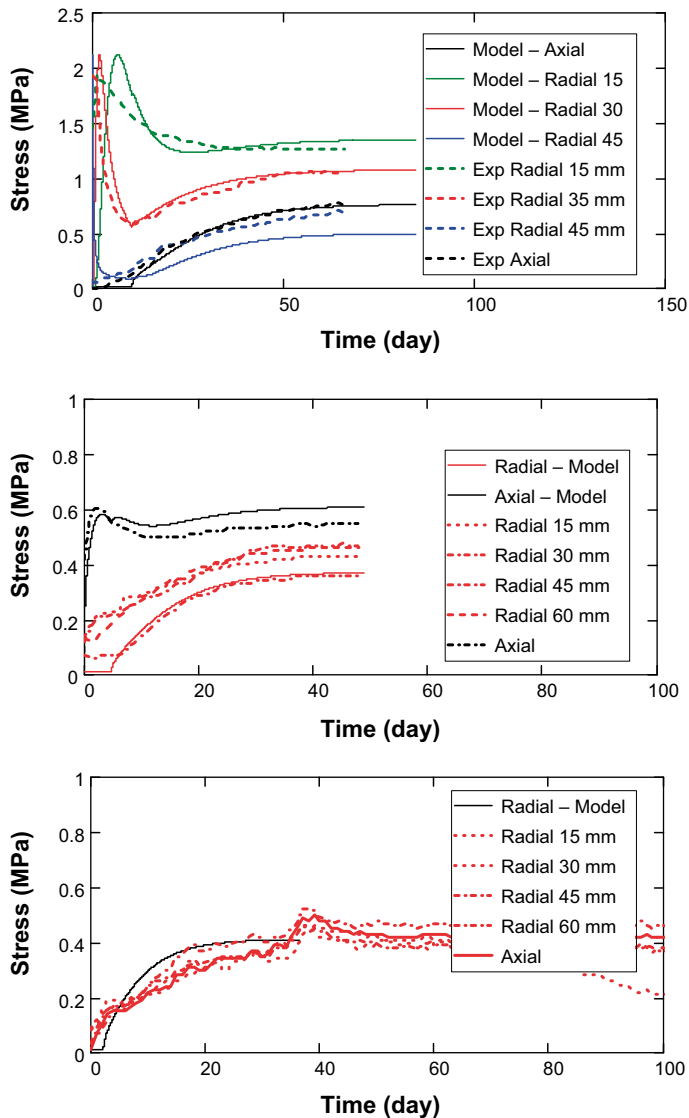


Figure 6-7. Evolution of measured and modelled stresses for axial (upper graph), radial (centre graph) and spherical swelling (lower graph).

In order to further illustrate the behaviour of the material model and the swelling model additional results for the models with axial, radial and spherical swelling are shown in Figure 6-9, Figure 6-10 and Figure 6-11, respectively. Each figure is composed of eight diagrams which show corresponding results. The three upper diagrams on the left side of each figure show stress paths in the $e-\Psi$ plane (void ratio versus clay potential) for the seven elements closest to the outer boundary (node n) of each model. The lower diagrams on the left side of each figure show the final state of all elements in the $e-\Psi$ plane. The three upper diagrams on the right-side show stress distributions at different times, and the lower right diagrams correspondingly show suction distributions.

The stress paths for the axial swelling (Figure 6-9) originate from the initial point located on the mid-line at a void ratio of 0.7 and a potential of 12 MPa. During the swelling phase, the stress paths for the axial potential asymptotically follow the swelling line ($\Psi_M - \Delta\Psi/2$) until the outermost element reaches the boundary stress (10 kPa). During the subsequent redistribution phase, the stress paths turn, after which they cross the midline and asymptotically follow the consolidation line ($\Psi_M + \Delta\Psi/2$). The corresponding stress paths for the two radial potentials (with zero strains) all follow the mid-line. The final states in the $e-\Psi$ plane show that the axial potential was the same in all elements, and that elements on the swelling side (towards the moving boundary) fell on the consolidation line and reached the highest void ratio, whereas elements on the other side (close to the fixed boundary) fell on the swelling line and reached the lowest void ratio. The axial stress distribution simply followed flat lines which increases during the redistribution phase. The radial stress, in contrast, showed a rapid “wave” moving from the swelling side. During the redistribution phase the stress profile was levelled out to the final remaining heterogeneity. The suction profiles followed a diffusion-like transient from the initial level to the zero level.

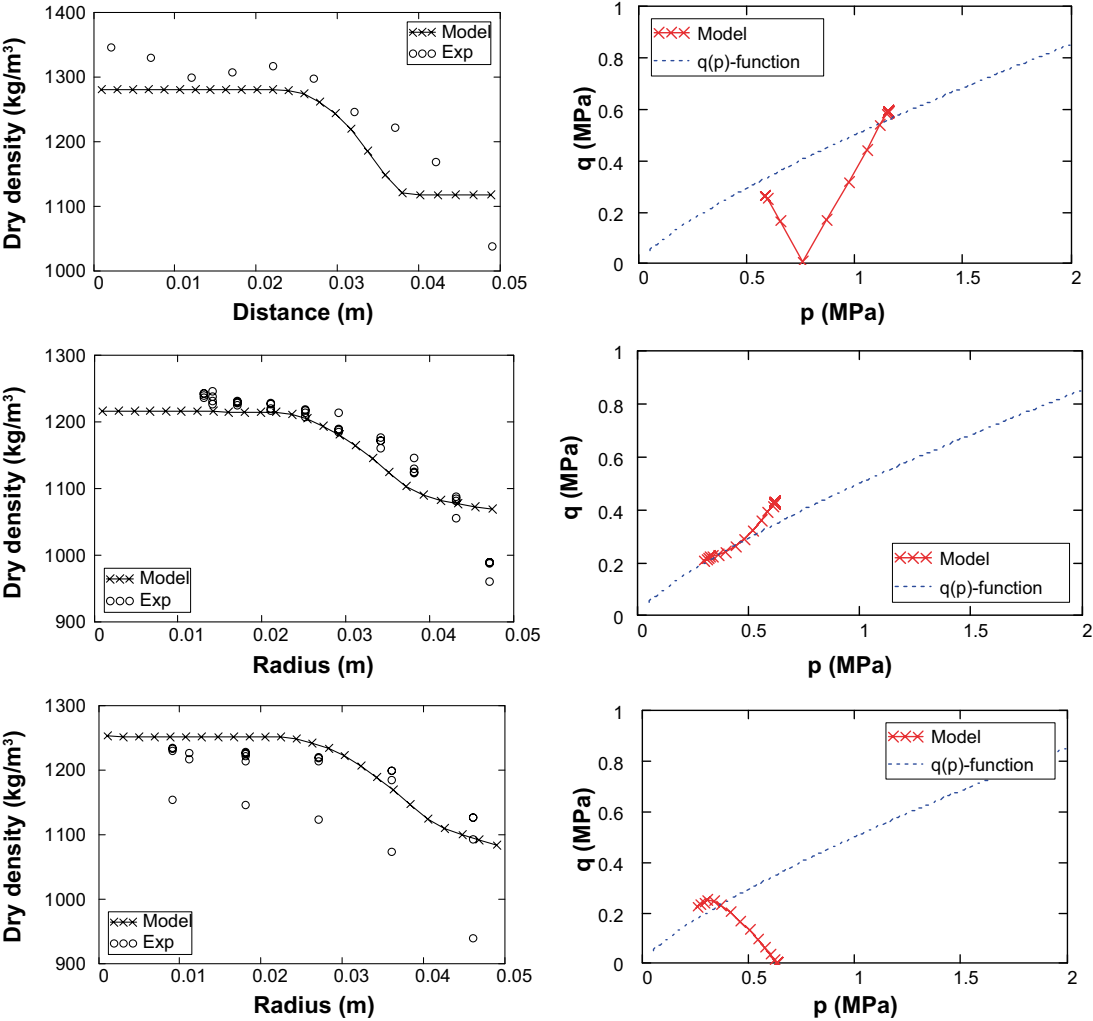


Figure 6-8. Final dry density distribution: model and measured (left); and final state in $q-p$ plane and empirical $q(p)$ function(right). Axial (upper graphs), radial (centre graphs) and spherical swelling (lower graphs).

The corresponding stress paths for the radial swelling are shown in Figure 6-10. The radial potentials are similar to the axial in the previous example and the stress path for the outer elements initially also follow the swelling line after which they turn and follow the mid line. This is an effect of Equation 6-20. The tangential potentials, in contrast, approach the swelling line during the swelling phase, but not as much as the radial potentials. During the subsequent redistribution phase, the tangential potential for all elements reach the swelling line. The axial potentials (with zero strains) all follow the mid-line. The final states in the e - Ψ plane show that the radial potential was slightly lower on the outer boundary than in the inner part of the model, and (similar to the axial potential in the previous case) that the elements on the two sides fell on the consolidation line and mid line, respectively. The stress distributions displayed some resemblance with the case with axial swelling (fairly flat profile for radial stresses and rapid waves for the tangential and axial stress), but with one major difference: tensile stresses were found during the early stage of the swelling phase. The suction profiles resembled the case with axial swelling but displayed a slight increase during the early stage of the swelling phase.

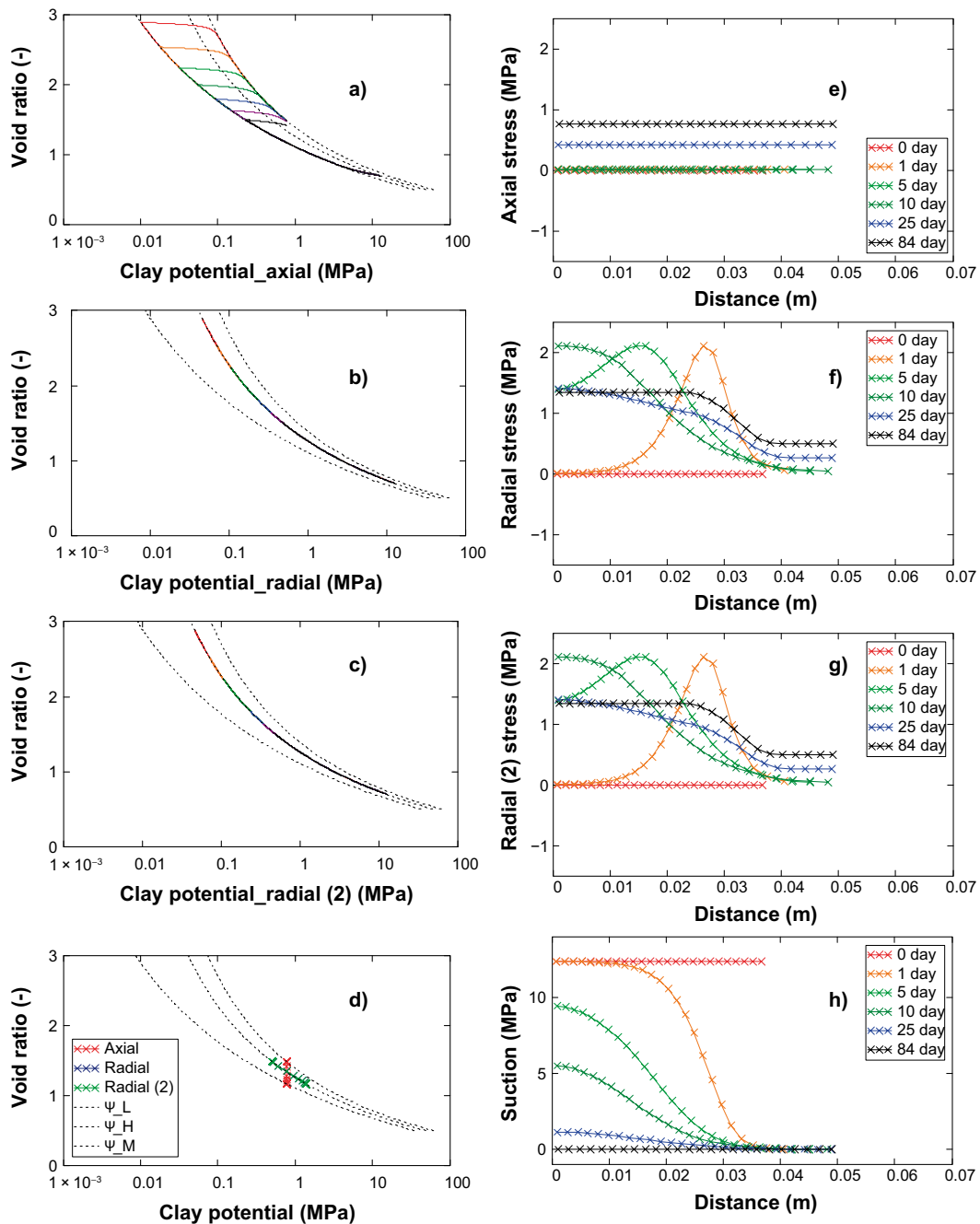


Figure 6-9. Results from model for axial swelling. Stress paths in e - Ψ plane for seven outer elements: axial (a) and radial (b and c) clay potential. Final state in e - Ψ plane (d). Stress distributions for different times: axial (e) and radial (f and g). Suction distributions for different times (h).

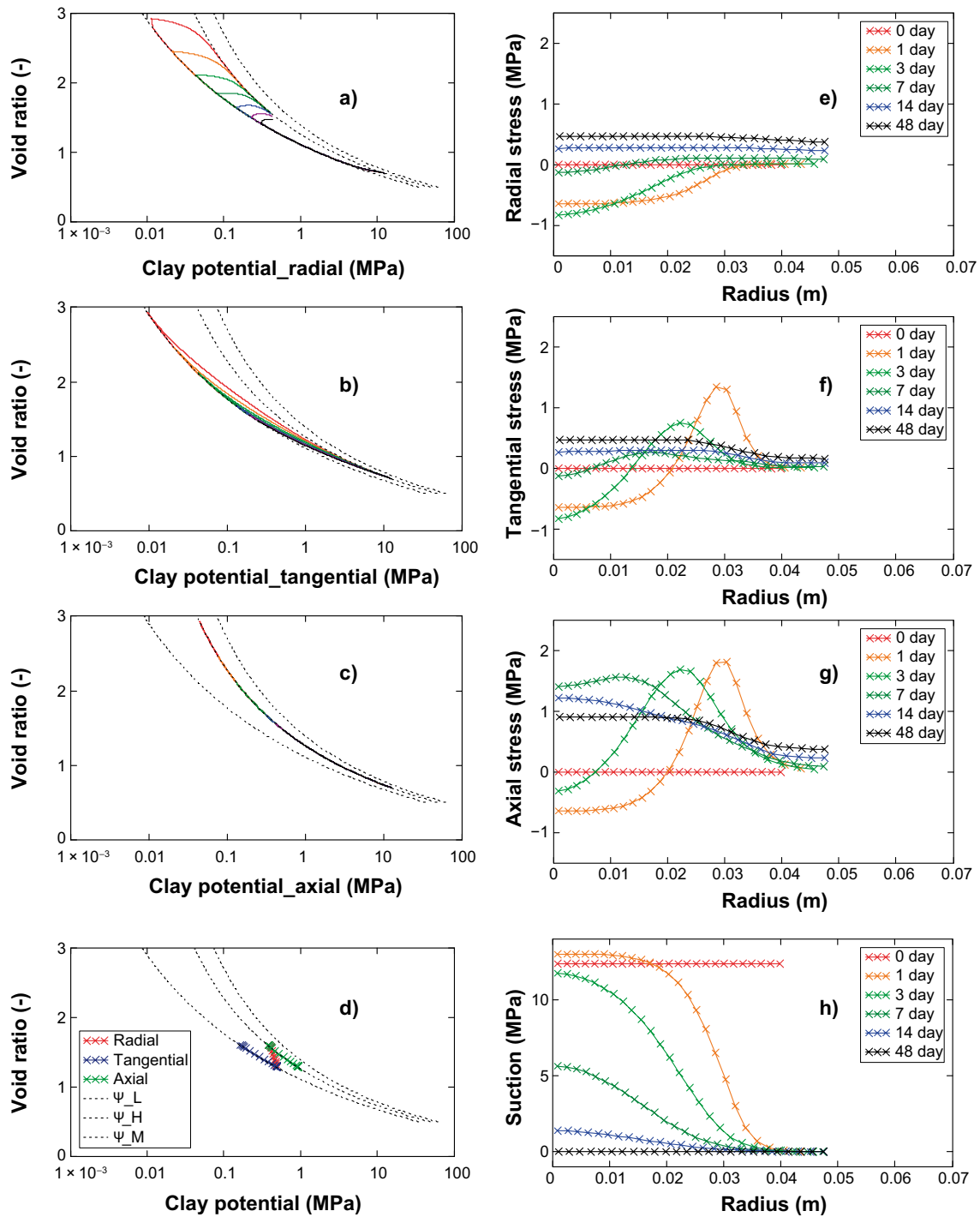


Figure 6-10. Results from model for radial swelling. Stress paths in e - Ψ plane for seven outer elements: radial (a), tangential (b) and axial (c) clay potential. Final state in e - Ψ plane (d). Stress distributions for different times: radial (e), tangential (f) and axial (g). Suction distributions for different times (h).

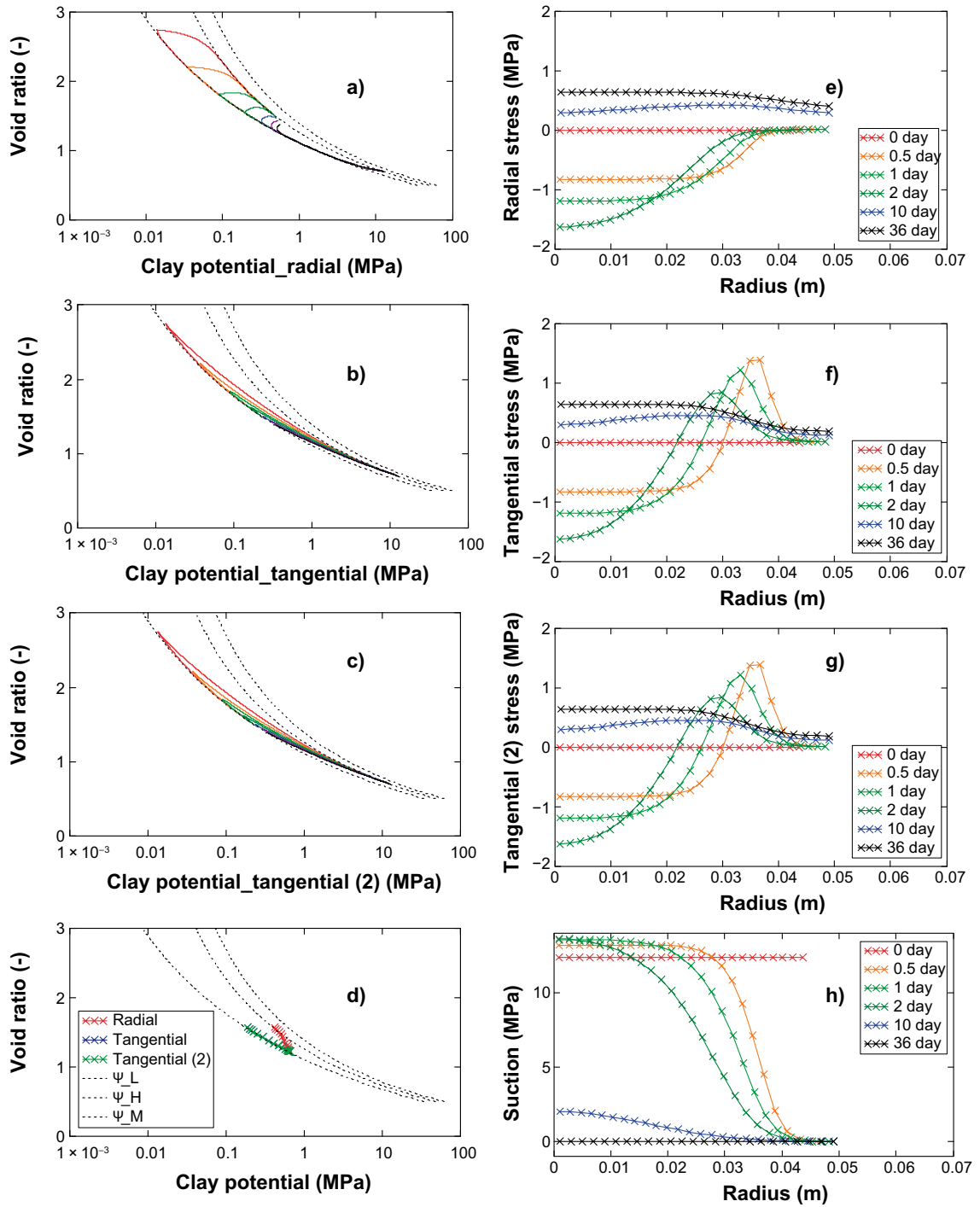


Figure 6-11. Results from model for spherical swelling. Stress paths in e - Ψ plane for seven outer elements: radial (a) and tangential (b and c) clay potential. Final state in e - Ψ plane (d). Stress distributions for different times: radial (e) and tangential (f and g). Suction distributions for different times (h).

The stress paths for the spherical swelling (Figure 6-11) were similar to the stress paths for radial swelling: both the radial and the tangential potentials. For spherical swelling there were two identical tangential potentials and no direction with zero strains. This was also reflected by the final states in the $e-\Psi$ plane, which were similar to the radial and tangential potentials in the previous case with radial swelling. The stress distributions were quite similar to the case with radial swelling: fairly flat profile for radial stresses, rapid waves for the tangential stresses, and tensile stresses during the early stage. The suction profiles also resembled the case with radial swelling.

Finally, dry density distributions are shown for different times for the three models in Figure 6-12. It can be noted that the transient behaviour is quite similar for the modes of swelling. The dry density on the swelling side drops rapidly down to $\sim 700 \text{ kg/m}^3$, after which the inner parts swell and compress (or dehydrate) the outer parts.

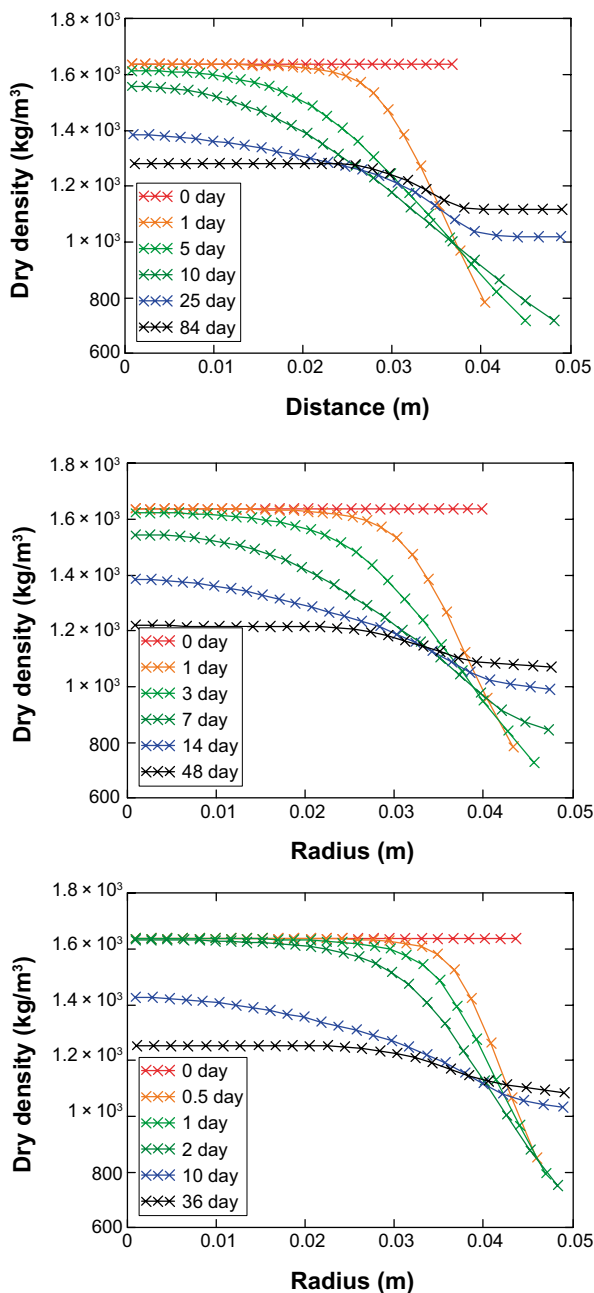


Figure 6-12. Dry density distributions for different times and for axial (upper graph), radial (centre graph) and spherical swelling (lower graph).

6.6 Concluding remarks

Homogenization tests are characterized by wide ranges of void ratios and water contents and therefore require that the material models can represent the behaviour of the bentonite as accurately as possible for such wide ranges. During the course of this work it therefore became more and more clear that the available constitutive laws were insufficient to use for these tests, and effort was therefore made to develop a new model.

The development of a new constitutive law is a laborious, although stimulating, endeavour. In order to motivate such an effort, the developer should try to demonstrate: i) that the new model is able to capture the results from all relevant problems; and ii) that the existing models are not. The first part should be simple enough as long as the model is accurate, and the problems are simple and well-defined. In the presented work, the experimental data from oedometer tests, triaxial and unconfined compression tests as well as water retention curve have continuously been used for comparison (Figure 6-1). The second part is more difficult, especially if a large number of parameters are used in the model which means that it may be virtually impossible for the modeler to ensure that all possible parameter combinations has been tested. Moreover, one of the existing models (BBM) has been used quite successfully for different *unsaturated* homogenization problems in SR-Site (Åkesson et al. 2010a). The models presented in Chapter 5 were very simple tests with one or two homogenous elements, which could be used to investigate certain features of the models, which for the BBM case did show discouraging results. No attempt was made to create any rigorous models of the actual homogenization tests. Instead, some efforts have been made to demonstrate the limitations of the existing models in terms of different aspects.

One such aspect is the used state variables in BBM and for the macro voids in BExM: i.e. suction and net mean stress. This can be compared with the clay potential (i.e. the sum of suction and total stress) used in the new model. The clay potential is basically an equivalent to the effective stress, whereas the net stress is almost the same as the total stress (if the gas pressure is small compared to the total stress). This means that the clay potential is divided in two independent state variables in BBM, which in turn means that two sets of *identical* relations between the variables and the void ratio should be defined. For instance, the consolidation/swelling/-consolidation (or drying/wetting/drying) loop shown in Figure 6-13 should be possible to generate for both suction and net mean stress as state variable. However, the frameworks in term of modules and yield surfaces are incomplete for such loops, especially in the case with suction for which there is only one module (κ_s) and no yield surface (although the SI yield locus was proposed by Alonso et al. (1990)).

Another aspect is the extent of the yield surface. Even if the new model doesn't include any mean stresses or von Mises stresses it can be illustrative to combine the two bounding lines of the clay potential as an extension in the q - Ψ - e space with a half-ellipse envelope. This is shown in Figure 6-14 together with the yield surface for the BBM (originally from the Modified Cam Clay model). One major difference between these models is that the size of the half ellipse in BBM is changed (through the hardening law) whenever this is reached by the stress path. The corresponding surface in the new model is pre-defined and all stress paths move asymptotically towards this surface. Another difference is that the half ellipse in BBM extends down to, or even below, the point $p' = 0$, which means that isotropic swelling cannot be captured. This also means that there is no mechanism for the yield surface to *contract during isotropic swelling*. Attempt to address this has been made indirectly through the double porosity description in the BExM model (see Section 5.3). However, such a strain softening has been attributed to the macro voids, even at water saturated conditions. This in turn means that the division of the void space in micro and macro voids has to be defined (and calibrated) in order to describe the irreversible loops (shown in Figure 6-13), while a more obvious definition would be based on the fluid in each void type, i.e. water in micro voids and gas in macro voids. In contrast, isotropic swelling is intrinsically represented with the new model.

In addition, there are a number of features which should be fulfilled by any hydro-mechanical model of bentonite, but which, in several cases, are not for the existing models (BBM and BExM).

- The empirical data (e.g. Figure 6-1) shows that the description of stress paths (i.e. stress-strain relation) should address void ratio dependences. Parameter in the existing models however, (e.g. κ , λ , M) generally have no such dependences.

- Any description of bentonite should be able to represent suction (larger than zero) for water saturated specimen. This is generally not the case with existing models in which suction is associated with unsaturated conditions. The use of an independent retention curve also means that the same material property will be represented in three different ways in the same model (together with $e-\ln(p')$ and $e-\ln(s)$ relations)
- From the thermodynamic description of the chemical potential of the clay water, Equation 6-1, it can be shown that the clay potential (equivalent to $s + p'$) is the most relevant state variable (also for $s > 0$). This has only been adopted for the micro voids in BExM which means that only this model has a consistent representation of simple unloading or loading.

Finally, the new model with two bounding lines and a path variable can apparently mimic the main features of different tests, such as water retention measurements, homogenization tests, oedometer tests, and triaxial compression tests, for a wide range of dry densities, and with a quite limited set of parameters. Still, these parameters (Ψ_M ; $\Delta\Psi$; K) display some uncertainties, which calls for a more systematic quantification. This will probably have to involve new dedicated experiments.

Moreover, in order to address more complex geometries, it is of course of major interest to be able to implement the presented stress/strain relation in a FEM code. This should also include the relation between suction and the density of water, Equation 6-21, which could be overlooked in the calculations presented in Section 6.3 and 6.5. The presented model could possibly also be used as a core for a generalization of the approach to water unsaturated conditions.

A problem which hasn't been touched upon in this work is the question of the long-term stability of remaining heterogeneities.

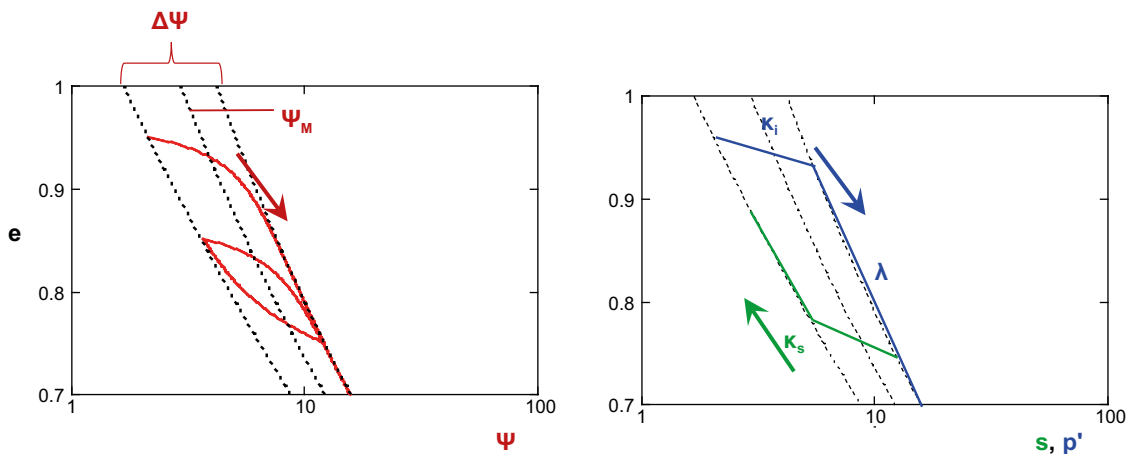


Figure 6-13. Schematic stress path in $e-\Psi$ (left) and similar paths in $e-s$ and $e-p'$ -planes with marked modules (right). Modules and path related to p' and s marked blue and green, respectively.

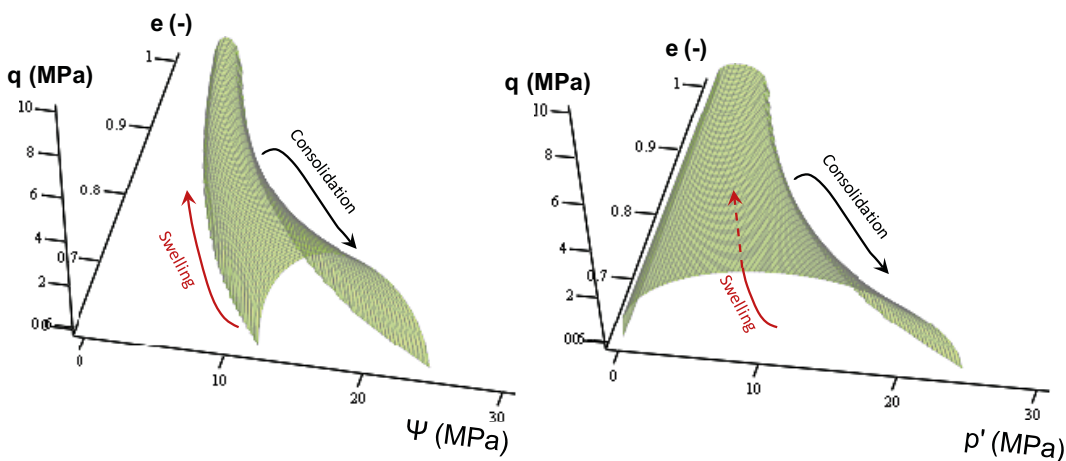


Figure 6-14. Yield surface in $q-\Psi-e$ space, tentatively based on clay potential functions and shear strength relation (left). BBM yield surface in $q-p'-e$ space (right).

References

SKB's (Svensk Kärnbränslehantering AB) publications can be found at www.skb.com/publications.

Alonso E E, Gens A, Josa A, 1990. Constitutive model for partially saturated soils. *Géotechnique* 40, 405–430.

Alonso E E, Vaunat J, Gens A, 1999. Modelling the mechanical behaviour of expansive clays. *Engineering Geology* 54, 173–183.

Birgersson M, Karnland O, Nilsson U, 2010. Freezing of bentonite. Experimental studies and theoretical considerations. SKB TR-10-40, Svensk Kärnbränslehantering AB.

Börgesson L, Johannesson L-E, Sandén T, Hernelind J, 1995. Modelling of the physical behaviour of water saturated clay barriers. Laboratory tests, material models and finite element application. SKB TR-95-20, Svensk Kärnbränslehantering AB.

Börgesson L, Sandén T, Andersson L, Johannesson L-E, Goudarzi R, Åkesson M, 2015. System design of Dome Plug. Preparatory modelling and tests of the sealing and draining components. SKB R-14-25, Svensk Kärnbränslehantering AB.

Börgesson L, Åkesson M, Birgersson M, Hökmark H, Hernelind J, 2016a. EBS TF – THM modelling. BM 1 – small scale laboratory tests. SKB TR-13-06, Svensk Kärnbränslehantering AB.

Börgesson L, Åkesson M, Kristensson O, Dueck A, Hernelind J, 2016b. EBS TF – THM modelling. BM 2 – Large scale field tests. SKB TR-13-07, Svensk Kärnbränslehantering AB.

Dueck A, 2004. Hydro-mechanical properties of a water-unsaturated sodium bentonite: laboratory study and theoretical interpretation. PhD thesis. Lund University.

Dueck A, Nilsson U, 2010. Thermo-hydro-mechanical properties of MX-80. Results from advanced laboratory tests. SKB TR-10-55, Svensk Kärnbränslehantering AB.

Dueck A, Börgesson L, Johannesson L-E, 2010. Stress-strain relation of bentonite at undrained shear. Laboratory tests to investigate the influence of material composition and test technique. SKB TR-10-32, Svensk Kärnbränslehantering AB.

Dueck A, Goudarzi R, Börgesson L, 2011a. Buffer homogenisation, status report. SKB TR-12-02, Svensk Kärnbränslehantering AB.

Dueck A, Johannesson L-E, Kristensson O, Olsson S, 2011b. Report on hydro-mechanical and chemical-mineralogical analyses of the bentonite buffer in Canister Retrieval Test. SKB TR-11-07, Svensk Kärnbränslehantering AB.

Dueck A, Goudarzi R, Börgesson L, 2014. Buffer homogenisation, status report 2. SKB TR-14-25, Svensk Kärnbränslehantering AB.

Dueck A, Goudarzi R, Börgesson L, 2016. Buffer homogenisation. Status report 3. SKB TR-16-04, Svensk Kärnbränslehantering AB.

Karnland O, Sandén T, Johannesson L-E, Eriksen T E, Jansson M, Wold S, Pedersen K, Motamedi M, Rosborg B, 2000. Long term test of buffer material. Final report on the pilot parcels. SKB TR-00-22, Svensk Kärnbränslehantering AB.

Karnland O, Olsson S, Nilsson U, 2006. Mineralogy and sealing properties of various bentonites and smectite-rich clay materials. SKB TR-06-30, Svensk Kärnbränslehantering AB.

Karnland O, Olsson S, Dueck A, Birgersson M, Nilsson U, Hernan-Håkansson T, Pedersen K, Nilsson S, Eriksen T E, Rosborg B, 2009. Long term test of buffer material at the Äspö Hard Rock Laboratory, LOT project. Final report on the A2 test parcel. SKB TR-09-29, Svensk Kärnbränslehantering AB.

Åkesson M, Börgesson L, Kristensson O, 2010a. SR-Site data report. THM modelling of buffer, backfill and other system components. SKB TR-10-44, Svensk Kärnbränslehantering AB.

Åkesson M, Kristensson O, Börgesson L, Dueck A, Hernelind J, 2010b. THM modelling of buffer, backfill and other system components. Critical processes and scenarios. SKB TR-10-11, Svensk Kärnbränslehantering AB.

Task 1 Basic tests for model development – task description and results

A1.1 Swelling tests

A1.1.1 General

Swelling of water saturated bentonite specimens with access to water will be modelled for the following three test geometries, illustrated in Figure A1-1:

- Axial swelling in a device with constant radius and limited height. Variation of the height of the gap. (A = axial swelling.)
- Radial swelling of the outer surface in a device with constant height and limited radius. Variation of the radial gap. (Ro = radial outwards swelling.)
- Radial swelling into a cylindrical cavity in a device with constant height and radius. Variation of the radius of the cavity. (Ri = radial inwards swelling.)

These tests are performed in swelling pressure devices, shown in next section.

The tests are mainly done with free swelling surfaces, i.e. no counteracting force until the swelling bentonite gel has reached the outer limited surface. The friction is minimized by use of mineral-oil based lubricant on relevant surfaces.

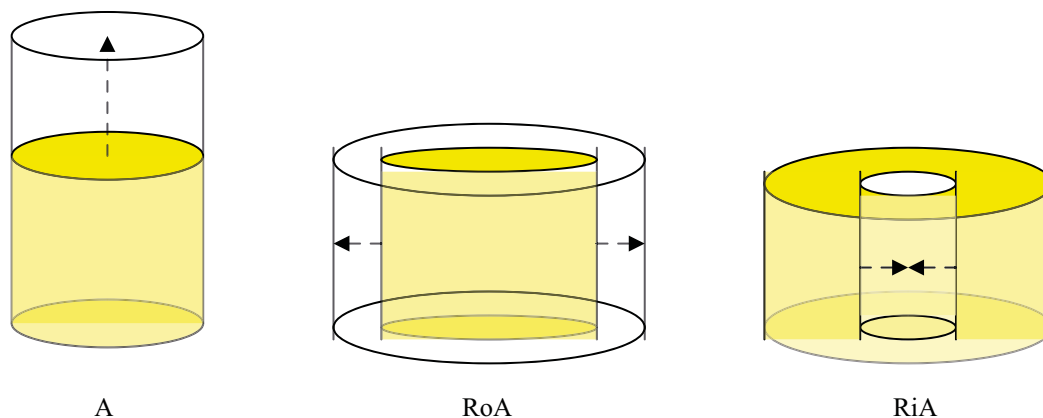


Figure A1-1. Illustration of the geometry of the test types carried out.

A1.1.2 Equipment

The three different types of test were carried out in devices with the design shown in Figure A1-2 to Figure A1-4.

The device used for the axial swelling consists of a steel ring surrounding the specimen having filters on both sides. Two pistons are placed vertically, in the axial direction, above and below the specimen. For both types of radial swelling a device, which consists of a steel ring surrounding the specimen equipped with a radial filter, is used. A piston is placed vertically, in the axial direction, above the specimen. A small horizontal radial piston is placed in a hole through the steel ring and the radial filter for measurement of the radial total stress.

In both types of device the bottom and top plates and the steel ring are bolted together to keep the volume constant. Two load cells are placed in the vertical and radial direction, respectively. The load cells are placed between a fixed plate and a movable piston where the small deformation required by the load cell is admitted. During the entire course of the tests the forces are measured by the load cells, which are calibrated prior to and checked after each test. By dividing the measured force by the surface area the total stress can be calculated.

A1.1.3 Preparation of specimen

Cylindrical specimens are prepared by compaction of powder to a certain density. The dimension of the specimens used for the axial type of swelling is a diameter of 50 mm and a height of 20 mm. For the radial types of swelling the diameter is 46.8 mm and the height 40 mm.

A1.1.4 Test procedure

The tests consist of two phases; the water saturation phase and the swelling phase. After mounting the specimen in one of the devices shown in Figure A1-2 to Figure A1-4, de-ionized water is applied to the filters after air evacuation of the filters and tubes. The specimens have free access to water during the water saturation. When only small changes in swelling pressure with time are noticed the water is evacuated from the filters and tubes and the second phase i.e. the swelling starts. Depending on the type of swelling the following measures are taken;

- For the axial swelling (A) the upper piston is moved upwards and fixed with spacers admitting a certain volume for the swelling. After evacuation of air, the empty space and the upper filter are filled with water.
- For the radial swelling of the outer surface (Ro) the water saturated specimen is taken out and an outer volume is cut off the circumference of the specimen leaving a certain volume for swelling after re-mounting it in the same device. After evacuation of air the filter and empty space are filled with water.
- For the radial swelling of an inner cavity (Ri) the lower lid is opened and a cylindrical volume drilled out from the center of the specimen. The cavity and filter are then filled with water.

After finished swelling and homogenization, i.e. when no or negligibly small changes are noticed in the swelling pressure with time, the specimen is dismantled and cut in slices for determination of the water content and density distribution in the direction of swelling.

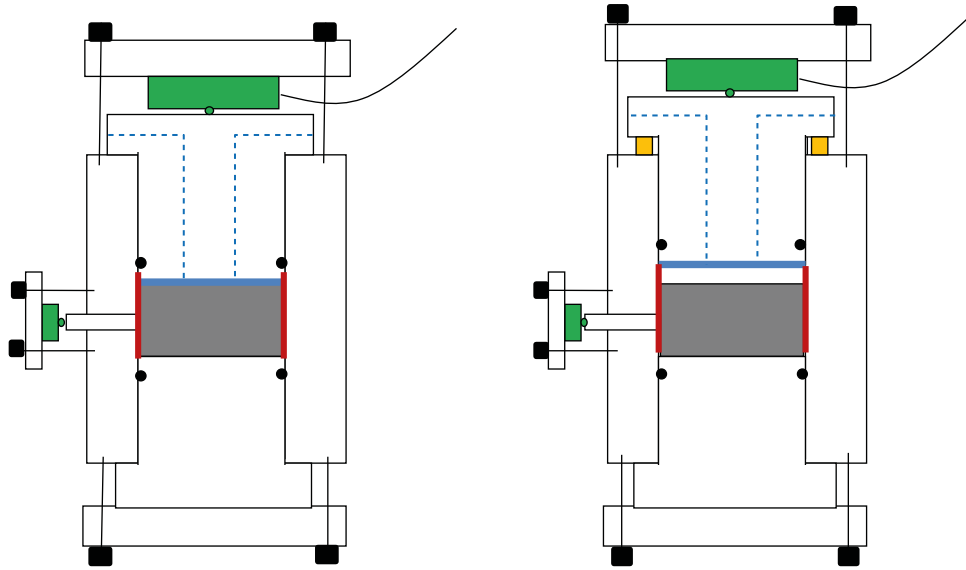


Figure A1-2. Set-up used for the axial swelling tests (A). The red lines represent the lubricated surfaces and the blue lines represent filters and water supply. The radial pressure transducer is placed 10 mm from the bottom end of the specimen.

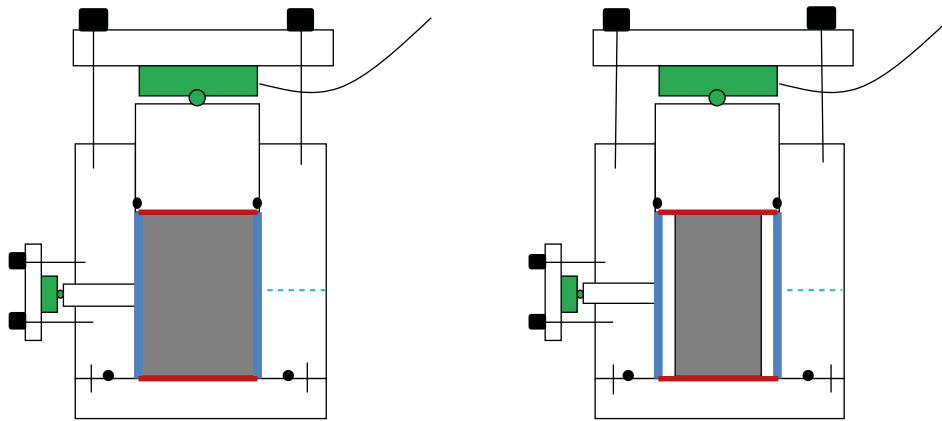


Figure A1-3. Set-up used for the radial outward swelling tests (Ro). The red lines represent the lubricated surfaces and the blue lines represent filters and water supply. The radial pressure transducer is placed 20 mm from the bottom end of the specimen.

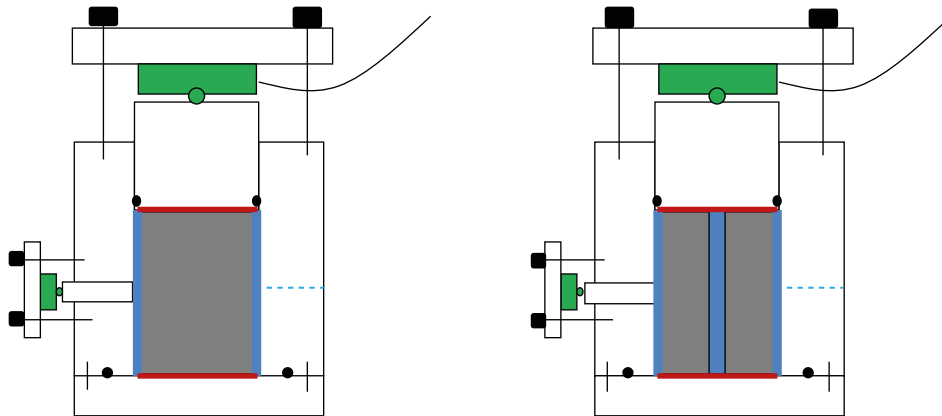


Figure A1-4. Set-up used for the inward radial swelling tests (Ri). The red lines represent the lubricated surfaces and the blue lines represent filters and water supply. The radial pressure transducer is placed 20 mm from the bottom end of the specimen.

A1.1.5 Material

The material used in the test series is MX-80 bentonite powder. The powder is delivered with a water content of about 12 %. The bentonite powder is compacted to specimen with intended density in compaction devices before installation.

For the determination of void ratio and degree of saturation the particle density $\rho_s = 2\,780\text{ kg/m}^3$ and water density $\rho_w = 1\,000\text{ kg/m}^3$ are been used.

A1.2 Modelling tasks

A1.2.1 Task 1

The following modelling tasks are proposed for Task 1.

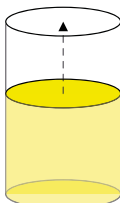
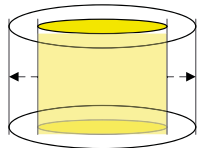
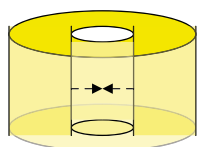
Modelling of the three test types, using specimen with the same history and initial conditions as the test specimen.

- Compaction conditions:
 - Compaction pressure 35.6 MPa
 - $w \approx 12\%$
- Water saturation under constant volume conditions.
- Initial conditions after water saturation:
 - $e = 0.68$ (void ratio)
 - $\rho_d = 1\,655\text{ kg/m}^3$ (dry density)
 - $\rho_m = 2\,060\text{ kg/m}^3$ (density after water saturation)
 - $S_r = 100\%$ (degree of water saturation)

Modelling cases

Two different degree of swelling at each test type will be modeled. Table A1-1 shows the modelling cases.

Table A1-1. Modelling cases.

Model	Swelling	Initial height (mm)	Final height (mm)	Initial diameter (mm)	Final diameter (mm)	Comment Inner hole radius (mm)	
A1 A2	25 % 40 %	20	25 28	50	50		
Ro1 Ro2	15 % 30 %	40	40	43.6 41.0	46.8		
Ri1 Ri2	5 % 20 %	40	40	46.8	46.8	$r_i = 5.25$ $r_i = 9.5$	

Requested results:

For each model the following results are requested:

History plots of

- total axial stress, and
- total radial stress,

at the location of the transducer.

Paths (variable plotted as function of the axial (tests A) or radial (tests Ro and Ri) distance) at different times of

- void ratio,
- pore pressure,
- total axial stress,
- total radial stress.

Mises stress versus average stress (stress path) at nodes along a path.

Contour plots at different times of

- void ratio,
- pore pressure,
- total axial stress,
- total radial stress.

A1.3 Results to be compared with

Tests with the configuration and test conditions described above and specified in Table A1-1 have been performed. The results are compiled in this chapter. Some additional tests and results, which can also be used for model check and model calibration, are also shown.

The exact geometries and densities are not in complete agreement with the task description but are anyhow considered to be within the acceptable range of accuracy, considering scatter that always is present at such tests. However, it is of course free for the modellers to adapt the measured conditions instead of the given ones.

A1.3.1 Axial swelling

The axial swelling test results are summarized in Table A1-2.

Table A1-2. End of test results for series A (axial swelling).

Test number		Dry density (kg/m ³)	Axial stress (kPa)	Radial stress (kPa)	Swelling (%)
A00 (A01-12)	Before	1655	9629	12600	0
	After	1591	5976	8436	4.3 (4.0)
A0 (A01-13)	Before	1655	8604	9994	0
	After	1449	2566	3240	14.3 (14.2)
A1 (A01-9)	Before	1655	8783	9915	0
	After	1319	1333	1716	26.1 (25.5)
A2 (A01-10)	Before	1656	9631	9698	0
	After	1204	771	775	38.1 (37.5)

Tests A1 and A2 refer to the suggested modelling cases. The test numbers within parenthesis are local numbers referred to in the figures.

Figures A1-5 and A1-6 show the distribution of dry density and degree of water saturation measured after dismantling.

Figure A1-7 shows the radial and axial stress evolution with time.

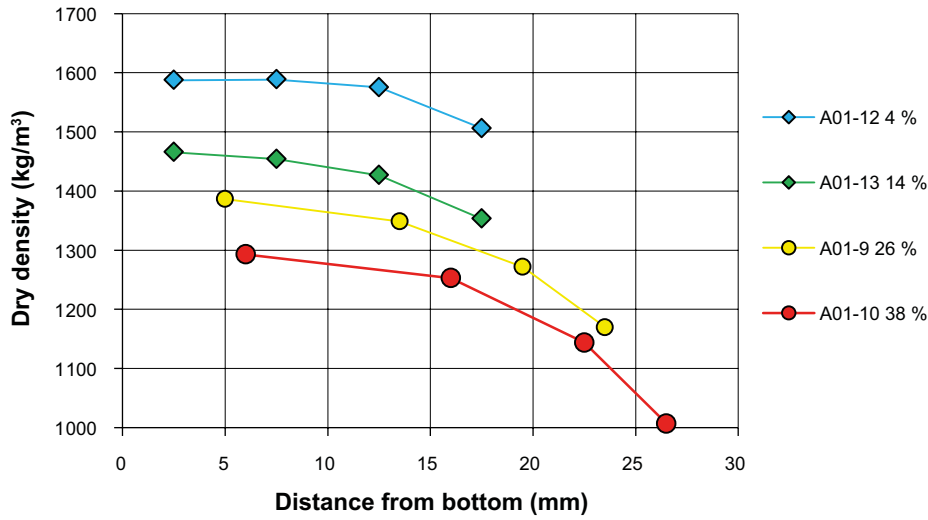


Figure A1-5. Density distribution after dismantling of the axial swelling tests.

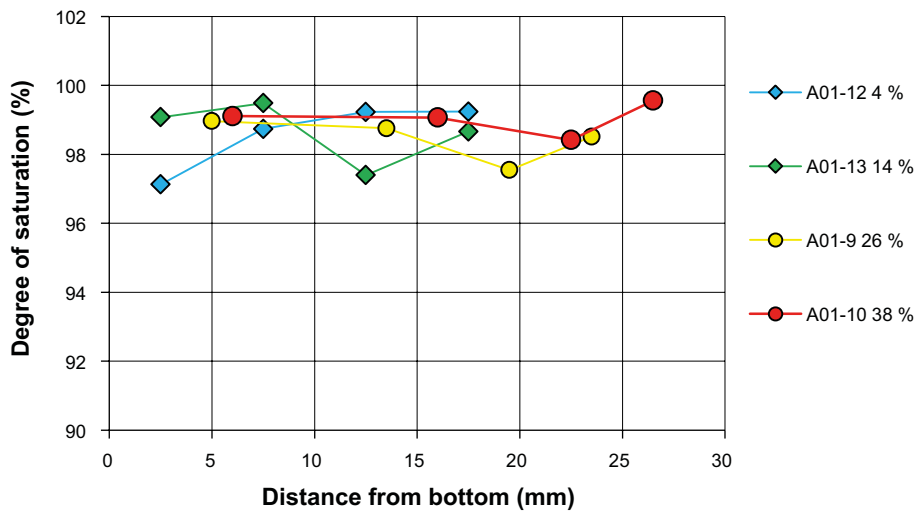


Figure A1-6. Distribution of degree of water saturation after dismantling of the axial swelling tests.

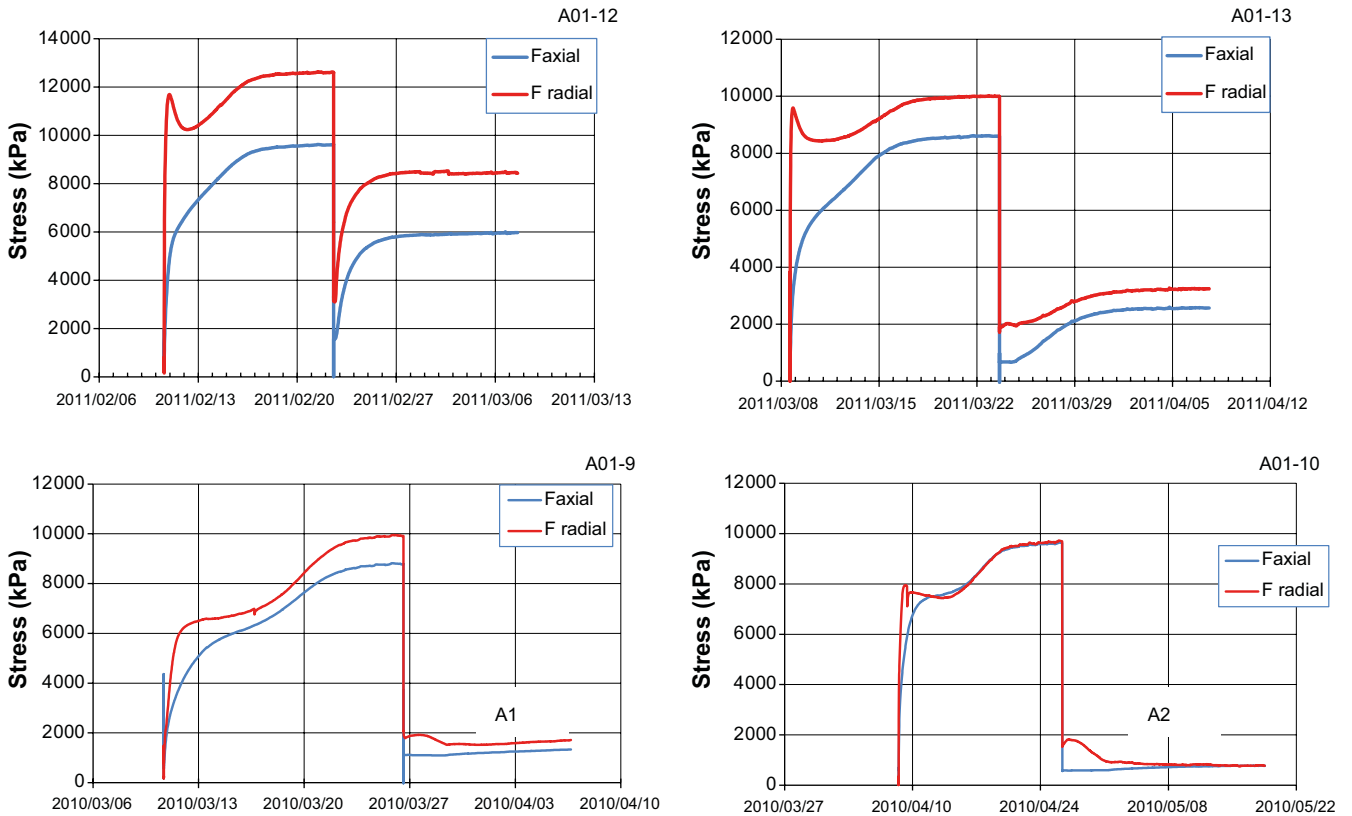


Figure A1-7. Evolution of measured axial and radial stress for axial swelling.

A1.3.2 Radial outwards swelling

The test results after radial outwards swelling are summarized in Table A1-3.

Table A1-3. End of test results for series Ro (radial outwards swelling).

Test number		Dry density (kg/m ³)	Axial stress (kPa)	Radial stress (kPa)	Swelling (%)
Ro1 (R11-18)	Before	1655	11979	9926	0
	After	1401	3077	2683	14.2 (18.1)
Ro2 (R11-19)	Before	1655	12857	10565	0
	After	1255	383	182	31.6 (31.9)

The test numbers within parenthesis are local numbers referred to in the figures.

Figures A1-8 and A1-9 show the distribution of dry density and degree of water saturation measured after dismantling.

Figure A1-10 shows the radial and axial stress evolution with time.

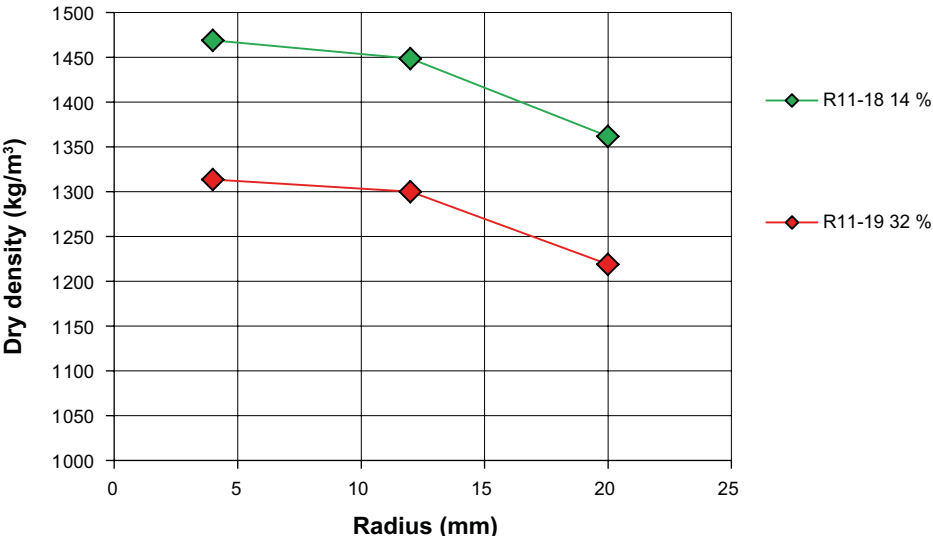


Figure A1-8. Density distribution after dismantling of the tests with radial outwards swelling.

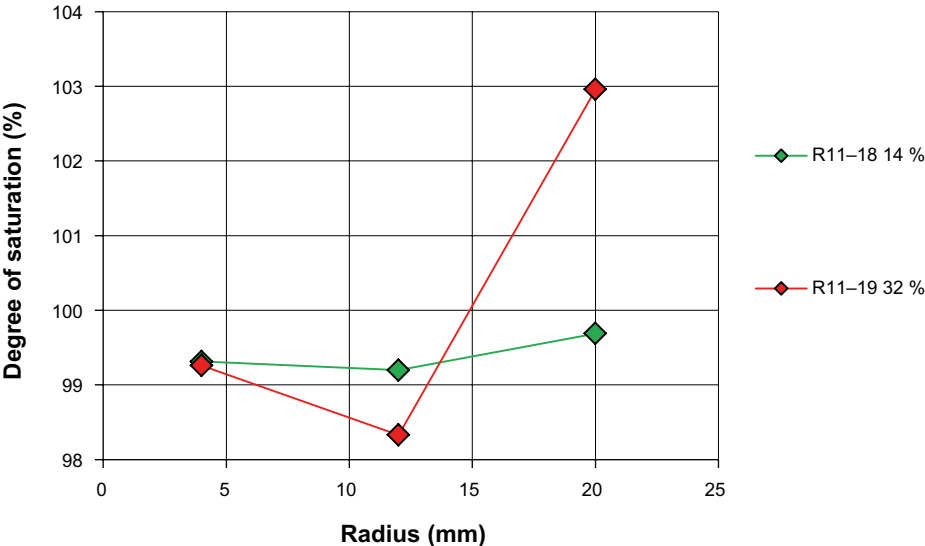


Figure A1-9. Distribution of degree of water saturation after dismantling of the tests with radial outwards swelling.

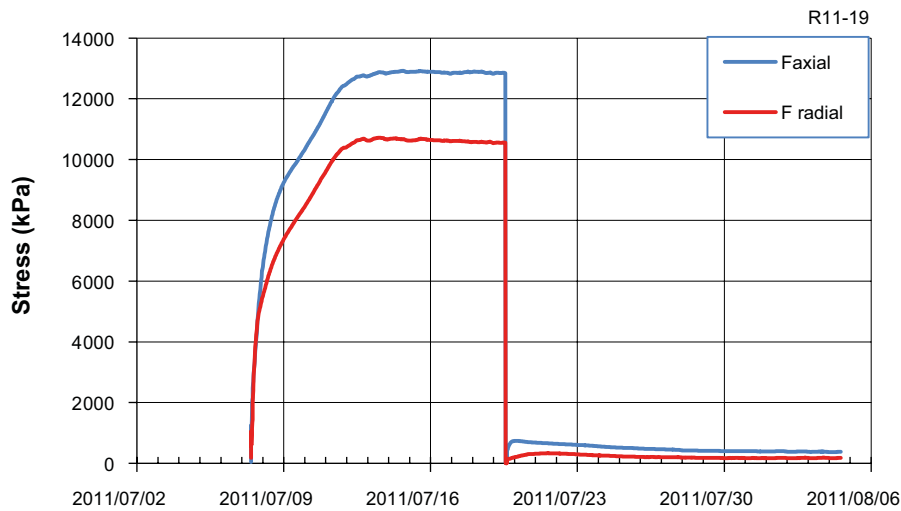
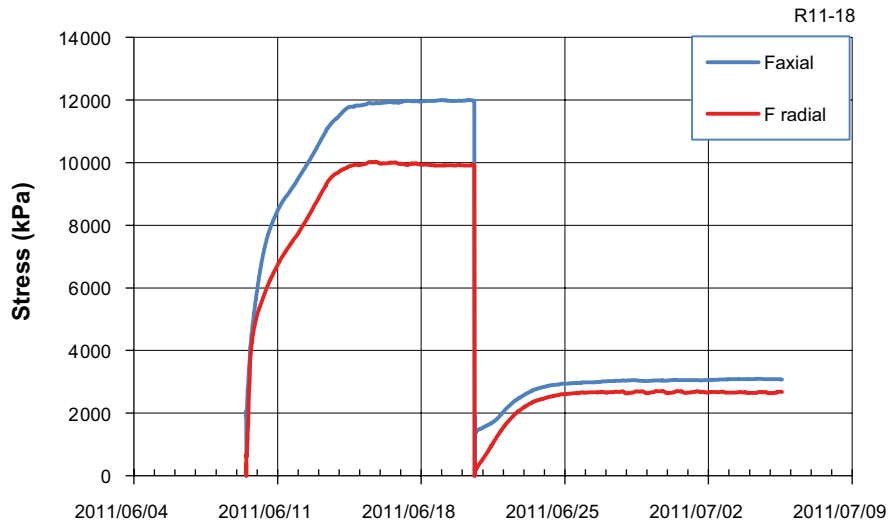


Figure A1-10. Evolution of measured axial and radial stress for radial outwards swelling.

A1.3.3 Radial inwards swelling

The test results at radial inwards swelling are summarized in Table A1-4.

Table A1-4. End of test results for series A (axial swelling).

Test number		Dry density (kg/m ³)	Axial stress (kPa)	Radial stress (kPa)	Swelling (%)
Ri0	Before	1655	12048	11355	0
(R21-11)	After	1596	8015	7607	3.0 (3.8)
Ri1	Before	1655	12017	9863	0
(R21-9)	After	1588	6799	6497	5.3 (4.2)
Ri2	Before	1655	11856	13818	0
(R21-10)	After	1345	2366	1692	19.7 (23.0)
Ri3	Before	1655	11472	10104	0
(R21-12)	After	1256	1727	1477	31.8 (31.8)

Tests Ri1 and Ri2 refer to the suggested modelling cases. The test numbers within parenthesis are local numbers referred to in the figures.

Figures A1-11 and A1-12 show the distribution of dry density and degree of water saturation measured after dismantling.

Figure A1-13 shows the radial and axial stress evolution with time.

A1.3.4 Comments

Measured swelling pressures in all tests shown in this task description are compiled in Figure A1-14. The values are mainly between the relation proposed by Börgesson et al. (1995) and the relation proposed by Åkesson et al. (2010a). However the results at the density 1255 kg/m³ deviate from the trend and from those references.

The tests with deviating results are test Ri3 (circular legend and slightly too high pressure), which is not a modelling task, and especially test Ro2 (triangles and too low pressure), which is a modelling task. It is recommended to be careful with using these results. Additional tests will be performed.

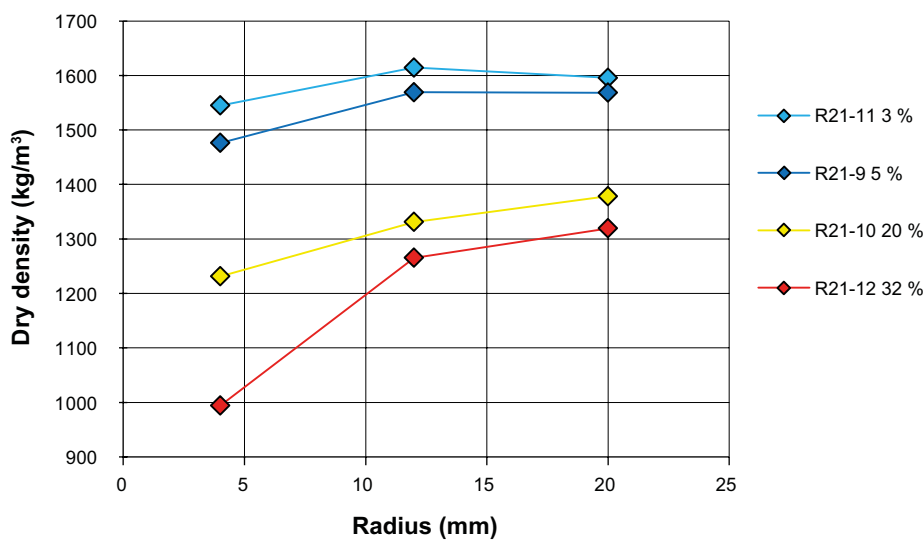


Figure A1-11. Density distribution after dismantling of the tests with radial inwards swelling.

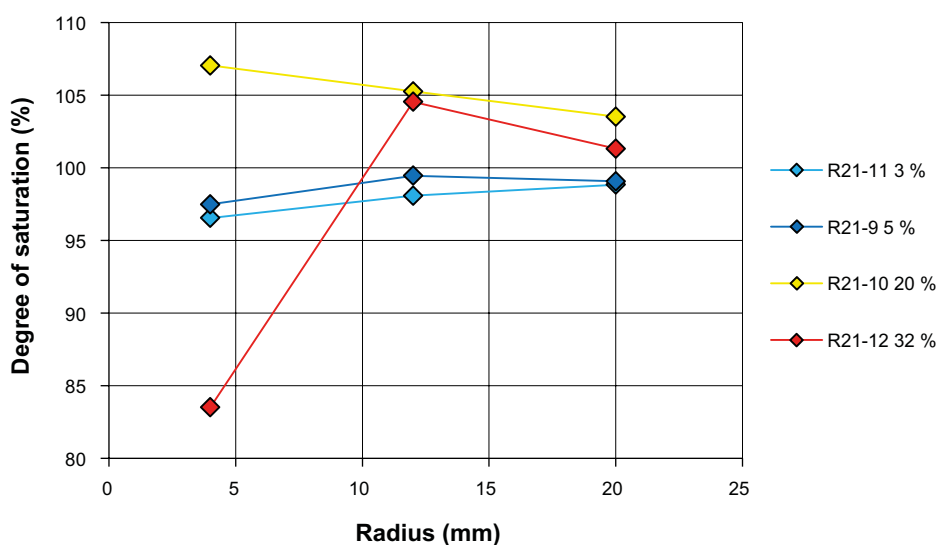


Figure A1-12. Distribution of degree of water saturation after dismantling of the tests with radial inwards swelling.

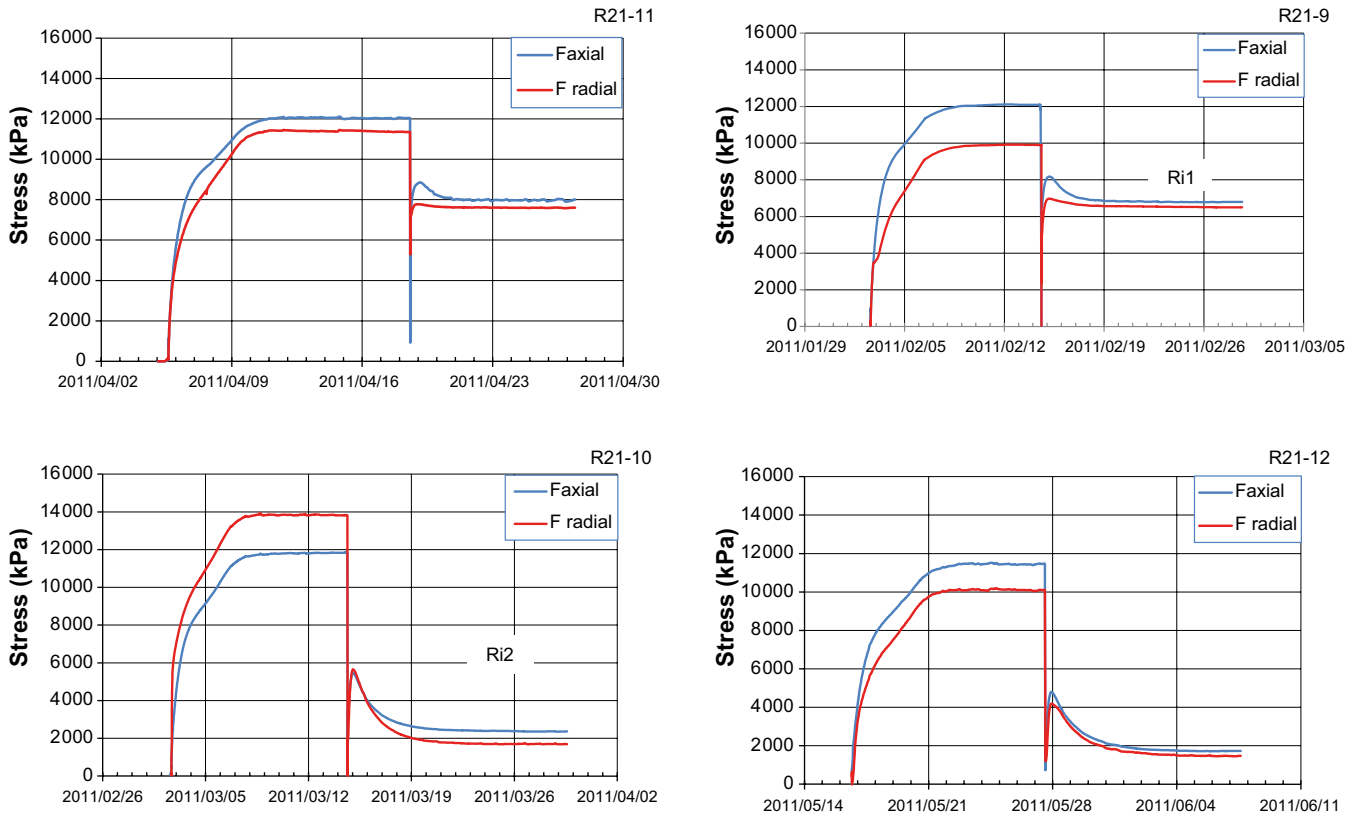


Figure A1-13. Evolution of measured axial and radial stress for the tests with radial outwards swelling.

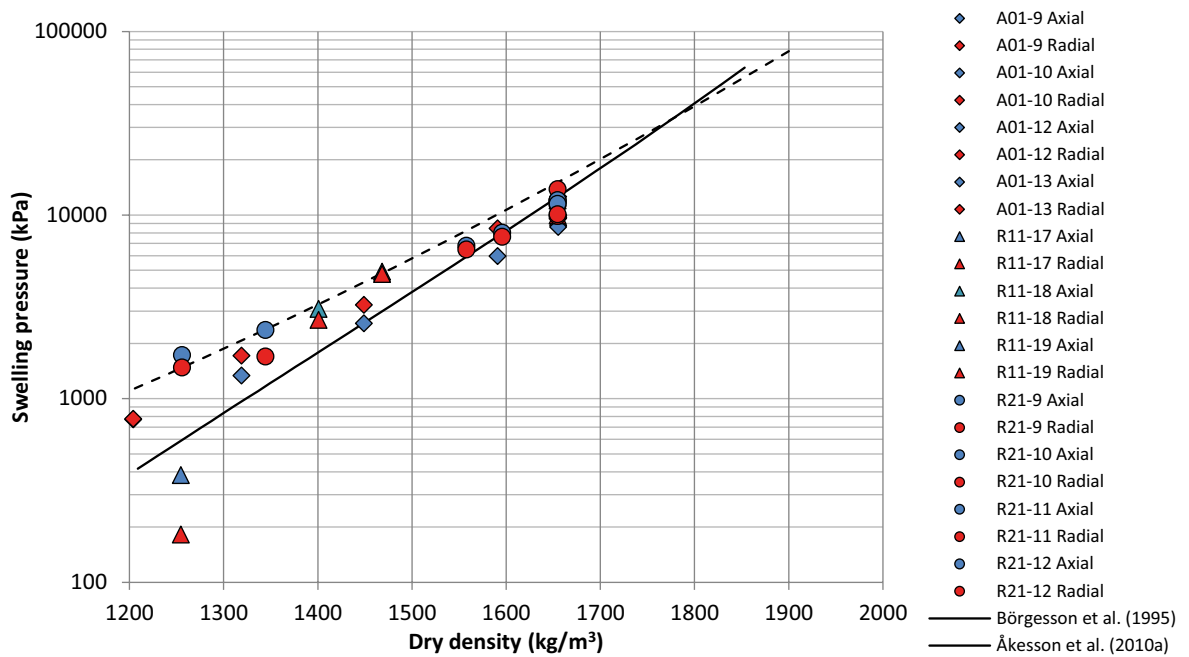


Figure A1-14. Compilation of measured swelling pressure. The values at the dry density 1655 kg/m^3 are before swelling. All other data refer to after swelling.

Task 1 HR tests – additional tests with high resolution, descriptions and results

A2.1 Fundamental swelling tests with high resolution

In the High Resolution (HR) series the same type of tests as in the basic series were run. The main difference between the two series was the size of the specimens where the larger specimens in the HR-series admitted higher resolution in the distribution of base variables over the specimens.

As in the basic series swelling is studied in three series; axial swelling (HR-A), radial outward swelling (HR-Ro) and radial inward swelling (HR-Ri). As in the basic series the tests are mainly done with free swelling surfaces, i.e. no counteracting force until the swelling bentonite gel had reached the outer limited surface. In all tests the friction was minimized by use of a mineral-oil based lubricant on relevant surfaces.

A2.1.1 Equipment

The three different types of test are carried out in devices with the design shown in Figures A2-1 to A2-3. The devices consist of a steel ring surrounding the specimen. A movable piston is placed vertically, in the axial direction above the specimen. Radial pistons are placed in holes through the steel ring for measurement of radial forces.

In the device used for the axial swelling a steel filter is placed on the upper side of the sample while in case of radial swelling a radial plastic filter is placed between the surrounding steel ring and the specimen.

The bottom and top plates and the steel ring are bolted together to keep the volume constant. Load cells are placed in the vertical and radial directions. The load cells are placed between a fixed plate and the movable piston where the small deformation required by the load cell is admitted. During the entire course of the tests the forces are measured by the load cells which are calibrated prior to, and checked after, each test.

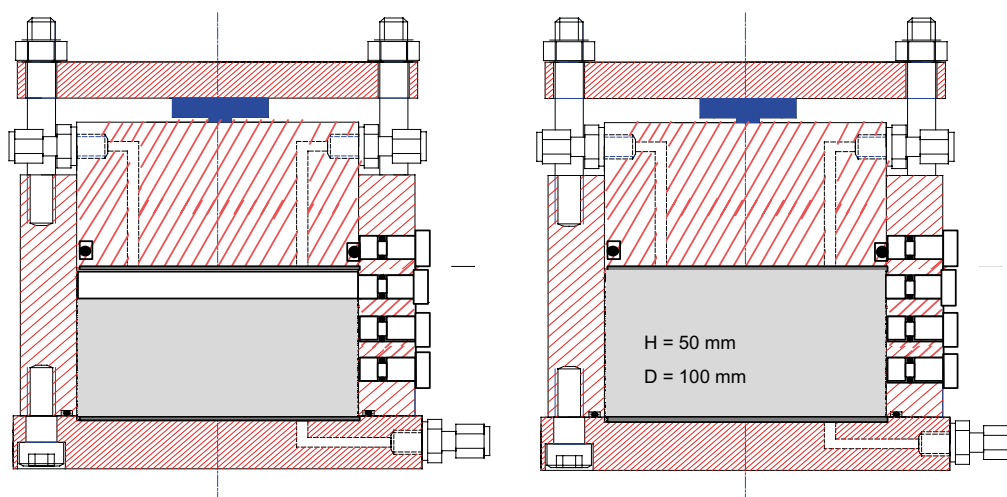


Figure A2-1. Set-up used for the axial swelling tests (HR-A). Water is only supplied from a filter placed above the specimen.

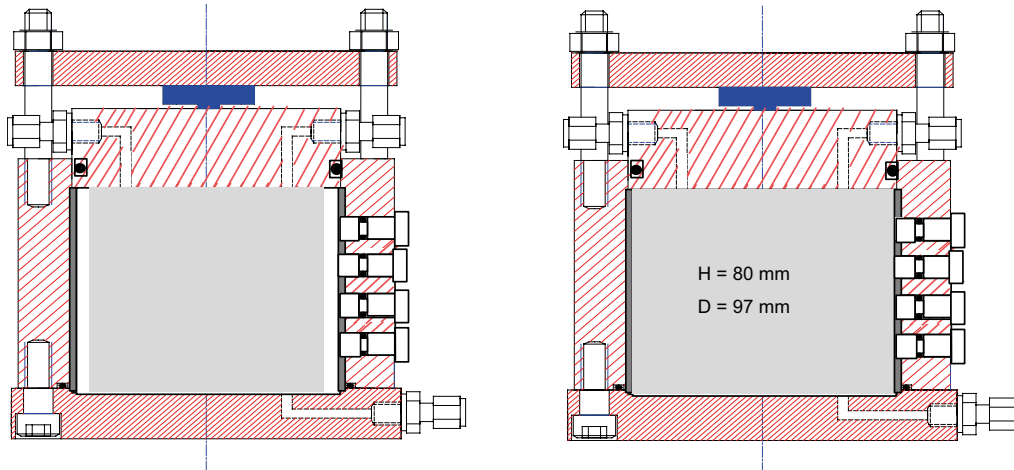


Figure A2-2. Set-up used for the radial outward swelling tests (HR-Ro). Water is supplied from a radial filter between the surrounding steel ring and the specimen.

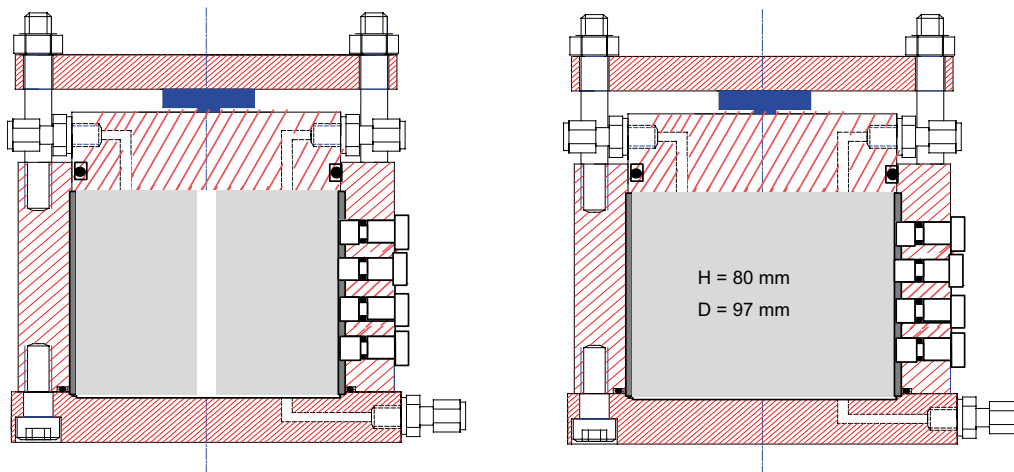


Figure A2-3. Set-up used for the inward radial swelling tests (HR-Ri). Water is initially filled into the cavity and then only supplied from a radial filter between the surrounding steel ring and the specimen.

A2.1.2 Preparation of specimens

The specimens are sawn and trimmed from larger blocks with the initial water content 24 %. The initial height and diameter for the specimens swelling axially are 40 mm and 100 mm, respectively and for the specimens swelling radially the initial height and diameter are 80 mm and 97 mm, respectively.

A2.1.3 Test procedure

In the HR-series the initial degree of saturation is very high (close to 100 %) and for that reason the swelling started directly, i.e. no saturation took place in the test devices before the swelling phase. After preparation the specimens are mounted into one of the devices shown in Figures A2-1 to A2-3 and de-ionized water is applied to the filters after air evacuation of the filters and tubes. After completed swelling and homogenization, i.e. when no or negligibly small changes were noticed in the measured swelling pressure, the specimens are dismantled and cut in slices for determination of water content and density distribution in the direction of swelling.

A2.1.4 Evaluation of test results

The test results are presented with w , ρ_d and S , as a function of the specimen height (series HR-A) or radius (series HR-Ro and HR-Ri), i.e. as distribution in the direction of swelling. The measured stresses are also shown and compared with a model of swelling pressure presented by Börgesson et al. (1995). The swelling ratio s is calculated according to Equation A2-1 where V_i , V_f , ρ_{di} and ρ_{df} are the initial volume, final volume, initial dry density and final dry density, respectively.

$$s = \frac{\Delta V}{V_i} = \frac{V_f}{V_i} - 1 = \frac{\rho_{di}}{\rho_{df}} - 1 \quad (\text{A2-1})$$

A2.1.5 Test series

Test series with different types of swelling, one type of axial swelling and two types of radial swelling, are planned and so far two tests have been run.

A2.2 Measurements of friction between buffer and other surfaces

Friction between confined specimens at saturation and different types of surfaces is studied with a new test set-up.

A2.2.1 Equipment

The tests are carried out in the device shown in the schematic in Figure A2-4. The swelling pressure device, used during saturation, consists of a steel ring surrounding the specimen having filters on both sides. The inner surface of the ring can be prepared in different ways for example with or without lubrication. Two pistons are placed vertically, in the axial direction, above and below the specimen. A radial piston is placed in a hole through the steel ring for measurement of the radial force.

The bottom and top plates are bolted together to keep the volume constant. Three load cells are used to measure the swelling pressure, two in the vertical direction and one in the radial direction. Each load cell is placed between a fixed plate and a movable piston where the small deformation required by the load cell is admitted. At shearing a third load cell and a deformation transducer are installed for measuring force and deformation in the axial direction. The transducer and load cells are calibrated prior to, and checked after, each test.

A2.2.2 Preparation of specimen

Cylindrical specimens are prepared by compaction of powder to a prescribed density. The specimens have a diameter of 50 mm and a height of 20 mm.

A2.2.3 Test procedure

The tests consist of two phases; the water saturation and the shearing phase. The entire tests are done at constant volume conditions. The saturation starts by mounting the specimen in the swelling pressure device (Figure A2-4, left) and applying de-ionized water to the filters after air evacuation of the filters and tubes. When only small change in measured swelling pressure is noticed the friction phase starts.

During the friction phase the swelling pressure device is placed in a load frame (Figure A2-4, right) where the ring is fixed while the specimen is moved upwards with a constant rate, i.e. the specimen is pushed through the ring. During this phase the required force to keep the ring in place as well as the deformation and swelling pressure are measured. The specimen has free access to water during both the saturation and the subsequent friction phase. After moving the ring a distance similar to the height of the specimen the test is finished and the bentonite specimen is dismantled. The distribution of water content and density over the specimen height are then determined.

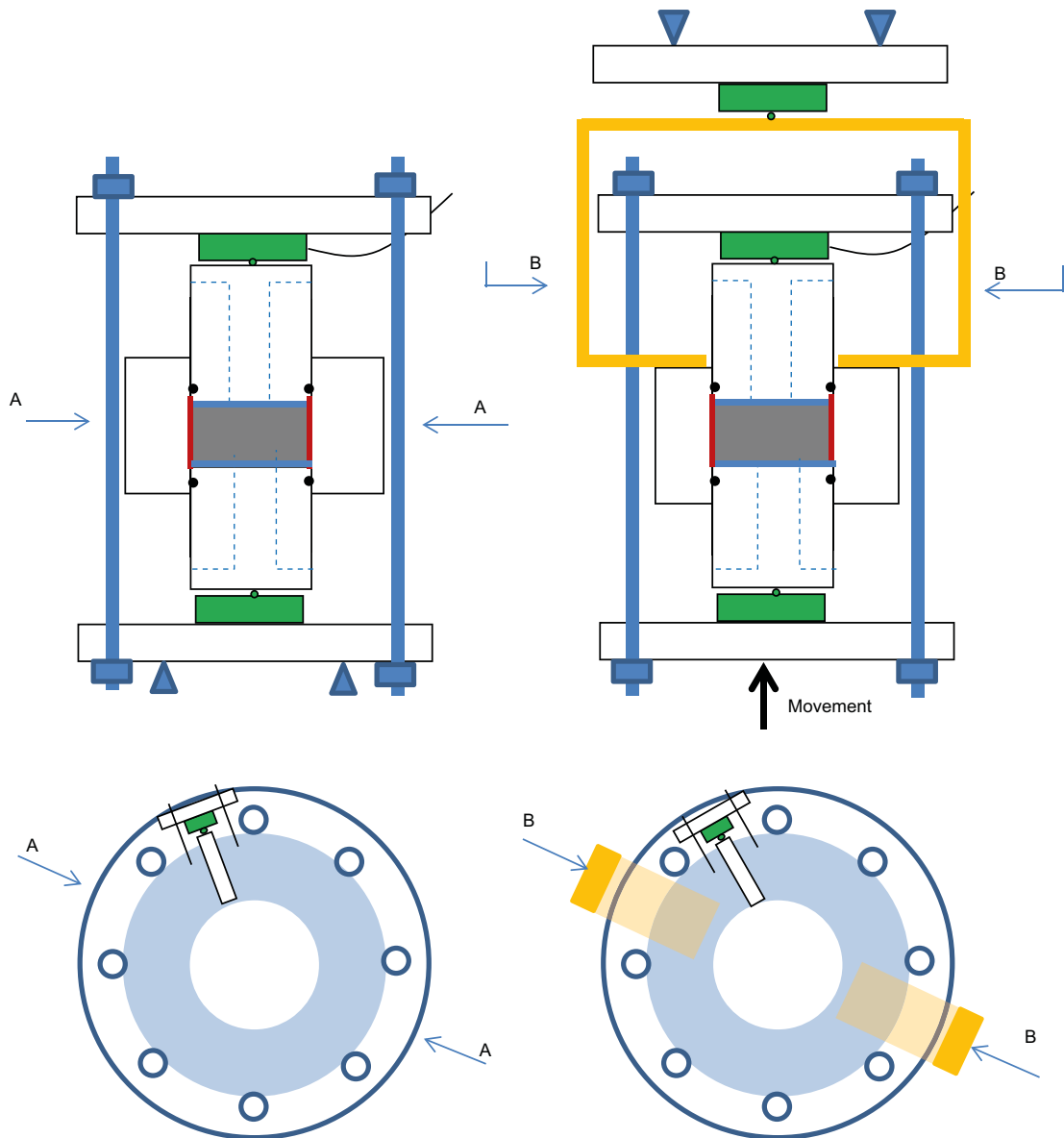


Figure A2-4. Set-up used for the study of friction between buffer and other surfaces. The set-up used during saturation (left) and during shearing (right).

A2.2.4 Evaluation of test results

The friction is evaluated from Equation A2-2 where F is the measured force from the upper load cell, A_s is the surface area of the specimen, P_r is the radial stress perpendicular to the ring, and δ is the friction angle between the ring and the bentonite specimen. The swelling pressure and friction angle are presented with average values of w , ρ_d and S_r over the specimens.

$$F = A_s \cdot P_r \cdot \tan(\delta) \quad (\text{A2-2})$$

A2.2.5 Test series

The specimens are saturated with a minimum of swelling and the tests are run with and without lubricant on the inner surface of the ring, surrounding the specimen.

A2.3 Results from the fundamental tests with high resolution

In the diagrams with results the labels include the swelling in %. The swelling ratio is calculated from the initial and final dry densities. The swelling ratio is also given as swelling after saturation (given in brackets in the tables) calculated from height before and after the swelling. The difference between the values is mainly caused by a small scatter in the initial density, swelling between the saturation phase and swelling phase and swelling at dismantling.

A2.3.1 Axial swelling

In the series with axial swelling in the high resolution series so far one test has completed, Table A2-1. In Figure A2-5 to A2-7 the distribution of w , ρ_d and S_r measured after termination of the test are shown. The results are shown with comparable test results from the basic series.

Table A2-1. Specimens used in the series HR-A.

	Initial w (%)	Initial ρ_d (kg/m ³)	Constant radius (mm)	Initial height (mm)	Final height (mm)	Swelling ¹ $\rho_{d1}/\rho_{d0}-1$ (%)	Remarks
HR-A1	23.7	1 666	100	40	50	32 (26)	

¹ Swelling after saturation, in brackets, calculated from measured diameters and calculated as change in volume to initial volume.

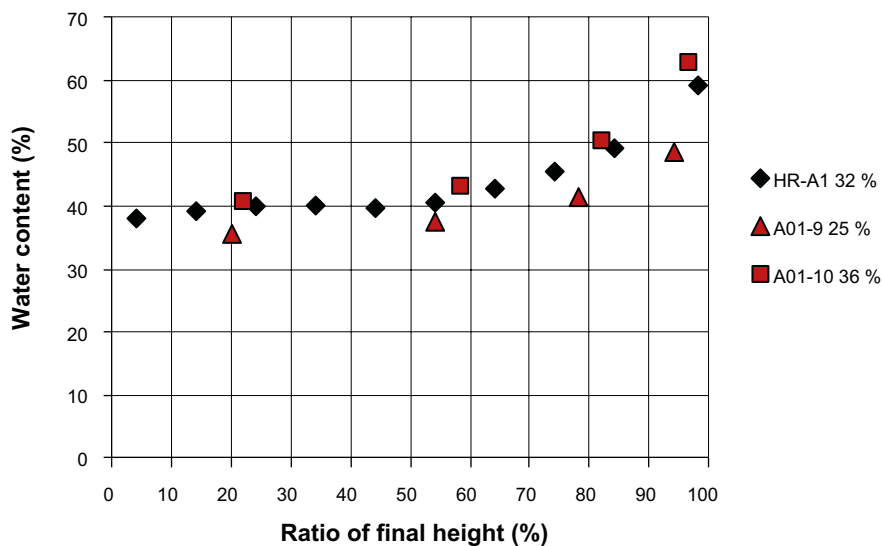


Figure A2-5. Distribution of water content over specimen height, from bottom end surface. Result from HR-A1 is shown with results from the basic series; A01-9 and A01-10.

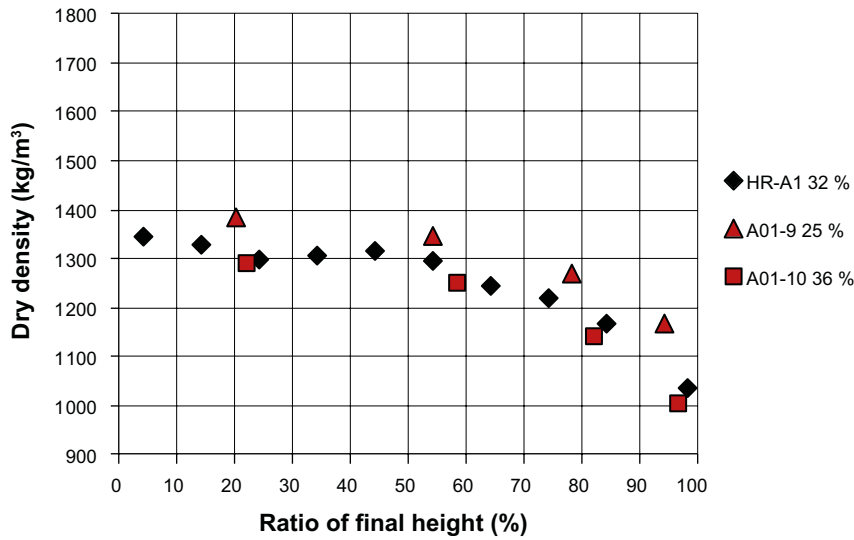


Figure A2-6. Distribution of dry density over specimen height, from bottom end surface. Result from HR-A1 is shown with results from the basic series; A01-9 and A01-10.

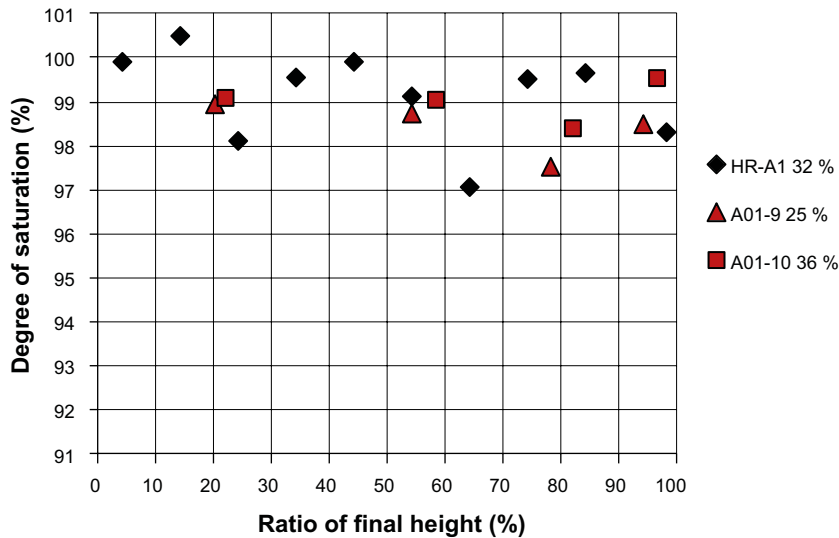


Figure A2-7. Distribution of degree of saturation over specimen height, from bottom end surface. Result from HR-A1 is shown with results from the basic series.

The time evolution of the swelling pressure is shown in Figure A2-8. In Figure A2-9 the final swelling pressure is plotted as a function of dry density. The radially measured swelling pressures from test HR-A1 are plotted with the dry densities measured at the corresponding distances from the bottom surface. The axial swelling pressure from test HR-A1 is plotted with the average dry density and an error bar corresponding to the maximum and minimum dry density over the specimen height. In addition, results from the basic test series are shown.

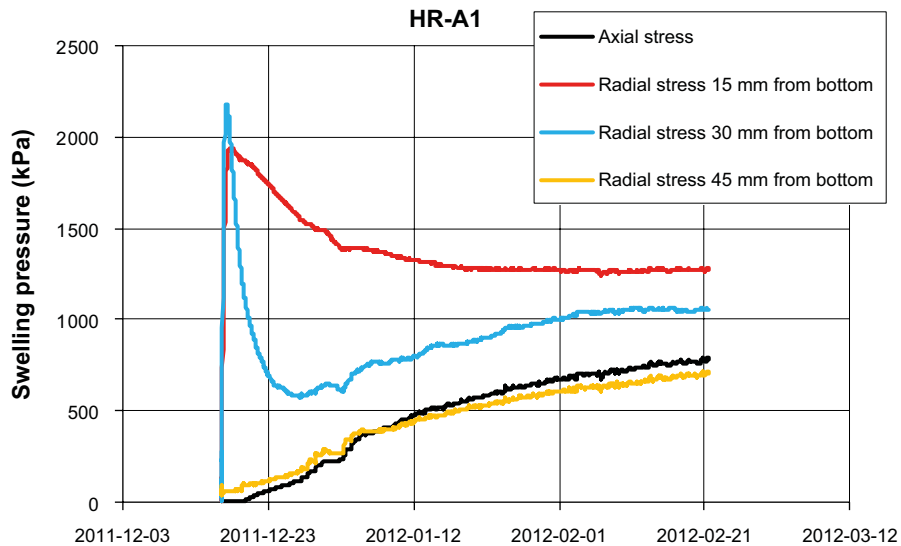


Figure A2-8. Time evolution of the swelling pressure from test HR-A1.

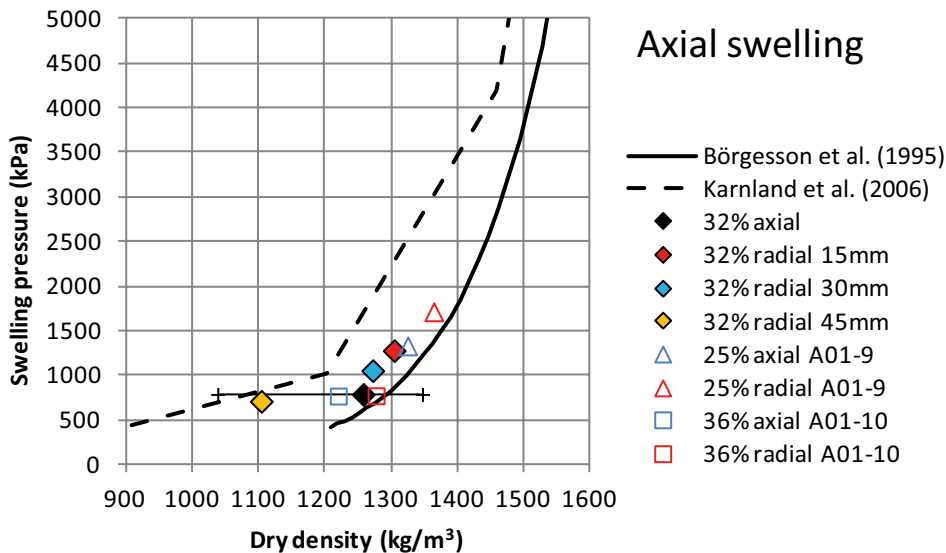


Figure A2-9. Swelling pressure plotted as a function of dry density. The radially measured pressures are plotted with the dry density measured at the corresponding locations. Axially measured pressure is plotted with the average dry density. Also shown are results from the basic series; A01-09 and A01-10.

A2.3.2 Radial outward swelling

In the series with radial swelling in the high resolution series so far one test has been completed, Table A2-2. In Figure A2-10 to A2-12 the distribution of w , ρ_d and S_r measured after termination of the test are shown. The labels shown in the diagrams include the specimen ID and the swelling in %. The results are shown with comparable tests from the basic series.

Table A2-2. Specimens used in the series HR-Ro.

	Initial w (%)	Initial ρ_d (kg/m ³)	Constant height (mm)	Initial radius (mm)	Final radius (mm)	Swelling ¹ $\rho_{d1}/\rho_{d0}-1$ (%)	Remarks
HR-Ro1	23.7	1666	80	81	96.8	42 (43)	

¹ Swelling after saturation, in brackets, calculated from measured diameters and calculated as change in volume to initial volume.

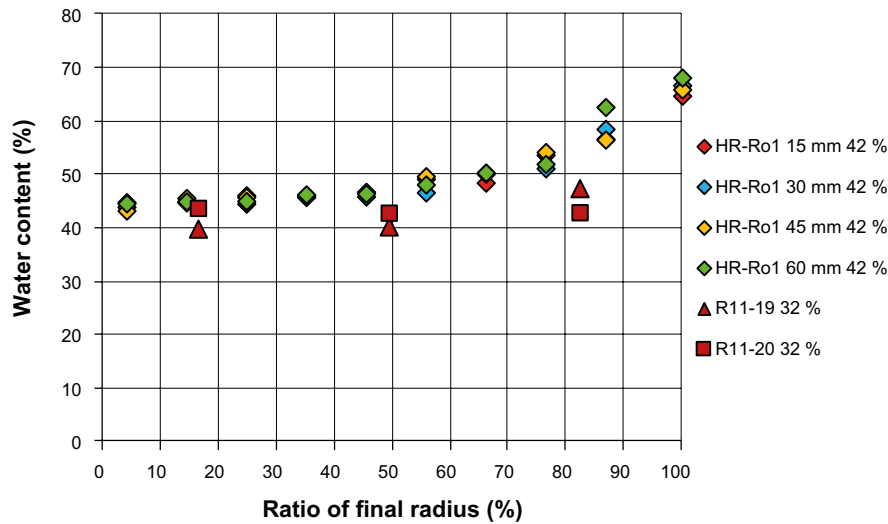


Figure A2-10. Distribution of water content over the radius. Result from HR-Ro1 is shown with results from the basic series; R11-19 and R11-20.

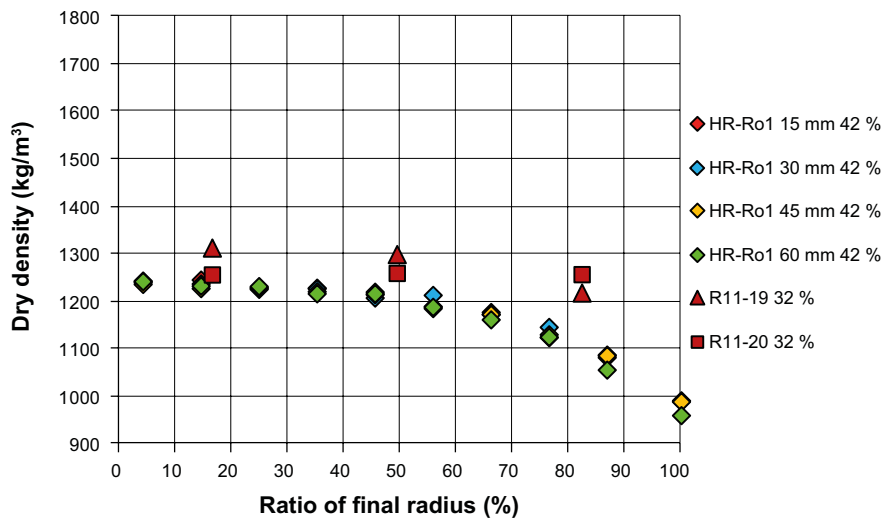


Figure A2-11. Distribution of dry density over the radius. Result from HR-Ro1 is shown with results from the basic series; R11-19 and R11-20.

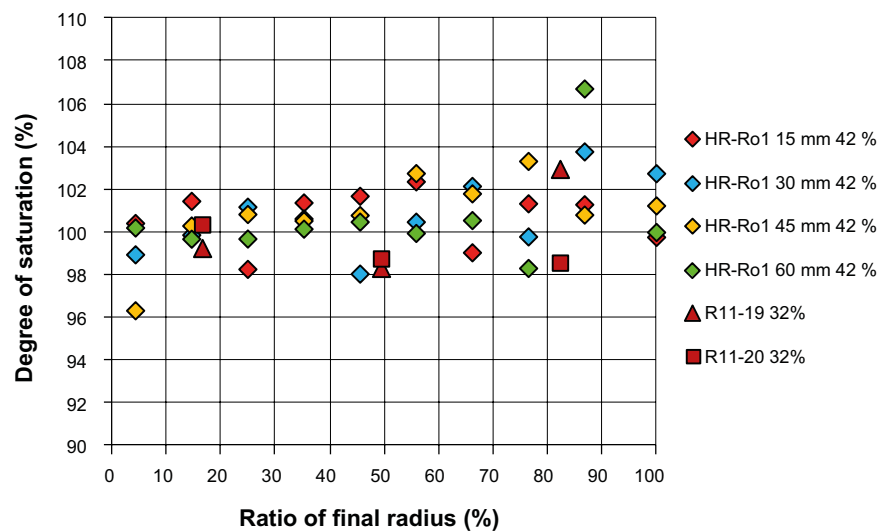


Figure A2-12. Distribution of degree of saturation over the radius. Result from HR-Ro1 is shown with results from the basic series; R11-19 and R11-20.

The time evolution of the swelling pressure is shown in Figure A2-13. In Figure A2-14 the swelling pressure is plotted as a function of dry density. The radially measured final swelling pressures from test HR-Ro1 are plotted with the dry densities measured at the corresponding distances from the bottom surface. The axial swelling pressure from test HR-Ro1 is plotted with the average dry density and an error bar corresponding to the maximum and minimum dry density over the specimen height. In addition, results from the basic test series are shown.

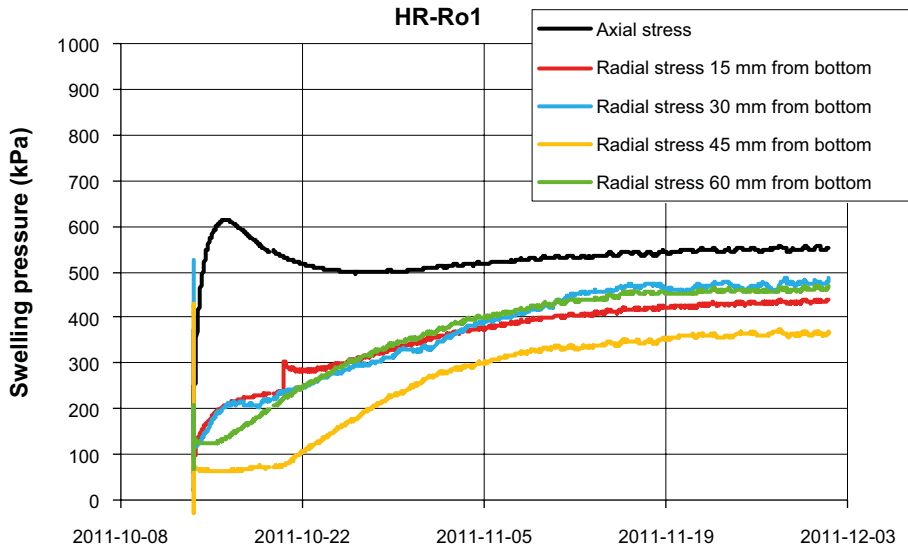


Figure A2-13. Time evolution of the swelling pressure from test HR-Ro1.

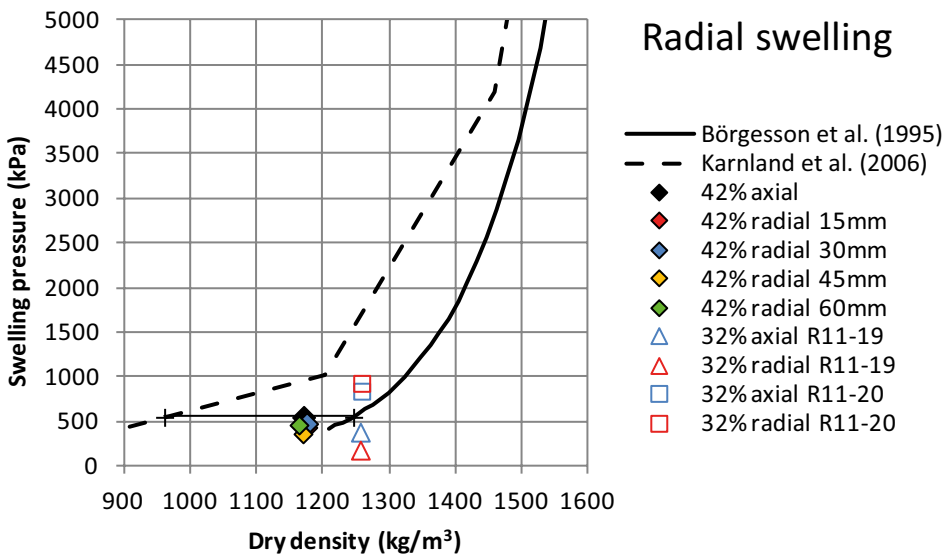


Figure A2-14. Swelling pressure as a function of dry density. The radially measured pressures are plotted with the dry density measured at the corresponding locations. Axially measured pressure is plotted with the average dry density. Also shown are results from the basic series R11-19 and R11-20.

Observations

In general the main purpose of the report was to provide results that can be used for modelling, but the following observations could also be made:

- Good agreement was seen in the distribution of w and ρ_d from the larger specimens (HR series) and the smaller specimens (basic series). This indicates there is an insignificant influence of the scale.
- A high degree of saturation was achieved; larger than 98 %.
- The stresses corresponded fairly well with the swelling pressure from the model presented by Börgesson et al. (1995), especially when the density present at the location of the transducer was used. The density present at the lowest measured swelling pressure was outside the limit of the model but agreed well with results presented by Karnland et al. (2006).
- The axial swelling pressure after 32 % of axial swelling was similar to the lowest radial swelling pressure. The axial swelling pressure after 42 % of radial swelling was similar to the radial swelling pressures.

A2.3.3 Radial inwards swelling

The equipment used for the radial inwards swelling test is identical to the one used for the outwards swelling. Figure A2-15 shows the set-up.

Axial swelling pressure was measured on the top lid and radial swelling pressure was measured 40 mm from the bottom of the oedometer. Only one of the radial transducers was used.

The initial dry density was 1666 kg/m^3 corresponding to a void ratio of $e = 0.67$. The swelling was about 40 % and the test ran for about 130 days. The results of this test are not described in the Appendix 2, but will be shown here.

Figure A2-16 shows the pressure evolution.

The water ratio and density distribution after completed swelling after the test was measured by dividing the central part of the specimen in 5 mm pieces as shown in Figure A2-17. It is desired to have the sampling done so that the density distribution could be plotted as a function of the radius but since this would give too small samples close to the centre, the sampling had to be done as shown in the figure. The density distribution is shown in Figure A2-18. The degree of saturation was in average 100 %.

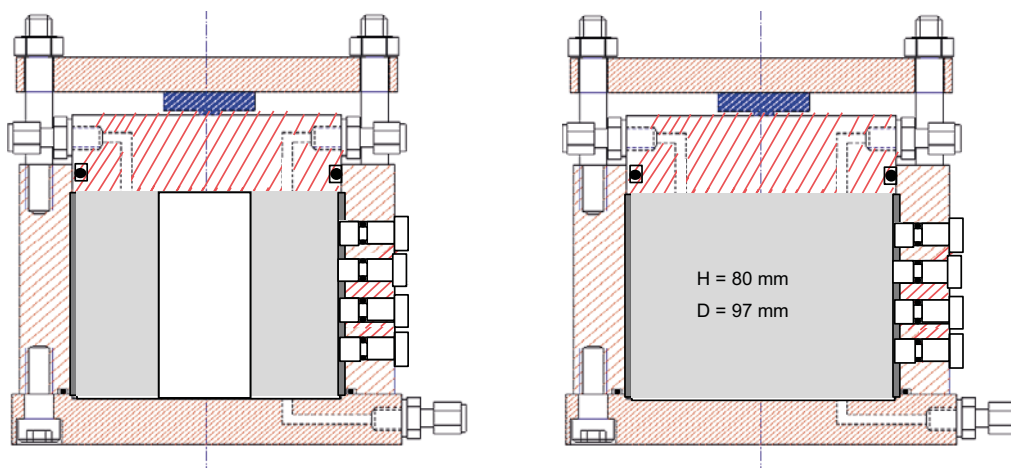


Figure A2-15. Set-up used for the inward radial swelling tests (HR-Ri). Water is initially filled into the cavity and then only supplied from a radial filter between the surrounding steel ring and the specimen.

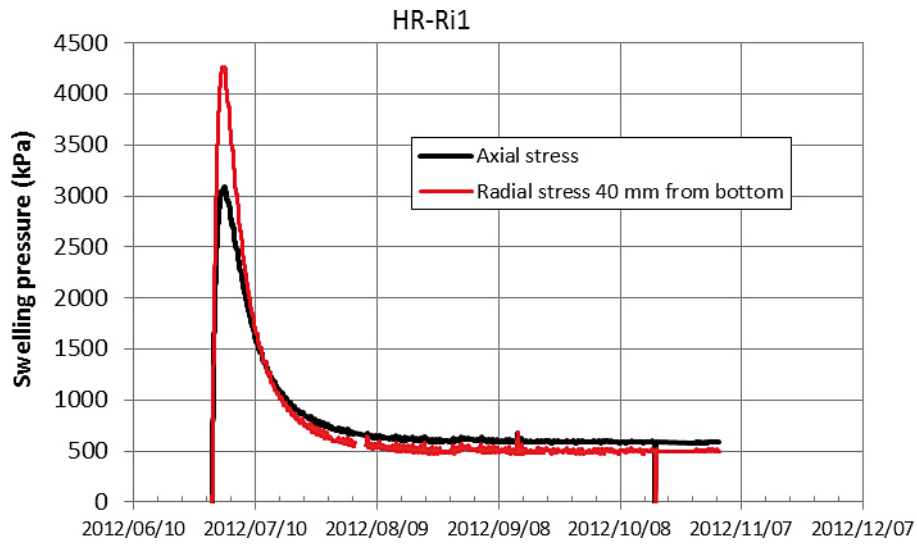


Figure A2-16. Evolution of the swelling pressure from test HR-Ri1.

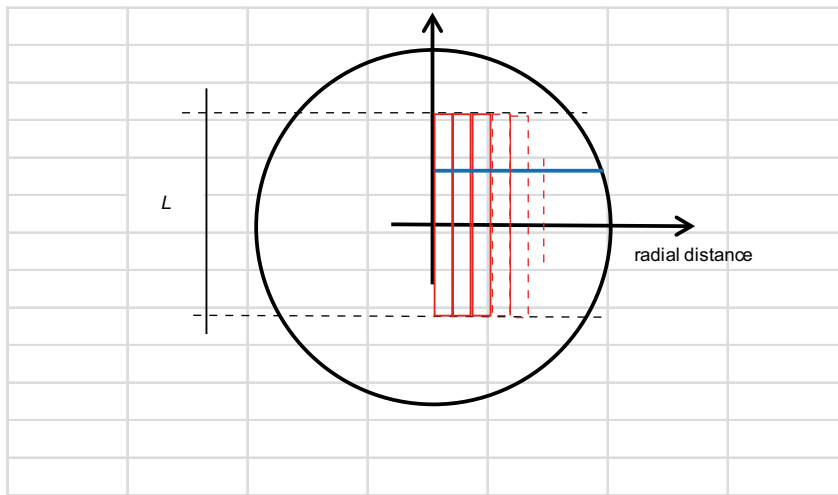


Figure A2-17. Sampling scheme for the HR-Ri1 test.

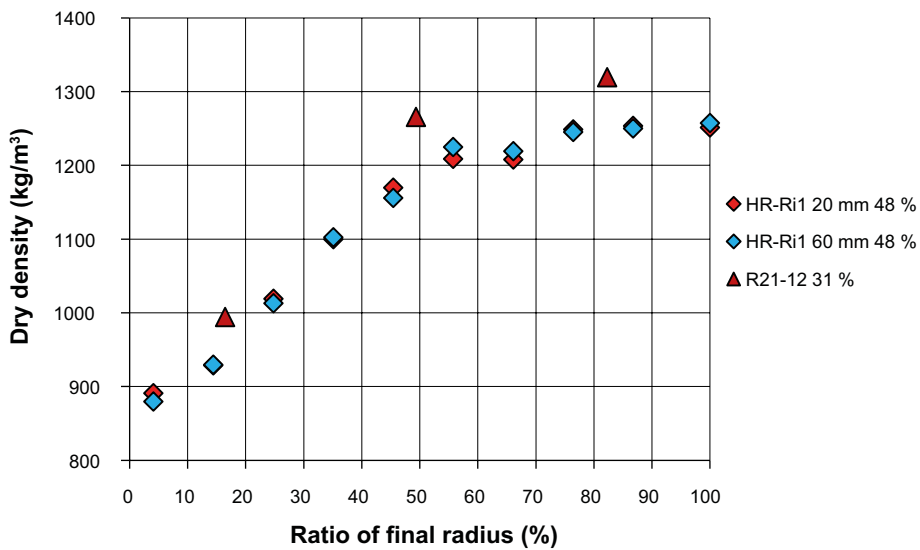


Figure A2-18. Dry density distribution measured in two levels. Results from a test in smaller scale (50 mm diameter) are also shown R21-12 (31 % swelling).

The results in Figure A2-18 are not a correct representation of the density as function of the radius since the average distance of the samples to the centre is larger than shown. The average distance of each sample is better represented by the blue line in Figure A2-17 since the x-axis is also a symmetry plane. This is analyzed in Figure A2-19.

The centre of gravity of the samples is where the inclined arrow is pointed at since the horizontal line is a symmetry plane. The correct radius r_c will thus be expressed as a function of the apparent radius r_a according to Equation A2-3.

$$r_c = (r_a^2 + a^2)^{0.5} \tag{A2-3}$$

For the HR-Ri1 test $L = 35$ mm, which yields $a = 8.75$ mm.

The corrected results are shown in Figure A2-20.

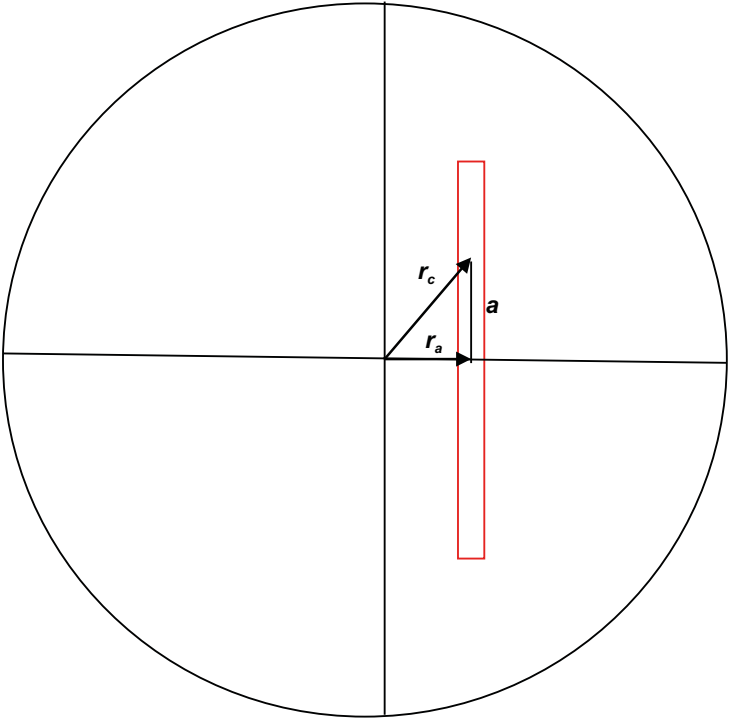


Figure A2-19. Calculation of the correct radius of the sampling.

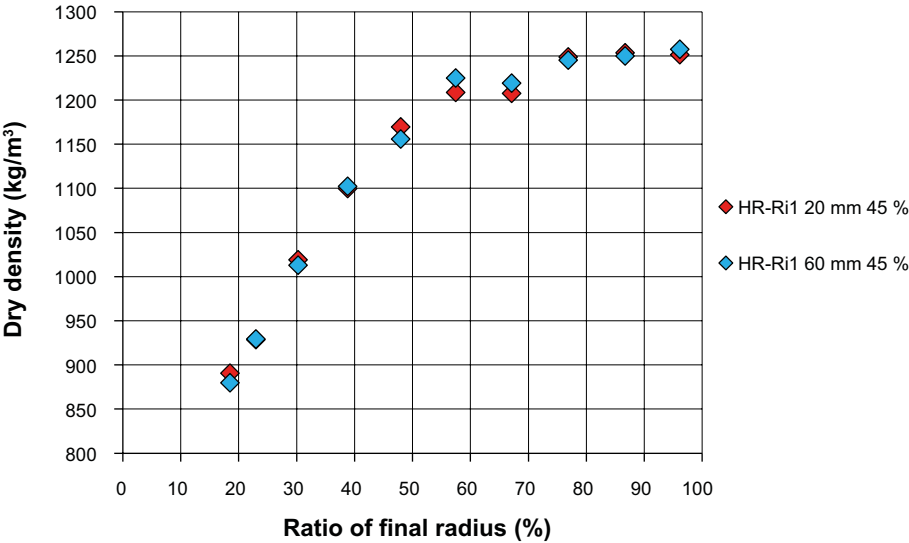


Figure A2-20. Dry density distribution expressed as function of the corrected radius.

A2.4 Results from tests on friction between buffer and other surfaces

Results from the test series where friction between buffer and other surfaces was studied are presented in Table A2-3. The friction angle δ (Equation A2-2) is interpreted both as the peak value at the beginning of the deformation and as the more or less constant value reached after approximately 1 mm of deformation. The swelling pressure used for the evaluation was the radially measured values. However, in tests Fr1_3 and Fr1_7 the swelling pressure was not measured radially and for these tests the axially measured pressure was used. Test Fr1_6 was considered irrelevant due to rapidly increasing friction force presumably due to an inclined set-up.

Table A2-3. Results from measurement of friction between buffer and steel. Evaluated angle of friction δ for the deformation rate 0.01 mm/min and the given swelling pressure P_r . Peak values δ_{peak} are also evaluated. Water content w , dry density ρ_d and degree of saturation S_r after dismantling are given.

Test ID	Friction angle δ (δ_{peak}) (°)	Swelling pressure P_r (kPa)	Surface (lubricated steel surface)	After dismantling			Remarks
				w (%)	ρ_d (kg/m ³)	S_r (%)	
Fr1_1	2.8 (3.6)	14200	lubricated	24.8	1630	97	
Fr1_2	4.4 (4.7)	11100		24.6	1630	97	
Fr1_3	5.5 (6.1)	12400	lubricated	24.3	1640	97	P_a used, δ not levelled out
Fr1_4	5.6 (5.6)	6300		27.2	1560	97	
Fr1_5	4.7 (7.6)	2300		34.6	1410	99	
Fr1_7	3.9 (5.3)	9900	lubricated	25.4	1610	97	P_a used
Fr1_8	5.9 (7.7)	800		47.9	1190	100	
Fr1_9	4.9 (7.1)	900	lubricated	44.5	1230	99	δ not levelled out

The angle of friction δ in A2-3 was evaluated at a deformation rate of 0.01 mm/min. In tests Fr1_8 and Fr1_9 other deformation rates were also used. No large influence of the deformation rates used; 0.01, 0.1 and 1 mm/min, was seen.

In Figure A2-21 the evaluated angle of friction from Table A2-3 is plotted as a function of swelling pressure. In the diagram a relation for the buffer friction angle ϕ presented by Åkesson et al. (2010a) is also given.

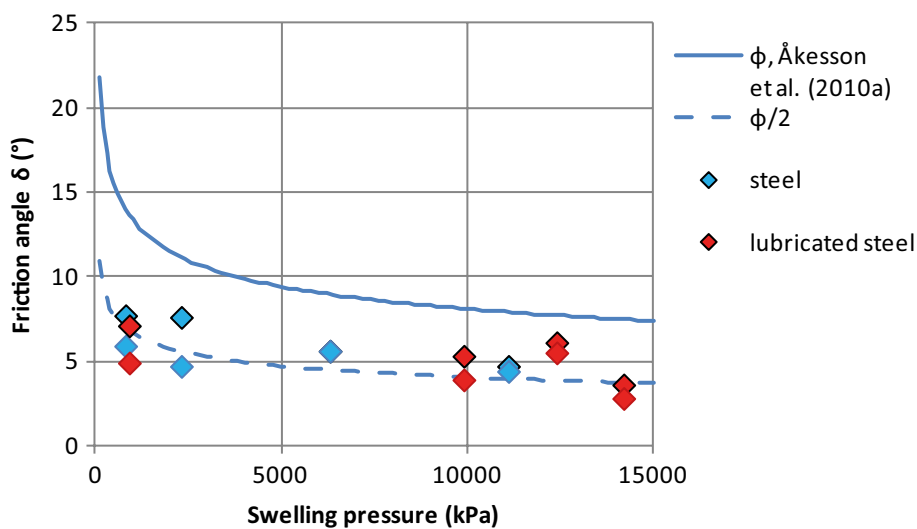


Figure A2-21. Test results plotted with a relation derived by Åkesson et al. (2010a).

Observations

In general the main purpose of the tests was to provide results that can be used for modelling, but the following observations could also be made:

- A peak value was seen in the friction force and the calculated friction angle δ at the first small deformation, i.e. less than 1 mm.
- No influence of deformation rate was seen on the friction angle.
- No effect of lubrication was seen in the evaluated friction angle.
- The friction angle δ between bentonite and a steel cylinder seemed to have a value approximately equal to half the bentonite internal friction angle ($\phi/2$).

Task 1 Description of test techniques and test results from an isotropic swelling test

A3.1 General

In one part of the buffer homogenisation project specimens with different geometry are combined with axial or radial swelling. In the present test the objective was to study the density profile and swelling pressure evolution after isotropic swelling i.e. swelling in all directions at the same time with a stress path with decreasing average stress without deviator stresses in order to study the purely elastic swelling that does not affect the cap position in the mechanical cap model of water saturated swelling clay. The test was run in a device with relatively large dimensions, the so called high resolution device, which gave the possibility to measure the density distribution and pressure evolution in detail.

The material used was the Wyoming bentonite with the brand name Volclay MX-80 which is a sodium-dominated bentonite produced by American Colloid Company. The water used was de-ionized water. For evaluation of base parameters the particle density 2780 kg/m^3 and water density 1000 kg/m^3 were used.

A3.2 Equipment

The test was carried out in a device with the design shown in Figure A3-1. The device consists of a steel ring surrounding the specimen and a movable piston placed vertically, in the axial direction above the specimen. Radial pistons were placed in holes through the steel ring for measurements of radial stresses. A filter of sintered steel, fixed to the bottom side of the vertical piston, was used to distribute the water from above and over the cross section of the specimen.

The bottom and top plates and the steel ring were bolted together to keep the volume constant. Load cells were placed in the vertical and radial directions and each load cell was placed between a fixed plate and a movable piston. The small deformation required by the load cells was admitted. Stresses were registered continuously during the test.

A3.3 Preparation of specimens and test procedure

The specimen was sawn and trimmed from a larger bentonite block with a high degree of saturation (close to 100 %). The specimen with the approximate dimensions shown to the left in Figure A3-1, was placed centric inside the test device, cf. Figure A3-2. The swelling started when water was supplied from above through the filter. Water was supplied after evacuation of the system. During the test period the filter was flushed regularly.

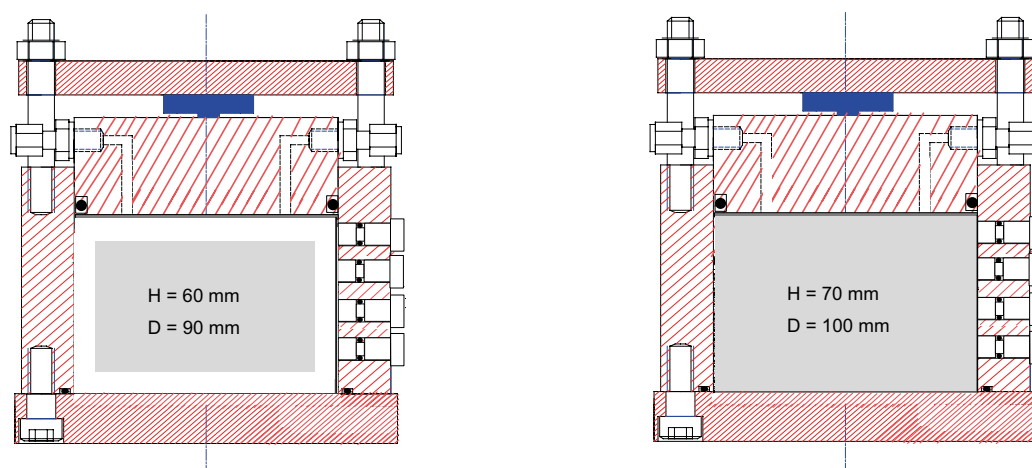


Figure A3-1. Set-up used for the test HR-Iso.



Figure A3-2. Photo of the specimen, suspended in the upper piston, before mounting into the test device.

After completed swelling and homogenisation, i.e. when no or negligibly small changes were noticed in the measured swelling pressure, the specimen was dismantled and cut in slices for determination of mainly the water content distribution. Some determinations of dry density were also done to check the degree of saturation.

A3.4 Results from the HR-Iso test

The initial and final average conditions of the specimen are shown in Table A3-1. The final dry density was calculated from the initial dry mass and the final volume. The distribution of water content and dry density are given in Figures A3-3 to A3-6 where the dry densities are calculated values based on the measured water contents and an assumed degree of saturation of 100 %. The degree of saturation was checked on some samples taken from the inner part of the specimen and it was determined to be between 99.5 % and 100.2 %. In Figure A3-3 the water contents are shown as average of two specimens, sampled at the same radius but in opposite directions. In Figure A3-5 all measured values are shown. The time evolution of the swelling pressure, i.e. measured stresses, is shown in Figure A3-7

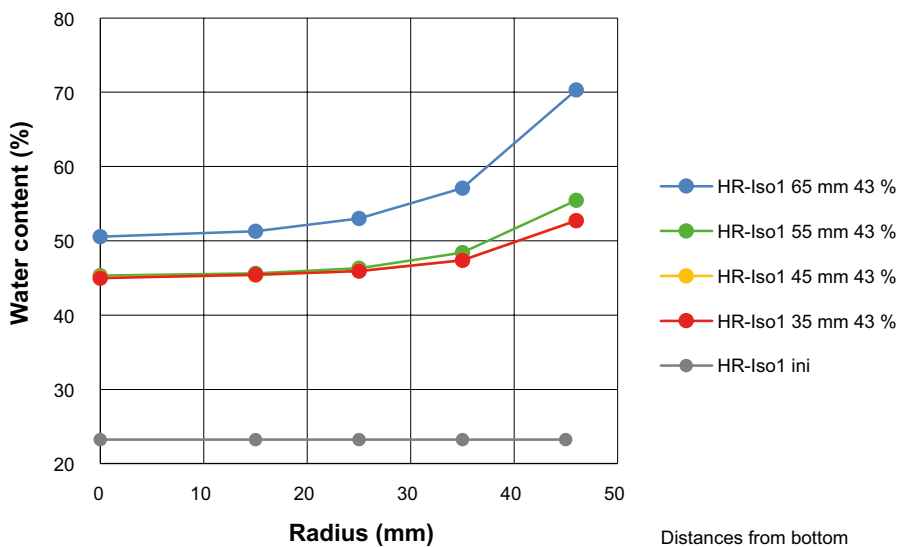


Figure A3-3. Distribution of water content as a function of the radius at four different distances from the bottom. The values are given as average of two specimens taken at the same radius but in opposite directions. The initial water content is also given.

Table A3-1. Specimen used for the HR-Iso test.

	Initial w (%)	Initial ρ_d (kg/m ³)	Initial S_r (%)	Initial diameter (mm)	Initial height (mm)	Final diameter (mm)	Final height (mm)	Final density (kg/m ³)	Swelling ρ_{d1}/ρ_{d1}^{-1} (%)
HR-Iso	23.2	1684	99	89	62	100	70	1180	43

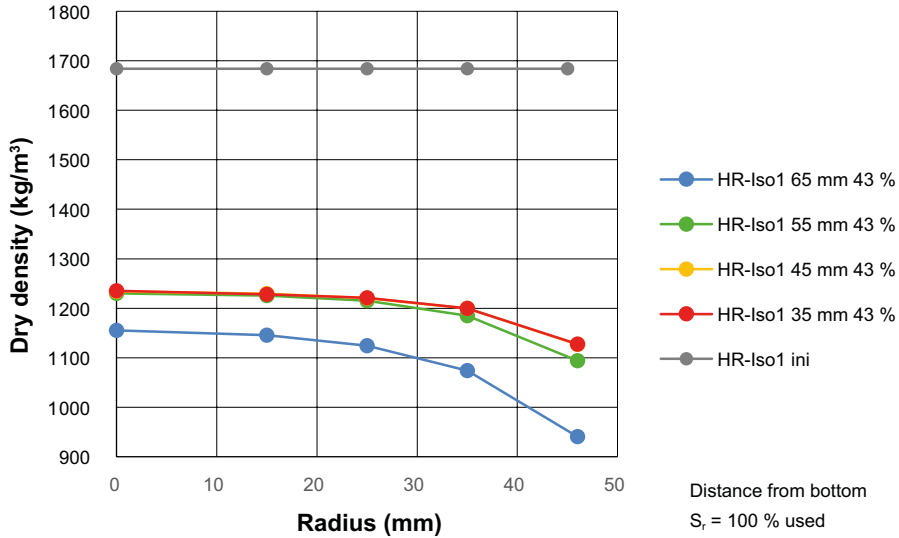


Figure A3-4. Distribution of dry density as a function of the radius at four different distances from the bottom. The values are calculated from the water contents in Figure 2-1. The initial dry density is also given.

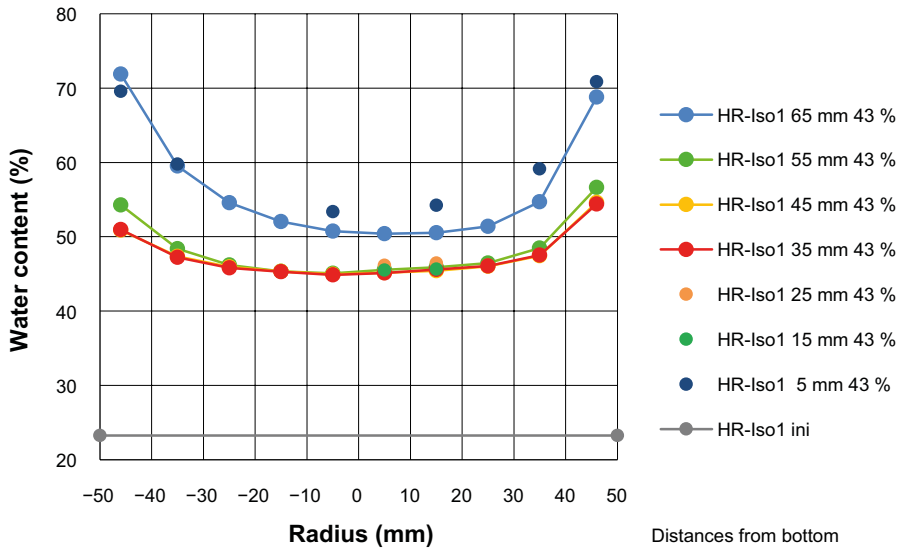


Figure A3-5. Distribution of water content as a function of the radius in two directions at different distances from the bottom. The initial water content is also given.

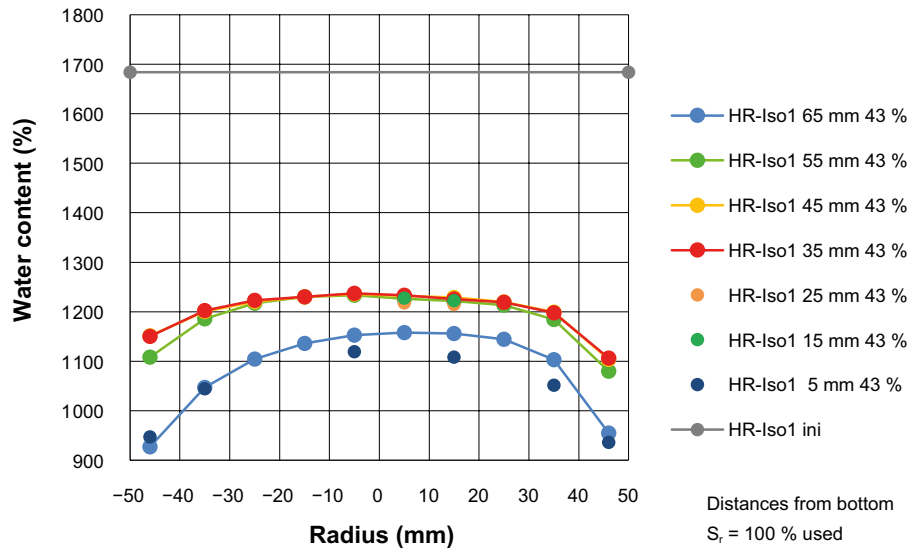


Figure A3-6. Distribution of dry density as a function of the radius at different distances from the bottom. Values are calculated from the water contents in Figure 2-3. The initial dry density is also given.

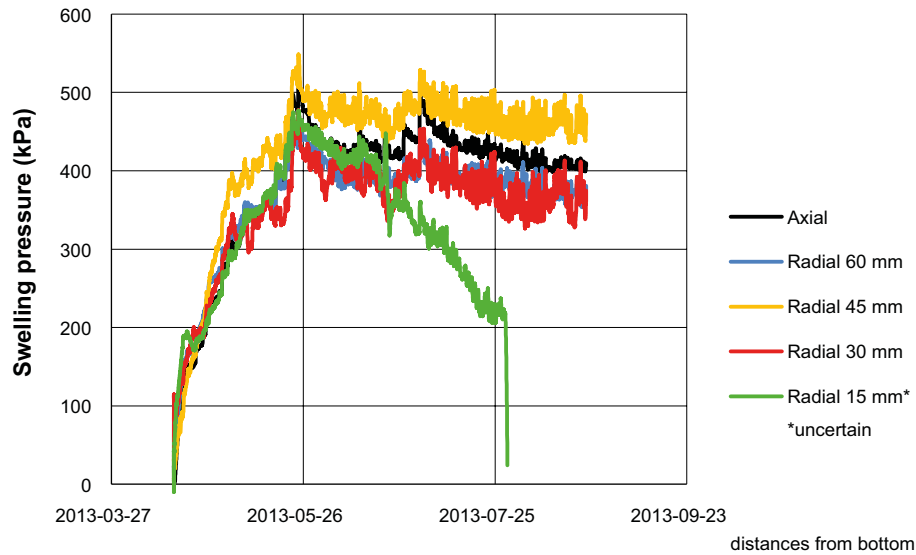


Figure A3-7. The time evolution of the swelling pressure from test HR-Iso.

Task 2 Self Healing Test – task description

A4.1 Test setup

The geometry is shown in Figure A4-1. The device is a very stiff cylinder with the diameter 300 mm and the height 100 mm. A simulated canister with the diameter 100 mm is included in the centre. A stiff filter has been mounted to the inside of the ring with the purpose to provide water to the bentonite. A bentonite block with very good fitting has been made of MX-80 bentonite. The block was made with uniaxial compression of MX-80 bentonite with the water content 23.6 %. The block has been machined to the following dimensions:

Height: 100.0 mm

Diameter: 298.7 mm

Inner diameter 100.0 mm

There is thus a small gap of 0.65 mm between the block and the outer ring and virtually no gap at the inner ring and at the lid.

A cavity with the dimensions $35 \times 50 \times 70 \text{ mm}^3$ has been cut in two diametrical positions as shown in the figure. Water is provided in the radial surfaces and in the cavities. Nine transducers for measuring swelling pressure and two for measuring suction are included as shown in Figure A4-2.

Six of the pressure transducers are unique (P1–P6) while three are placed in mirrored positions (P33, P55 and P66) for repeatability reasons. The suction devices are placed in positions where the pore pressure equilibrium is foreseen to be reached at the latest time in order to see when the test is finished.

After mounting of transducers, bentonite ring and lids the test was started by filling the filter and the cavities with water and applying a low water pressure (10 kPa). The ring is equipped with four water inlet positions placed on each side of the cavities. Two of them are used for water supply. Once a week these inlets are used for flushing the filter in order to eliminate air bubbles that may be collected in the filter. After about one month a steady water pressure of 100 kPa was applied. Figure A4-3 shows two pictures taken during mounting of the test.

The properties of the installed bentonite ring are shown in Table A4-1.

Table A4-1. Properties of installed bentonite.

Properties excluding the cavities	Density ρ (kg/m ³)	Particle density ρ_s (kg/m ³)	Water density ρ_w (kg/m ³)	Water content w (%)	Dry density ρ_d (kg/m ³)	Void ratio e	Degree of saturation S_r (%)
Initial conditions, final dimensions	2009	2780	1000	23.6	1626	0.71	95–97

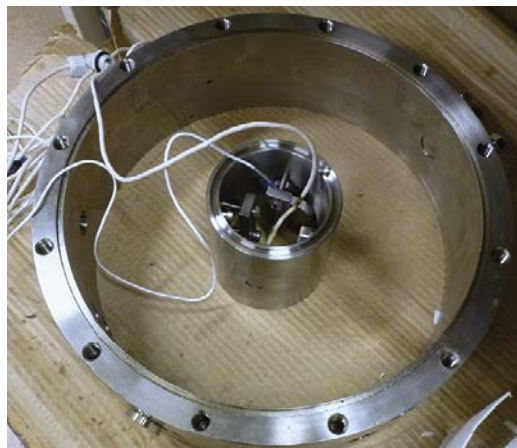
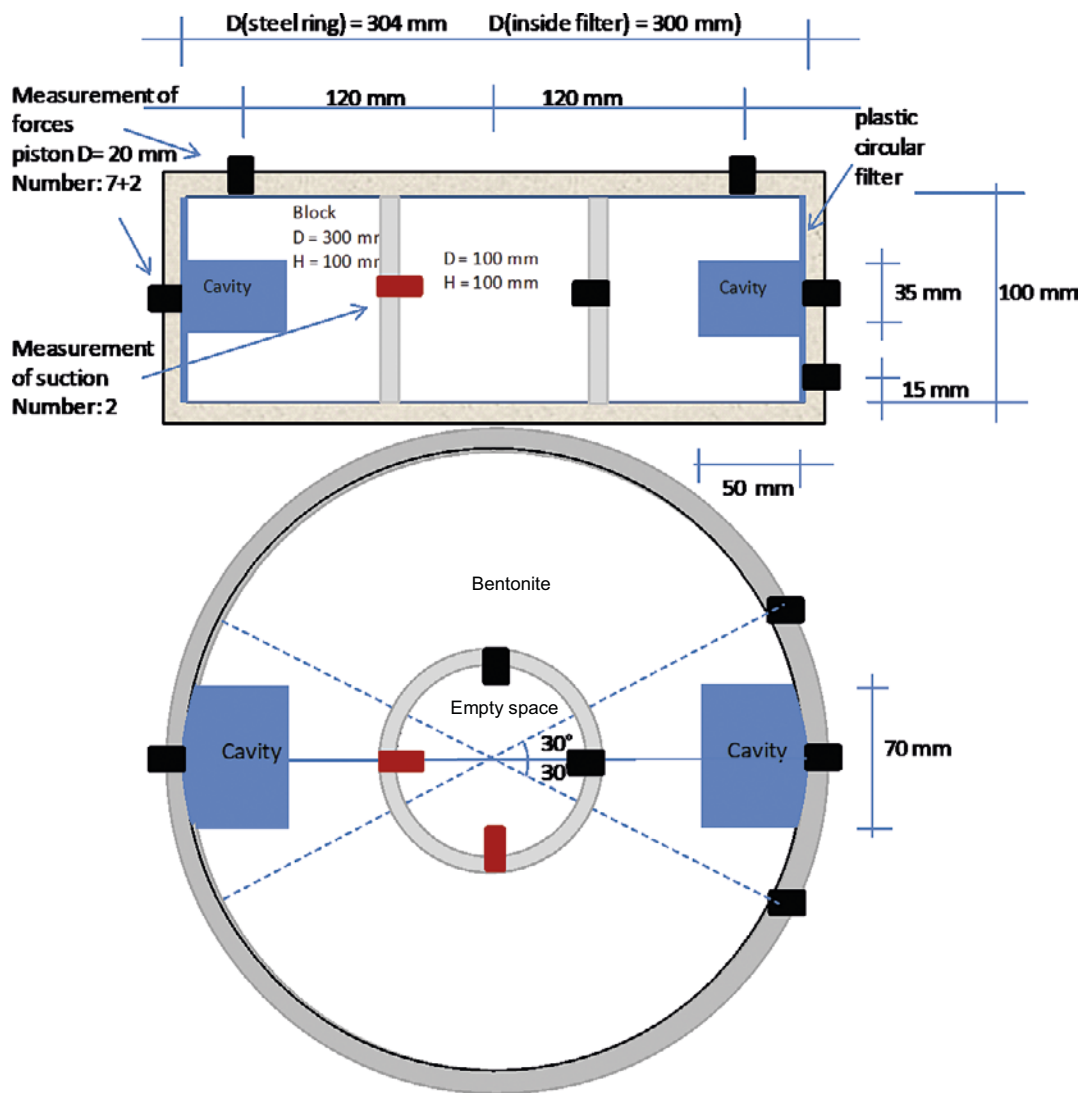


Figure A4-1. Test device.

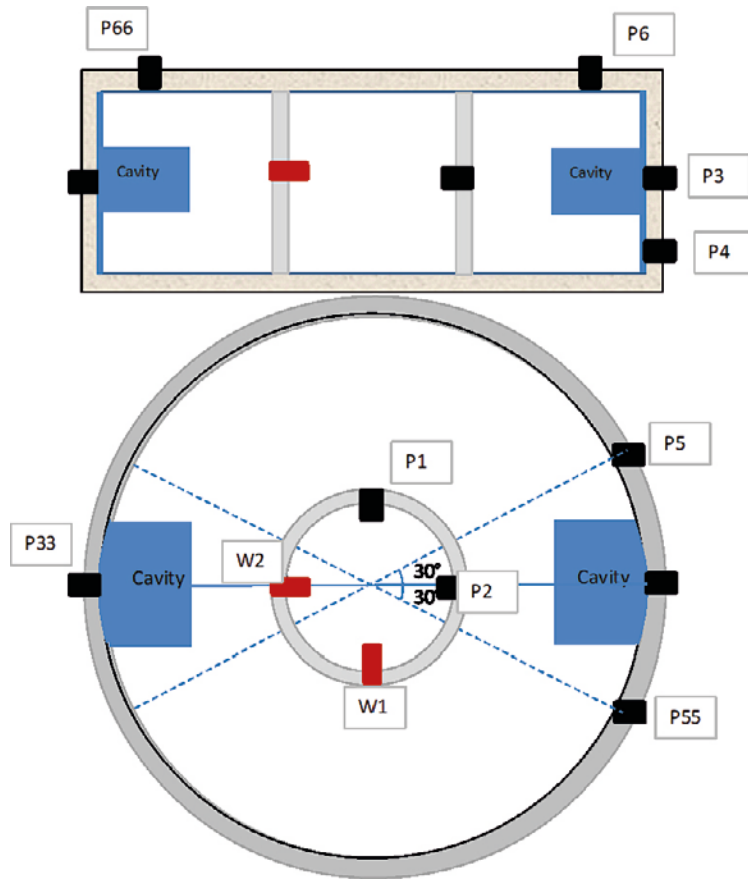


Figure A4-2. Location of sensors.

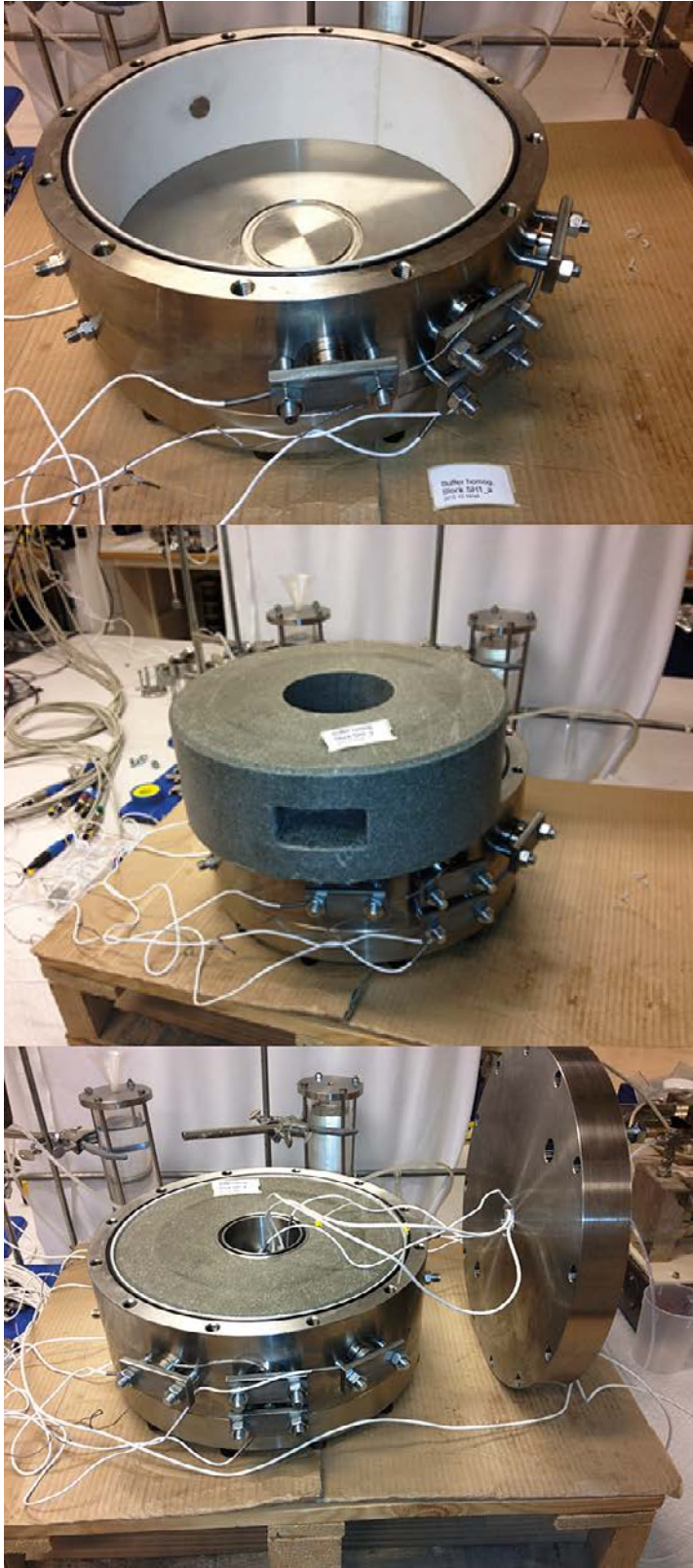


Figure A4-3. Mounting of the test.

The test started on December on 18, 2012. It will run until the bentonite is fully homogenised, and the pore pressure has stabilised at 100 kPa. This is expected to take at least one year.

After completed test, the bentonite will be carefully sampled and water ratio and density measured, which will yield a 3D-model of the density (void ratio) distribution in and around the cavity. Figure A4-4 shows the preliminary sampling scheme for one of the two identical halves, which yields about 1 215 samples. In addition a similar but reduced sampling will be done for the other half. For all samples the water ratio will be determined. Since the bentonite is expected to be water saturated the density will only be determined on a limited amount of samples e.g. every 10th sample.

Additional specifications will be submitted later.

A4.2 Requested results

The modeler should supply a full description of the material model and the modeling technique used.

The following results are requested:

- History plots of the total radial stress in the measuring points (P1–P6).
- History plots of the suction in the measuring points (W1 and W2).
- 3D illustration of the dry density or void ratio at test termination.

These results can be compared to measurements. The measured results will be distributed in Excel sheets after sampling.

In addition to the results that can be compared to measurements, the following results should also be supplied:

- 3D-illustration of the dry density or void ration after 5 days, 15 days, 30 days and 100 days.
- 3D illustrations of the average total stress after 5 days, 15 days, 30 days, 100 days and at termination.
- Additional results for illustrating the swelling progress.

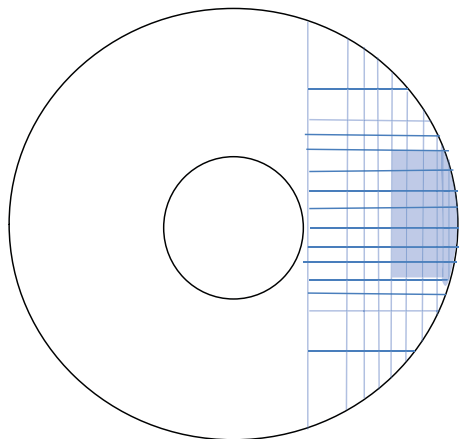
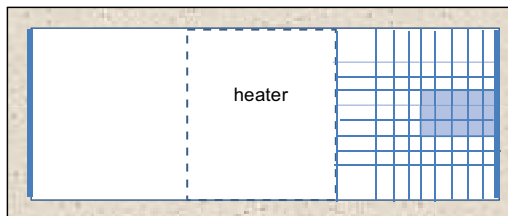


Figure A4-4. Preliminary sampling plan.

Task 2 Self Healing Test – dismantling

A5.1 Scope

The main focus of this appendix is the detailed description of the test SH1; the preparation, the start condition, the dismantling and the results from the sampling. Important results are also the measured swelling pressure and water potential.

A5.2 Experiment description

The self-sealing ability of large and irregular cavities was studied in this part of the project. Since it was important to be able to determine the final density distribution in detail a suitable combination of block size and cavity size was important to find. The size of the blocks, i.e. cylinder rings, was chosen to be as large as possible, still having a reasonable estimated time to saturation and homogenisation while the size of the cavities was chosen large enough to get good resolution of the sampling after termination of the tests. In addition, the evolution of swelling pressure was measured at strategic points in SH1 in order to follow the evolution of the homogenisation.

A5.2.1 Test set-up

The geometry of the set-up used for SH1 is shown with photos in Figure A5-1 and a sketch in Figure A5-2. The positions of the sensors used in SH1 are shown in Figure A5-3. The containment is a very stiff cylinder with the inner diameter 300 mm and the height 100 mm. An inner cylinder with the outer diameter 100 mm is included in the center mainly with the purpose to measure the swelling pressure and RH inside the bentonite block and to reduce the time for saturation and homogenisation. A stiff filter is mounted to the inside of the outer ring with the purpose to provide water to the bentonite from the radial surface. In each bentonite block two cavities were cut out in two diametrical positions in order to simulate loss of material. In the set-up of SH1 nine transducers for measuring swelling pressure and two for measuring suction were included.

Figure A5-2 also shows the geometry of SH2. In addition to the instrumentation, the main differences between SH1 and SH2 were the total time used for the tests (double time was used for SH1 compared to SH2) and the initial size of the cavities (larger cavities were cut in SH2).



Figure A5-1. Photos of the device and bentonite block used for SH1.

A5.2.2 Test procedure

The preparation of the bentonite rings for SH1 and SH2 was made by compaction of blocks, which were machined to rings with the correct dimensions and by cutting the cavities. After mounting of transducers, bentonite rings and lids each test was started by filling the filter and the cavities with de-ionized water and applying a low water pressure (10 kPa). The water was supplied through the filters, which were attached to the inside of the cylinder rings. Circulation of water through the filters was possible by use of the water inlet and outlet, located in two diametrical positions of the steel rings, see Figure A5-2.

After about three weeks a steady water pressure of 100 kPa was applied to SH1 and after approximately 11 months 100 kPa was also applied to SH2. During the test period the filters were flushed regularly in order to eliminate air bubbles that may have been collected in the filters.

Both tests were started in December 2012 by the opening of the water supplies to the filters but while SH2 was finished after 17 months (2012-12-17 to 2014-05-13) SH1 was running for 33 months (2012-12-18 to 2015-08-19).

A5.3 Results

The focus of this chapter is the results from SH1. In Appendix 6–8 additional information about SH1 can be found; additional photos, a timetable for the test and tabulated test results. Results from SH2 are shown in Dueck et al. (2016).

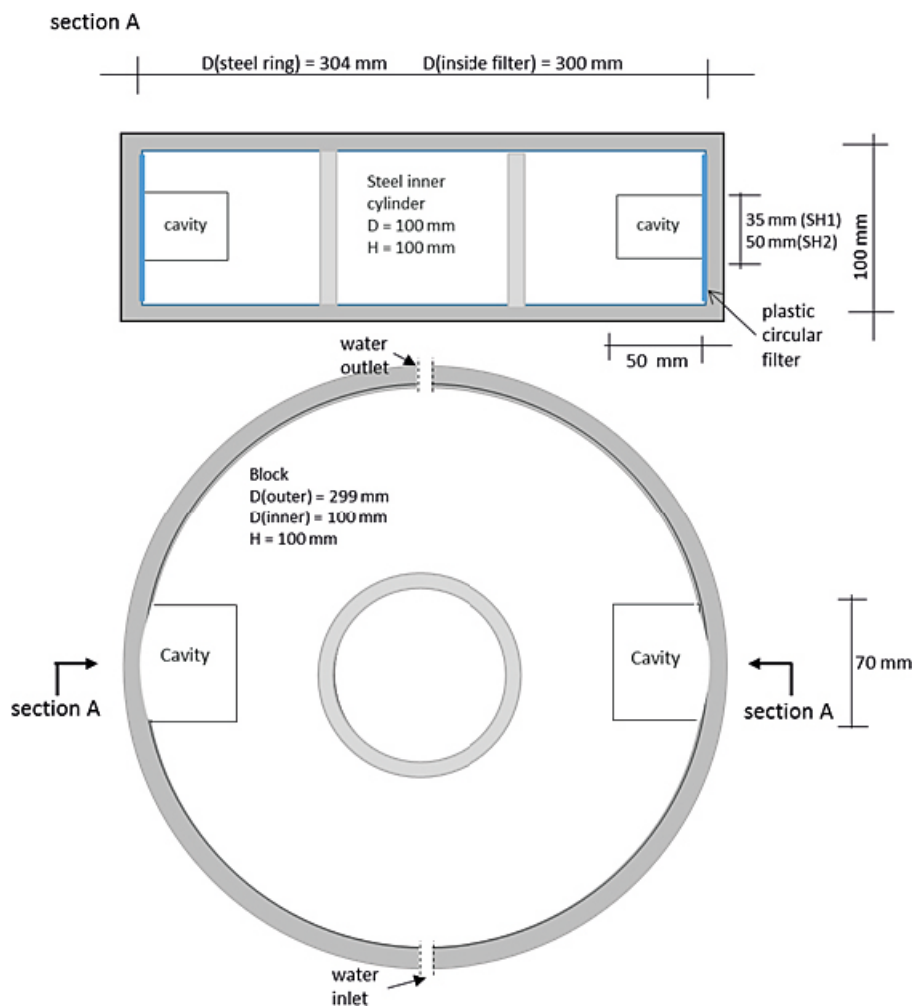


Figure A5-2. A sketch of the set up used for the tests SH1 and SH2. The dimensions of the outer and inner steel cylinders and the bentonite block with the cavities are shown as well as the plastic filters and the locations of the water inlet and outlet.

A5.3.1 Preparation and installation

The geometry of the test set-up was shown in Figure A5-2. Powder of MX-80 was mixed with de-ionized water to get a water content of 24 % in order to reach a high initial degree of saturation after compaction. Aiming at a dry density of approximately $1\,660\text{ kg/m}^3$ a compaction pressure of 40–60 MPa was used for the uniaxial compacted cylinder block. The block was machined with a rotating lathe to the following dimensions: height = 100 mm, outer diameter = 298.7 mm and inner diameter = 100.0 mm. There was thus a small gap of 0.65 mm between the block and the outer ring and virtually no gap at the inner ring and at the lids. More details from the compaction can be found in Dueck et al. (2016). The density was measured on samples from the removed center cylinder to $1\,657 \pm 4\text{ kg/m}^3$. Cavities were cut in two diametrical positions and the dimensions (height \times length \times depth) of the cavities in SH1 was $35 \times 70 \times 50\text{ mm}^3$, cf. Figure A5-2.

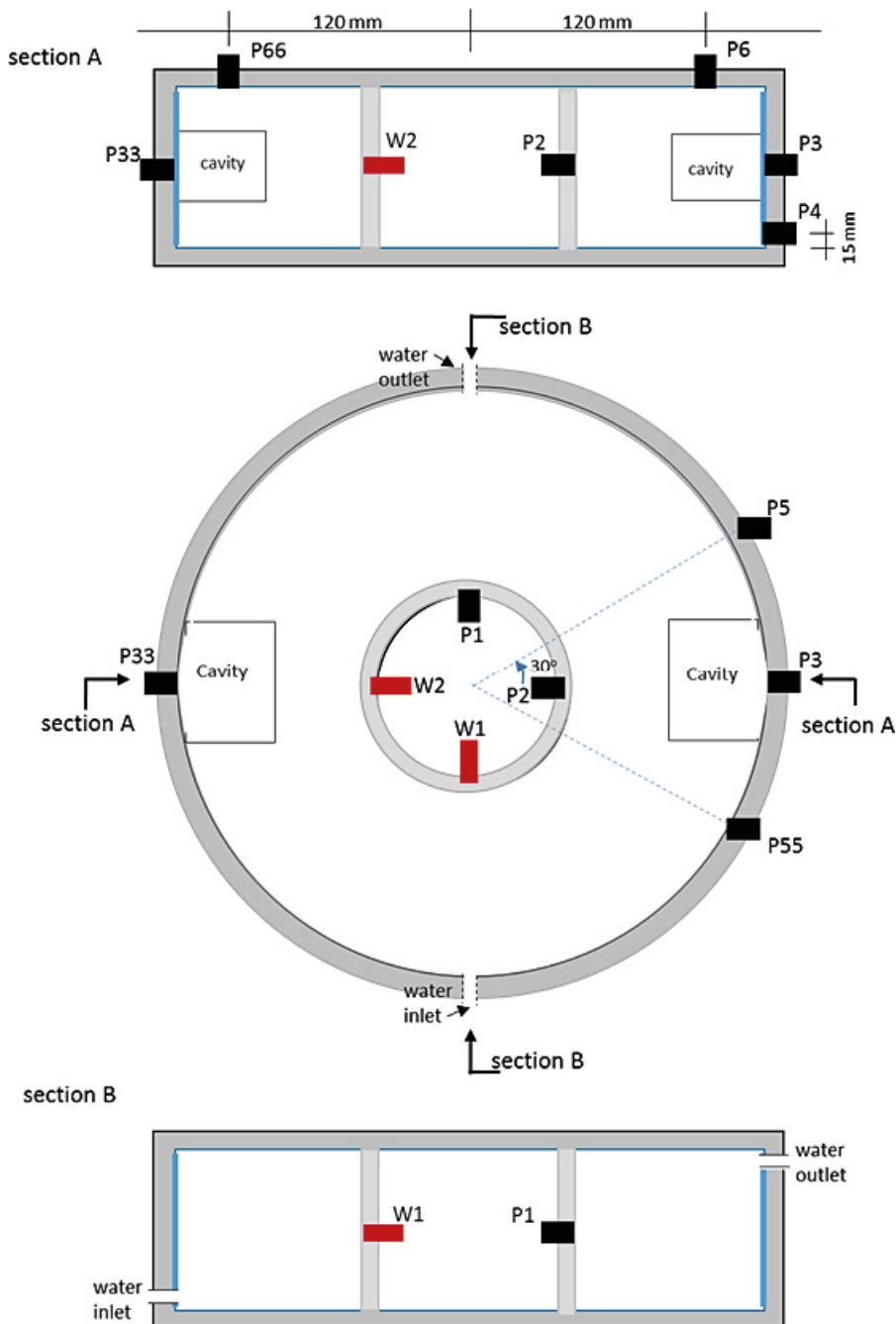


Figure A5-03. A sketch showing the positions of the sensors used in test SH1. The locations of the cavities and the water inlet and outlet are also shown.

In Table A5-1 the initial condition of the installed bentonite block is presented in terms of bulk density ρ , water content w , dry density ρ_d and degree of saturation S_r . The variables are derived in four different ways (Case 1–4);

1. Initial block density calculated from the initial mass and the initial volume of the block.
2. Initial block density measured on a sample of the removed center cylinder at preparation.
3. Final average density calculated from the initial mass and the final dimensions inside the containment without including the cavities.
4. Final average density calculated in the same way as 3 with the filter deformation taken into account without including the cavities.

Table A5-1. Initial conditions of the installed bentonite block in SH1. The base variables bulk density ρ , water content w , dry density ρ_d , void ratio e and degree of saturation S_r are shown for the initial conditions 1–4.

Case	ρ (kg/m ³)	w (%)	ρ_d (kg/m ³)	e (-)	S_r (%)	Remarks
1	2029	23.6	1642	0.69	95	Calculated from the initial mass and the initial volume of the block.
2	2047	23.6	1657	0.68	97	Measured on a center sample of the block, sampled at preparation.
3	2009	24.2	1618	0.72	94	Calculated from the initial mass and the final dimensions inside the containment with water in the gap.
4	2006	24.2	1616	0.72		Calculated according to Case 3, with the filter deformation taken into account.

A5.3.2 Water saturation and water supply

After one hour approximately 94 % of the available empty space mainly consisting of filter, gaps and cavities, was filled with water. 24 hours after the start approximately 97 % of the available volume was filled. The initial empty space was estimated to 3.8 dl and the total volume to be filled with water including the saturation of the bentonite was estimated to 4.7 dl. The water supply was open during the entire course of the test with a constant water pressure of 100 kPa applied after 20 days and then kept constant. The in- and outflow of water for SH1 as a function of time is shown in Figure A5-4.

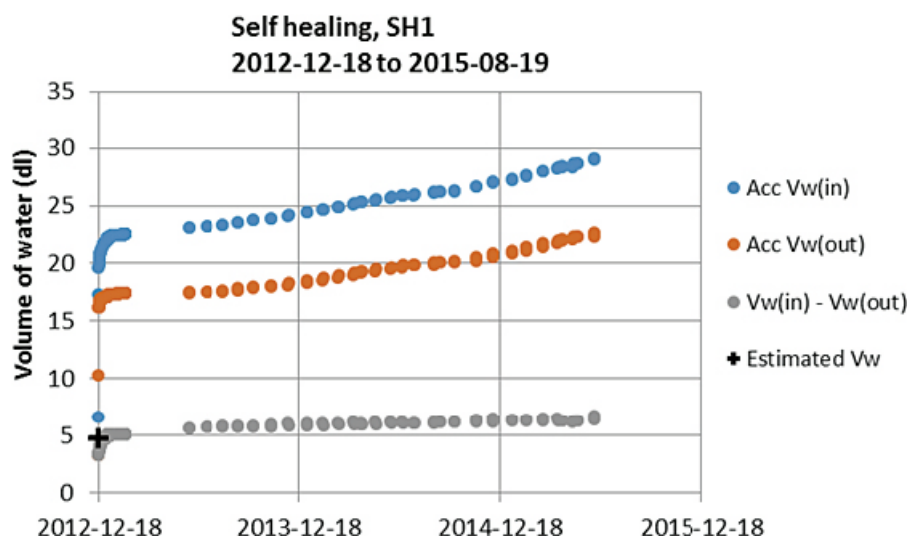


Figure A5-4. Accumulated in- and outflow of water are shown as a function of time. The difference between the in- and outflow is also shown together with the estimated available empty volume shown with a black plus sign. A water pressure of 100 kPa was applied 20 days after start and then kept during the entire course of the test.

A5.3.3 Swelling pressure and water activity measurements

The results from the swelling pressure measurements in test SH1 are presented in Figure A5-5. The maximum values (blue lines) and minimum values (green lines) were all measured at the outside and at the middle height of the cylinder ring but the minimum values were measured in the center of the cavities and the maximum values were measured well outside of the cavities. The locations of the sensors are shown in Figure A5-3. The control of the transducers after the test showed an error less than 2 %.

Measurement of the water potential Ψ , Figure A5-6, was made to follow the saturation of the bentonite in positions furthest away from the water source, cf. sensors W1 and W2 in Figure A5-3. The measurements were made by thermocouple psychrometers from Wescor© which evaluate the water potential by the Dew Point method (DP) and the Psychrometric method (P). The sensor W1 gave uncertain values from start and stopped working after 7.5 months (from 2013-08-20). The sensor W2 showed decreasing water potential until 16.5 months after start (2014-05-15) and after that no values were measured. After some time though a low constant value was measured with the sensor W2 but at the control after dismantling the sensor did not function properly. However, at the dismantling water was observed inside the casings surrounding the sensors W1 and W2, showing availability of water at the actual positions. This also confirms that the block was completely saturated.

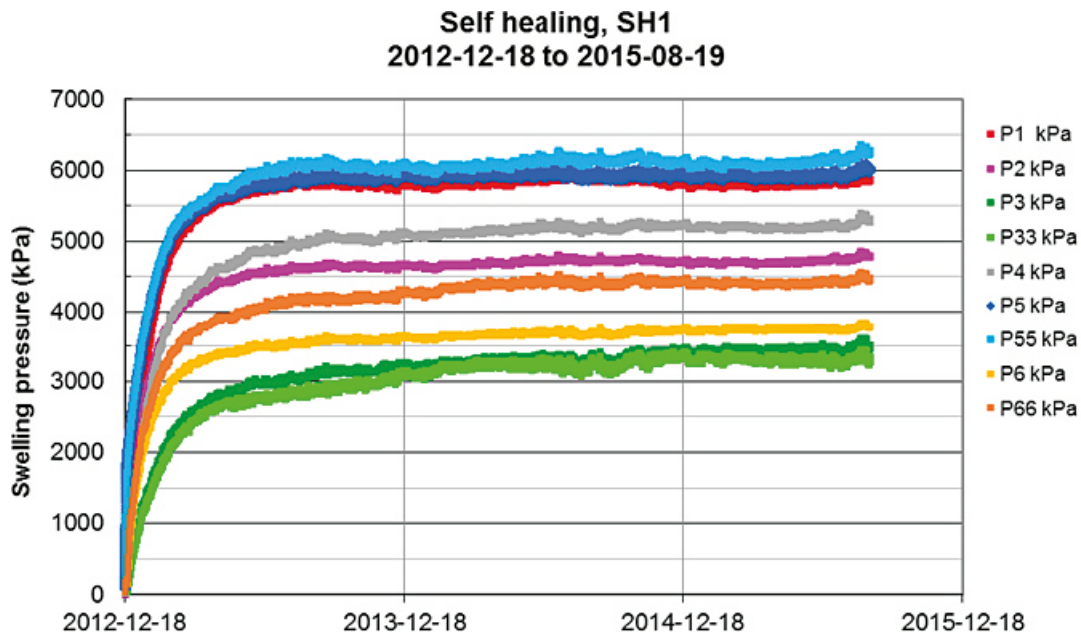


Figure A5-5. Evolution of swelling pressure from the transducers installed in test SH1. The locations of the sensors are shown in Figure A5-3.

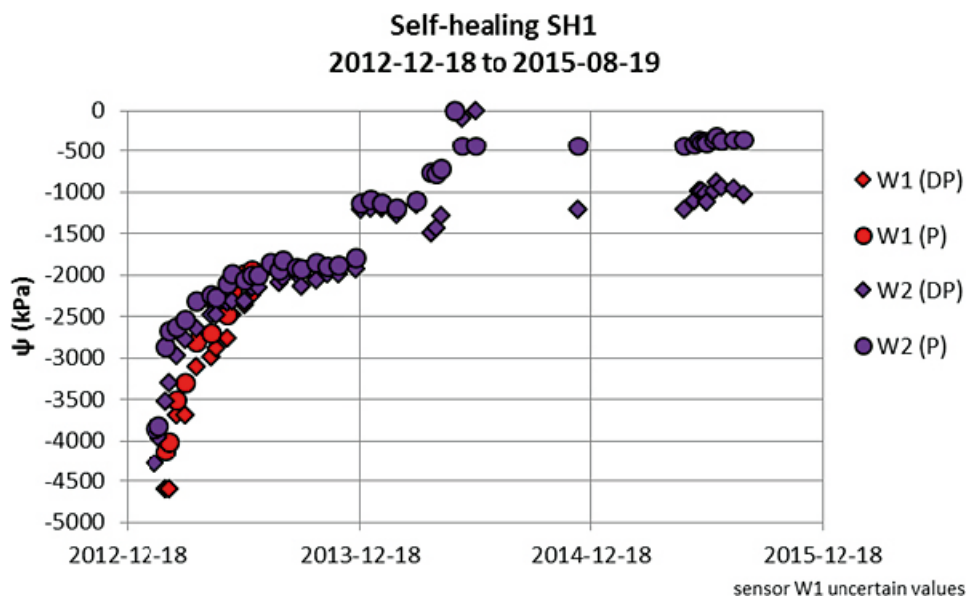


Figure A5-6. Evolution of water potential (suction) measured with thermocouple psychrometers installed in test SH1. The evaluation was made by both the dew point method (DP) and the psychrometer method (P). The labels show the number of the sensor (W1, W2) and the evaluation method (DP, P). The locations of the sensors are shown in Figure A5-3.

A5.4 Termination and dismantling

The test was terminated on 2015-08-19 and five days before the termination the applied water pressure of 100 kPa was lowered to zero. Before the opening of the device an attempt was made to evacuate the filter from water but only a small volume of water was possible to remove. The dismantling started with lifting the lid and removing the bottom from the cylinder ring and then marking the planned sampling on the uncovered bentonite surfaces. The dismantling continued by free-drilling and removing the inner steel cylinder and dividing the bentonite cylinder into two half circles by sawing radially. Figure A5-7 shows photos taken during the dismantling.

A5.4.1 Sampling and denomination of the samples

The bentonite cylinder ring was divided into two half-cylinders during the dismantling. One of the half-cylinders was directly used for the sampling and determination of water content and density distributions while the other one was sealed and stored for later analyses. The division of the bentonite ring in different parts and the sampling plan are illustrated in Figure A5-8 and Figure A5-9.

The half-cylinder for sampling was further divided axially at mid-height and the determinations of density were made on the upper part while the determinations of water content were made on the lower part, illustrated to the right in Figure A5-8. Extensive sampling was made with two different strategies, i.e. along four lines and continuously within a sector. The lines and the sector are marked red and yellow, respectively, to the left in Figure A5-8.



Figure A5-7. Photos from the dismantling of SH1.

The lines were located at the approximate angles 0° , 20° , 65° , 85° and 95° from the middle of the initial cavity and samples taken along these lines were denominated L0, L20, L65, L85 and L95, see Figure A5-9. The sector with continuous sampling was located between 0° and 45° from the middle of the cavity and it included parts both inside and outside of the initial cavity. The sector was divided into the sub-sectors A, B, C and D with the center angles 6° , 17° , 28° and 39° , respectively, from the center of the cavity. The sub-sectors A–D were further divided into two parts each, along which the samples were taken. The denominations of all subsectors starting from the center of the cavity are A(2), A(1), B(2), B(1), C(2), C(1), D(2), D(1), see Figure A5-9. Both the water content and the density were determined at three different levels axially; 1 – outermost, 2 – second outermost and 3 – innermost, which are illustrated to the right in Figure A5-9. The approximate size of each type of sample is shown in Figure A5-10.

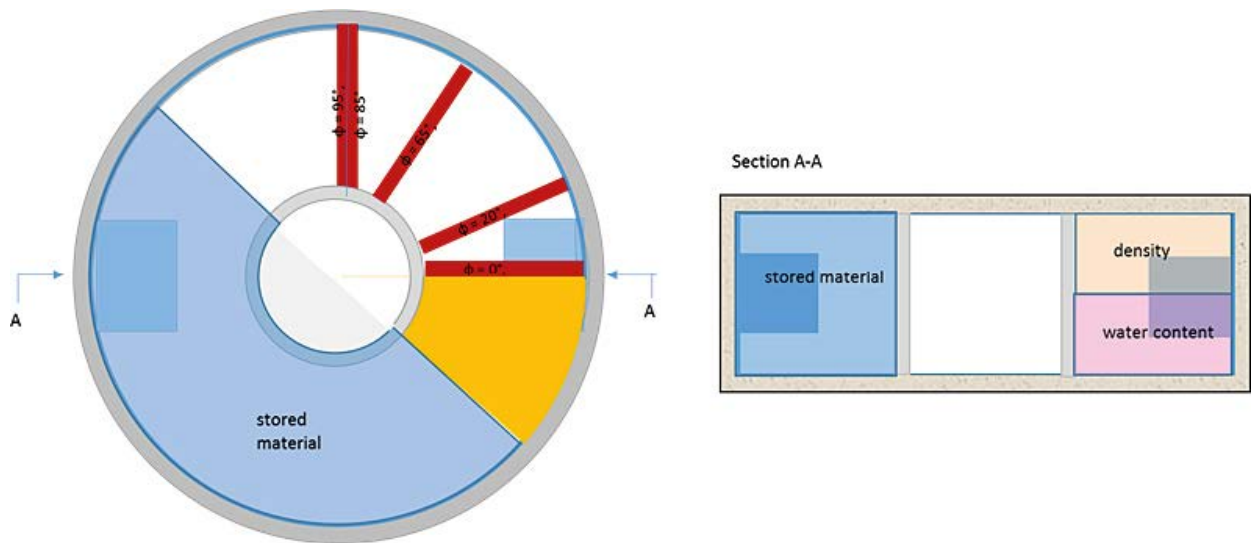


Figure A5-8. Plan view (to the left) and section (to the right) of the bentonite block at dismantling. The plan view shows the bentonite cylinder ring with the stored material (blue area), the lines of sampling (red lines) and the sector for continuous sampling (yellow area) marked. The section shows the stored part and the parts used for determinations of density and water content.

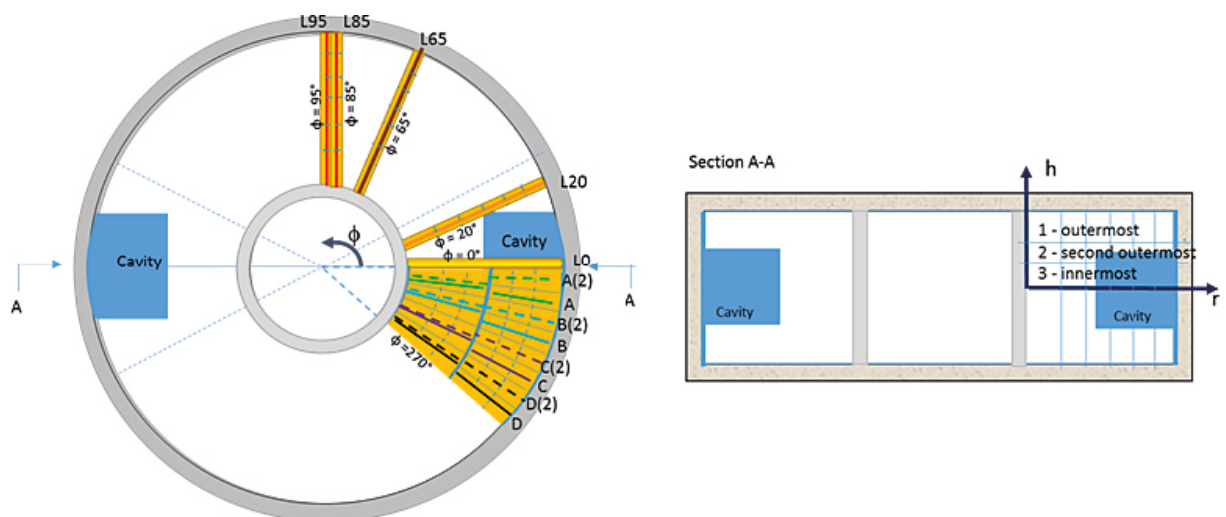


Figure A5-9. Plan view (to the left) which shows the sampling along lines at different angles from the middle of the cavity; 0° (yellow), 20° (orange), 65° (brown) and $85^\circ/95^\circ$ (red) and the sampling continuously within a sector along the dotted and solid lines (green, blue, purple and black). The section (to the right) shows the different axial levels for the sampling; outermost, second outermost and innermost.

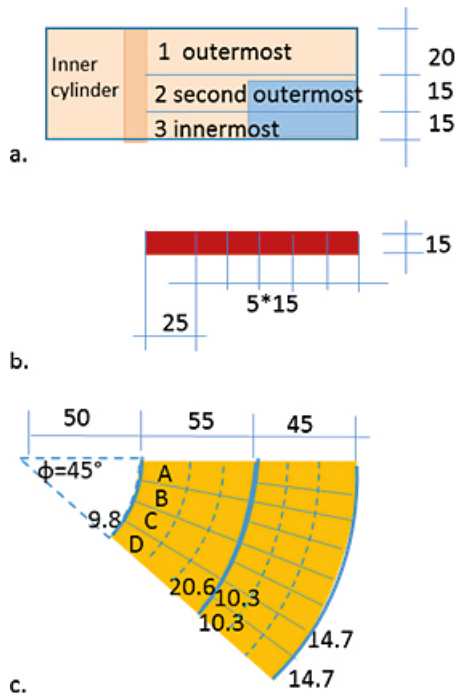


Figure A5-10. Positions and sizes of the samples. Different parts and views are shown; a) section with different sampling levels, b) plan view of one of the five sampling lines and c) plan view of the sampled sector with subsectors. The numbers show the approximate dimensions of the samples in the unit mm. As shown the center angle of the sampled sector is 45°.

A5.4.2 Distribution of water content and density

The measured distributions of dry density determined after dismantling of SH1 at the levels 1, 2, and 3 (outermost, second outermost and innermost) are shown in Figure A5-11, Figure A5-12 and Figure A5-13, respectively. The dry densities of the samples from the sector were calculated from the measured bulk densities and water contents. For the samples along the lines the dry densities were calculated from the measured water contents and a degree of saturation of 100 % which was proven to be valid in areas where this was analyzed, see below. In each diagram a small illustration of the location of the samples is given. The initial dry density of the block was approximately 1 657 kg/m³.

The distribution of dry density in different directions are shown as a function of the radial distance. The colors (red, brown, orange, yellow) show the results from the sampling lines (L85, L65, L20, L0) at the angles (85°, 65°, 20°, 0°) from the center of the initial cavity. Within the sector with continuous sampling the colors (green, blue, purple, black) show the sampling lines at the angles (6°, 17°, 28°, 39°) from the center of the initial cavity. Each subsector was further divided into two parts, marked with dotted and solid lines of each of the colors and from the center of the cavity the denomination of all sub-sectors are A(2), A(1), B(2), B(1), C(2), C(1), D(2), D(1).

The lowest values (green points) and the highest values (red points) were seen in the directions coinciding with and perpendicular to the direction of the cavity, respectively. A comparison of densities at the outermost (Figure A5-11), second outermost (Figure A5-12) and innermost (Figure A5-13) levels give generally decreasing densities, which is logical. In Appendix 8 tabulated values of the distribution of water content and dry density are given.

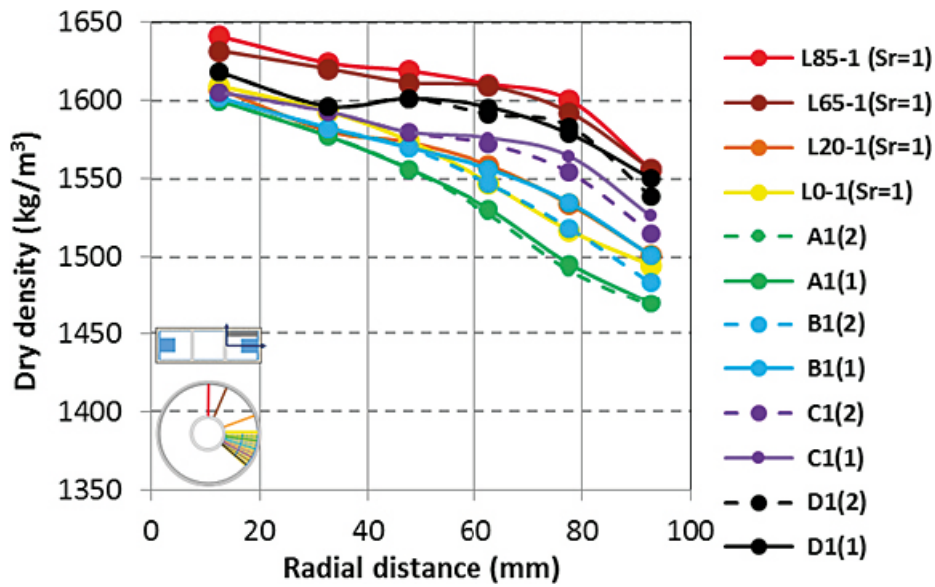


Figure A5-11. Distribution of dry density at the outermost level 1 in different directions. The colours (red, brown, orange, yellow, green, blue, purple, black) show the angles (85° , 65° , 20° , 0° , -6° , -17° , -28° , -39°) to the center of the cavity. The values are calculated from measured water contents and 100 % water saturation when the labels include ($S_r = 1$).

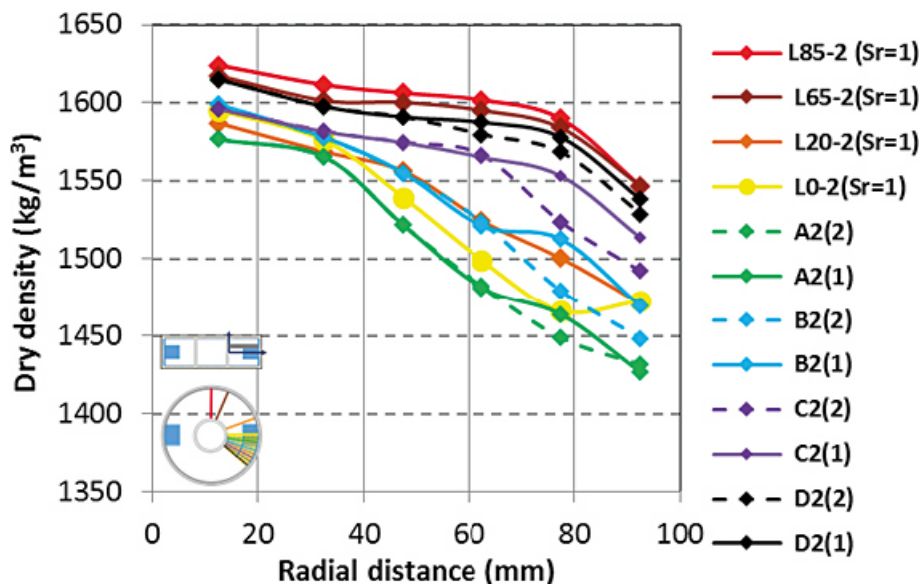


Figure A5-12. Distribution of dry density at the second outermost level 2 in different directions. The colours (red, brown, orange, yellow, green, blue, purple, black) show the angles (85° , 65° , 20° , 0° , -6° , -17° , -28° , -39°) to the center of the cavity. The values are calculated from measured water contents and 100 % water saturation when the labels include ($S_r = 1$).

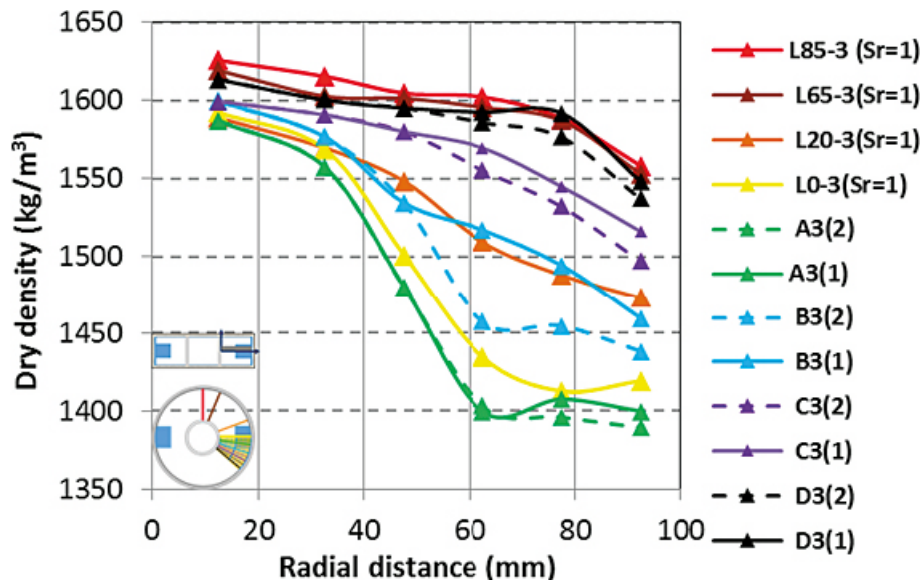


Figure A5-13. Distribution of dry density at the innermost level 3 in different directions. The colours (red, brown, orange, yellow, green, blue, purple, black) show the angles (85° , 65° , 20° , 0° , -6° , -17° , -28° , -39°) to the center of the cavity. The values are calculated from measured water contents and 100 % water saturation when the labels include ($S_r = 1$).

A5.4.3 Comments

The diagrams show that the dry density increases logically from the lines through the center of the cavity (A(2) and L0, green and yellow lines) to the lines perpendicular to the center of the cavity (L85/L90, red lines). The relatively low density of the samples at the radial distance of 92 mm, and at all three levels, of the most distant peripheral part L85 (red lines) was caused by the 0.65 mm gap between the bentonite ring and the outer ring with filter.

In addition, to the results presented above samples were taken in order to study the vertical symmetry mirrored by the horizontal symmetry plane, i.e. the correspondence between the results from samples taken from the upper and from the lower half of the bentonite ring. Along line L85 the water content was determined at all levels on both the lower half (levels 1, 2 and 3) and the upper half (levels 4, 5 and 6). The results are shown in Figure A5-14 where each colour represents a specific level, i.e. outermost, second outermost and innermost. The water contents determined on samples from the upper and lower half agree well and the maximum difference is seen between the outermost samples at the outermost radial distance which differ 0.6 %.

In the results from the sampled lines, i.e. L0–L85, presented in Figures A5-11 to A5-14 only the measured distribution of water content was taken into account and for the calculation of dry density the degree of saturation was assumed to be 100 %. Within the 45° sector and along one of the sampling lines, the measured bulk densities were also analyzed and the degree of saturation calculated. Within the sector the degree of saturation was analyzed at 108 points and the values varied between 99 % and 102 % with an average of 101 %, Table A5-2. Along the sampling line L85 all samples, from both the upper and lower part of the bentonite ring, were used for determination of water content. In parallel, bulk densities were measured on all samples taken from the sampling line L95, i.e. from both the upper and lower part of the bentonite ring. From the water contents and bulk densities measured along L85 and L95 the degrees of saturation were calculated. In those 36 points the degree of saturation varied between 100 % and 103 % with an average of 101 %.

Table A5-2. Degree of saturation of all samples from the 45° sector.

Degree of saturation (%)	Number of samples
99	2
100	19
101	59
102	24
103	4
104	
<hr/>	
Average	101
<hr/>	
Sum	108

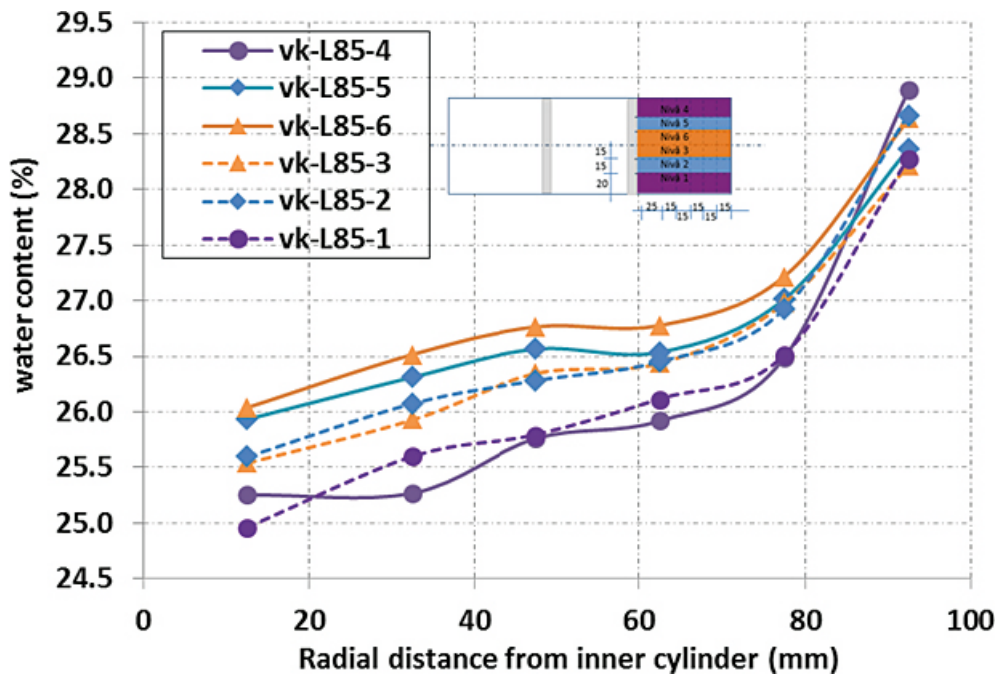


Figure A5-14. Water contents determined on samples taken along the sampling line L85. Samples were taken from both the upper half (solid lines) and lower half (dotted lines) of the bentonite ring. The colours (purple, blue, orange) show the levels (outermost, second outermost, innermost).

Photos of the bentonite ring and equipment used for the test SH1



Figure A6-1. Photo of cylinder ring with cavity used for test SH1.



Figure A6-2. Photos of the inner cylinder used for test SH1.

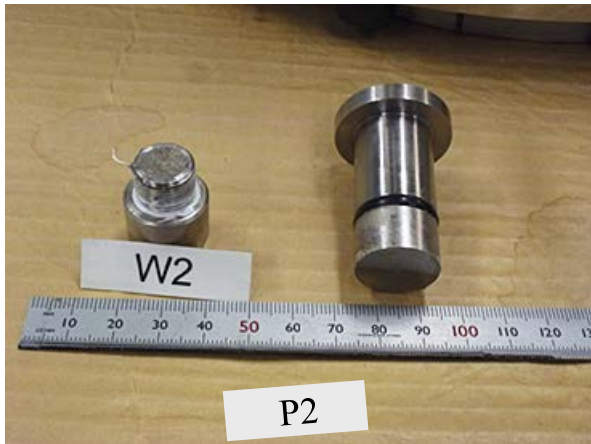


Figure A6-3. Photo of the casing used for the W2-thermocouple psychrometer and one of the pistons used for stress measurement P1 and P2.



Figure A6-4. Photos of the bentonite ring after dismantling of SH1. The bentonite ring, still inside the steel device but without the inner steel ring, sawn radially and with the sampling marked on the upper surface (to the left) and the dismantled bentonite ring with the filter still left on the outer surface and the sampling marked on the bottom surface (to the right).

Timetable for SH1 during start and end of test

Project	Buffer homogenisation
Material	MX-80
Type of water	de-ionized
Dimension	
Diameter	D (outer) = 300 mm, D (inner) = 100 mm
Height	H = 100 mm
Gaps	Length = 70 mm (circumferential) Height = 35 mm Depth = 50 mm
Estimated ingoing volume of water	
At start	3.8 dl
Including saturation of the bentonite	4.7 dl
Date	Activity
	Start of test
2012-11-26	Compaction of block to SH1
2012-11-30	The block was machined with a drill and a rotating lathe
2012-12-17	Sensors were mounted
2012-12-18	The test started by applying water from the lower inlet and approximately 5 kPa
2012-12-20	Water was flushed with 20 kPa for the first time
2013-01-02	Water was flushed with 100 kPa for the first time
2013-01-07	A constant water pressure of 100 kPa was applied
	End of test
2015-08-14 15:30	The water pressure was lowered from 100 kPa to 0 kPa
2015-08-19 08:45	The self healing test SH1 was terminated
2015-08-19 09:45	The sensors were removed and the upper lid was opened
2015-08-19 12:45	The bottom plate was removed
2015-08-19 14:50	The block was dismantled and the outer filter separated from the block
2015-08-19	The block was divided into two half circles. One was stored for later studies
2015-08-20	Determination of water contents was completed
2015-08-21	Density determination was completed
2015-09-04	All sensors were controlled

Tabulated values of water content after dismantling of SH1

Table A8-1, Table A8-2 and Table A8-3 contain tabulated values of the water contents determined after dismantling of SH1 at the levels 1, 2 and 3, i.e. outermost, second outermost and innermost levels. The Sample ID contains information about the location of the samples and the last figure shows the level. The first part of the Sample ID shows the location of the sampling profile. The line denominations (L0, L20, L65, L85) indicate that the samples were taken along lines at specific angles (0°, 20°, 65°, 85°) from the center of the cavity. The sector denominations (A(2), A(1), B(2), B(1), C(2), C(1), D(2), D(1)) indicate that the samples were taken within the sector with continuous sampling between 0 and -45° from the center of the cavity.

Table A8-1. Distribution of water content at level 1, i.e. outermost and towards the lid. For the samples from the lines, i.e. L0–L85, the dry density was calculated from the water content and $S_r = 100\%$.

Sample ID	Distance (mm)	Water content (%)	Dry density* (kg/m ³)
L0-1	12.5	26.2	1610
L0-1	32.5	26.8	1590
L0-1	47.5	27.5	1570
L0-1	62.5	28.6	1550
L0-1	77.5	29.9	1520
L0-1	92.5	30.9	1500
L20-1	12.5	26.2	1610
L20-1	32.5	27.3	1580
L20-1	47.5	27.6	1570
L20-1	62.5	28.2	1560
L20-1	77.5	29.2	1530
L20-1	92.5	30.6	1500
L65-1	12.5	25.3	1630
L65-1	32.5	25.7	1620
L65-1	47.5	26.1	1610
L65-1	62.5	26.2	1610
L65-1	77.5	26.8	1590
L65-1	92.5	28.3	1560
L85-1	12.5	25	1640
L85-1	32.5	25.6	1620
L85-1	47.5	25.8	1620
L85-1	62.5	26.1	1610
L85-1	77.5	26.5	1600
L85-1	92.5	28.3	1560
A(2)-1	12.5	26.7	1600
A(2)-1	32.5	27.5	1580
A(2)-1	47.5	28.4	1560
A(2)-1	62.5	29.8	1530
A(2)-1	77.5	31.2	1490
A(2)-1	92.5	33	1470
A(1)-1	12.5	26.7	1600
A(1)-1	32.5	27.5	1580
A(1)-1	47.5	28.4	1560
A(1)-1	62.5	29.8	1530
A(1)-1	77.5	31.2	1500
A(1)-1	92.5	32.7	1470
B(2)-1	12.5	26.5	1600
B(2)-1	32.5	27.3	1580
B(2)-1	47.5	27.8	1570
B(2)-1	62.5	28.9	1550

Sample ID	Distance (mm)	Water content (%)	Dry density* (kg/m ³)
B(2)-1	77.5	30.3	1520
B(2)-1	92.5	32	1480
B(1)-1	12.5	26.5	1600
B(1)-1	32.5	27.3	1580
B(1)-1	47.5	27.8	1570
B(1)-1	62.5	28.8	1560
B(1)-1	77.5	30	1530
B(1)-1	92.5	31.5	1500
C(2)-1	12.5	26.5	1610
C(2)-1	32.5	27.1	1590
C(2)-1	47.5	27.5	1580
C(2)-1	62.5	27.9	1570
C(2)-1	77.5	28.8	1550
C(2)-1	92.5	30.5	1520
C(1)-1	12.5	26.5	1610
C(1)-1	32.5	27.1	1590
C(1)-1	47.5	27.5	1580
C(1)-1	62.5	28	1580
C(1)-1	77.5	28.4	1560
C(1)-1	92.5	30	1530
D(2)-1	12.5	25.9	1620
D(2)-1	32.5	27	1600
D(2)-1	47.5	26.7	1600
D(2)-1	62.5	27.2	1590
D(2)-1	77.5	27.4	1580
D(2)-1	92.5	29.4	1540
D(1)-1	12.5	25.9	1620
D(1)-1	32.5	27	1600
D(1)-1	47.5	26.7	1600
D(1)-1	62.5	26.9	1600
D(1)-1	77.5	27.5	1580
D(1)-1	92.5	28.8	1550

Table A8-2. Distribution of water content at level 2, i.e. the second outermost level. For the samples from the lines, i.e. L0–L85, the dry density was calculated from the water content and $S_r = 100\%$.

Sample ID	Distance (mm)	Water content (%)	Dry density* (kg/m ³)
L0-2	12.5	26.7	1600
L0-2	32.5	27.5	1580
L0-2	47.5	29	1540
L0-2	62.5	30.7	1500
L0-2	77.5	32.2	1470
L0-2	92.5	31.9	1470
L20-2	12.5	27	1590
L20-2	32.5	27.8	1570
L20-2	47.5	28.3	1560
L20-2	62.5	29.6	1520
L20-2	77.5	30.7	1500
L20-2	92.5	32	1470
L65-2	12.5	25.9	1620
L65-2	32.5	26.5	1600
L65-2	47.5	26.5	1600
L65-2	62.5	26.7	1600
L65-2	77.5	27.2	1580
L65-2	92.5	28.7	1550

Sample ID	Distance (mm)	Water content (%)	Dry density* (kg/m ³)
L85-2	12.5	25.6	1620
L85-2	32.5	26.1	1610
L85-2	47.5	26.3	1610
L85-2	62.5	26.5	1600
L85-2	77.5	26.9	1590
L85-2	92.5	28.7	1550
A(2)-2	12.5	27.2	1580
A(2)-2	32.5	28	1570
A(2)-2	47.5	29.9	1520
A(2)-2	62.5	31.7	1480
A(2)-2	77.5	33.1	1450
A(2)-2	92.5	34.1	1430
A(1)-2	12.5	27.2	1580
A(1)-2	32.5	28	1570
A(1)-2	47.5	29.9	1520
A(1)-2	62.5	31.8	1480
A(1)-2	77.5	32.8	1460
A(1)-2	92.5	34.2	1430
B(2)-2	12.5	26.9	1600
B(2)-2	32.5	27.7	1580
B(2)-2	47.5	28.7	1560
B(2)-2	62.5	31	1520
B(2)-2	77.5	32.4	1480
B(2)-2	92.5	33.7	1450
B(1)-2	12.5	26.9	1600
B(1)-2	32.5	27.7	1580
B(1)-2	47.5	28.7	1560
B(1)-2	62.5	29.8	1520
B(1)-2	77.5	30.8	1510
B(1)-2	92.5	32.8	1470
C(2)-2	12.5	26.9	1600
C(2)-2	32.5	27.5	1580
C(2)-2	47.5	27.7	1570
C(2)-2	62.5	28.5	1570
C(2)-2	77.5	29.8	1520
C(2)-2	92.5	31.4	1490
C(1)-2	12.5	26.9	1600
C(1)-2	32.5	27.5	1580
C(1)-2	47.5	27.7	1570
C(1)-2	62.5	28.3	1570
C(1)-2	77.5	29	1550
C(1)-2	92.5	30.4	1510
D(2)-2	12.5	26.4	1620
D(2)-2	32.5	26.8	1600
D(2)-2	47.5	27.1	1590
D(2)-2	62.5	27.9	1580
D(2)-2	77.5	28.5	1570
D(2)-2	92.5	30.1	1530
D(1)-2	12.5	26.4	1620
D(1)-2	32.5	26.8	1600
D(1)-2	47.5	27.1	1590
D(1)-2	62.5	27.5	1590
D(1)-2	77.5	28	1580
D(1)-2	92.5	29.4	1540

Table A8-3. Distribution of water content at level 3, i.e. innermost and at the cavity centre. For the samples from the lines, i.e. L0–L85 the dry density was calculated from the water content and $S_r = 100\%$.

Sample ID	Distance (mm)	Water content (%)	Dry density* (kg/m ³)
L0-3	12.5	26.8	1590
L0-3	32.5	27.8	1570
L0-3	47.5	30.7	1500
L0-3	62.5	33.7	1430
L0-3	77.5	34.8	1410
L0-3	92.5	34.5	1420
L20-3	12.5	27	1590
L20-3	32.5	27.7	1570
L20-3	47.5	28.6	1550
L20-3	62.5	30.3	1510
L20-3	77.5	31.2	1490
L20-3	92.5	31.9	1470
L65-3	12.5	25.8	1620
L65-3	32.5	26.4	1600
L65-3	47.5	26.5	1600
L65-3	62.5	26.7	1600
L65-3	77.5	27	1590
L65-3	92.5	28.4	1550
L85-3	12.5	25.5	1630
L85-3	32.5	25.9	1620
L85-3	47.5	26.4	1600
L85-3	62.5	26.4	1600
L85-3	77.5	27	1590
L85-3	92.5	28.2	1560
A(2)-3	12.5	27.3	1590
A(2)-3	32.5	28.6	1560
A(2)-3	47.5	31.9	1480
A(2)-3	62.5	35.6	1400
A(2)-3	77.5	35.9	1400
A(2)-3	92.5	36.8	1390
A(1)-3	12.5	27.3	1590
A(1)-3	32.5	28.6	1560
A(1)-3	47.5	31.9	1480
A(1)-3	62.5	35.3	1400
A(1)-3	77.5	35.8	1410
A(1)-3	92.5	35.8	1400
B(2)-3	12.5	26.6	1600
B(2)-3	32.5	27.6	1580
B(2)-3	47.5	29.5	1530
B(2)-3	62.5	32.9	1460
B(2)-3	77.5	33.2	1450
B(2)-3	92.5	33.8	1440
B(1)-3	12.5	26.6	1600
B(1)-3	32.5	27.6	1580
B(1)-3	47.5	29.5	1530
B(1)-3	62.5	30.3	1520
B(1)-3	77.5	31.6	1490
B(1)-3	92.5	33.4	1460
C(2)-3	12.5	26.7	1600
C(2)-3	32.5	27.2	1590
C(2)-3	47.5	27.6	1580
C(2)-3	62.5	28.8	1560
C(2)-3	77.5	29.6	1530

Sample ID	Distance (mm)	Water content (%)	Dry density* (kg/m ³)
C(2)-3	92.5	31	1500
C(1)-3	12.5	26.7	1600
C(1)-3	32.5	27.2	1590
C(1)-3	47.5	27.6	1580
C(1)-3	62.5	28.1	1570
C(1)-3	77.5	29	1540
C(1)-3	92.5	30.3	1520
D(2)-3	12.5	26.2	1610
D(2)-3	32.5	26.7	1600
D(2)-3	47.5	26.9	1600
D(2)-3	62.5	27.4	1590
D(2)-3	77.5	27.8	1580
D(2)-3	92.5	29.2	1540
D(1)-3	12.5	26.2	1610
D(1)-3	32.5	26.7	1600
D(1)-3	47.5	26.9	1600
D(1)-3	62.5	27	1590
D(1)-3	77.5	27.1	1590
D(1)-3	92.5	28.5	1550

Claytech plastic cap model

A9.1 General

This appendix is largely taken from Börjesson et al. (1995).

The plastic model defines

- The boundaries of the elastic zone in the stress space (the yield surface).
- The boundaries of the plastic zone where failure occurs (the failure surface).
- The volumetric behaviour of the plastic zone (the flow surface and flow rules).

The following special functions of the plastic model have been included:

- The failure surface is curved so that no cohesion intercept is required. Figure A9-1 shows that the failure envelope may be drawn as a straight line in a log-log diagram over a large range of stresses for all types of bentonites and other conditions. A model of the failure envelope of the following form will thus yield the desired relation between the average effective stress p and the Mises' stress q :

$$q = ap^b \quad (\text{A9-1})$$

- There is a cap that limits the elastic part in the p -direction in order to make the model more general and to consider the hysteresis at compression and swelling.
- A post-failure reduction in strength (strain-softening) is also included.
- A small dilation at failure is also included in accordance with the measurements.

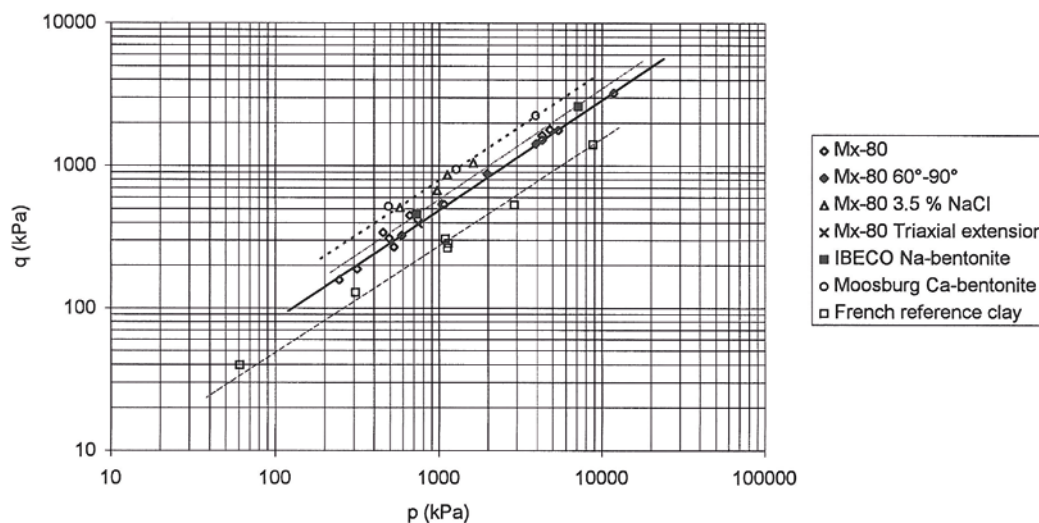


Figure A9-1. Compilation of a number of failure stress states determined by triaxial tests.

A9.2 Yield, failure, and flow surfaces

The laboratory testing and the modelling have yielded a proposal of a general material model. The model is described in Figures A9-2 and A9-3. Figure A9-2 shows the yield and failure surfaces in the q - p plane as well as the flow surface. The behaviour in the q - p plane is controlled by two lines that limit the allowable Mises' stress q :

$$q = ap^b \quad (\text{A9-2})$$

$$q = cp^b \quad (\text{A9-3})$$

where $a > c$

The upper line (Equation A9-2) is a combined yield and failure surface (1) at the over-consolidated state (dry side) while the lower line (Equation A9-3) is the failure surface (4) at the normally consolidated side (wet side) corresponding to the critical state line of the Cam Clay model. The lower line is also the top point of the yield surface at all states. The other parts of the yield surface are the elliptic cap (3) which intersects the p -axis at p_b and an elliptic transition surface between the other two parts (2).

The plastic behaviour at the yield surface is controlled by the flow surface (plastic potential), which is also shown in Figure A9-2. The flow surface consists of two ellipses. One ellipse for parts 1 and 2, where the flow is not associated since the tangent of the flow surface does not coincide with the tangent of the yield surface, and one for the cap (3), which coincides with the cap and where the flow is thus associated. By letting the ellipse at 1 and 2 be large, the inclination of the flow surface and thus the dilatancy can be made small.

The behaviour of a material modelled in this way resembles the Cam-Clay model but differs in some vital parts. The behaviour is illustrated in Figure A9-3, where the stress strain behaviour (q - ϵ) and the change in location of the yield and failure surfaces are shown for two stress paths. The upper stress path from A to B shows the behaviour on the wet side. The stress path at first goes in the elastic region. When the stress path intersects the cap the material starts to plasticize, decrease in volume, and move the cap upwards with the top following the lower failure line. The other stress path from C to D shows the behaviour in the over-consolidated dry part. The stress path is located entirely in the elastic domain and remains so until it intersects the combined failure and yield surface, where the material starts to yield and increase its volume. The volume increase makes the cap of the yield surface shrink at constant q until the transition surface has reached the point D. At that occasion we have a new yield surface, which is illustrated by broken lines in the figure. If the strain is further increased, q will decrease and the cap will be further reduced until the top part hits point E on the "critical state line", where no further change in q or volume will take place.

The following parameters are required for the definition of the cap plasticity.

a = parameter defining the failure surface

c = parameter defining the critical state line

b = parameter defining the shape of those lines

K = influence of the intermediate principal stress on q_f

γ = relation between the two axes of the elliptic yield transition surface. Vertical axis divided with the horizontal axis. $0 < \gamma \leq 1$

R = relation between the two axes of the elliptic cap. Horizontal axis divided with the vertical axis. $0 < R \leq 1$

p_b = intersection between the cap and the p -axis

p_f = intersection between the elliptic flow surface and the p -axis at $p < 0$

p versus $e \log(1 + e^V_{pl})$ = cap hardening relation

The location of the cap is defined by the intercept p_b between the cap and the p axis. The location of the flow surface is defined by the intercept p_f between the flow surface and the p axis (usually a large negative value). The shape of the elliptic transition surface needs to be defined. This is made by the ratio γ of the size of the minor and the major axes of this ellipse.

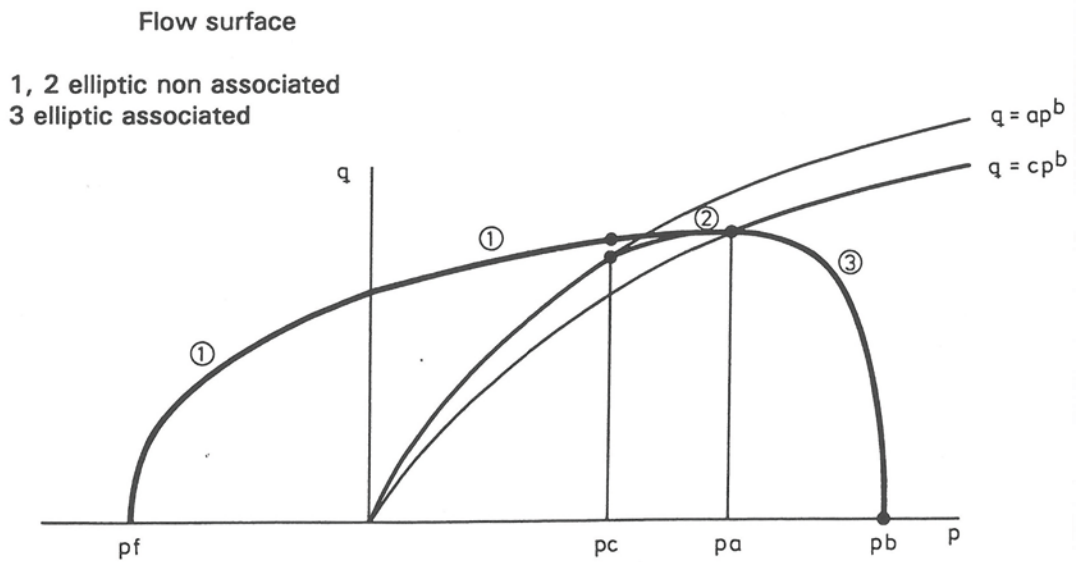
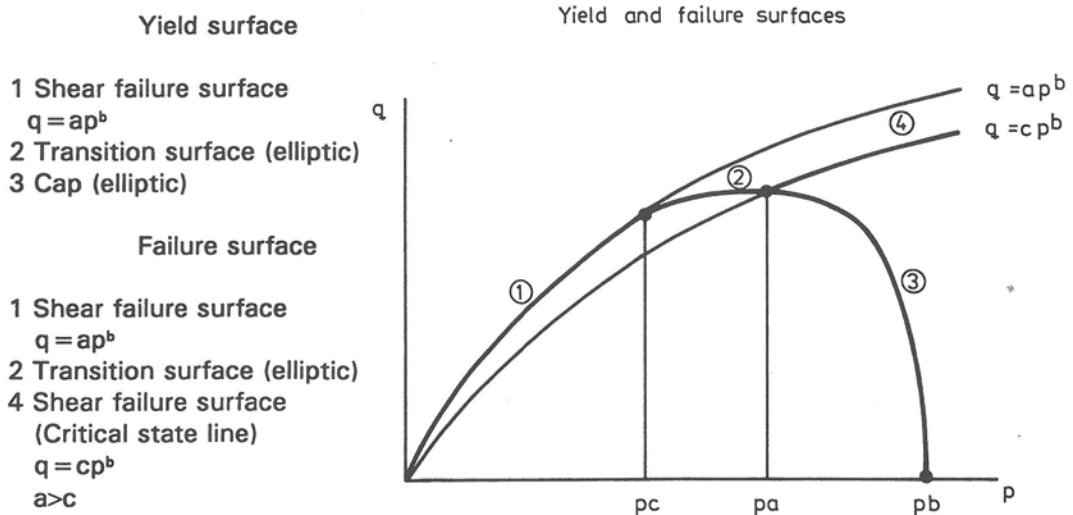


Figure A9-2. Claytech plastic cap model. The yield surface, failure surface and plastic flow surface are shown in the q - p plane.

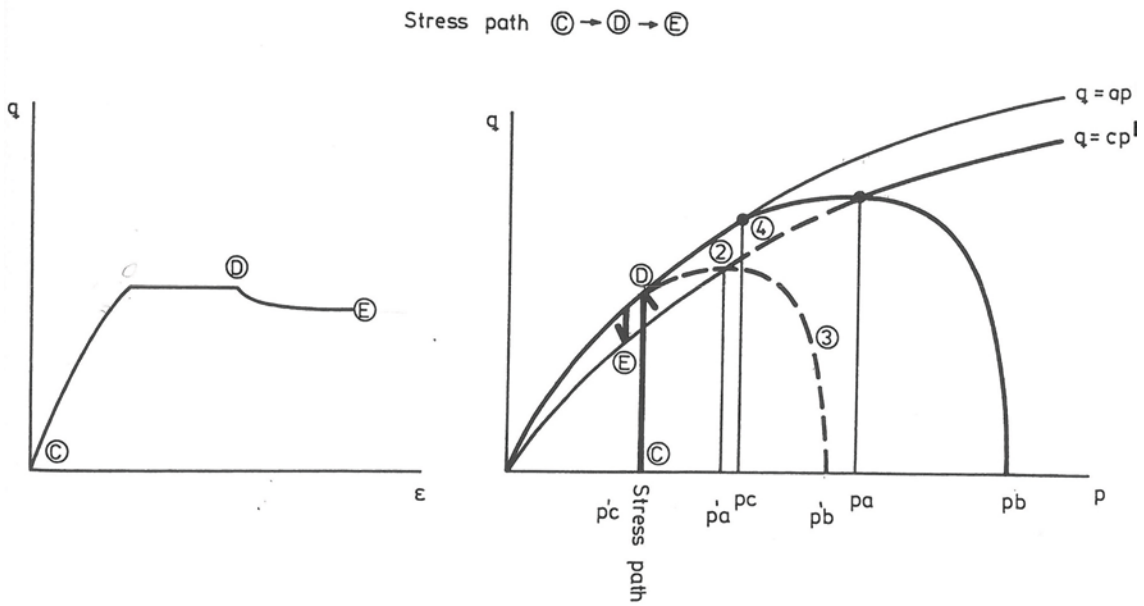
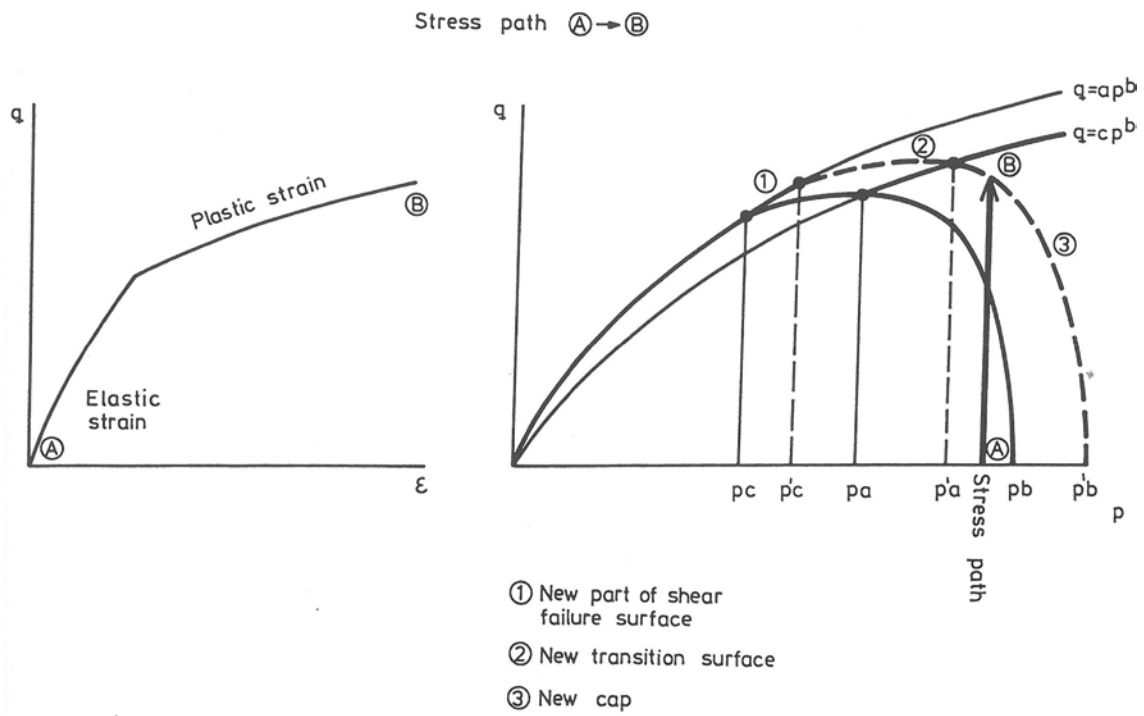


Figure A9-3. Illustration of the behaviour of the model at two stress paths.

A9.3 Cap hardening

When the average stress p exceeds the “preconsolidation pressure” p_b the result will be a non-recoverable plastic volume decrease and the cap will expand. The total volume decrease is the sum of the elastic and plastic volume decreases. The plastic volume change is thus the difference between the total volume change and the elastic volume change. It can be described as a relation between the average stress and the plastic volume change according to Equation A9-4.

$$e_{pl}^v = f(p_b) \quad (A9-4)$$

The expansion of the cap at the plastic volume decrease has a corresponding shrinkage of the cap when the material expands the volume plastically due to dilation close to the failure envelop. The magnitude of the cap shrinkage is given by the relation in Equation A9-4.

The expansion of the cap or “cap hardening” is defined as the relation between the average stress p and the logarithmic plastic volumetric strain ${}^e\log(1+e_{pl}^v)$ where $e_{pl}^v = \Delta V_{pl}/V$ is the “engineering strain”.

ABAQUS works with logarithmic strain which differs from the engineering strain definition. The strains are added according to Equation A9-5.

$${}^e\log(1+e_{tot}^v) = {}^e\log(1+e_{el}^v) + {}^e\log(1+e_{pl}^v) \quad (A9-5)$$

where

e_{tot}^v = total volumetric strain ($= \Delta V/V$)

e_{el}^v = elastic volumetric strain ($= \Delta V_{el}/V$)

e_{pl}^v = plastic volumetric strain ($= \Delta V_{pl}/V$)

The cap hardening thus forms a list of how the logarithmic plastic strain increases with increasing average stress.

SKB is responsible for managing spent nuclear fuel and radioactive waste produced by the Swedish nuclear power plants such that man and the environment are protected in the near and distant future.

skb.se